

# Closing the loops on Southern Ocean dynamics: From the circumpolar current to ice shelves and from bottom mixing to surface waves

Luke G. Bennetts<sup>1</sup>, Callum J. Shakespeare<sup>2,3</sup>, Catherine A. Vreugdenhil<sup>4</sup>,  
 Annie Foppert<sup>5,6</sup>, Bishakhdatta Gayen<sup>4,7,8</sup>, Amelie Meyer<sup>3,6</sup>,  
 Adele K. Morrison<sup>2,8</sup>, Laurie Padman<sup>9</sup>, Helen E. Phillips<sup>5,6,8</sup>,  
 Craig L. Stevens<sup>10,11</sup>, Alessandro Toffoli<sup>4</sup>, Navid C. Constantinou<sup>2,3</sup>,  
 Jesse Cusack<sup>12</sup>, Ajitha Cyriac<sup>3,6,8,13</sup>, Edward W. Doddridge<sup>5,6</sup>,  
 Matthew H. England<sup>8,14</sup>, D. Gwyn Evans<sup>15</sup>, Petra Heil<sup>5,16</sup>,  
 Andrew McC. Hogg<sup>2,3</sup>, Ryan M. Holmes<sup>17</sup>, Wilma G. C. Huneke<sup>2,3</sup>,  
 Nicole L. Jones<sup>18</sup>, Shane R. Keating<sup>14</sup>, Andrew E. Kiss<sup>2</sup>, Noa Kraitzman<sup>19</sup>,  
 Alena Malyarenko<sup>10</sup>, Craig D. McConnochie<sup>20</sup>, Alberto Meucci<sup>4</sup>,  
 Fabien Montiel<sup>21</sup>, Julia Neme<sup>14</sup>, Maxim Nikurashin<sup>6</sup>,  
 Ramkrushnbhai S. Patel<sup>3,6</sup>, Jen-Ping Peng<sup>18</sup>, Matthew Rayson<sup>18</sup>,  
 Madelaine G. Rosevear<sup>4,8</sup>, Taimoor Sohail<sup>8,14</sup>, Paul Spence<sup>5,6,8</sup>,  
 Geoffrey J. Stanley<sup>14,22</sup>

<sup>1</sup>University of Adelaide, Adelaide, SA, Australia

<sup>2</sup>Australian National University, Canberra, ACT, Australia

<sup>3</sup>ARC Centre of Excellence for Climate Extremes, Australia

<sup>4</sup>University of Melbourne, Melbourne, VIC, Australia

<sup>5</sup>Australian Antarctic Program Partnership, TAS, Australia

<sup>6</sup>University of Tasmania, Hobart, TAS, Australia

<sup>7</sup>Centre for Atmospheric and Oceanic Sciences, Indian Institute of Science, Bengaluru, India

<sup>8</sup>ARC Centre for Excellence in Antarctic Science, Australia

<sup>9</sup>Earth and Space Research, Corvallis, OR, USA

<sup>10</sup>National Institute of Water and Atmospheric Research, New Zealand

<sup>11</sup>University of Auckland, Auckland, New Zealand

<sup>12</sup>Oregon State University, Corvallis, OR, USA

<sup>13</sup>CSIRO, Perth, WA, Australia

<sup>14</sup>University of New South Wales, Sydney, NSW, Australia

<sup>15</sup>National Oceanography Centre, Southampton, United Kingdom

<sup>16</sup>Australian Antarctic Division, Kingston, TAS, Australia

<sup>17</sup>University of Sydney, Sydney, NSW, Australia

<sup>18</sup>University of Western Australia, Perth, WA, Australia

<sup>19</sup>Macquarie University, Sydney, NSW, Australia

<sup>20</sup>University of Canterbury, Christchurch, New Zealand

<sup>21</sup>University of Otago, Dunedin, New Zealand

<sup>22</sup>University of Victoria, Victoria, BC, Canada

## Key Points:

- Contemporary perspectives on the different components of the Southern Ocean dynamic system from distinct research communities are reviewed
- Key connections between different components of Southern Ocean dynamics are highlighted
- Cross-cutting priorities for future Southern Ocean physical science are identified

---

Corresponding author: Luke G. Bennetts, [luke.bennetts@adelaide.edu.au](mailto:luke.bennetts@adelaide.edu.au)

**Abstract**

A holistic review is given of the Southern Ocean dynamic system, in the context of the crucial role it plays in the global climate and the profound changes it is experiencing. The review focuses on connections between different components of the Southern Ocean dynamic system, drawing together contemporary perspectives from different research communities, with the objective of “closing loops” in our understanding of the complex network of feedbacks in the overall system. The review is targeted at researchers in Southern Ocean physical science with the ambition of broadening their knowledge beyond their specific field and facilitating better-informed interdisciplinary collaborations. For the purposes of this review, the Southern Ocean dynamic system is divided into four main components: large-scale circulation; cryosphere; turbulence; and gravity waves. Overviews are given of the key dynamical phenomena for each component, before describing the linkages between the components. The reviews are complemented by an overview of observed Southern Ocean trends and future climate projections. Priority research areas are identified to close remaining loops in our understanding of the Southern Ocean system.

**Plain Language Summary**

The United Nations has identified 2021–2030 as the Decade of Ocean Science, with a goal to improve predictions of ocean and climate change. Improved understanding of the Southern Ocean is crucial to this effort, as it is the central hub of the global ocean. The Southern Ocean is the formation site for the dense water that fills the deep ocean, sequesters the majority of anthropogenic heat and carbon, and controls the flux of heat to Antarctica. The large-scale circulation of the Southern Ocean is strongly influenced by interactions with sea ice and ice shelves, and is mediated by smaller scale processes, including eddies, waves and mixing. The complex interplay between these dynamic processes remains poorly understood, limiting our ability to understand, model and predict changes to the Southern Ocean, global climate and sea level. This article provides a holistic review of Southern Ocean processes, connecting the smallest scales of ocean mixing to the global circulation and climate. It seeks to develop a common language and knowledge-base across the Southern Ocean physical science community to facilitate knowledge-sharing and collaboration, with the aim of closing loops on our understanding of one of the world’s most dynamic regions.

## 1 Introduction

The Southern Ocean is a harsh, dynamic and remote environment, which has profound influence over Earth’s present and future climates. It is home to the global ocean’s strongest winds, coldest ocean surface temperatures, largest ice shelves, most voluminous ocean currents, most extreme surface waves, and more. The Southern Ocean acts as a central hub of the global ocean where waters from the Atlantic, Pacific and Indian basins converge and mix. As such, it regulates the uptake of heat and carbon at a global scale. To the south, the unique dynamics of the Southern Ocean control the flux of heat to Antarctica’s fringes, thus controlling the stability of the Antarctic Ice Sheet (which holds the volumetric equivalent of about 60 m in global mean sea level; [Fretwell et al., 2013](#); [Morlighem et al., 2020](#)). However, the Southern Ocean is experiencing profound, large-scale changes, many at unprecedented and accelerating rates. These include the lowest ever recorded sea ice minima in the past two Austral summers ([NISDC, 2023](#)), rapid melting of the West Antarctic Ice Sheet ([Paolo et al., 2015](#)), and the warming and freshening of the abyssal waters formed in the Southern Ocean ([Purkey & Johnson, 2013](#)).

The observed large-scale changes in the Southern Ocean climate assimilate a rich spectrum of dynamics, spanning thousand-kilometre scale ocean currents, tens- to hundred-kilometre scale polynyas, ten-kilometre wide eddies, kilometre-scale convection, hundred-metre scale surface waves, metre-scale pancake sea ice and millimetre-scale turbulent mixing. The network of linkages and feedbacks between the different components of the Southern Ocean dynamic system creates challenges in understanding and predicting this vitally important region and its role in global climate and ecosystems. The objective of this review is to “close loops” in understanding of the Southern Ocean dynamic system by drawing together contemporary perspectives on the different components of the system from different research communities within the broader field of Southern Ocean physical science. It aims to help the range of Southern Ocean researchers understand the context of their own work within the broader field, thereby facilitating better informed collaborations. As such, the focus is on a holistic physical understanding of the Southern Ocean, rather than associated aspects of atmospheric dynamics, land-based ice, and dynamical interactions with biogeochemistry. Instead, the reader is directed to reviews by [Noble et al. \(2020\)](#) for Antarctic Ice Sheet dynamics and [Henley et al. \(2020\)](#) for Southern Ocean biogeochemistry. In addition, there exist a number of reviews into different aspects of atmospheric dynamics and air–sea coupling, including the Southern Annular Mode ([Fogt & Marshall, 2020](#)), Southern Ocean precipitation ([Siems et al., 2022](#)) and air–sea–ice exchanges ([S. Swart et al., 2019](#)).

There are several definitions of the Southern Ocean extent; we take a dynamical perspective and consider the Southern Ocean system to be bounded by the northern most extent of the Antarctic Circumpolar Current, and that its southern boundary includes the sub-ice shelf cavities fringing the Antarctic continent, which terminate at the glacial ice shelf grounding zone. In the vertical direction, we consider dynamics stretching from the ocean surface, which is occupied by surface gravity waves or sea ice, to the ocean bottom, which is a key region for the generation of internal waves and subsequent mixing. We divide the Southern Ocean dynamic system into four main components: large-scale circulation; cryosphere; turbulence; and gravity waves. Large-scale circulation incorporates the Antarctic Circumpolar Current, Antarctic Slope Current, sub-polar gyres, and the meridional overturning circulation. The cryosphere includes sea ice and glacial ice shelves, as well as dynamic phenomena in the sub-shelf cavities. We define turbulence as chaotic dynamics spanning from mesoscale eddies and polynya convection at the largest end, down to millimetre-scale diapycnal mixing. Gravity waves includes surface waves, internal waves and tides. [Fig. 1](#) gives a spatio-temporal perspective of phenomena reviewed, which shows the broad range of scales covered. We focus the review on the connected nature of interactions between the different phenomena.

We structure the review around the four main dynamical components identified above, commencing with large-scale circulation (§2) to provide an global perspective on the South-

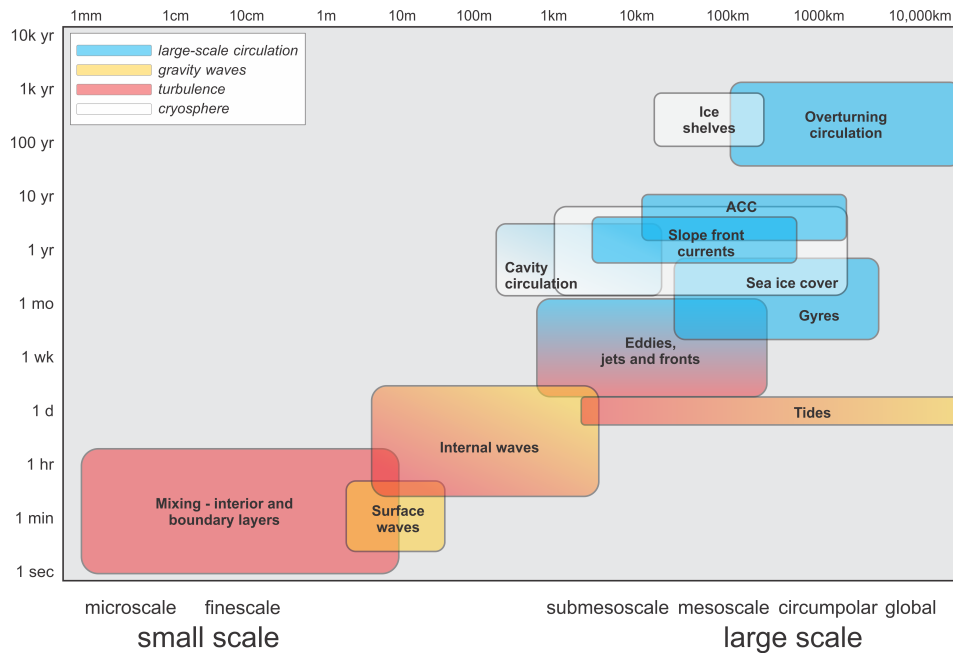


**Figure 1.** Spatio-temporal perspective of key dynamic phenomena reviewed, where colours indicate association to the four key dynamical components. The scales represented in this diagram indicate the time (and space) scales of the phenomena themselves, rather the much broader range of time scales over which these phenomena vary (e.g., internal waves exist at timescales of hours, but internal wave amplitudes vary on daily, seasonal and interannual timescales due to changes in stratification and atmospheric forcing).

128 ern Ocean dynamical environment, followed by cryosphere (§ 3), turbulence (§ 4) and gravity  
129 waves (§ 5). In each section, we give an overview of the fundamental physics of the dynam-  
130 ical component being considered, before describing the linkages between these components.  
131 In prioritising these linkages, we focus on the most impactful, those in areas of growing  
132 research activity, and those where significant outstanding questions remain. We typically  
133 describe the linkages in the section corresponding to the component that is being impacted,  
134 thereby minimising repetition. Each section ends with a short overview of the impacts of the  
135 component in the other sections to ‘close the loops’. The sections dedicated to the four dy-  
136 namical components are followed by an overview of relevant Southern Ocean climate trends  
137 and future climate projections (§ 6). We close the review with a summary of our present  
138 understanding of Southern Ocean dynamics and by identifying cross-cutting priorities for  
139 future Southern Ocean physical science (§ 7).

## 2 Large-scale circulation

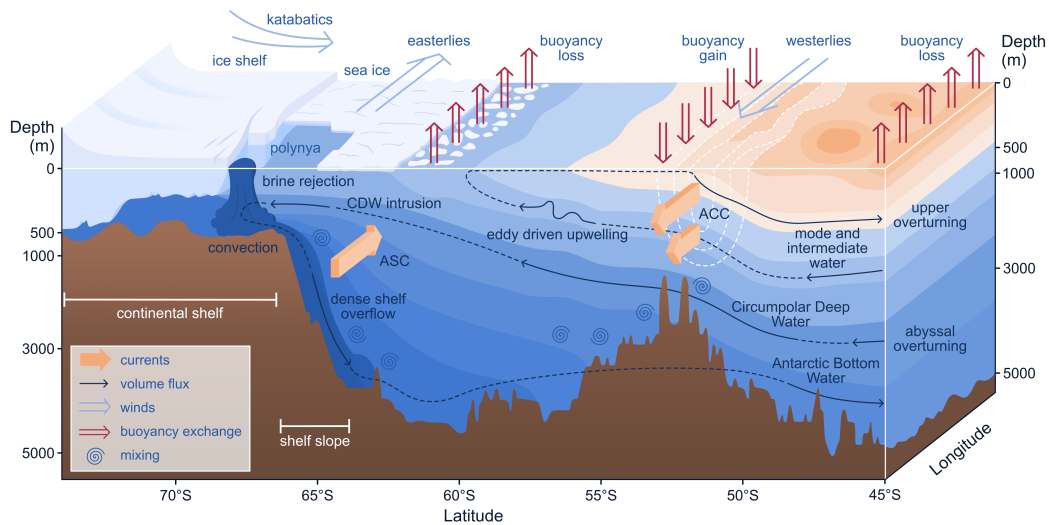


**Figure 2.** Schematic of the Southern Ocean’s large-scale circulation, where the ocean colours indicate the density, ranging from lighter (dark orange) to denser (dark blue) waters, and isopycnal contours are the interfaces between the layers. The horizontal gradients in density are correlated with largely geostrophic currents, including the Antarctic Circumpolar Current (ACC) and Antarctic Slope Current (ASC), above the shelf slope/break. Antarctic Bottom Water is generated by convection and brine rejection on the continental shelf, and flows down into the abyssal ocean. Warmer Circumpolar Deep Water (CDW) is upwelled in the mid-depths and plays a key role in the melt rate of glacial ice shelves. These processes collectively form the Southern Ocean component of the upper and abyssal overturning cells, as indicated by the dashed lines. Farther to the north, at the density fronts of the ACC, are the formation sites of northward flowing mode and intermediate waters. The topography, isopycnals, and glacial ice shelf profile on the southern side of the schematic are from observations in the Ross Sea, although they are artificially extended to the north to represent a more typical condition for the Antarctic Circumpolar Current. Note that the depth scale is not linear.

141 Large-scale circulation is here interpreted as flows at horizontal scales larger than  
 142 mesoscale eddies (greater than  $\sim 300$  km). A schematic representation of the large-scale  
 143 circulation in the vertical–latitude plane (Fig. 2) identifies the ‘meridional overturning cir-  
 144 culation’, which includes the upper (clockwise in Fig. 2; §2.4) and abyssal (anticlockwise;  
 145 §2.5) branches. Figure 3 shows a plan view of the entire Southern Ocean to highlight the  
 146 horizontal circulation features: the Antarctic Circumpolar Current (§2.1), Antarctic Slope  
 147 Current (§2.2), and Weddell and Ross gyres (§2.3).

148 The large-scale circulations are broadly in geostrophic balance, although multi-scale  
 149 interactions play a fundamental role in their variability and response to forcing. The aim of  
 150 this section is to offer a perspective on the processes involved in sustaining these circulations  
 151 and the links that bring them together. In broad terms, they are sustained through multi-  
 152 scale interactions between mean flows, turbulence, topography, dynamic stresses, isopycnal  
 153 mixing and buoyancy fluxes. The understanding of how the exchange of tracers, momentum,  
 154 and vorticity connect the different components of the large-scale Southern Ocean circulation  
 155 together is rapidly evolving. The reader is referred to previous reviews on Southern Ocean  
 156 circulation for more details on specific processes. In particular, [Rintoul and Naveira Gara-](#)

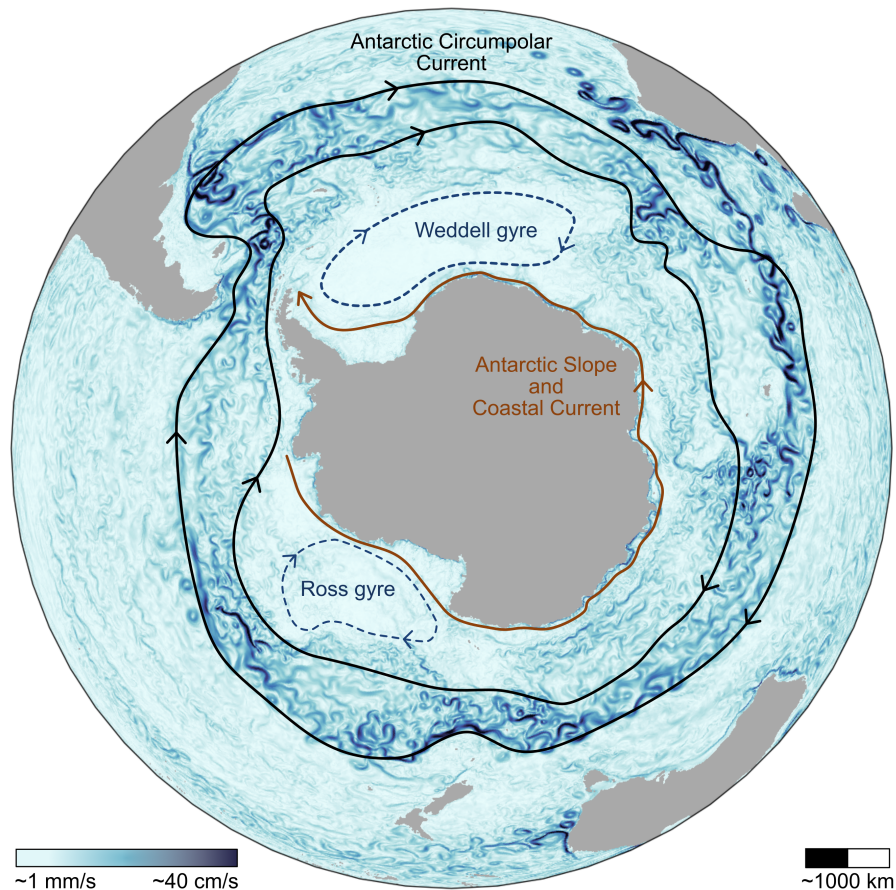


**Figure 3.** A schematic plan view of the large-scale circulation of the Southern Ocean. The key features are the braided network of eddies and jets circumnavigating the continent that comprise the eastward-flowing Antarctic Circumpolar Current (for which the northern and southern limits, or fronts, are represented by black contours), the Weddell and Ross gyres (blue dotted lines), and the westward-flowing Antarctic Slope/Coastal Current nearer the continent (brown line). The Slope Current exists everywhere except along the western side of the Antarctic Peninsula, where the Circumpolar Current flows very close to the shelf slope. The current/gyre lines represent contours of streamfunction, sketched based on typical time-mean flows in a global ocean model. The background image shows a typical snapshot of daily mean surface flow speed from the ACCESS-OM2-01 global ocean model (Kiss et al., 2020).

157 [bato \(2013\)](#) provide a detailed discussion of the Southern Ocean’s role in the global ocean  
 158 circulation and climate, while [A. F. Thompson et al. \(2018\)](#) and [Vernet et al. \(2019\)](#) provide  
 159 detailed reviews of the Antarctic Slope Current and Weddell Gyre, respectively. There is no  
 160 review article specifically focused on the Ross Gyre; however, the research article of [Dotto  
 161 et al. \(2018\)](#) provides a focused examination of its strength, forcing and variability.

## 162 2.1 Antarctic Circumpolar Current

163 The Antarctic Circumpolar Current is the largest ocean current in the world by volume  
 164 flux. It encircles Antarctica, in places extending from the surface to the seafloor, connecting  
 165 the Atlantic, Pacific and Indian ocean basins, and forming the hub of the global ocean

166 circulation (e.g., see Fig. 1 of Meredith, 2022). The sloping density surfaces (isopycnals)  
 167 associated with the Antarctic Circumpolar Current provide a connection between the ocean  
 168 surface and the abyss. They allow fluid from the deep ocean to upwell without changing its  
 169 density, which is a crucial component of the global overturning circulation (§§ 2.4–2.5). The  
 170 regions of sharpest meridional density gradient at the surface are described as the (density)  
 171 fronts of the Antarctic Circumpolar Current, with the northern- and southern-most fronts  
 172 (Fig. 3) enclosing the region of strongest current speed.

173 The geometry of the Antarctic Circumpolar Current is unique; unlike other ocean cur-  
 174 rents, there are no continents blocking its quasi-zonal flow around the globe. This unique  
 175 configuration means that the dynamics of the Antarctic Circumpolar Current cannot be ex-  
 176 plained using the classical geophysical fluid dynamics theories that govern gyres, although  
 177 some have tried to apply these concepts, such as the Sverdrup balance (e.g., Stommel, 1957;  
 178 Webb, 1993; C. W. Hughes, 1997). The integrated momentum balance of the Antarctic Cir-  
 179 cumpolar Current is extremely simple: wind stress at the surface is predominantly balanced  
 180 by topographic form stress at the bottom (Masich et al., 2015a), as originally proposed by  
 181 Munk and Palmén (1951). However, despite the wind stress being the dominant source of  
 182 momentum for the Antarctic Circumpolar Current, changing the wind has almost no effect  
 183 on the total zonal baroclinic transport (Straub, 1993; Hallberg & Gnanadesikan, 2001; Tans-  
 184 ley & Marshall, 2001; Munday et al., 2013; Constantinou & Hogg, 2019), and increasing the  
 185 bottom drag increases the total zonal transport (D. P. Marshall et al., 2017; Constantinou,  
 186 2018). Moreover, although mesoscale turbulence is believed to play a crucial role in fluxing  
 187 momentum downwards from the surface to be dissipated at depth, the momentum budget  
 188 adjusts to wind changes within a month (Ward & Hogg, 2011; Masich et al., 2015b), while  
 189 the response of the mesoscale turbulence is much slower, taking months to years to adjust  
 190 (Meredith & Hogg, 2006; Sinha & Abernathy, 2016; Hogg et al., 2022). Modelling results  
 191 also suggest that the Antarctic Circumpolar Current responds in different ways to specific  
 192 spatial patterns of wind stresses, such as those associated with the interplay of the different  
 193 phases of the Southern Annular Mode and El Niño-Southern Oscillation (Langlais et al.,  
 194 2015).

195 The Antarctic Circumpolar Current appears as a single monolithic current in a time-  
 196 mean view, but the instantaneous current is better described as a complex network of  
 197 interconnected jets and eddies (§ 4.1). This smaller-scale structure supports a plethora of  
 198 multiscale interactions: eddy-jet interactions shorten eddy lifetimes (R. Liu et al., 2022);  
 199 jet-topography interactions can lead to rapid changes in ocean ventilation (Klocker, 2018);  
 200 and a unique set of interactions occur where the eastward flowing Antarctic Circumpolar  
 201 Current in the Southern Ocean is fast enough to arrest westward propagating Rossby waves  
 202 (Klocker & Marshall, 2014). Downstream of large bathymetric features, the time-mean flow  
 203 field exhibits standing meanders, which are thought to be the result of arrested Rossby  
 204 waves (A. F. Thompson & Naveira Garabato, 2014). Arrested Rossby waves also affect  
 205 the stability of the current, allowing instabilities to grow when the wave speed matches or  
 206 exceeds the flow speed and is oriented in the opposing direction, i.e., the wave is travelling  
 207 upstream (Stanley et al., 2020). These standing meander regions are also highly energetic,  
 208 with enhanced cross-frontal exchange (A. F. Thompson & Sallée, 2012), eddy heat flux  
 209 (Foppert et al., 2017) and upwelling (Tamsitt et al., 2017). The Antarctic Circumpolar  
 210 Current flows along standing meanders, whose curved paths lead to horizontal divergence  
 211 and vortex stretching that couples the upper and lower water column, modifying deep  
 212 currents and cross-frontal exchange in patterns locked to the phase of the meander (Meijer  
 213 et al., 2022).

## 214 2.2 Antarctic Slope Current

215 The steep gradient of the Antarctic continental shelf slope imposes a strong geometric  
 216 constraint on cross-slope flow as it invokes a large potential vorticity gradient. Consequently,  
 217 ocean flows in this region are (to first order) oriented in an along-slope direction, and

218 known as the Antarctic Slope Current. The Antarctic Slope Front is the associated front  
219 and is manifested by a large cross-slope density gradient; the slope front may at times  
220 be composed of multiple individual fronts. The Antarctic Slope Current is strongest in  
221 East Antarctica and exists everywhere along the continental slope except for the western  
222 Antarctic Peninsula, where the Antarctic Slope Current is replaced by the southernmost  
223 edge of the Antarctic Circumpolar Current (Mathiot et al., 2011; Armitage et al., 2018;  
224 A. L. Stewart et al., 2019; Pauthenet et al., 2021; Huneke et al., 2022). The Antarctic Slope  
225 Current advects tracers, such as heat, salt and nutrients around the continent, and the  
226 exchange of distinct water masses across the current is pivotal for the climate system (see  
227 § 3.1.1, § 2.5). The advancement of numerical ocean model capabilities over the past decade,  
228 as well as increased efforts to collect observations (ship-based, moorings/fixed, animal-borne,  
229 autonomous vehicles), has led to a rapidly improved understanding of the Antarctic Slope  
230 Current dynamics.

231 The Antarctic Slope Current is driven primarily by winds and buoyancy forcing from  
232 both the atmosphere and meltwater. At leading order, easterly winds around Antarctica  
233 are oriented in an along-slope direction (Hazel & Stewart, 2019), driving onshore Ekman  
234 transport, creating a cross-slope density gradient, and thereby driving an along-slope current  
235 in thermal wind balance. The momentum transfer from the atmosphere to the ocean occurs  
236 via the sea ice that covers the continental shelf for most of the year. Recent high resolution  
237 model simulations indicate that the surface stress over the continental shelf slope vanishes in  
238 the presence of sea ice (A. L. Stewart et al., 2019; Si et al., 2021), and the sea ice distributes  
239 the momentum input provided by the wind away from the continental slope. In addition  
240 to winds, buoyancy fluxes from sea ice, ice shelves and the atmosphere help sustain the  
241 cross-slope pressure gradients that support the Antarctic Slope Current. Freshwater forcing  
242 from ice shelf melting plays a particularly important role (Fahrback et al., 1992; Moffat et  
243 al., 2008), with new observations suggesting that glacial melt is especially important for the  
244 generation of the Antarctic Slope Current in the Amundsen Sea (A. F. Thompson et al.,  
245 2020). This mechanism is supported by model simulations with amplified freshwater forcing  
246 (to represent basal melting of ice shelves), which show an increased cross-slope density  
247 gradient and enhanced Antarctic Slope Current (Naughten et al., 2018; Moorman et al.,  
248 2020; Beadling et al., 2022). The Antarctic Slope Current is reinforced by tides through a  
249 process called tidal rectification (§ 5.2.1; A. L. Stewart et al., 2019; Si et al., 2021).

250 The state of the Antarctic Slope Current is closely related to Dense Shelf Water export,  
251 which occurs downstream of the Ross Sea, Adelie Land, Prydz Bay, and the Weddell Sea  
252 (A. F. Thompson et al., 2018). The presence of dense water lifts the isopycnals at depth,  
253 connecting the shelf with the offshore ocean and creating a pathway for eddy-driven cross-  
254 slope heat exchange (A. L. Stewart & Thompson, 2015). Further, the Dense Shelf Water  
255 descending the continental shelf gives rise to a bottom-intensified Antarctic Slope Current  
256 flow in these locations, unlike other regions where it is surface intensified (e.g., Heywood et  
257 al., 1998; Huneke et al., 2022).

## 258 2.3 Weddell and Ross Gyres

259 The Weddell and Ross gyres are dominant features of the lateral circulation of the  
260 Southern Ocean, located south of the Antarctic Circumpolar Current and north of the  
261 Antarctic continental shelf (Fig. 3). They play a mediating role in the exchange of waters  
262 between the relatively warm waters within the Antarctic Circumpolar Current and the cold  
263 continental shelf. Both gyres are located adjacent to one of the formation sites of Dense  
264 Shelf Water around Antarctica (Purkey et al., 2018; Meredith, 2013). Thus, the properties  
265 of exported Antarctic Bottom Water (Bai et al., 2022; Meredith et al., 2014) and the source  
266 waters that participate in Dense Shelf Water production (Narayanan et al., 2019; Foster  
267 & Carmack, 1976) can be influenced by gyre circulation. Therefore, there is a connection  
268 between the Ross and Weddell Gyre circulation and processes relevant to global climate,  
269 such as ocean heat and carbon uptake (MacGilchrist et al., 2019; P. J. Brown et al., 2015).

270 The circulation of the gyres has also been found to influence polynya formation (Zhou et al.,  
271 2022; Cheon & Gordon, 2019; Cheon et al., 2018), sea ice variability (Morioka & Behera,  
272 2021; Neme et al., 2021) and iceberg drift (Barbat et al., 2021; Bouhier et al., 2018).

273 The average climatological wind field makes the gyres a region of divergent Ekman  
274 transport, fostering a vertical structure characterised by isopycnals sloping upwards towards  
275 the centre of the gyre, with local upwelling and mixing of subsurface Circumpolar Deep  
276 Water (Jullion et al., 2014). Circumpolar Deep Water is able to enter the gyres through  
277 permeable eastern boundaries, where there is no topographic constraint to their circulation  
278 (Bebieva & Speer, 2021; Roach & Speer, 2019; Donnelly et al., 2017; Ryan et al., 2016;  
279 Cisewski et al., 2011; Fahrbach et al., 2011; A. H. Orsi & Wiederwohl, 2009). Due to the  
280 lack of a topographic constraint, the eastern extent of the gyres is highly variable (Wilson  
281 et al., 2022; Vernet et al., 2019; Dotto et al., 2018; Roach & Speer, 2019), with eddies and  
282 high frequency variability associated with topographic discontinuities playing an important  
283 role in the exchange of waters (Bebieva & Speer, 2021; Roach & Speer, 2019; Donnelly et  
284 al., 2017; Ryan et al., 2016). Within the gyres, Circumpolar Deep Water is shielded from  
285 interaction with the atmosphere by a shallow layer of colder and fresher water that builds up  
286 during winter and erodes during summer. Upwelling and entrainment via diapycnal mixing  
287 of warm and salty Circumpolar Deep Water into the surface layer contributes to sea ice melt  
288 (Bebieva & Speer, 2021; Wilson et al., 2019) and polynya formation (§ 4.2.3; Campbell et  
289 al., 2019).

290 As Dense Shelf Water cascades down the continental shelf it enters the gyres and  
291 undergoes further transformation as it becomes entrained with ambient waters to produce  
292 Antarctic Bottom Water (Akhoudas et al., 2021; Gordon et al., 2009; A. Orsi et al., 1999). In  
293 the Weddell Gyre, it has been suggested that the properties and rates of export of Antarctic  
294 Bottom Water across gyre boundaries are dependent on the gyre's horizontal circulation  
295 due to two different mechanisms. From a baroclinic perspective, an acceleration of the gyre  
296 induces an increase in the isopycnal tilt at its northern boundary, effectively trapping the  
297 densest varieties of bottom waters that are not able to overflow through the shallow passages  
298 (Gordon et al., 2009; Meredith et al., 2008). From a barotropic perspective, an acceleration  
299 of the gyre induces changes in the strength of the deep boundary current near the outflow  
300 locations (Meredith et al., 2011). The Ross Gyre is more sparsely observed, but there is  
301 evidence that its circulation modulates the salinity of the Dense Shelf Water formed at  
302 the western Ross Sea (Guo et al., 2020) and induces changes in the properties and volume  
303 of Antarctic Bottom Water in the south-eastern Pacific Ocean (Bai et al., 2022). Warm  
304 intrusions of Circumpolar Deep Water onto the Amundsen and Bellingshausen shelf are also  
305 related to the Ross Gyre's strength (Nakayama et al., 2018). In addition to dense waters,  
306 meltwater coming from ice shelves in the Ross and Weddell Seas is also partly distributed  
307 within the gyres' circulation (Kusahara & Hasumi, 2014).

308 There are few studies addressing the variability of the Ross and Weddell gyres across  
309 different time scales in connection to possible forcing mechanisms. Satellite-based studies  
310 have found links between the gyres' sea surface height and wind stress curl (Auger, Sallée,  
311 et al., 2022; Armitage et al., 2018). However, the extensive sea ice coverage in the region  
312 modulates the transfer of momentum from the wind to the ocean surface, which has to be  
313 taken into account when considering surface stresses (Neme et al., 2021; Naveira Garabato,  
314 Dotto, et al., 2019; Dotto et al., 2018). By including sea ice in the total stress over the  
315 ocean surface, the correlation with sea surface height breaks down (Auger, Sallée, et al.,  
316 2022), as it does with gyre strength on both seasonal and interannual timescales (Neme et  
317 al., 2021). There are different processes within the gyres that could be playing a role in their  
318 variability, thus obscuring a direct relation with surface stress, such as variability of water  
319 mass exchange across gyre boundaries or variability of dense water formation. Fahrbach  
320 et al. (2011) suggest that the northern and southern limbs of the Weddell Gyre can vary  
321 independently due to variations in wind forcing across the gyre. Moreover, there are studies  
322 suggesting that ocean gyres can develop in response to surface buoyancy fluxes (Hogg &

323 [Gayen, 2020; Bhagtni et al., 2023](#)). In support of this hypothesis, the Ross and Weddell  
 324 Gyre strengths in climate models have been found to be correlated with the near-surface  
 325 meridional density gradients generated by gradients in surface buoyancy fluxes, whilst being  
 326 largely independent of wind stress curl ([Z. Wang & Meredith, 2008](#)).

## 327 2.4 Upper overturning circulation

328 The upper overturning circulation of the Southern Ocean consists of southward up-  
 329 welling flow along steeply tilted isopycnals in the mid-depths and a return northward flow  
 330 of lighter waters (called ‘mode’ or ‘intermediate’ waters, due to their density being inter-  
 331 mediate between abyssal and surface waters) in the upper ocean (Fig. 2). The lifting (or  
 332 ‘upwelling’) of deep waters to the surface and subsequent subduction north of the Antarctic  
 333 Circumpolar Current has a large impact on the global climate by enabling rapid exchange  
 334 of heat and carbon between the atmosphere and interior ocean ([Morrison et al., 2015](#)). A  
 335 large fraction of the global ocean uptake of anthropogenic heat ( $\sim 70\%$ ) and carbon ( $\sim 40\%$ )  
 336 has occurred in the Southern Ocean, due to the constant replenishment of surface waters  
 337 with colder and carbon-depleted water from below ([Frölicher et al., 2015; Zanna et al., 2019;](#)  
 338 [Khatiwala et al., 2009](#)).

339 Buoyancy fluxes (i.e., the combined effect of sensible, latent, radiative and freshwater  
 340 fluxes) and wind stresses at the ocean surface have a strong control over the strength and  
 341 structure of the upper overturning circulation. The westerly winds drive Ekman upwelling  
 342 south of the maximum wind stress ( $\sim 55^\circ\text{S}$ ) and downwelling to the north ([Toggweiler &](#)  
 343 [Samuels, 1993; Speer et al., 2000; J. Marshall & Speer, 2012](#)). In the absence of additional  
 344 diabatic processes, this Ekman pumping at the surface drives along-isopycnal flows below  
 345 the mixed layer ([Wolfe & Cessi, 2015](#)). The overturning transport increases with increasing  
 346 wind stress (e.g., [Viebahn & Eden, 2010; Bishop et al., 2016](#)), although the sensitivity is less  
 347 than the Ekman transport response due to the additional impact of buoyancy forcing and  
 348 eddies on the dynamics (e.g., [Abernathey et al., 2011](#)). Buoyancy input, predominantly from  
 349 sea ice melt and precipitation, transforms the dense upwelled waters into lighter, northward  
 350 flowing waters at the surface ([Abernathey et al., 2016](#)). Surface buoyancy forcing also  
 351 plays a critical role in the formation of mode waters on the northern edge of the Antarctic  
 352 Circumpolar Current in the Indian and Pacific sectors ([Wong, 2005; Sloyan & Rintoul, 2001;](#)  
 353 [Sallée et al., 2010](#)). In particular, surface cooling and evaporation drive strong wintertime  
 354 convection, forming Subantarctic Mode Water ([Hanawa & Talley, 2001; Abernathey et al.,](#)  
 355 [2016](#)). The shoaling of the deep mixed layers during spring then results in a net subduction  
 356 of waters from the mixed layer to beneath the permanent pycnocline ([Z. Li et al., 2022;](#)  
 357 [Morrison et al., 2022](#)).

358 Eddies (§ 4.1) play a critical role in the upwelling branch of the overturning circulation.  
 359 Southward flow in the mid-depths of the Southern Ocean is dominated by eddy transport  
 360 along isopycnals, due to the lack of land barriers required for zonal mean geostrophic flows  
 361 in the meridional direction ([J. Marshall & Speer, 2012](#)). The generation of eddy kinetic  
 362 energy through baroclinic instability extracts available potential energy from the sloping  
 363 isopycnals. This energy conversion results in a flattening of the isopycnals and, therefore,  
 364 a net southward (and upwards) transport in the upper and mid-depth ocean ([Morrison et](#)  
 365 [al., 2015](#)). The southward flow has a highly heterogeneous spatial distribution around the  
 366 Southern Ocean, with southward volume transport collocated with baroclinic eddy genera-  
 367 tion downstream (eastward) of topographic hotspots ([Tamsitt et al., 2017; Barthel et al.,](#)  
 368 [2022; Yung et al., 2022](#)). The hotspots of eddy generation and southward transport are  
 369 located  $\sim 100$  km upstream (westward) of the eddy kinetic energy hotspots ([Foppert et al.,](#)  
 370 [2017; Yung et al., 2022](#)). Eddies impact the dynamics of the upper overturning circula-  
 371 tion by limiting the sensitivity of the overturning transport to changing wind stress (e.g.,  
 372 [Hallberg & Gnanadesikan, 2006; Viebahn & Eden, 2010; Gent, 2016](#)), and by influencing  
 373 the formation rate of mode and intermediate waters ([Sallée et al., 2010; Z. Li et al., 2022](#)).  
 374 The eddy response in limiting the overturning circulation sensitivity to wind changes is

375 known as “eddy compensation” (Fig. 4). Eddy compensation occurs because the southward  
 376 eddy transport extends all the way into the surface layers, directly opposing the northward  
 377 Ekman transport in the upper ocean (J. Marshall & Radko, 2003). Following an increase  
 378 in westerly wind stress, and if the buoyancy forcing is able to adapt (Abernathy et al.,  
 379 2011), the northward Ekman transport and the southward eddy transport in the surface  
 380 layers both increase. This results in a reduced sensitivity of the overturning to wind stress  
 381 compared to a hypothetical situation with no change in eddy activity. However, the over-  
 382 turning transport (i.e., the maximum value of the zonal-mean overturning streamfunction  
 383 in latitude-depth coordinates) still increases with increasing wind stress, because much of  
 384 the southward eddy transport occurs below the Ekman layer and does not play a role in the  
 385 compensation (Morrison & Hogg, 2013).

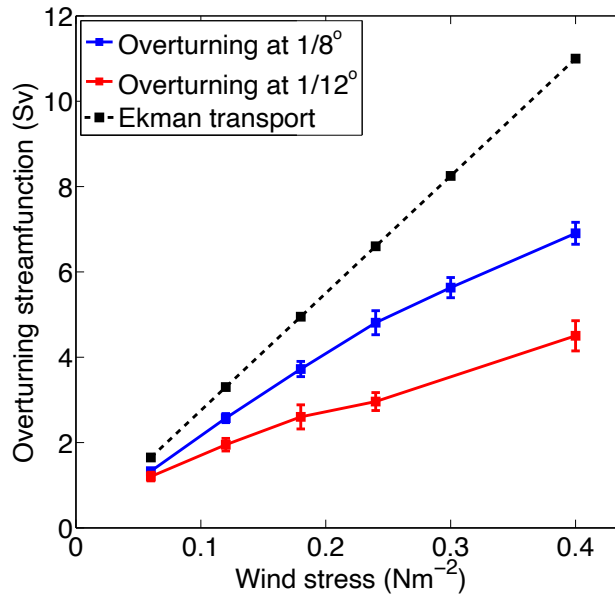


**Figure 4.** Simulated eddy compensation of the upper overturning circulation in a numerical model with no eddy parameterisation. With no eddy compensation (by resolved or parameterised eddies), the overturning would linearly increase with the magnitude of the westerly wind stress following the surface Ekman transport (black dashed line). As model resolution is increased such that mesoscale eddies become fully resolved (red line), the sensitivity of the overturning circulation to wind stress decreases, but remains non-zero. Figure reproduced from Morrison and Hogg (2013).

386 Isopycnal mixing (§ 4.3) is capable of driving diapycnal flow by coupling to two nonlin-  
 387 earities in the equation of state of seawater (McDougall, 1987), and these play a key role in  
 388 the overturning circulation. First, mixing two water parcels with the same density but differ-  
 389 ent temperature and salinity yields a mixture that is denser than the original parcels. This  
 390 process, known as cabbeling, is particularly strong in the Southern Ocean where mesoscale  
 391 eddies stir the strong along-isopycnal temperature and salinity gradients. In fact, cabbeling  
 392 is essential to the formation of Antarctic Intermediate Water (part of the northward return  
 393 limb of the upper overturning circulation; Fig. 2), and numerical models that use a linear  
 394 equation of state, and therefore lack cabbeling, do not reproduce the salinity minimum asso-  
 395 ciated with Antarctic Intermediate Water (Fig. 5; Nycander et al., 2015; Groeskamp et al.,  
 396 2016; Z. Li et al., 2022). Second, mixing two water parcels having different pressures but the  
 397 same density when brought to their average pressure (i.e., isopycnal mixing of two parcels  
 398 with an isopycnal pressure gradient) yields a mixture that may be either denser or lighter  
 399 than the original parcels. This process, known as thermobaricity, occurs (primarily) because

400 the thermal expansion coefficient of seawater depends on pressure. This thermobaric effect  
 401 is responsible for making North Atlantic Deep Water lie above Antarctic Bottom Water: the  
 402 density of the relatively colder yet fresher Antarctic Bottom Water increases more rapidly  
 403 with depth (pressure) than does the density of North Atlantic Deep Water (Nycander et al.,  
 404 2015).

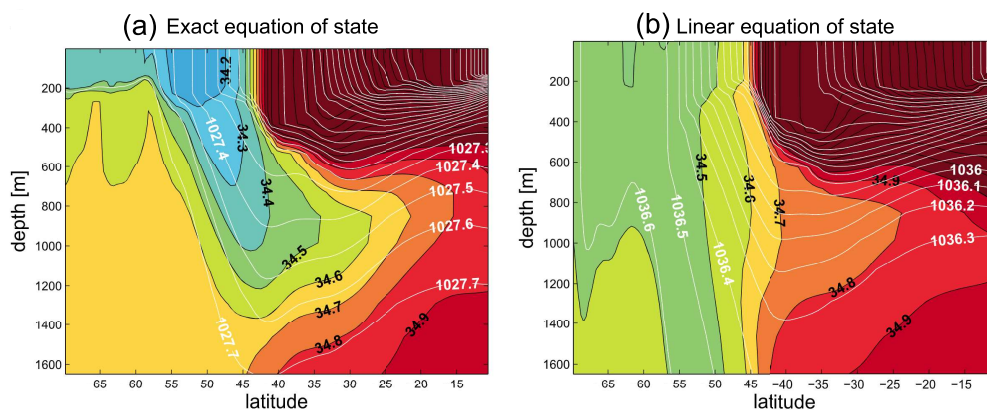


**Figure 5.** Impact of the nonlinear equation of state (i.e., the equation describing the dependence of the density of seawater on temperature, salinity and pressure) on simulated Antarctic Intermediate Water formation. (a–b) Latitudinal transects along  $23.5^{\circ}\text{W}$  of salinity (colour, with contours labelled in black) and potential density (white labelled contours) in the South Atlantic. The simulation shown in (a) uses a full non-linear equation of state, while (b) uses a linear equation of state. Antarctic Intermediate Water (blue to green freshwater pathway shown in a) forms through isopycnal mixing leading to cabelling and is only able to form in the model configuration using a nonlinear equation of state. Figure reproduced from Nycander et al. (2015).

## 2.5 Abyssal overturning circulation

405

406 The Southern Ocean abyssal overturning circulation is considered, in a zonally integrated  
 407 sense, to consist of two compensating flows: (i) a poleward flow of Circumpolar Deep  
 408 Water; and (ii) an equatorward flow of Antarctic Bottom Water (Fig. 2). Circumpolar  
 409 Deep Water is modified by mixing as it travels poleward to the Antarctic continental shelf,  
 410 where it is transformed into Dense Shelf Water through surface buoyancy fluxes and brine  
 411 rejection due to sea ice formation. Dense Shelf Water mixes with and entrains Circumpolar  
 412 Deep Water as it descends into the abyssal ocean to form Antarctic Bottom Water (A. Orsi  
 413 et al., 1999). The resulting water mass accounts for 30–40% of the ocean’s total volume,  
 414 and fills the abyssal depths of the Atlantic, Pacific and Indian Oceans with carbon- and  
 415 oxygen-rich water (Johnson, 2008). It is estimated that the maximum northward Antarctic  
 416 Bottom Water transport is about 20–30 Sv near  $30^{\circ}\text{S}$  (Ganachaud et al., 2000; Lumpkin &  
 417 Speer, 2007; Talley et al., 2003; Talley, 2008, 2013).

418 The cryosphere influences abyssal overturning by modulating Dense Shelf Water forma-  
419 tion through three main pathways: ice shelves, sea ice, and major cryospheric events (i.e.,  
420 major changes in the cryosphere). Regions of strong ice shelf basal melting support the  
421 formation of polynyas within areas of landfast ice (Nihashi & Ohshima, 2015), and glacial  
422 meltwater has been connected to changes in Antarctic Bottom Water properties (§6.1).  
423 Brine rejection during sea ice formation influences the amount of Dense Shelf Water forma-  
424 tion, and its salinity and density (e.g., Jacobs, 2004; Iudicone et al., 2008; Abernathy et  
425 al., 2016; Silvano et al., 2020). Large cryospheric events, such as the calving of the Mertz  
426 Glacier Tongue (Tamura et al., 2012; Shadwick et al., 2013; Aoki et al., 2017; Snow et  
427 al., 2018) or the opening of the Weddell Sea polynya (Martinson, 1991; Akhoudas et al.,  
428 2021), reorganise the circulation and stratification and, therefore, alter Dense Shelf Water  
429 formation (see the discussion of polynya convection in §4.2.2).

430 The export of Dense Shelf Water occurs predominantly in submerged canyons that cross  
431 the continental shelf (Nakayama, Ohshima, et al., 2014). Dense Shelf Water accumulates in  
432 these deeper sections of the shelf and eventually spills down the continental slope, sometimes  
433 in short bursts lasting a few days (Foppert et al., 2021). The export of Dense Shelf Water  
434 is modulated by tidal mixing, which modifies the water mass properties and helps to bring  
435 Circumpolar Deep Water onshore (Muench et al., 2009; Q. Wang et al., 2013; Bowen et  
436 al., 2021). Morrison et al. (2020) find that the Circumpolar Deep Water inflow is partly  
437 forced by a pressure gradient set up by the overflowing Dense Shelf Water. Eddies are  
438 also a major contributor to Dense Shelf Water and Circumpolar Deep Water transport  
439 across the continental slope (A. L. Stewart & Thompson, 2015; Q. Wang et al., 2009;  
440 Nakayama, Ohshima, et al., 2014; Nøst et al., 2011). The Dense Shelf Water component of  
441 Antarctic Bottom Water is primarily formed in the Weddell Sea, Prydz Bay, Ross Sea, and  
442 Adelie Coast regions (Purkey et al., 2018), which links the properties of Antarctic Bottom  
443 Water globally to conditions in these small formation regions. The degree of mixing of the  
444 exported Antarctic Bottom Water is unclear from observations (Purkey et al., 2018), but  
445 high-resolution modelling shows the export is split by the topography of Drake Passage  
446 and Kerguelen Plateau to form distinct Weddell–Prydz-sourced and Ross–Adelie-sourced  
447 mixtures in the Atlantic–Indian and Indian–Pacific, respectively (Solodoch et al., 2022).  
448 This result suggests that regional changes in Dense Shelf Water formation could produce  
449 planetary-scale contrasts in Antarctic Bottom Water properties, and associated changes in  
450 the three-dimensional structure of the global overturning circulation.

451 In contrast to upper overturning circulation, which is largely adiabatic at depth with  
452 upwelling along sloped isopycnals in the Southern Ocean (Toggweiler & Samuels, 1995),  
453 abyssal overturning circulation fundamentally requires diabatic transformation below the  
454 sea-surface, because the northward flowing Antarctic Bottom Water must reduce its den-  
455 sity and upwell across stable (albeit weak) stratification in the abyss before it can return  
456 to the sea-surface (Ganachaud & Wunsch, 2000; Talley, 2013). Diapycnal mixing is the  
457 main process that lightens water masses in the abyssal ocean, with geothermal heating a  
458 secondary contribution accounting for perhaps 20% (Hofmann & Morales Maqueda, 2009;  
459 Emile-Geay & Madec, 2009). Thus, the planetary-scale abyssal overturning is supported  
460 by turbulent processes at the Batchelor scale (i.e., the scale on the order of millimetres at  
461 which molecular diffusion effectively smooths tracer gradients; Munk, 1966; Ferrari et al.,  
462 2016). How and where this buoyancy gain occurs is poorly understood, in part because  
463 the interaction between these largest and smallest scales is mediated on intermediate scales,  
464 notably by eddies (§4.1) and internal gravity waves (§5.3).

465 Diapycnal mixing (§4.3.2) of Antarctic Bottom Water is thought to primarily occur  
466 where abyssal flows encounter rough bathymetry (Bryden & Nurser, 2003; Fukamachi et al.,  
467 2010). Observations near Southern Ocean bathymetry find diapycnal diffusivities that are  
468 10–1000 times greater than upper ocean values (e.g., Heywood et al., 2002; Garabato et al.,  
469 2004; Polzin, Naveira Garabato, Abrahamsen, et al., 2014). This rapid increase of diapycnal  
470 diffusivity with depth causes downwelling in the ocean interior, as water mixes rapidly with

471 denser water beneath it and mixes more slowly with lighter water above it. However, this  
 472 is compensated by upwelling in the bottom boundary layer where the diapycnal diffusivity  
 473 goes to zero at the seafloor (Stanley, 2013; de Lavergne et al., 2016; McDougall & Ferrari,  
 474 2017; de Lavergne et al., 2017; Cimoli et al., 2019; Holmes & McDougall, 2020). Diapycnal  
 475 mixing is thought to be sustained by breaking internal gravity waves created from two  
 476 primary sources: barotropic tides and lee waves resulting from currents interacting with  
 477 rough topography (§5.3.1). Estimates of the amount of Antarctic Bottom Water upwelling  
 478 driven by tides and lee waves ranging from 7–25 Sv (Nikurashin & Ferrari, 2013; Melet et  
 479 al., 2014; de Lavergne et al., 2016). Meanwhile, geothermal heat fluxes are estimated to  
 480 sustain roughly 2–6 Sv of the abyssal flow (Hofmann & Morales Maqueda, 2009; Emile-Geay  
 481 & Madec, 2009). These two upwelling effects are offset by a net downwelling driven by the  
 482 cabbeling and thermobaric effects of the non-linear equation of state of seawater of 6–10 Sv,  
 483 occurring primarily in the Southern Ocean (Klocker & McDougall, 2010). For the purposes  
 484 of rough comparison, assuming that the mixing and geothermal upwelling occurs north of  
 485 30°S and the non-linear equation of state driven downwelling occurs south of 30°S, gives a  
 486 mass flux of 9–31 Sv, which is broadly consistent with the maximum northward Antarctic  
 487 Bottom Water transport of 20–30 Sv near 30°S estimated from observations (Talley, 2013).

488 Accounting for multiscale processes can alter our fundamental understanding of the  
 489 dynamics of the abyssal overturning circulation, such as its response to changing the west-  
 490 erly winds over the Southern Ocean. The classic view is that stronger Southern Hemisphere  
 491 westerly winds, by steepening Southern Ocean isopycnals and altering the abyssal stratifi-  
 492 cation, should weaken the abyssal overturning (Ito & Marshall, 2008; Nikurashin & Vallis,  
 493 2011; Shakespeare & Hogg, 2012). However, there is an energetic pathway through which  
 494 some of the extra wind energy input at the surface leads to enhanced diapycnal diffusion  
 495 in the abyss, thereby strengthening the abyssal overturning; specifically, stronger winds  
 496 steepen isopycnals, driving more baroclinic instability and stronger mesoscale eddies. In the  
 497 Southern Ocean, these mesoscale eddies are deep-reaching and lead to larger eddy bottom  
 498 velocities that interact with rough bathymetry to generate lee waves and, ultimately, diapy-  
 499 cnal mixing that strengthens the abyssal overturning (D. P. Marshall & Naveira Garabato,  
 500 2008; Saenko et al., 2012). When this energetic link is included in idealized models, stronger  
 501 Southern Ocean westerly winds can actually drive a stronger abyssal overturning (Stanley  
 502 & Saenko, 2014). Using an estimated climatology of wave energy fluxes, Melet et al. (2014)  
 503 also found that accounting for lee wave-driven mixing accelerates the abyssal overturning in  
 504 a realistic global ocean model.

## 505 2.6 Closing the loops

506 The large scale circulation of the Southern Ocean exerts a major control on the global  
 507 climate state. In particular, the meridional overturning circulation in the Southern Ocean  
 508 regulates heat transfer across the Antarctic margin, the strength of bottom water and mode  
 509 water formation, and heat and carbon uptake by the global oceans. This section has de-  
 510 scribed how this meridional circulation is closely coupled to the other components of the  
 511 large scale circulation (the subpolar gyres and Antarctic Circumpolar Current) and, cru-  
 512 cially, other components of the Southern Ocean dynamic system. These connections include  
 513 the role of mesoscale turbulence (§4.1) and associated seafloor interactions (§4.1.5) in regu-  
 514 lating the response of the circulation to forcing changes, the role of brine rejection during sea  
 515 ice formation in supporting the formation of the dense water that fills the Southern Ocean  
 516 abyss (§3.2.3), and the role of diapycnal mixing in supporting the upwelling of abyssal water  
 517 and closing the global overturning circulation (§4.3). These dynamics will be described in  
 518 more detail in subsequent sections, starting with the Cryosphere in §3.

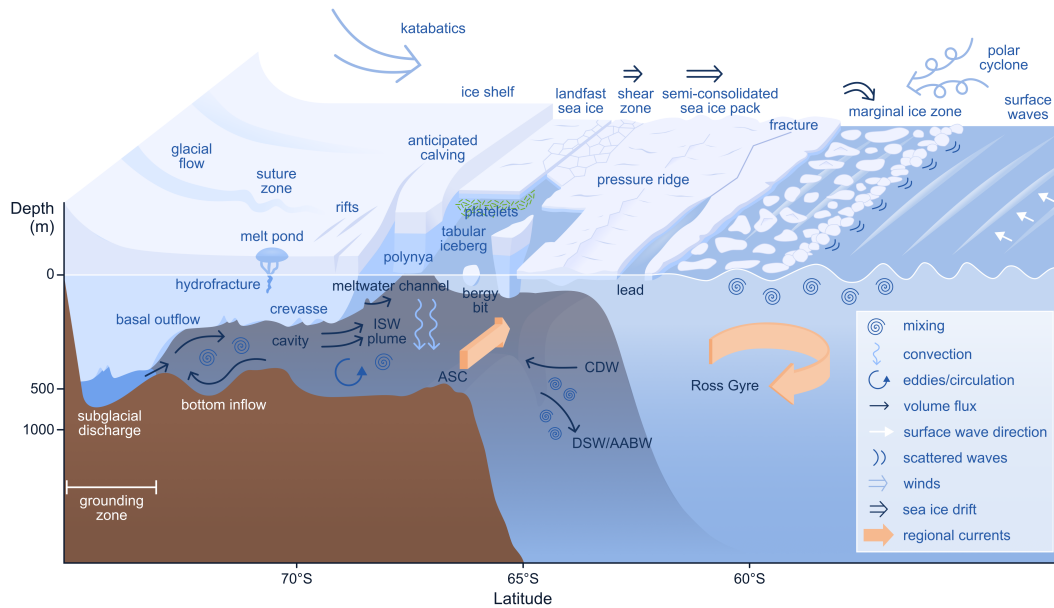


**Figure 6.** Schematic of the oceanic margin of the southern cryosphere, including key dynamic connections with the Southern Ocean. The ice shelf is the floating extension of the Antarctic Ice Sheet formed from multiple glaciers flowing onto the ocean surface that fuse in suture zones. The ice shelf contains features, such as a melt pond at its surface (that can result in hydrofracture), crevasses and meltwater channels at its base, and rifts that extend throughout the shelf depth and propagate to the shelf front to calve tabular icebergs, from which bergy bits break off. Here, the giant ice shelf partially encloses a cold-water cavity that experiences Mode One circulation (§ 3.1.1), involving bottom inflow of cold water fed by dense shelf water created in a polynya, and outflow of basal meltwater that exits the cavity as a plume of Ice Shelf Water (ISW). At the ice shelf grounding zone, subglacial discharge of ice sheet meltwater flows into the cavity, which creates platelets that attach to the underside of local sea ice. The shelf front is occupied by a polynya (created by katabatic winds) and immobile landfast sea ice (attached to the shelf). Pack ice bounds the polynya and landfast sea ice towards the ocean. The pack consists predominantly semi-consolidated sea ice with features, such as pressure ridges, leads and fractures, but with a shear zone at its boundary with the landfast sea ice and a marginal ice zone at its boundary with the open ocean, where floe sizes are relatively small due to the presence of surface waves. Large-scale sea ice drift is dictated by winds, such as those during polar cyclones, as well as ocean tides, currents and gyres.

### 519 3 Cryosphere

520 A major characteristic of the Southern Ocean is that its waters interact with segments of  
 521 an icy shell created from both freshwater and salt water, respectively, ice shelves and sea ice  
 522 (Fig. 6). Ice shelves and sea ice (along with icebergs and polynyas) form an oceanic margin  
 523 of the cryosphere that interacts with the Southern Ocean at a number of scales, ranging from  
 524 large-scale circulation, via many processes, to the small diffusive-viscous scales influencing  
 525 melt and dissolution rates. There are several existing monographs on sea ice, such as Weeks  
 526 (2010) and Leppäranta (2011), which include the fundamental governing equations of sea ice  
 527 dynamics. There are also collections of reviews, such as D. N. Thomas (2017), including its  
 528 dynamic interactions with the ocean, although often focused on Arctic sea ice. In addition,  
 529 there are review articles and collections on specific components of sea ice, including its  
 530 rheology (Feltham, 2008), its engineering properties (Timco & Weeks, 2010), landfast sea

531 ice (Fraser et al., 2023), and marginal ice zone dynamics (Bennetts, Bitz, et al., 2022b).  
 532 Wadhams (2000) is a monograph covering both sea ice and icebergs and their role in the  
 533 climate system. In contrast to sea ice, there is little synthesis information on ice shelves  
 534 (and/or ice shelf cavities), other than in the context of numerical modelling (Dinniman  
 535 et al., 2016) or basal melt (Burgard et al., 2022), where the former contains some of the  
 536 fundamental governing equations.

### 537 3.1 Ice shelves and sub-ice shelf cavities

538 Ice shelves (and ice tongues) comprise many merged glacial flows fused together in  
 539 suture zones (Fig. 6). Ice shelves create unique ocean environments in the sub-ice shelf  
 540 water cavities they enclose. The cavities are bound on the landward side at the “grounding  
 541 zone” where the ice sheet leaves the land and begins to float. The oceanward open boundary  
 542 is beneath the “shelf front”, i.e., the terminal face of the ice shelf, which is typically a sharp  
 543 vertical wall formed by calving of icebergs from the ice shelf (Fig. 6). The ice shelf–ocean  
 544 basal interface is the upper boundary of the cavity, where melting and re-freezing takes  
 545 place. Total ice shelf mass loss is roughly equally divided between melting and iceberg  
 546 calving (Rignot et al., 2013; Depoorter et al., 2013; Greene et al., 2022). The rate and  
 547 distribution of melting is determined by a complex set of processes (§§ 3.1.1–3.1.6), which  
 548 start with the transport of ocean heat into and within sub-shelf cavities.

#### 549 3.1.1 Ice shelf cavity exchange with the Southern Ocean

550 Water mass exchange between the Southern Ocean and ice shelf cavities is typically  
 551 divided into three modes of circulation (Fig. 7) resulting in the “cold” or “warm” cavity  
 552 descriptor, based on the absence or presence of water well above the local freezing point  
 553 (typically Circumpolar Deep Water) in the cavity (Jacobs et al., 1992; Joughin et al., 2012;  
 554 Silvano et al., 2016). The giant cold cavities of the Filchner-Ronne, Ross and Amery Ice  
 555 Shelves span hundreds of kilometres across and are typically dominated by Mode One cir-  
 556 culation. In this situation, katabatic winds (cold, dense air masses flowing off the polar  
 557 plateau; L. Thompson et al., 2020; Gutjahr et al., 2022) drive sea ice production in coastal  
 558 polynyas (§ 4.2.2) at the ice shelf front. This creates dense shelf water, which floods the  
 559 cavity and ensures relatively low average melt rates, with some areas of the shelf underside  
 560 re-freezing (Galton-Fenzi et al., 2012). In addition, the circulation provides protection from  
 561 warm water inflow (Hattermann et al., 2021; Darelius et al., 2016). Results from smaller  
 562 shelves, such as the Nansen (Friedrichs et al., 2022) and Sorsdal (Gwyther et al., 2020) Ice  
 563 Shelves, indicate cold conditions and Mode One circulation can possibly also exist at these  
 564 scales.

565 As well as being closer to the Antarctic Circumpolar Current, warm water cavities lack  
 566 the protection of wide, shallow continental shelves, so that (relatively warm) Circumpolar  
 567 Deep Water has direct access to the underside of the ice shelves. Warm water cavities  
 568 typically sustain Mode Two circulation (Fig. 7), whereby the inflow of Circumpolar Deep  
 569 Water leads to high melt rates deep within the cavity. Ice shelves of the Amundsen and  
 570 Bellingshausen seas (e.g., Thwaites, Pine Island, Dotson, Crosson and Getz ice shelves) are  
 571 particularly vulnerable and have been observed to have the highest basal melt rates around  
 572 Antarctica (Rignot et al., 2013; Adusumilli et al., 2020).

573 Mode Three cavity circulation is associated with the melting that results from an accu-  
 574 mulation of warm water along the shelf front. This tends to be more variable than the other  
 575 modes. In the Amundsen Sea region, Mode Three circulation is associated with Circumpolar  
 576 Deep Water circulation near the ice shelf front (Davis et al., 2022). Recent observations  
 577 from the frontal region of the Ross Ice Shelf cavity have shown evidence of high melt rates  
 578 caused by surface water inflow in the frontal zone directly connected with summer surface  
 579 ocean warming (C. L. Stewart et al., 2019; Aoki et al., 2022). This buoyant water can  
 580 potentially pool against the shelf terminal face and form a blocking “wedge” that can in-

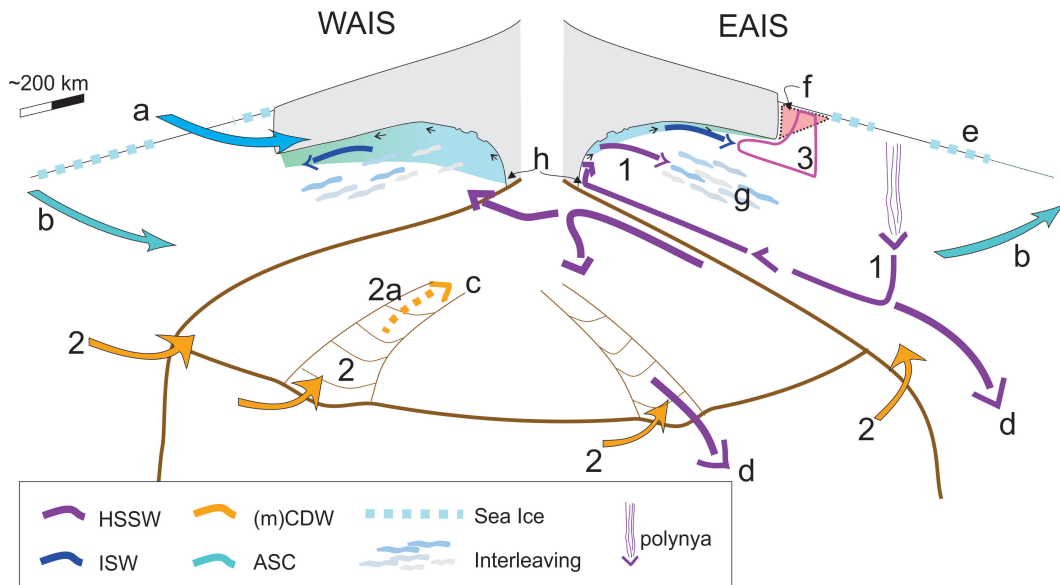


**Figure 7.** Idealised modes of cavity circulation (Jacobs et al., 1992; Tinto et al., 2019) and the influence of a polynya, which are visualised for the Ross Sea and cavity and to emphasize the three-dimensionality. The modes (one, two and three) are shown together for convenience but do not necessarily co-exist nor is there a substantial amount of direct observation of these modes. Mode 2a refers to uncertainty of the penetration of modified Circumpolar Deep Water (mCDW) into the cavity. Additional features include (a) melt water from the east (Nakayama, Timmermann, et al., 2014), (b) Antarctic Slope Current (ASC) (A. L. Stewart et al., 2019), (c) continental shelf troughs and possible penetration of mCDW, and (d) high salinity shelf water (HSSW) draining off the continental shelf. On the continental shelf itself there are (e) sea ice driving polynya and convection and (f) the shelf front wedge, which is a buoyant front associated with summer warming that interacts with the Mode Three circulation (Malyarenko et al., 2019). Within the cavity there are (g) cavity interleaving (Stevens et al., 2020) affecting the cavity circulation and (h) subglacial discharge flows at the grounding line.

fluence how waters offshore of the wedge are advected beneath the ice shelf (Malyarenko et al., 2019). While localised, this circulation mode may still have a profound effect on the entire shelf system, depending on where the warming is happening. For example, increased melt rates near Ross Island influence the flow rate of the entire ice shelf (Reese et al., 2018). Meltwater from these ice shelves moves westward in the Antarctic Slope Current (§2.2), and may affect vertical mixing, sea ice production and downstream cavities (Silvano et al., 2018; Nakayama, Timmermann, et al., 2014).

### 3.1.2 Cavities, gyres and eddies

The three modes of large-scale cavity circulation (§3.1.1; Fig. 7) need to be augmented with improved understanding of mesoscale variability. Here, the literature uses terms like “gyre” and “eddy” inconsistently. The terms describe rotating coherent horizontal-plane motions, with gyres being larger, wind-driven and relatively stationary compared to the smaller, mobile eddying motions. These structures have been observed to influence cavity–open ocean exchange, whereby the circulation and associated influence on mixing increases the heat flux into the cavity, thus enhancing basal melting and ultimately resulting in greater freshwater flux into the ocean. This is seen in both warm cavities (Naveira Garabato et al., 2017; Yoon et al., 2022) and cold cavities (Friedrichs et al., 2022). The Pine Island Glacier Ice Shelf is a warm cavity example, which shows a system dominated by a gyre that fills the bay in front of the glacier. The Nansen Ice Shelf is an example of a small cold cavity influenced by eddies, which acts as a pump for moving warm water into the cavity (Friedrichs et al., 2022). In this case, the eddies are associated with regional topography, including the large Drygalski Ice Tongue.

Topographically-influenced gyres (such as those discussed above) are relatively large (several tens of kilometres in scale) and stationary, whereas in large cavities and/or away from direct topographic control, eddies are smaller and free to move. Freely moving eddies are typically at the scale of the local Rossby radius of deformation at which rotation effects are comparable to buoyancy effects, which is typically around a few kilometres. Numerical modelling has been the primary way to examine eddy processes within cavities (e.g., Mack et al., 2019). However, there are a few recent direct observations of the ocean within ice shelf cavities, via boreholes (Stevens et al., 2020) or using robotic technology (providing a view of the vertical structure and its spatial variations; Gwyther et al., 2020; Graham et al., 2022; Davis et al., 2022). Data of this type provide direct evidence of water masses, meltwater drivers and mixing in these under-observed environments. This is particularly important because of the often long circulation timescales (several years in some cases) within cavities, and limited set of drivers. As models have been developed with little direct data, even modest departures from modelled diffusion, because of the long timescales and limited drivers, can result in a different outcomes for the cavity. This is in contrast to boundary-driven mixing in the Southern Ocean with many coincident driving processes (§4.3.3).

### 3.1.3 Tidal influence on cavities

Due to the absence of direct weather forcing within a cavity, ocean tides (both internal and surface; §5.2) are the primary forcing at periods within the 0.5–10 day range. The elastic response of an ice shelf to any large-scale perturbation means that, other than close by the shore (at the grounding zone), the ice shelf responds hydrostatically and rapidly. Thus, determination of tidal excursions and currents can be achieved in the same way as elsewhere in the oceans, by combining water column height observations, knowledge of the bathymetry and numerical tools to extrapolate to any location in space and time (Padman et al., 2018). There are subtleties to tidal mechanics at such high latitudes, as the influence of tides on ice shelf melting is related to the latitude of an ice shelf relative the semidiurnal critical latitude, where the tidal frequency equals the inertial frequency (§5.3.3; Robertson, 2013). In general, tides can be important drivers of meltwater production for ice shelves on

632 cold water cavities (e.g., Makinson et al., 2011; Arzeno et al., 2014; Mueller et al., 2018;  
 633 Hausmann et al., 2020), but are less important for ice shelves on warm water cavities (e.g.,  
 634 Robertson, 2013; Jourdain et al., 2020).

635 Accepted melt rate parameterisations involve the local under-ice velocity (D. M. Holland  
 636 & Jenkins, 1999; Rosevear, Galton-Fenzi, & Stevens, 2022). However, including tides in  
 637 regional/cavity scale models is computationally expensive due to required short timesteps.  
 638 Despite this, recent regional (Mueller et al., 2018; Hausmann et al., 2020) and pan-Antarctic  
 639 (Richter et al., 2022) modelling studies have shown that tide-enhanced melting significantly  
 640 increases boundary layer turbulence, and the increase can be offset by the cooling associated  
 641 with the increased meltwater (which is exported slowly). In addition, there is the potential  
 642 for tides interacting with the basal underside to drive internal waves (§5.3) within the cavity  
 643 (Foster, 1983), which would influence overall thermal dynamics (Stevens et al., 2020) and  
 644 requires more advanced approaches to modelling cavity circulation (Mack et al., 2019).

#### 645 *3.1.4 Meltwater plumes and marine ice*

646 In the far reaches of an ice shelf cavity, once the inflowing oceanic water mass comes  
 647 in contact with the ice shelf, production of meltwater results in a buoyant plume at the ice  
 648 shelf base (Fig. 6). The meltwater plume typically ascends as it travels oceanwards, steered  
 649 by the ice base topography and coastlines, and drives cavity-scale convective circulation.  
 650 The evolution of the meltwater plume is governed by friction, planetary rotation and the  
 651 entrainment of underlying watermasses (Jenkins, 1991). Since the in situ melting point is  
 652 reduced by approximately  $0.75^\circ\text{C}$  per kilometer of depth, cold water, such as Dense Shelf  
 653 Water that is typically at the surface freezing temperature, drives rapid melting at depth.

654 For cold cavities, rapid melting at deep grounding zones can lead to potentially “su-  
 655 percooled” plumes that rise along the ice base to a point where in situ freezing occurs —  
 656 the so-called “ice pump”. This occurs when basal melting at the grounding zone results  
 657 in a meltwater plume that then can re-freeze at shallower depths (Lewis & Perkin, 1986;  
 658 Schodlok et al., 2016), sometimes through the formation of platelet ice crystals (Hoppmann  
 659 et al., 2020). At that point, ice forms and rises to accrete to the ice shelf base as “marine  
 660 ice” (Stevens et al., 2020). The spatial patterns of melting and refreezing can be seen in  
 661 satellite altimetry data (Adusumilli et al., 2020). Under warm cavities, not all in-flowing  
 662 ocean heat is consumed. Instead, the meltwater plume brings ocean heat to the surface and  
 663 forms near-ice-front sensible heat polynyas (e.g., Mankoff et al., 2012).

664 The characteristics of the meltwater plumes are influenced by ice base topography, with  
 665 basal channels being sites of enhanced basal melting (e.g. W. Wei et al., 2020), and the  
 666 presence of other forcing (primarily tides; §5.2) of turbulent mixing at the ice shelf–ocean  
 667 interface. Plume circulation and melt rates are expected to be altered by the presence  
 668 of tides, but the direction and magnitude of the change depends on the balance between  
 669 tide-enhanced drag, entrainment and melting (Anselin et al., 2023).

#### 670 *3.1.5 Subglacial discharge*

671 Subglacial discharge is the flow of meltwater from the ice sheet basal bedrock interfacial  
 672 zone that finds its way into the cavity coastal zone (Fig. 8a). The meltwater is formed  
 673 by pressure and geothermal warming (Fricker et al., 2016). While difficult to access in  
 674 Antarctica, subglacial discharges of meltwater have been extensively studied in the context  
 675 of the Greenland Ice Sheet, where they are often linked to elevated melt rates (I. J. Hewitt,  
 676 2020). Satellite observations provide evidence for a large number of active subglacial lakes  
 677 across Antarctica, which experience sporadic but rapid drainage events (Fricker et al., 2007;  
 678 Siegfried & Fricker, 2018). As in Greenland, it is likely that these drainage events alter  
 679 the water properties at the edge of the ice sheet and have a significant effect on ice shelf–  
 680 ocean processes (Miles et al., 2018; Jouvet et al., 2018). However, the nature, frequency,

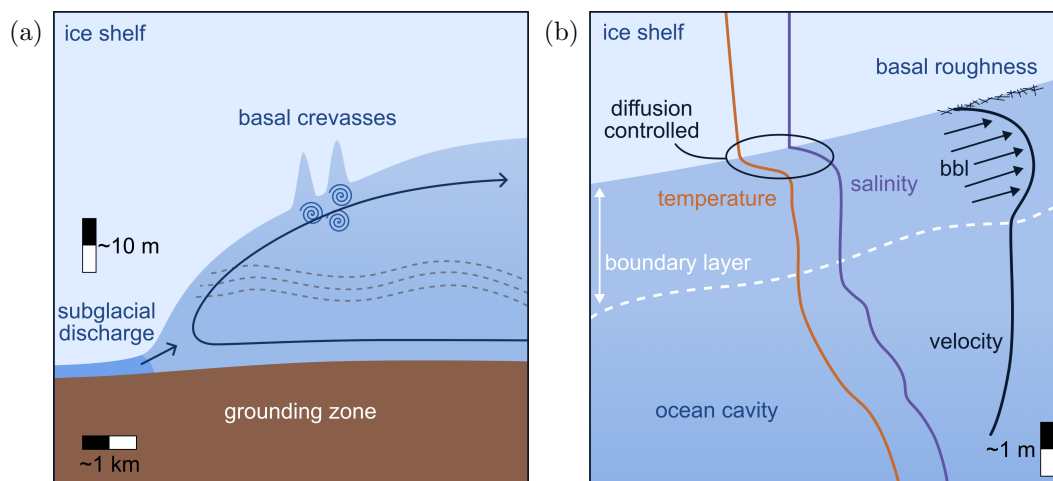


**Figure 8.** Small-scale views of an ice shelf and sub-shelf water cavity showing some of the under-observed but critical processes likely to be present. (a) Grounding zone region including subglacial discharge of meltwater from beneath the ice sheet, basal crevasses, stratification/baroclinic waves (dashed lines), in/outflow. (b) The basal boundary layer (bbl), temperature and salt stratification and roughness variations. The basal boundary layer shows the 1–10 m thick region close to the ice-shelf base, where the fluid velocity and turbulence is affected by the presence of buoyant meltwater. Temperature and salinity increase rapidly through the boundary layer from diffusion-controlled melting conditions at the ice–ocean interface through to the boundary layer itself and then to ocean-cavity conditions at the edge of the boundary (the circulation of which is not well known).

681 and location of these subglacial drainage events remain unclear, largely due to challenges in  
682 making oceanographic observations deep within the ice shelf cavity.

683 The injection of freshwater, either from sub-glacial discharge or from basal melt, causes  
684 the water column near grounding lines to exhibit aspects of an estuary with landward-flowing  
685 deeper water exchanging with this freshwater flux (Horgan et al., 2013). The resulting  
686 stratification is influenced by tidal mixing processes through both mixing and baroclinic  
687 waves (Fig. 8a), with a key question being at what point does the tidal mixing become  
688 sufficient to homogenize the water column (P. R. Holland, 2008). The few observations  
689 available suggest stratification can persist in even quite thin water columns (e.g., 10–30 m;  
690 Begeman et al., 2018; Lawrence et al., 2023; Davis et al., 2023). This suggests that inflowing  
691 warm water can directly access the basal boundary layer right at the formation of the ice  
692 shelf meltwater plume.

### 693 3.1.6 Cavity basal boundary layers

694 The basal boundary layer is the oceanic boundary layer just beneath the base of an  
695 ice shelf (Fig. 8b), which is responsible for setting the ice shelf basal melt rate and drives  
696 the basal meltwater outflow from the cavity. The archetypal model of the ice shelf basal  
697 boundary layer (Fig. 8b) is of a boundary layer formed by velocity shear due to friction  
698 between the ice shelf base and ocean currents. These currents may be buoyant meltwater  
699 plumes, tidal currents, eddies, or other mean circulation within the cavity (Stanton et al.,  
700 2013; Padman et al., 2018), all of which are poorly known in cavities (Fig. 8b). In this  
701 “shear-driven” regime, the basal melt rate depends on the friction velocity (a turbulent  
702 velocity scale related to the current speed) and ocean temperature (Davis & Nicholls, 2019;  
703 Vreugdenhil & Taylor, 2019; Rosevear, Gayen, & Galton-Fenzi, 2022). This model forms the

704 basis of common ice shelf–ocean parameterizations (e.g., [D. M. Holland & Jenkins, 1999](#);  
 705 [Jenkins et al., 2010](#)). However, comparisons between observed and predicted melt rates of  
 706 ice shelves, as well as idealised models, have brought into question the appropriateness of this  
 707 approach when current velocities are low ([Malyarenko et al., 2020](#); [Rosevear, Galton-Fenzi,](#)  
 708 [& Stevens, 2022](#)) or the near-ice stratification is strong ([Vreugdenhil & Taylor, 2019](#)).

709 Meltwater is less dense than ambient seawater, primarily due to salinity differences, and  
 710 will drive convection in the form of a buoyant plume if the ice shelf base is sloped (Figs. 6,8).  
 711 This gives rise to a convective melting regime (seen in laboratory experiments and sim-  
 712 ulations), in which melting is driven by gravitational instability ([Kerr & McConnochie,](#)  
 713 [2015](#); [McConnochie & Kerr, 2017b](#); [Gayen et al., 2016](#)). Antarctic ice shelves typically  
 714 have low slope angles, which inhibits the gravitational instability. Thus, convective melting  
 715 may be more relevant to near-vertical ice, such as icebergs and shelf fronts. A transition  
 716 from convective- to shear-driven melting is expected as a buoyant plume gains momentum  
 717 ([Malyarenko et al., 2020](#); [McConnochie & Kerr, 2017a](#)). However, this transition is poorly  
 718 constrained and may vary over only small scales ([Schmidt et al., 2023a](#)). A general de-  
 719 scription of this important boundary condition has yet to be derived. The role played by  
 720 buoyant meltwater depends on whether the ice shelf base is sloped or horizontal, and what  
 721 other forcing is present. For a shear-dominated boundary layer beneath a horizontal ice  
 722 shelf base, meltwater is expected to stratify the boundary layer and suppress turbulence.  
 723 Recent numerical simulations have shown that buoyancy inhibits melting by decreasing the  
 724 efficiency of heat and salt transport to the ice shelf boundary ([Vreugdenhil & Taylor, 2019](#))  
 725 and insulating the ice shelf from warmer water below ([Rosevear, Gayen, & Galton-Fenzi,](#)  
 726 [2022](#)). When shear is weak, the heat and salt fluxes associated with basal melting provide  
 727 an opportunity for double-diffusive convection to occur, and the formation of well mixed  
 728 layers separated by thin interfaces called “thermohaline staircases” ([Radko, 2013](#)). Obser-  
 729 vations from beneath the George VI Ice Shelf show a persistent staircase ([Kimura et al.,](#)  
 730 [2015](#)), and weak dissipation, which is uncorrelated to current speed ([L. Middleton et al.,](#)  
 731 [2022](#)), suggesting that diffusive-convection is the primary driver of turbulence. There is also  
 732 evidence of diffusive-convection-susceptible conditions beneath the Ross Ice Shelf ([Begeman](#)  
 733 [et al., 2018](#)).

734 Smaller-scale basal texture or “roughness” (Fig. 8b) is expected to enhance boundary-  
 735 layer turbulence, leading to higher melt rates ([Gwyther et al., 2015](#)), and sapping momentum  
 736 from buoyant plumes through increased drag (e.g., [Smedsrud & Jenkins, 2004](#)). There are  
 737 very few direct measurements of turbulence or drag beneath ice shelves ([Stanton et al.,](#)  
 738 [2013](#); [Davis & Nicholls, 2019](#); [Venables et al., 2014](#); [L. Middleton et al., 2022](#)). This is  
 739 in part because boreholes can affect the boundary layer making undisturbed measurement  
 740 challenging. Autonomous vehicles are providing a platform that circumvents this challenge  
 741 ([Davis et al., 2022](#)). Beneath the warm Larsen C Ice Shelf, a relatively low drag coefficient  
 742 was observed ([Davis & Nicholls, 2019](#)). However, sea ice analogs for marine ice zones  
 743 (refreezing regions formed by the accretion of frazil ice) suggest that drag coefficients up to  
 744 two orders of magnitude higher are possible ([N. J. Robinson et al., 2017](#)).

### 745 **3.1.7 Iceberg calving**

746 Ice shelf calving events are a consequence of the propagation of rifts (crevasses that  
 747 penetrate the full shelf thickness) to the shelf front, such that they isolate ice blocks from  
 748 the main shelf (an anticipated calving site is represented in Fig. 6). Spatial variations in  
 749 ice shelf velocity are the “first-order control” on calving, as they cause strain rates that  
 750 determine the location and depth of crevasses and, subsequently, propagate the crevasses  
 751 and resulting rifts ([Benn et al., 2007](#)). These phenomena occur at the scale of the ice shelf  
 752 flow structure ([Meier, 1997](#)). However, smaller scale processes are also present, such as  
 753 “hydrofracturing”, where the water in surface melt ponds flows into and expands surface  
 754 crevasses, which can have significant influence on ice shelf resilience (Fig. 6; [Lai et al., 2020](#)).

755 Once crevasses or rifts have formed in ice shelves, force imbalances due to the sur-  
 756 rounding water also drive crevasse and rift propagation (Benn et al., 2007). Hence, dynamic  
 757 couplings between ice shelves and the Southern Ocean exert important “second-order con-  
 758 trols” on iceberg calving (i.e., superimposed on the first-order control; Benn et al., 2007;  
 759 Y. Liu et al., 2015). There is evidence that this only occurs once the ice shelf has thinned  
 760 sufficiently or for a rift system that is close to detachment (Bassis et al., 2008). Moreover,  
 761 if present, fast ice or *mélange* (a consolidated agglomeration of icebergs and fast ice) exerts  
 762 a backstress on ice shelves (Massom et al., 2010; Greene et al., 2018), which can delay or  
 763 prevent iceberg calving (Stevens et al., 2013; Massom et al., 2015, 2018; Arthur et al., 2021;  
 764 Gomez-Fell et al., 2022).

765 In addition to these slowly varying drivers of iceberg calving, there are wave-driven  
 766 mechanisms of relevance. Ice shelf flexure has been detected in response to swell (§ 5.1),  
 767 as well as tides (§ 5.2), infragravity waves and tsunamis (Bromirski et al., 2010; Brunt  
 768 et al., 2011; Padman et al., 2018). Flexure due to swell is greatest in the outer shelf  
 769 margins (Chen et al., 2018; Bennetts, Liang, & Pitt, 2022) and during summer when the  
 770 sea ice barrier is at its weakest or absent (Massom et al., 2018; Chen et al., 2019). Swell-  
 771 induced shelf stresses peak at crevasses (Bennetts, Liang, & Pitt, 2022), and they have been  
 772 associated with crevasse and rift propagation (Banwell et al., 2017; Lipovsky, 2018), iceberg  
 773 calving (MacAyeal et al., 2006; Cathles IV et al., 2009) and triggering catastrophic ice shelf  
 774 disintegration events (Massom et al., 2018).

775 Surface waves also initiate small-scale calving through a combination of warm surface  
 776 water and forced convection. The combination of conditions causes a relatively high rate  
 777 of melting at the shelf front waterline and a so-called “wavecut”. The wavecut isolates the  
 778 overhanging ice, which becomes unstable and collapses (Orheim, 1987; T. Hughes, 2002),  
 779 leaving behind a protruding “ice bench” (or “ice foot”) at the shelf front. The bench exerts  
 780 a buoyant vertical force, deforming the shelf front into a so-called “rampart moat” structure.  
 781 The associated internal ice stresses can propagate basal crevasses and, hence, calve relatively  
 782 small, but full-thickness icebergs along the crevasse.

### 783 3.2 Sea ice

784 The Antarctic sea ice zone is divided into four seasonally changing areas: (i) the largely  
 785 immobile landfast sea ice (or fast ice), which is attached to many stretches of the coastline,  
 786 including ice shelf fronts; (ii) the shear zone that sits between the coastline/fast ice and  
 787 (iii) the semi-consolidated ice pack; and (iv) the highly dynamic outer tens to hundreds of  
 788 kilometres of the ice cover, known as the marginal ice zone, which is characterised by the  
 789 presence of surface waves (Fig. 6). Sea ice forms a nearly-continuous torus (interrupted by  
 790 the Antarctic Peninsula) around Antarctica, which usually expands to an annual maximum  
 791 of 18–19 million km<sup>2</sup> in extent during winter and contracts to a minimum of 2–4 million km<sup>2</sup>  
 792 during summer. The majority of Antarctic sea ice is less than one year old, and only  
 793 approximately half a metre to two metres thick on average (Kacimi & Kwok, 2020; Magruder  
 794 et al., 2024), with the thickest ice resulting from mechanical deformation, for example, into  
 795 pressure ridges (Fig. 6). From the global climate perspective, there is a focus on circumpolar  
 796 Antarctic sea ice extent and/or volume metrics. A range of large- to small-scale dynamic  
 797 (and thermodynamic) ocean processes directly determine the Antarctic sea ice distribution  
 798 and properties relevant to the global scale.

799 Polynyas are an additional phenomenon that form around the Antarctic margin. They  
 800 are typically large openings within the sea ice (i.e., not leads or fractures) where sea ice  
 801 would be expected for thermodynamic reasons alone, which are created by local melting  
 802 of sea ice by warm water upwelling and/or katabatic winds driving sea ice offshore from  
 803 near-coastal areas. Polynyas range from small, ephemeral polynyas, through to the very  
 804 large Ross Sea and Cape Darnley polynyas, as well as the open ocean Maud Rise polynya.  
 805 In winter, they are “sea ice factories”, in which  $\approx 10\%$  of Antarctic sea ice is produced

806 and with the Ross Sea polynya by far the most prolific (Tamura et al., 2008; Ohshima et  
 807 al., 2016; Zhou et al., 2023). A contemporary review of polynyas is given in §§ 4.2.2–4.2.3,  
 808 rather than in § 3.2, due to their important influence on turbulent convection.

### 809 3.2.1 Sea ice drift

810 Sea ice away from the coast, islands or icebergs (where it is usually found as fast ice)  
 811 is able to drift under forcing from the atmosphere and ocean, and is known as “drift ice” or  
 812 “pack ice”. This drift redistributes the pack, and influences sea ice extent, with changes in  
 813 concentration and thickness being the result of differential ice velocities. Generally slower  
 814 speeds are found in the shear zone, where grinding, rafting and locking between ice floes  
 815 (discrete chunks of sea ice) create internal stresses that slow the drift. Faster drift speeds  
 816 occur at more equatorward latitudes (north of the Antarctic Divide), where the sea ice  
 817 cover follows the Antarctic Circumpolar Current (§ 2.1). The fastest speeds are found in the  
 818 unconsolidated outer margins of the ice cover, i.e., in the marginal ice zone (Heil & Allison,  
 819 1999; Doble & Wadhams, 2006; Alberello et al., 2020).

820 On time scales of hours or less, atmospheric stress due to winds is generally the dominant  
 821 driver of sea ice drift (Weeks, 2010), with the motion opposed by oceanic stress. Both  
 822 atmospheric and oceanic stresses are usually modelled using quadratic drag laws (Weeks,  
 823 2010). The drag coefficients can be decomposed into viscous “skin” drag and “form” drag,  
 824 where the latter depends on the sea ice roughness, created by an accumulation of relatively  
 825 small-scale features, particularly floe edges in the marginal ice zone and pressure ridges in  
 826 the semi-consolidated sea ice pack (Tsamados et al., 2014). The oceanic stress also involves a  
 827 turning angle, which represents the difference in direction between the geostrophic flow and  
 828 the stress on the sea ice surface due to the Coriolis force (counter-clockwise in the Southern  
 829 Hemisphere; Weeks, 2010). For simplicity, turning angles are often applied directly in the  
 830 sea ice–ocean drag term, but more sophisticated models derive them from the ocean surface  
 831 Ekman layer (Park & Stewart, 2016).

832 Atmospheric and oceanic drag manifest from similar underlying physics (Leppäranta,  
 833 2011). However, as typical sea ice motion are much slower than wind speeds but comparable  
 834 to ocean current speeds, the wind acts as an external force, whereas ice and ocean dynamics  
 835 are coupled as the sea ice is embedded within the upper ocean (Heil & Hibler, 2002). The  
 836 coupled ice and ocean dynamics are dependent on the relative sea ice velocity, sea ice basal  
 837 roughness and the ocean stratification, all under the influence of the Coriolis force (McPhee,  
 838 2008). The Coriolis force influences sea ice drift through the sea surface tilt, which has been  
 839 attributed as the source of sea ice drift rotation close to the inertial frequency in water too  
 840 deep to be caused by tidal currents (Alberello et al., 2020).

### 841 3.2.2 Surface wave–floe interactions in the marginal ice zone

842 The outer fringes of Antarctic sea ice are in contact with the sea ice-free Southern  
 843 Ocean and its energetic surface waves (§ 5.1.3). Thus, Antarctic sea ice has a wide and  
 844 almost circumpolar marginal ice zone (Day et al., 2023). Surface waves affect sea ice in  
 845 the marginal ice zone (Fig. 9) by (i) breaking up larger floes (see below), (ii) herding the  
 846 floes into bands (Wadhams, 1983; Shen & Ackley, 1991), (iii) promoting growth of new ice  
 847 (e.g., frazil) during freezing conditions, (iv) forcing ice drift through momentum transfer  
 848 (radiation stress; T. D. Williams et al., 2017; P. Sutherland & Dumont, 2018; Dumont,  
 849 2022), (v) causing floes to collide and raft (S. Martin & Becker, 1987, 1988; Dai et al., 2004;  
 850 Rottier, 1992; Bennetts & Williams, 2015; Yiew et al., 2017; Herman et al., 2019), which  
 851 may erode the floe edges and produce ice rubble, (vi) overwashing the floes (Skene et al.,  
 852 2015; Nelli et al., 2020; Pitt et al., 2022), which influences thermodynamic ice properties  
 853 by removing snow cover and creating saline ponds on the floe surfaces (Ackley & Sullivan,  
 854 1994; Massom et al., 1997, 2001), and (vii) generating turbulence in the water below floes  
 855 that increases basal melt (Wadhams et al., 1979; M. Smith & Thomson, 2019). Overall,

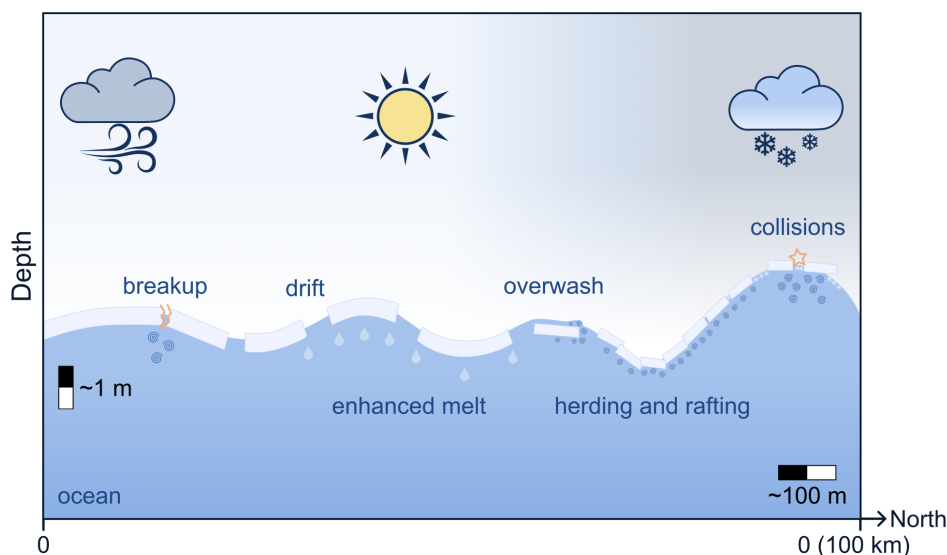


**Figure 9.** Schematic of surface wave–ice floe interaction processes in the marginal ice zone, including (from left to right): wave-induced breakup of a large floe; subsequent northward drift of small broken floes due to off-ice winds, and enhanced melt in summer (indicates by white tear drops below ice floes); wave overwash of a floe; herding and rafting of small floes; floe–floe collisions; production of frazil in the open water created between floes during winter. The spirals indicate turbulent mixing.

856 the waves create a fragmented ice matrix in the marginal ice zone, containing a mixture of  
 857 floes (smaller than in the semi-consolidated sea ice pack) and unconsolidated sea ice (grease,  
 858 pancakes, etc.). Sea ice in the marginal ice zone is highly mobile and responds rapidly to  
 859 forcing by strong winds over the Southern Ocean (Vichi et al., 2019; Alberello et al., 2020).

860 Breakup of large floes is considered to be the primary effect of waves on sea ice. Ice  
 861 floes larger than prevailing wavelengths experience a hydroelastic response to wave motion  
 862 (Montiel, Bonnefoy, et al., 2013; Montiel, Bennetts, et al., 2013; Meylan et al., 2015),  
 863 creating so-called “flexural-gravity waves” (Bennetts et al., 2007; Vaughan et al., 2009).  
 864 Sea ice is a brittle material (Timco & Weeks, 2010), which fractures when the flexural  
 865 stresses/strains exceed the material strength (Montiel & Mokus, 2022). The generally held  
 866 view of the wave-induced breakup process (Squire et al., 1995) is of a large wave event  
 867 breaking up a quasi-continuous sea ice (e.g., a very large floe) into smaller floes that then  
 868 form or expand the marginal ice zone, in which floes larger than the prevailing wavelengths  
 869 are broken up further, thus forming a marginal ice zone where mean floe sizes increase  
 away from the sea ice edge as wavelengths increase (Squire & Moore, 1980). The standard  
 theoretical description of the wave-induced breakup process is of regular (unidirectional  
 and monochromatic) flexural-gravity waves in a homogeneous floating elastic plate causing  
 stresses/strains that exceed a critical threshold (Kohout & Meylan, 2008; Vaughan & Squire,  
 2011; Mokus & Montiel, 2021; Montiel & Mokus, 2022). Experiments in ice tanks (Dolatshah  
 et al., 2018; Herman et al., 2018; Passerotti et al., 2022) and in a “natural laboratory” (in  
 a bay of the Gulf of St Lawrence using ship generated waves; Dumas-Lefebvre & Dumont,  
 2023) have given new understanding of the breakup process. However, measuring breakup  
 in the marginal ice zone remains challenging, despite it being identified as a priority three  
 decades ago (Squire et al., 1995; Voermans et al., 2020, 2021).

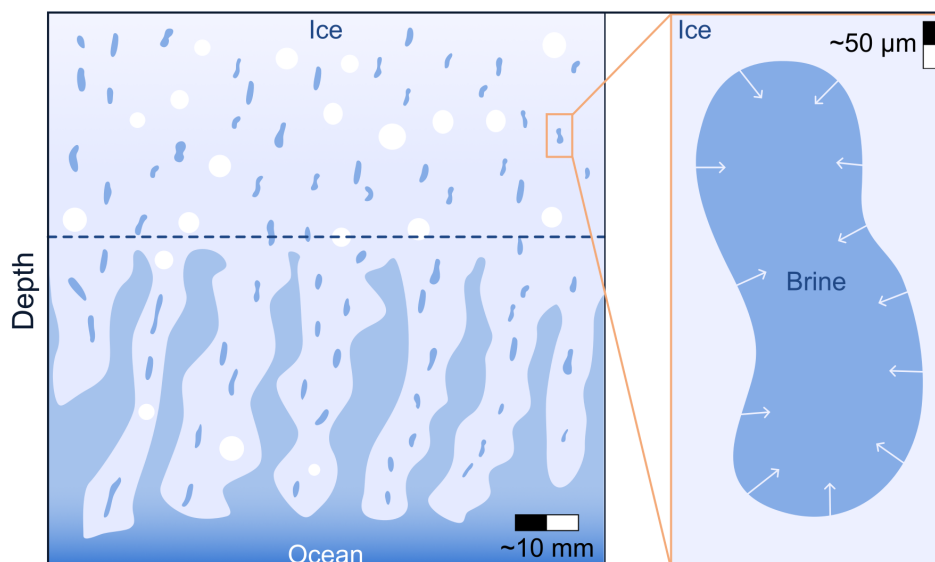


**Figure 10.** The main panel (left-hand side) is a schematic of sea ice at finescale. Above the dashed line, air bubbles (white circles) and brine inclusions (elongated blue shapes) are trapped within the impermeable, solid ice (sky blue). Below the line the ice is permeable, allowing brine drainage and fresh water inflow, i.e., a mushy layer. A zoom in on the microscale for a brine inclusion is given (right). The liquid brine region is surrounded by ice, and the arrows point in the direction of the salt flux during the freezing process.

880 Wave–floe interaction potentially link directly to sea ice extent and, hence, the large-  
 881 scale climate, through a positive (summer) feedback (Bennetts et al., 2010; Montiel &  
 882 Squire, 2017; Horvat, 2022). The positive feedback involves an initial weakening of the sea  
 883 ice that allows waves to travel farther into the sea ice-covered ocean, so that a wave event  
 884 can break the ice cover at a deeper location than prior to the initial weakening. The breakup  
 885 leaves the floes more susceptible to lateral melting during the summer (Steele, 1992), which  
 886 further weakens the sea ice and allows waves to travel even deeper, and so on. It has been  
 887 suggested that the positive feedback has already been triggered in the Arctic due to initial  
 888 weakening by warming temperatures (Squire, 2011), although this has not been quantified  
 889 through direct measurements yet. However, the feedback is implicit in the comparison  
 890 between trends in Antarctic ice edge latitude and local significant wave heights (Kohout  
 891 et al., 2014). A negative (winter) feedback has also been proposed, in which wave-induced  
 892 breakup creates openings in the ice cover (leads; Fig. 6) that freeze over to strengthen the  
 893 sea ice and protect the location against future wave events (Squire, 2011; Horvat, 2022).

### 894 3.2.3 Brine inclusions to convective channels

895 The small-scale structure of sea ice alters its thermal and physical properties, which is  
 896 important to understand how it interacts with the Southern Ocean (and the atmosphere).  
 897 Sea ice is a complex blend of solid H<sub>2</sub>O crystals, liquid brine inclusions, air bubbles and  
 898 precipitated salts (Fig. 10), whose volume fractions, distributions and connectedness depend  
 899 strongly on temperature, salinity and depth (Perovich & Gow, 1996; Light et al., 2003;  
 900 Golden et al., 2007; Golden, 2009; D. N. Thomas, 2017; Kraitzman et al., 2022). Moreover,  
 901 sea ice usually consists of a layer of “granular textured ice” with random crystal orientations,  
 902 above a layer of “columnar textured ice” with well-ordered ice crystals, separated by a  
 903 transition layer (Eicken, 2003; Lund-Hansen et al., 2020; Oggier & Eicken, 2022). Due to  
 904 dynamic growth conditions in the Southern Ocean, more than 60% of the total thickness of

905 Antarctic sea ice is primarily composed of frazil ice, and, in the upper layer of the ocean,  
 906 frazil ice tends to form floes that contain a significant amount of ice with a granular texture.  
 907 This leads to the dominant layer of Antarctic sea ice being characterised by a granular  
 908 texture (Lange et al., 1989; D. N. Thomas, 2017).

909 The Southern Ocean controls Antarctic sea ice melt from mid-November to mid-January.  
 910 During the melt season, brine inclusions in the sea ice (micrometre–centimetre length scale  
 911 regions of high salt concentration; Fig. 10 zoom; Kraitzman et al., 2022) expand and merge  
 912 to form up to metre-long brine channels, which allow fluid, nutrients and salt to exchange  
 913 between the ocean and the ice (Golden et al., 1998; Golden, 2001). For Antarctic sea ice,  
 914 brine channels are vertically oriented with diameters  $\approx 200 \mu\text{m}$  (Weissenberger et al., 1992),  
 915 and the brine fluid flow in the channels is a critical factor in the facilitation of thermal  
 916 fluxes, which leads to an enhancement in the thermal conductivity (Lytle & Ackley, 1996;  
 917 Trodahl et al., 2001). Moreover, the brine drainage leads to the formation of air bubbles,  
 918 which result in greater sea ice albedo (Perovich, 1996).

919 On the centimetre–metre length scale, sea ice is commonly described as a “mushy  
 920 layer” (solid ice crystals mixed with interstitial liquid brine), bounded from above by an  
 921 impermeable layer and from below by a fully liquid layer (Fig. 10; Feltham et al., 2006). The  
 922 dense, salty interstitial fluid is trapped and stagnant within the ice matrix and is assumed  
 923 to be in local thermodynamic equilibrium, which prevents the solid ice from melting. As sea  
 924 ice grows, the interstitial liquid in the mushy layer undergoes convection due to differences  
 925 in temperature and density, leading to the release of salt into the ocean. This brine drainage  
 926 phenomenon is accompanied by inflow of less saline seawater from the surrounding mushy  
 927 layer (Worster et al., 2000; Worster & Jones, 2015; A. Wells et al., 2011; A. J. Wells et  
 928 al., 2019). With a local convective flow partially occupying the mushy layer, brine drainage  
 929 occurs in only part of the sea ice. However, as the temperature increases and the sea  
 930 ice becomes more porous, the convective flow eventually spreads throughout the entire sea  
 931 ice depth, utilising the network of brine channels. Oceanic currents exert pressure on the  
 932 interface layer between the sea ice and the ocean, affecting the convective brine flow (Feltham  
 933 et al., 2002). The brine rejection process is crucial in the formation of Dense Shelf Water  
 934 and ultimately the Antarctic Bottom Water that fills the abyss of the global oceans (see  
 935 §2.5).

### 936 3.3 Closing the loops

937 The Southern Ocean connects to the southern cryosphere through Antarctic ice shelves  
 938 (§ 3.1) and sea ice cover (§ 3.2). The Southern Ocean influences the extents and strengths of  
 939 both ice shelves and sea ice covers. Exchanges between the Southern Ocean and sub-ice shelf  
 940 water cavities over a range of scales dictate basal melting of ice shelves (§§ 3.1.1–3.1.6). The  
 941 Southern Ocean also plays a role in ice shelf mass loss via iceberg calving, through ice shelf  
 942 flexure forced by surface waves, although this phenomenon is suppressed in the presence  
 943 of surrounding sea ice cover (§ 3.1.7). Southern Ocean circulation influences the large-scale  
 944 redistribution of sea ice via drift (§ 3.2.1) and heat flux from the ocean connects with sea  
 945 ice microstructure to control sea ice melt (§ 3.2.3). Surface waves have a major impact on  
 946 the outer part of the sea ice cover (the marginal ice zone), which modulates its dynamics  
 947 and thermodynamic coupling with the ocean (and atmosphere; § 3.2.2). In turn, ice shelves  
 948 and sea ice have a major influence on Southern Ocean dynamics, by reducing or eliminating  
 949 momentum transfer between the atmosphere and ocean, which affects large-scale circulation  
 950 (§ 2), although sea ice drift can have the opposite effect and increase internal ocean stresses  
 951 (4.1.1). Ice shelves and sea ice can generate and trap internal waves (§ 5.3). In contrast, sea  
 952 ice also suppresses or eliminates the generation of surface waves by winds and attenuates  
 953 waves over distance travelled through the sea ice-covered ocean (§ 5.1.3), which reduces  
 954 upper ocean mixing in these regions (§ 4.3.1). Ice shelves also influence upper ocean mixing  
 955 (in combination with tides; § 4.3.1), as well as mesoscale turbulence (§ 4.1.5). Another  
 956 major influence of the Southern Ocean sea ice is through ice melt, which creates buoyancy

957 forcing to support large-scale circulation (as already described; §2) and turbulence, such  
958 as convection in coastal polynyas (§4.2.2). These turbulence processes will be described in  
959 detail in the next section (§4), with wave processes to follow in §5.

## 4 Turbulence

Southern Ocean turbulence is driven by a wide range of processes and acts on many different scales. Turbulence is inherently characterised by nonlinear and chaotic motions. It is often difficult to establish the drivers of turbulence, which makes quantifying and categorising turbulence a challenge. Here, Southern Ocean turbulence is broadly categorised into eddies, jets and fronts (§ 4.1), convection (§ 4.2) and mixing (§ 4.3). Eddies, jets and fronts lie broadly in the realm of mesoscale turbulence, close to geostrophic and hydrostatic balance. Mesoscale turbulent processes are affected by a large range of factors, such as wind and buoyancy forcing, along with interactions with the mean flow, eddies, topography and more. Convection is driven by vertical buoyancy differences and is characterised by vigorous vertical motion and turbulent plumes. It can be confined to the upper ocean or extend to depth as polynya convection (§§ 4.2.2–4.2.3). Mixing refers to three-dimensional turbulent processes that act to blend waters of different properties. To help categorise the wide range of processes that contribute to turbulence, we break the Southern Ocean into upper, interior and bottom layers (Fig. 11).

There exist past reviews and books on various aspects of ocean turbulence. For eddies, jets and fronts, the review by [A. F. Thompson et al. \(2018\)](#) (also mentioned in § 2) considers the Antarctic Slope Current, which is an area of strong mesoscale turbulence processes, [Ferrari and Wunsch \(2009\)](#) discuss the energy framework for oceans, and [McGillicuddy Jr \(2016\)](#) examines a range of interactions at the oceanic mesoscale. For convection, [J. Marshall and Schott \(1999\)](#) review open ocean convection across the whole of the Earth’s oceans, while [Morales Maqueda et al. \(2004\)](#) review polynyas, including polynya convection and dense water formation. For more detailed reviews of mixing processes, the reader is referred to [Whalen et al. \(2020\)](#), [Moum \(2021\)](#) and [Gille et al. \(2022\)](#), as well as other relevant chapters of the recent Ocean Mixing book by [Meredith and Naveira Garabato \(2021\)](#).

### 4.1 Eddies, Jets and Fronts

The Southern Ocean is renowned for having one of the strongest turbulence fields in the global ocean, which has been shown using the metric of eddy kinetic energy ([Ferrari & Wunsch, 2009](#)). A common definition of eddy kinetic energy is the kinetic energy of deviations from the time-mean velocity field ([A. R. Robinson, 1983](#)). Most of this energy is found in the form of mesoscale turbulence, defined here as nonlinear motion close to geostrophic and hydrostatic balance. Mesoscale turbulence spreads energy across a broad range of length scales through nonlinear interactions, resulting in a complex, highly inhomogeneous and unsteady state of motion ([Rhines, 1979](#)). Because of the latitudinal dependence of the Rossby radius of deformation, the mesoscale range varies over the Southern Ocean, from 1–10 km near the Antarctic continent to 100–1000 km in the Antarctic Circumpolar Current (Fig. 12).

A generic feature of mesoscale turbulence is its tendency to form long-lasting, spatially localised features, such as jets (narrow, quasi-zonal currents), fronts (sharp gradients in temperature or salinity), and eddies (spatially and/or temporally coherent vortices). There is no uniquely accepted definition of eddies, jets or fronts ([Chapman et al., 2020](#)). For example, the dominant circulation feature of the Southern Ocean is the Antarctic Circumpolar Current (§ 2.1), which is composed of numerous jets that interact with each other ([A. F. Thompson, 2008](#)), coinciding with and flanked by sharp fronts, and co-located with the most active eddy field in the global ocean ([Fu et al., 2010](#)). The view is further complicated by the strong feedbacks that exist between these features. For example, jets become baroclinically and/or barotropically unstable to generate eddies, while eddies can flux momentum to sharpen jets ([Waterman & Hoskins, 2013](#)). Thus, this review tends towards aggregating these features into the broad category of mesoscale geostrophic turbulence.

In order to provide an overview of the dynamics of Southern Ocean mesoscale turbulence, we examine the sources, interactions and sinks in the eddy kinetic energy budget. The primary source of eddy kinetic energy in the Southern Ocean is the generation of insta-

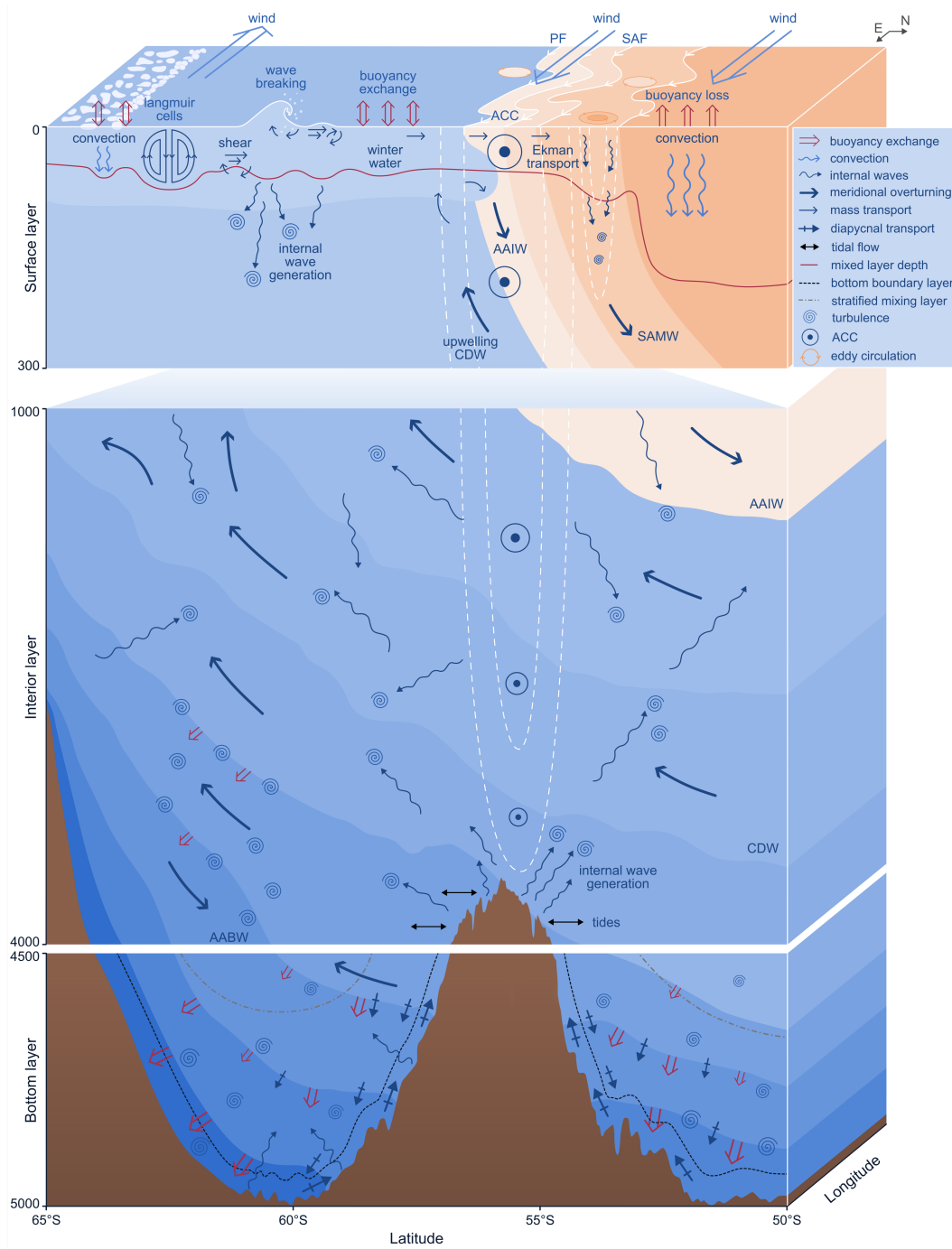


**Figure 11.** Schematic to illustrate surface, interior and bottom boundary layers in the Southern Ocean, with a summary of turbulence processes acting in each layer. The ocean colours indicate the density, from lighter (dark orange) to denser (dark blue) waters, and isopycnal contours are the interfaces between the layers. Note that the three layers are offset in latitude and disconnected in the vertical, with the surface layer 0–300 m depths, interior layer is 1000–4000 m and bottom layer 4500–5000 m. The water masses shown are Subantarctic Mode Water (SAMW), Antarctic Intermediate Water (AAIW), Circumpolar Deep Water (CDW), and Antarctic Bottom Water (AABW). Also shown on the top panel are the Antarctic Circumpolar Current (ACC), Polar Front (PF) and the Subantarctic Front (SAF).

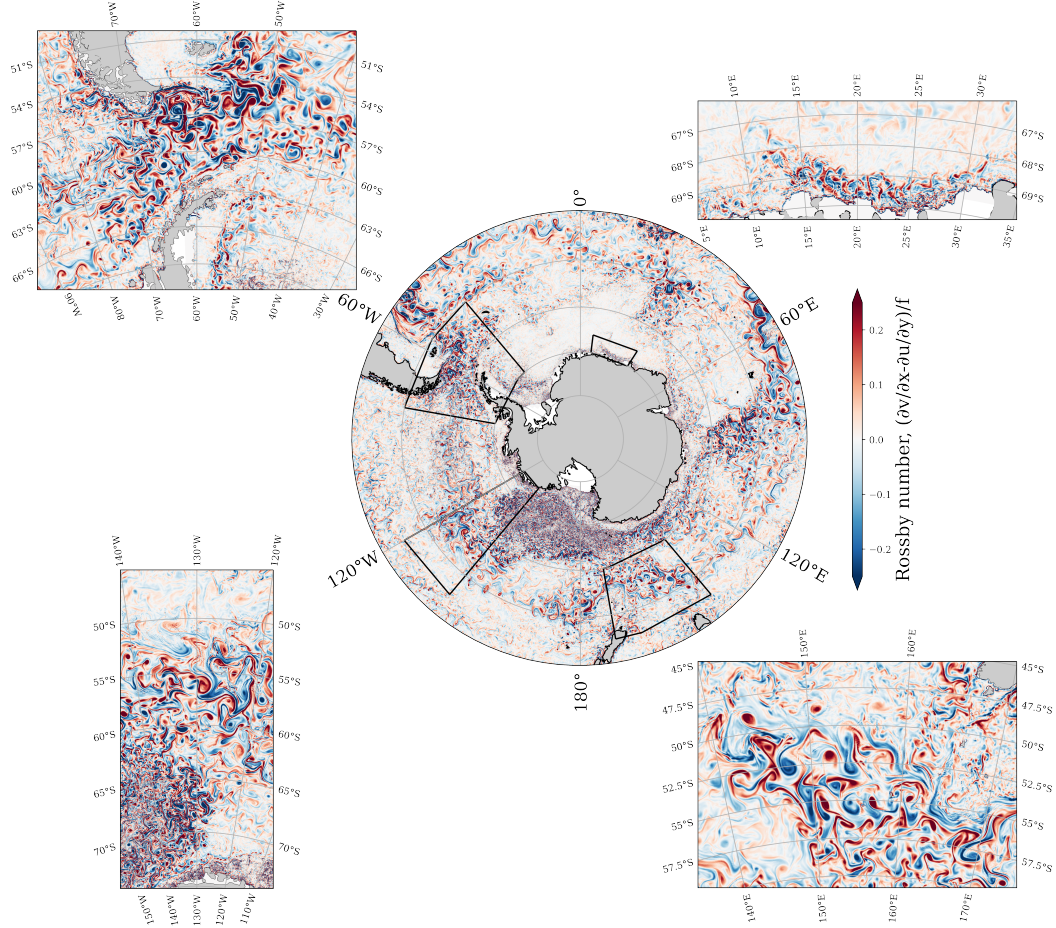


**Figure 12.** Mesoscale (and submesoscale) turbulent structures are ubiquitous in the Southern Ocean. The Rossby number, defined as the vertical component of relative vorticity ( $\partial v/\partial x - \partial u/\partial y$ ) divided by the planetary vorticity ( $f$ ), highlights dynamical features. The four insets show: the Antarctic Slope Current (top right), a large-scale meander near the Macquarie Ridge and the associated energetic mesoscale eddy field (bottom right), the spatial variation in the dominant dynamical scale in the Southern Ocean (bottom left), and the highly energetic turbulence in Drake Passage (top left). The velocity fields are snapshots from a regional simulation around Antarctica at a  $1/20^\circ$  lateral resolution, performed with the Modular Ocean Model, version 6 (Adcroft et al., 2019) by the Consortium for Ocean and Sea Ice Modelling in Australia (Kiss et al., 2020).

1011 bilities in the large-scale flow, ultimately powered by energy input from the wind (§ 4.1.1)  
 1012 and buoyancy forcing (§ 4.1.2). The equilibrium value of eddy kinetic energy in any region is  
 1013 governed by the energy source and redistribution of eddy kinetic energy by the background  
 1014 flow and other interactions, and also by the rate at which eddies dissipate their energy  
 1015 (§ 4.1.6). This view of the eddy kinetic energy reservoir as a source-sink problem makes it  
 1016 clear that a full understanding of the eddy field requires knowledge of both eddy formation  
 1017 processes and eddy dissipation dynamics.

1018 The mesoscale turbulence field is influenced directly via exchanges of energy with internal  
 1019 waves (§ 4.1.3). Feedbacks between different features can redistribute and influence  
 1020 energy via self-interaction of the mesoscale turbulence field (§ 4.1.4). Topography plays an  
 1021 important role in modulating the mesoscale dynamics of the Southern Ocean and connecting

1022 the large-scale circulation to smaller-scale, faster processes (§ 4.1.5). The geostrophic turbu-  
 1023 lence field is influenced indirectly by other components of the ocean–atmosphere–cryosphere  
 1024 system via their modulation of energy input by wind and buoyancy forcing. Thus, mesoscale  
 1025 turbulence acts as the bridge between the global-scale circulation and small-scale processes  
 1026 in the Southern Ocean.

#### 1027 4.1.1 Wind forcing

1028 The power input from the atmosphere into the ocean is determined by the surface  
 1029 wind stress. The wind stress describes an exchange of momentum between the air and  
 1030 the water, which is mediated through the sea surface and includes influences from surface  
 1031 gravity waves (§ 5.1). Wind stress is often calculated via a bulk formula, which implies that  
 1032 it is proportional to  $|\mathbf{U}_{\text{air}} - \mathbf{u}|(\mathbf{U}_{\text{air}} - \mathbf{u})$ , where  $\mathbf{u}$  is the ocean surface velocity and  $\mathbf{U}_{\text{air}}$  is the  
 1033 wind velocity at a reference height (typically 10 m) above the sea surface. Two features in  
 1034 the wind stress bulk formula are noteworthy. First, the wind stress is quadratic in velocity,  
 1035 which implies that even if the average wind speed is zero in a region, there can still be a net  
 1036 wind stress felt by the ocean. Second, the wind stress depends on the relative flow between  
 1037 the atmosphere and the ocean,  $\mathbf{U}_{\text{air}} - \mathbf{u}$ , and therefore the ocean flow affects how the ocean  
 1038 feels the atmosphere.

1039 For a long time it was thought that most of the wind energy input resulted from the  
 1040 correlation between the mean wind stress and mean currents, and that the time-varying  
 1041 wind and ocean flow variability contribution was negligible (Wunsch, 1998; Scott & Xu,  
 1042 2009). However, more recent studies have highlighted the important role of the synoptically  
 1043 varying winds (here, this refers to winds varying on “short” timescales of hours to days),  
 1044 which can result in a 70% increase in power input into the ocean from the winds (Zhai  
 1045 et al., 2012). Most of this energy enters the ocean in the winter time and in regions with  
 1046 strong synoptic wind variability, such as the Southern Ocean (Torres et al., 2022). The wind  
 1047 stress injects energy into both geostrophic and higher frequency motions (especially near  
 1048 the inertial frequency) and from the latter, near-inertial waves are energised that propagate  
 1049 down below the mixed layer into the deep ocean (§ 5.3).

1050 Generally, ocean velocities are much smaller than wind velocities, and, therefore, one  
 1051 might expect that the relative flow contribution to the wind stress power input would be  
 1052 insignificant. However, ocean flow features appear in much smaller length scales and vary  
 1053 at much longer time scales than the synoptic variability of the winds. If the relative wind  
 1054 and ocean flows are opposing, then winds damp the ocean flow and remove energy from the  
 1055 ocean, particularly in eddy-rich regions like the Southern Ocean (Zhai et al., 2012). The  
 1056 relative wind effect has a particularly large impact on mesoscale turbulence through “eddy  
 1057 killing”, which results in a 20–40% reduction in mesoscale eddy kinetic energy compared  
 1058 to a formulation of the surface stress that does not take ocean currents into account (e.g.,  
 1059 Renault et al., 2016; Jullien et al., 2020).

1060 The presence of sea ice alters the relationship between atmospheric winds and momen-  
 1061 tum transfer to the ocean surface. In regions with drift sea ice (§ 3.2.1), the momentum  
 1062 transfer from atmosphere to ocean can be three times that for an ice free interface (T. Mar-  
 1063 tin et al., 2014). However, at higher concentrations, the internal stresses in sea ice can  
 1064 reduce the momentum transfer into the ocean, potentially even resulting in an ice-ocean  
 1065 drag that decelerates ocean currents (Meneghello et al., 2018; A. L. Stewart et al., 2019).  
 1066 Landfast sea ice and ice shelves are critical elements of the coastal cryosphere through their  
 1067 complete removal of wind stress forcing (§ 3).

#### 1068 4.1.2 Buoyancy forcing

1069 Buoyancy forcing is another driver of mesoscale geostrophic turbulence in the South-  
 1070 ern Ocean. The presence of stratification allows baroclinic modes of instability to generate

1071 geostrophic turbulence, while also weakening the barotropic potential vorticity constraints  
 1072 on geostrophic flow (Cushman-Roisin & Beckers, 2011). The large scale meridional slop-  
 1073 ing of isopycnals across the Antarctic Circumpolar Current region is maintained by the  
 1074 wind (Ferrari & Wunsch, 2009). Mesoscale turbulence is tightly coupled to stratification  
 1075 by working to flatten these isopycnals. For example, increased heat storage north of the  
 1076 Subantarctic Front has been linked to an acceleration of the zonal flow (Shi et al., 2021).  
 1077 In addition, baroclinic instability is central to the dynamics of standing meanders of the  
 1078 Antarctic Circumpolar Current (Watts et al., 2016; Foppert et al., 2017; Youngs et al., 2017;  
 1079 Constantinou & Hogg, 2019). Interactions between Southern Ocean jets, topography, and  
 1080 stratification can also lead to rapid changes in ocean ventilation (Klocker, 2018).

1081 Southern Ocean stratification is influenced by many processes, which can also go on  
 1082 to impact mesoscale turbulence. Some processes, such as sea ice melt and surface heating,  
 1083 act to stratify the water column (Haumann et al., 2020). Others, such as convection and  
 1084 mixing, decrease the vertical stratification. Meltwater from ice sheets and ice shelves leads to  
 1085 fresh, cold surface water near Antarctica. For example, the meltwater plume from ice shelf  
 1086 melting modifies the ocean stratification and uptake of surface buoyancy, which will go on  
 1087 to influence the mesoscale turbulence field. Fast ice reduces ocean–atmosphere heat and salt  
 1088 exchanges, replacing them with ice–ocean exchanges of melting and freezing. Vertical mixing  
 1089 by mesoscale turbulence underneath sea ice dissipates eddy kinetic energy and reduces sea  
 1090 ice thickness by up to 10% (Gupta et al., 2020). Strong horizontal density gradients from  
 1091 vertical convective mixing can provide energy for geostrophic turbulence to restratify that  
 1092 region (H. Jones & Marshall, 1997; Kurtakoti et al., 2018).

#### 1093 *4.1.3 Internal wave interactions*

1094 The geostrophic turbulence field in the ocean continuously exchanges energy with the  
 1095 internal wave field (E. D. Brown & Owens, 1981; Polzin, 2010; Polzin & Lvov, 2011).  
 1096 Internal waves “see” eddies and jets as a slowly moving and usually larger-scale flow from  
 1097 which they can both extract or input energy, depending on the relative direction of the  
 1098 eddying flow and wave propagation. It has been argued that energy exchange with internal  
 1099 waves is a significant net sink of eddy energy (Polzin, 2008, 2010), although other studies  
 1100 in the Southern Ocean have found the opposite effect (Cusack et al., 2020; Shakespeare &  
 1101 Hogg, 2019). As such, the overall effect of internal waves on eddies and jets remains a topic  
 1102 of active research (§5.3).

#### 1103 *4.1.4 Mesoscale turbulence self-interactions*

1104 Mesoscale turbulence in the Southern Ocean exhibits many of the nonlinear self-interactions  
 1105 seen in two-dimensional and quasi-geostrophic turbulence under the constraints of rotation  
 1106 and stratification (Hopfinger & Van Heijst, 1993). The level of eddy self-interaction can  
 1107 be quantified using a nonlinearity parameter, which expresses the ratio of the rotational  
 1108 velocity of the eddy to its translational velocity (Chelton et al., 2011; Klocker et al., 2016).  
 1109 Southern Ocean eddies, particularly in the Antarctic Circumpolar Current, typically have  
 1110 large values of this parameter (of order ten), implying that the eddies cannot be regarded  
 1111 as linear perturbations to a quiescent background, but instead modify the surrounding flow  
 1112 by trapping and transporting fluid (Chelton et al., 2011). These self-interactions include  
 1113 eddy merging and splitting events (Cui et al., 2019), the formation of quasi-stable dipoles,  
 1114 quadrupoles and larger eddy assemblages (e.g., Gallet & Ferrari, 2020), and the cascade of  
 1115 energy from small to large scales (Salmon, 1998; Scott & Wang, 2005; Aluie et al., 2018;  
 1116 Balwada et al., 2022). The inverse energy cascade is consistent with a pronounced sea-  
 1117 sonal cycle in eddy kinetic energy and eddy diameter observed in a 25-year climatology  
 1118 of satellite altimetry measurements (Martínez-Moreno et al., 2021), where small-scale (di-  
 1119 ameter < 120 km) coherent eddies peaked in amplitude in mid-summer, while large-scale  
 1120 (> 120 km) eddies peaked in autumn. The findings suggest an inverse cascade from small

1121 scales, driven by baroclinic instability early in the summer, to large diameter eddies which  
 1122 grow in amplitude later in the season.

1123 Eddy-mean flow interactions are mediated by eddy fluxes of buoyancy and momentum  
 1124 (Q. Li et al., 2016). For example, strong jets become baroclinically and/or barotropically un-  
 1125 stable to generate eddies (Phillips & Rintoul, 2000; Chapman et al., 2015; Watts et al., 2016;  
 1126 Youngs et al., 2017; Foppert, 2019; Constantinou & Hogg, 2019), while eddies can flux mo-  
 1127 mentum upgradient to sharpen jets (Waterman & Hoskins, 2013). Eddy momentum fluxes  
 1128 act to accelerate (for a converging momentum flux) or decelerate (for a diverging momentum  
 1129 flux) the Antarctic Circumpolar Current near topographic features such as the Drake Pas-  
 1130 sage and Campbell Plateau (Morrow et al., 1994; Ivchenko et al., 1997; R. G. Williams et al.,  
 1131 2007). Eddy geometry (the eddy shape, size, and anisotropy) provides a useful framework  
 1132 for characterising eddy-mean flow interactions (D. P. Marshall et al., 2012; Waterman &  
 1133 Lilly, 2015). Eddy buoyancy fluxes are key in setting the slope of isopycnal surfaces, thereby  
 1134 influencing the strength and stability of the Antarctic Circumpolar Current (Karsten et al.,  
 1135 2002; J. Marshall & Radko, 2003; Olbers et al., 2004; Olbers & Visbeck, 2005).

#### 1136 **4.1.5 Topographic effects**

1137 Bottom topography plays an important role in modulating the Southern Ocean mesoscale  
 1138 turbulence field (Chelton et al., 1990; Gille & Kelly, 1996). Models and observations indicate  
 1139 that enhanced eddy kinetic energy, cross-frontal transport, and eddy-induced upwelling can  
 1140 be found downstream of major topographic features (Fig. 13; Foppert et al., 2017; Tamsitt  
 1141 et al., 2018; Barthel et al., 2022; Yung et al., 2022). Topography also plays a pivotal role  
 1142 in modulating jet evolution. Observations and idealised models show that the formation of  
 1143 jets, their meridional spacing and variability, and associated transport depend on the length  
 1144 scale and steepness of the topographic features (A. F. Thompson, 2010; Boland et al., 2012;  
 1145 Chapman & Morrow, 2014; Freeman et al., 2016; Constantinou & Young, 2017).

1146 Near the Antarctic margins, ice topography can also influence mesoscale geostrophic  
 1147 turbulence. Rapid changes in water column thickness near ice shelf and glacier tongues  
 1148 modify local angular momentum balances (van Heijst, 1987). Strong potential vorticity  
 1149 gradients occur at ice-shelf fronts (Steiger et al., 2022), where the ice draft may be greater  
 1150 than half the local seabed depth. The ice creates a barrier against which water may pool  
 1151 and a strong along-front flow may develop (Malyarenko et al., 2019). There is evidence that  
 1152 this front provides an impediment to barotropic processes but that baroclinic transport can  
 1153 persist (Wählin et al., 2020; Steiger et al., 2022) enabling penetration of heat beneath ice  
 1154 shelf frontal regions (C. L. Stewart et al., 2019; Davis et al., 2022).

#### 1155 **4.1.6 Dissipation of eddy kinetic energy**

1156 The primary source of eddy energy is the generation of instabilities in the large-scale  
 1157 flow, ultimately powered by wind and buoyancy forcing (§§ 4.1.1–4.1.2). In the Southern  
 1158 Ocean, both barotropic and baroclinic instability contribute to the eddy field, although  
 1159 baroclinic instability is expected to dominate at the mesoscale (Youngs et al., 2017). How-  
 1160 ever, the mesoscale energy has a largely upscale cascade, meaning that energy is returned  
 1161 to the large-scale flow field. This upscale cascade can be considered a consequence of the  
 1162 conservation of potential vorticity and theoretically applies to balanced flows at low Rossby  
 1163 number and in the interior of the ocean (Rhines, 1977). It follows that situations in which  
 1164 balance is broken yield the possibility of a forward cascade of energy to the submesoscales,  
 1165 internal waves and shear-driven turbulence. The main candidate mechanisms for loss of bal-  
 1166 ance involve interactions at the ocean surface or bottom. At the surface, eddies can generate  
 1167 filaments leading to “frontogenesis”, thereby breaking the constraint of low Rossby number  
 1168 flow and creating an active submesoscale flow field (Barkan et al., 2015; McWilliams, 2021).  
 1169 Additionally, the rotation of coherent vortices leads to a wind-stress torque that directly  
 1170 damps eddies (Zhai et al., 2012). Submesoscale instabilities near sloping bottom boundaries

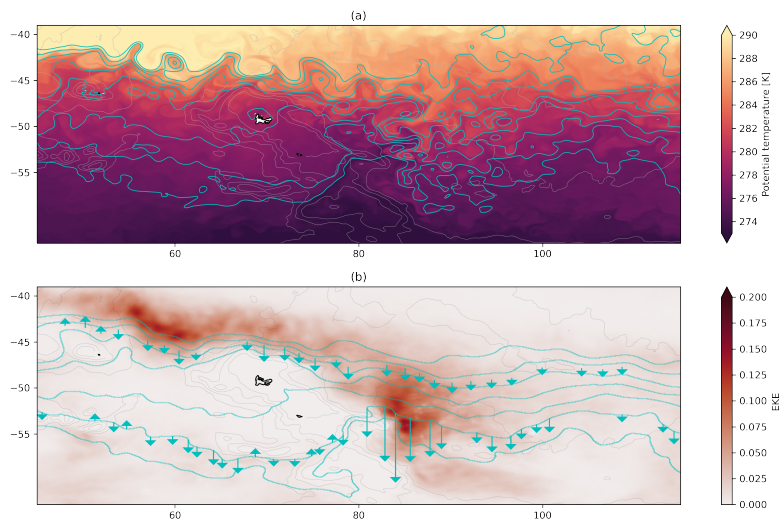


**Figure 13.** Eddies, fronts and jets in the Kerguelen Plateau region. (a) Snapshot of sea surface temperature (colours) and sea surface height (cyan contours) from the ACCESS-OM2-01 model. (b) Eddy kinetic energy (colours), sea surface height and southward eddy thickness fluxes (from results by Yung et al., 2022) averaged over a 10-year simulation. Gray contours in both panels show bathymetry.

1171 may drive loss of balance (Callies, 2018; Wenegrat et al., 2018; Wenegrat & Thomas, 2020).  
 1172 Western boundary currents may act as an “eddy graveyard” (Zhai et al., 2010), likely in-  
 1173 volving interactions between eddies and shoaling topography, such as frictional (Evans et  
 1174 al., 2020; Wright et al., 2013) or dynamical (Dewar & Hogg, 2010) mechanisms.

1175 One dynamical mechanism that removes energy from eddies is the generation of internal  
 1176 waves from eddy-topography interaction (§ 5.3.1). The intense and deep reaching mesoscale  
 1177 flow of the Southern Ocean results in bathymetric interactions that generate Doppler-shifted  
 1178 internal waves, such as lee waves. The breaking of these waves (§ 5.1.1) exerts a drag on  
 1179 the background mesoscale flow. Naveira Garabato et al. (2013) evaluated time-mean lee  
 1180 wave drag globally and found that, while it is a minor contributor to the ocean dynamical  
 1181 balance over much of the ocean, it is a significant player for Antarctic Circumpolar Current  
 1182 dynamics. Extending this estimate to transient eddies in the Southern Ocean, Yang et al.  
 1183 (2018, 2021) have shown that lee wave drag processes dominate over the turbulent bottom  
 1184 boundary layer drag for eddy dissipation, a result consistent with previous results from  
 1185 higher resolution idealised models (Nikurashin et al., 2013).

1186 It has also been proposed that loss of balance can occur spontaneously in the ocean, in  
 1187 the absence of surface forcing or bottom interactions (Molemaker et al., 2005; Shakespeare,  
 1188 2019). Simulations show that spontaneous emissions of internal gravity waves occurs in  
 1189 balanced flow, but while the energy transferred may be locally important, it is unlikely to  
 1190 be a regionally or globally significant sink of eddy energy (Vanneste, 2013; Nagai et al., 2015;  
 1191 Shakespeare & Hogg, 2017; Chouksey et al., 2018). Alternatively, the exchange of energy  
 1192 between eddies and surface- or bottom-generated internal waves can, in some circumstances,  
 1193 result in a net extraction of energy from the eddy field into internal waves (§ 5.3.2).

1194 Despite the range of available mechanisms for eddy dissipation, there is no clear view  
1195 of which mechanism dominates, nor a demonstration of the relative magnitude of these  
1196 mechanisms in the Southern Ocean.

## 1197 4.2 Convection

1198 Convection is a type of flow driven by a vertical buoyancy differential that, in the ocean,  
1199 is due to temperature and salinity differences. Unstable buoyancy differences, such as cold  
1200 and/or saline water overlying warm and/or fresh water, trigger small-scale three-dimensional  
1201 motions commonly known as “turbulent convection”. Convection is often characterised  
1202 by plumes that vertically flux buoyancy and mix with the ambient ocean. Buoyancy loss  
1203 through various surface drivers (net cooling, evaporation, and sea ice formation) is a primary  
1204 mechanism for triggering this turbulent convection and dense water formation. The domi-  
1205 nant convection processes influencing Southern Ocean dynamics are mixed layer convection  
1206 and polynya (coastal and open ocean) convection, as discussed in the following sections.

### 1207 4.2.1 Upper mixed layer convection

1208 Turbulent convection in the upper ocean occurs when surface cooling, evaporation  
1209 and/or brine rejection leads to a gravitationally unstable water column. Various surface  
1210 forcings (e.g., wind stress, evaporation and precipitation) drive small-scale eddies that trig-  
1211 ger convection. Turbulent convection is strongly linked to the mixed layer depth, which  
1212 is the uppermost part of the ocean characterised by a homogeneous density distribution.  
1213 Over the Southern Ocean, the mixed layer experiences a strong seasonal cycle and is deeper  
1214 during the Austral winter and shallower during the Austral summer (Fig. 14; Sallée et al.,  
1215 2006; Dong et al., 2008; Ren et al., 2011; Pellichero et al., 2017; Buongiorno Nardelli et al.,  
1216 2017). In broad terms, the deep winter mixed layer is mostly driven by convective processes,  
1217 either from temperature inversions during surface cooling or salinity inversions during brine  
1218 rejection, or from a combination of these two effects (Pellichero et al., 2017; Clément et al.,  
1219 2022). Convection becomes less pronounced during summer due to the increased stability  
1220 in the water column from surface heating and sea ice melting.

1221 Most Southern Ocean regions experience moderate to strong seasonality resulting in  
1222 a large variation of heat and salt fluxes at the ocean surface. Mixed layer properties and  
1223 dynamics are very different between sea ice covered and free zones. The spatial variation of  
1224 the mixed layer depth is more pronounced in the latitudinal direction due to both variation  
1225 of air–sea and ice–ocean fluxes, leading to a meridional banded structure of the winter mixed  
1226 layer depth across the Southern Ocean. This band is deep near the Antarctic continent,  
1227 becoming shallower farther offshore, before deepening again along the northern flank of the  
1228 Antarctic Circumpolar Current (Fig. 14c,f; Pellichero et al., 2017; Wilson et al., 2019). The  
1229 winter deep mixed layer region to the north of the Subantarctic Front is where Subantarctic  
1230 Mode Water is formed (McCartney, 1977).

1231 In the region free of sea ice, the seasonal cycle of air–sea interactions affects the heat  
1232 content in the mixed layer (Sallée et al., 2006; Dong et al., 2007, 2008; Pellichero et al., 2017)  
1233 with warming of the subsurface ocean during spring and summer and cooling during autumn  
1234 and winter. A large buoyancy loss from the ocean to the atmosphere during wintertime  
1235 causes an unstable temperature inversion leading to vertical convection and a deeper mixed  
1236 layer. A density inversion in the upper ocean is observed over a wide area spanning the  
1237 Antarctic Circumpolar Current and further north, including mode water formation regions.  
1238 The net vertical heat flux out of the ocean surface dominates the heat budget of the mixed  
1239 layer in autumn and winter (Pellichero et al., 2017), with secondary cooling effects from  
1240 vertical entrainment of cold ambient water at the bottom of the mixed layer (Dong et al.,  
1241 2007). Horizontal Ekman advection of cold water from the south due to strong winds across  
1242 the Southern Ocean also contributes to cooling the upper ocean throughout the year.

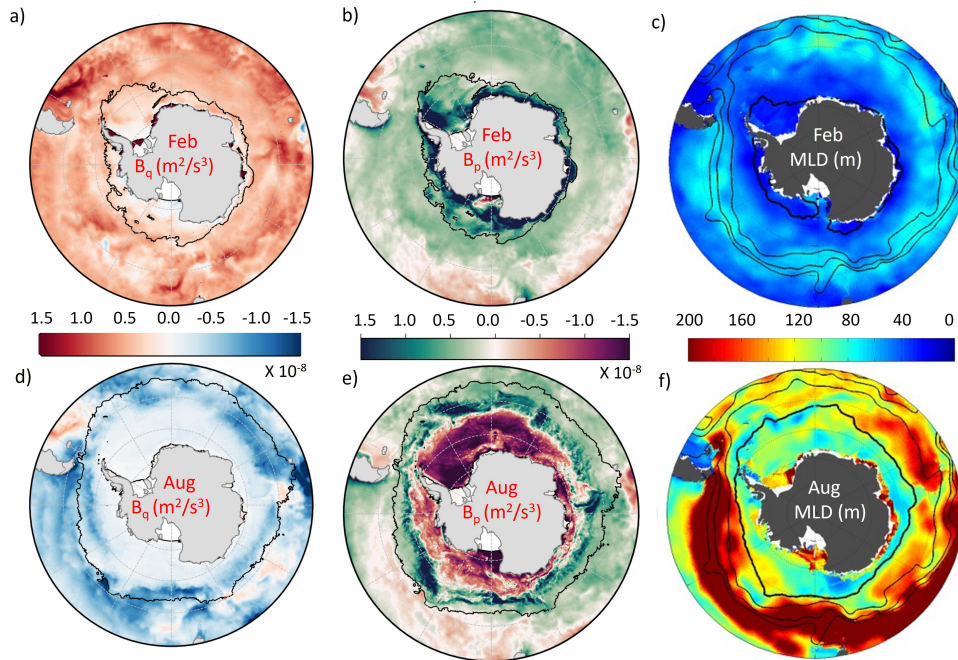


**Figure 14.** Surface fluxes and mixed layer depth in the Southern Ocean for Austral (a–c) summer and (d–f) winter. (a,d) The buoyancy flux due to the net surface heat flux,  $B_q$ . (b,e) The buoyancy flux due to the net surface salt flux,  $B_p$ . (c,f) Mixed layer depth (MLD). Fine black lines represent (a,b,d,e) sea ice extent, and (c,f) main fronts of the Antarctic Circumpolar Current, with the thick black line corresponding to the maximum seasonal sea ice extent. Fluxes are calculated based on the SOSE reanalysis product (Mazloff et al., 2010). (c,f) reproduced from Pellichero et al. (2017).

1243 Sea ice covers a major part of the Southern Ocean in winter, insulating the ocean from  
 1244 the cold atmospheric air and minimising the heat loss. The start of winter sees sea ice  
 1245 formation resulting in brine rejection and cold surface waters, which leads to a top-heavy  
 1246 water column susceptible to convective instabilities. The sea ice induced fluxes are the  
 1247 dominant contributors to the heat and salinity budgets of the upper ocean, with negligible  
 1248 contributions from lateral advection (by Ekman transport) and diffusion. The entrainment  
 1249 of salt flux from the bottom of the mixed layer does play an important role in the salinity  
 1250 budget of the mixed layer. From late autumn onward, the deepening of the mixed layer  
 1251 entrains the underlying, relatively salty Circumpolar Deep Water into the mixed layer in  
 1252 the Weddell Sea and Ross Ice Shelf regions, decreasing the overall buoyancy of the mixed  
 1253 layer. The degree to which the Circumpolar Deep Water interacts with the mixed layer varies  
 1254 around the Antarctic continent. For example, in the East Antarctic, the strong Antarctic  
 1255 Slope Current and easterly winds tend to inhibit the entrainment of the Circumpolar Deep  
 1256 Water into the surface mixed layer (A. F. Thompson et al., 2018). In addition to the above  
 1257 processes, leads exist in many sea ice covered areas there (§3.2.2; Muchow et al., 2021), which  
 1258 allow for the direct interaction between the cold atmosphere (frequently below  $-30^{\circ}\text{C}$ ) and  
 1259 the ocean, forming large localised convection driven by sensible heat loss and brine rejection  
 1260 (S. D. Smith et al., 1990; Simmonds & Budd, 1991).

1261 In early to mid-winter, the heat flux from the ocean, which warms the sea ice, is much  
 1262 less than the heat loss to the atmosphere through the upper surface of the ice, resulting in  
 1263 rapid sea ice growth and both temperature and salinity driven convection (Wilson et al.,  
 1264 2019). As the under-ice mixed layer deepens, it cools to about freezing point while also

1265 becoming saltier. This entrainment provides an efficient mode for exchanging freshwater  
1266 along with heat and atmospheric gases (e.g., carbon dioxide, oxygen) between the deep ocean  
1267 and the atmosphere (Gordon, 1991). The entrainment of warm water continues to increase  
1268 the heat flux from ocean to ice. In late winter, when the ocean heat flux to the sea ice is more  
1269 than the heat loss to the atmosphere, the entrained heat melts the sea ice from below, and a  
1270 strong surface stratification establishes due to the release of freshwater from melting that can  
1271 rapidly slow down surface-driven convection and mixed layer growth. However, turbulence  
1272 can also be sustained by double-diffusive convection processes as cold and freshwater overlies  
1273 warm and salty water (§ 3.1.6). Evidence for double-diffusive convection has been reported  
1274 in observations of the subsurface water column both in the Weddell and Ross Seas during  
1275 late winter time (Shaw & Stanton, 2014; Bebieva & Speer, 2019).

#### 1276 *4.2.2 Coastal polynya convection*

1277 The ocean around Antarctica is covered in sea ice during much of the year, particularly  
1278 in winter, except for pockets of open water known as polynyas (Morales Maqueda et al.,  
1279 2004). Polynyas generally lie close to the coast, with strong katabatic winds blowing any  
1280 newly-formed sea ice out to sea. Coastal polynyas are key regions for water mass transfor-  
1281 mation via atmosphere–sea ice–ocean interactions (Killworth, 1983; Tamura et al., 2008).  
1282 The process of coastal polynya convection begins at the surface, where there is buoyancy  
1283 loss due to a sudden cooling or an increase in sea ice production and brine rejection, or a  
1284 combination of both of these effects. In some circumstances, polynya convection is started  
1285 by brine rejection and then maintained by surface cooling, as convection continues to bring  
1286 warmer waters to the surface.

1287 Buoyancy loss, from brine rejection or surface cooling, causes deepening of the upper  
1288 ocean mixed layer followed by convection that can reach the ocean floor (J. Marshall &  
1289 Schott, 1999). The ocean floor on the Antarctic continental shelf is typically a few hundred  
1290 metres deep, extending to 1 km near the shelf break (Amblas & Dowdeswell, 2018). The  
1291 convection region or “patch” is made up of plumes of around 1 km or less in width. Baro-  
1292 clinic eddies form at the edge of the convective patch, due to the strong horizontal gradient  
1293 in buoyancy between the dense convective region and surrounding waters. However, these  
1294 eddies may be dissipated by the neighbouring ice shelf or sea ice cover. The width of these  
1295 eddies will depend on the Rossby radius of deformation, which is roughly 5–10 km in coastal  
1296 polynya regions (e.g.,  $\sim 4$  km near Ronne Ice Shelf; Årthun et al., 2013). Sustained coastal  
1297 convection is dependent on a number of driving factors coalescing under the right condi-  
1298 tions. In particular, coastal polynya convection needs continual access to the warm, salty  
1299 Circumpolar Deep Water heat reservoir that drives heat loss to the atmosphere and rapid  
1300 sea ice melt. Surface winds (katabatics and easterlies) are required to promote favourable  
1301 conditions for sea ice formation and the continued northward export of sea ice.

1302 Surface water mass transformation in polynyas is often seasonal and localised. While  
1303 some polynyas are strong factories of convection and dense water formation throughout large  
1304 portions of the year, other polynyas do not produce significant dense water mass. Some of  
1305 the most productive regions of dense water formation are the Weddell Sea, Prydz Bay, Adélie  
1306 Land and Ross Sea (Morales Maqueda et al., 2004). Polynya convection can also undergo  
1307 changes if the surface conditions differ from year-to-year. Large grounded icebergs can act  
1308 as islands, leading to modified convection and ocean circulation. For example, a polynya  
1309 in Adélie Land was noted to decrease in dense water formation (leading into Adélie Land  
1310 Bottom Water) after newly-formed sea ice was blocked from exiting the polynya region by  
1311 a large grounded iceberg (Snow et al., 2018). Observations and modelling also demonstrate  
1312 that meltwater plumes from neighbouring ice shelves may freshen the surface waters in the  
1313 polynya region and result in a shut down of convection (Silvano et al., 2018; Moorman  
1314 et al., 2020). This can then have a feedback effect on the convection in polynyas down-  
1315 stream, resulting in further reductions in convection (Silvano et al., 2018).

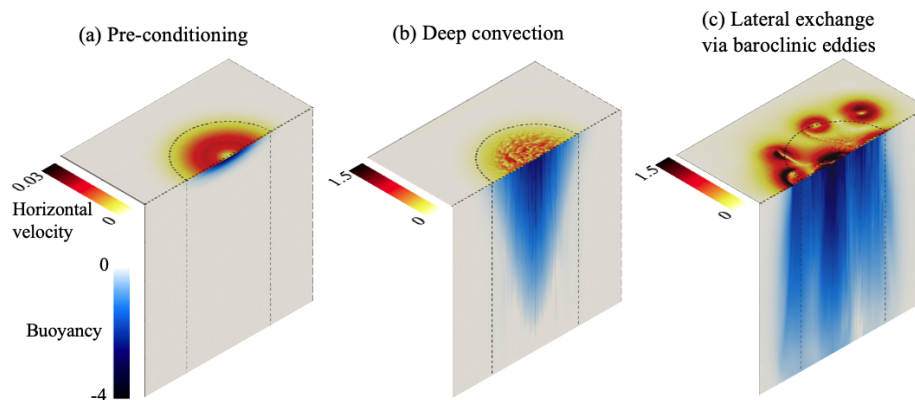


**Figure 15.** Different stages of open-ocean convection shown in high-resolution direct numerical simulations. Figure reproduced from [Vreugdenhil and Gayen \(2021\)](#) and based on the simulations by [Sohail et al. \(2020\)](#).

1316

#### 4.2.3 Open ocean polynya convection

1317

1318

1319

1320

1321

1322

1323

1324

1325

Open ocean convection is characterised by the rapid vertical heat exchange between the surface and deep ocean, driven predominantly by sensible heat loss or brine rejection at the surface of the ocean, and relatively unencumbered by local coastal processes ([J. Marshall & Schott, 1999](#)). It occurs further offshore than coastal convection and is a more intermittent phenomenon. In regions where open ocean convection is active, gaps in the sea ice cover (polynyas) emerge and persist for weeks and up to several months ([Comiso & Gordon, 1987](#)). Such polynyas have been observed in the Weddell Sea in 1974 ([Gordon, 1978](#)), and also to a lesser extent in 2016 and 2017 ([Jena et al., 2019](#); [Campbell et al., 2019](#)), and in the western Cosmonaut Sea (persistent in Austral autumn and winter; [Comiso & Gordon, 1987](#)).

1326

1327

1328

1329

1330

1331

1332

1333

1334

1335

1336

1337

1338

1339

The life cycle of a typical open ocean convection event is relatively well-understood ([J. Marshall & Schott, 1999](#)). In the first preconditioning phase, favourable local oceanic conditions are set up that lower the thermodynamic barrier to rapid sensible heat exchange with the atmosphere (Fig. 15a). In the second deep convection phase, deep, turbulent ocean convection is triggered which spawns multi-scale convective chimneys and a geostrophic rim current (Fig. 15b). Finally, given the right conditions, the rim current becomes baroclinically unstable, pinching off high-buoyancy baroclinic eddies, which rapidly mix the convective patch in the third lateral spreading phase (Fig. 15c). If favourable forcing conditions persist, the convective event will reach a quasi-equilibrium state in the lateral spreading phase, with minimal changes to the mixed layer or net vertical heat flux. The convection will only cease when the subsurface heat reservoir has been depleted, or freshwater input at the surface occurs, acting to restabilise the water column. Once such conditions cease, baroclinic eddies rapidly break down the convecting patch via lateral mixing, restratifying the ocean and encouraging reformation of sea ice ([H. Jones & Marshall, 1997](#)).

1340

1341

1342

1343

1344

1345

1346

1347

In the Southern Ocean, the Weddell Sea is a critical region for open ocean polynya formation and convection. In the Weddell Sea, open ocean polynyas have been intermittently observed around the Maud Rise seamount region, with the most recent notable example being in 2016 and 2017. In the mid-1970s, such Maud Rise polynyas were a precursor to the much larger and more consequential Weddell polynya, which emerged in 1974 and persisted through to 1976. Over its life, the Weddell polynya reached a maximum extent of 250,000 km<sup>2</sup>, generated dense water at an average rate of 1.6–3.2 Sv, and reduced the heat content of the underlying Weddell Deep Water by  $12.6 \times 10^{20}$  J (§ 2.5; [Gordon, 1982](#)).

1348 Several candidate processes have emerged that, through complex interactions, likely  
 1349 dictate the emergence and strength of the Maud Rise and Weddell polynyas. First, a period  
 1350 of prolonged negative Southern Annular Mode conditions, aided by La Nina, can create  
 1351 drier and cooler atmospheric conditions at the ocean surface, resulting in an increase in  
 1352 sea ice production. The subsequent brine rejection acts to salinify the ocean surface and  
 1353 reduce the stability of the water column (Gordon et al., 2007). Interactions of background  
 1354 flow with Maud Rise, particularly in these weakly stratified conditions, may give rise to  
 1355 a Taylor column (a stagnant region that can form over an obstacle in a rotating flow;  
 1356 G. I. Taylor, 1923) that is isolated to the seamount, bringing warm, salty Weddell Deep  
 1357 Water closer to the ocean mixed layer (Kurtakoti et al., 2018; Steur et al., 2007). Recent  
 1358 work using observational datasets has also highlighted the influence of eddy transport in  
 1359 warming the subsurface layer within the Taylor column in the lead up to the 2016–2017  
 1360 polynya opening (Gülk et al., 2023). Following all the various preconditioning effects, a  
 1361 negative wind stress curl over the Weddell Sea would strengthen the Weddell Gyre, causing  
 1362 the underlying Weddell Deep Water to upwell (Cheon et al., 2015) and melt sea ice in the  
 1363 region. Cyclonic eddies may shed off Maud Rise, opening gaps in the sea ice and enabling  
 1364 rapid heat loss to the atmosphere (D. M. Holland, 2001). Intermittent cyclones can also  
 1365 provide a strong mechanical forcing, opening the sea ice pack and exposing the ocean surface  
 1366 to the atmosphere (Francis et al., 2019; Z. Wei et al., 2022; Campbell et al., 2019).

1367 Once a Maud Rise polynya is triggered, westward propagation of the polynya can yield a  
 1368 larger Weddell polynya, especially if there is a large heat reservoir in the Weddell Deep Water  
 1369 and the wind stress curl and Southern Annular Mode are strongly negative (Kurtakoti et al.,  
 1370 2021). Note that Weddell polynya formation is not guaranteed once a Maud Rise polynya  
 1371 is formed. For example, the relatively large Maud Rise polynya in 2017 did not transition  
 1372 to a Weddell polynya, as a positive Southern Annular Mode index that year meant the  
 1373 water column was more stable and inhibited Weddell polynya formation (Cheon & Gordon,  
 1374 2019). A Maud Rise polynya, or Weddell polynya, will persist in quasi-equilibrium until  
 1375 it is destroyed by the loss of sub-surface heat, the input of surface freshwater, or through  
 1376 interactions with broader-scale gyre currents (D. M. Holland, 2001; Martinson et al., 1981).

### 1377 4.3 Mixing

1378 Three-dimensional turbulence and mixing in the Southern Ocean, whether in the in-  
 1379 terior or in the surface and bottom boundary layers, plays an important role in shaping  
 1380 air–sea and ice–ocean exchange (e.g., Holte et al., 2012; Rintoul, 2018), watermass transfor-  
 1381 mation (e.g., Downes et al., 2011; Cerovecki & Mazloff, 2016; Evans et al., 2018) and tracer  
 1382 transport (e.g., Mashayek, Ferrari, et al., 2017; Uchida et al., 2020). Three-dimensional  
 1383 turbulence lies at the bottom of the spatial and temporal scale range, acting to absorb the  
 1384 down-scale cascade of energy and scalar variance generated by motions at larger scales, and  
 1385 ultimately remove it at molecular scales. The millimetre to centimetre scales of turbulence,  
 1386 coupled with its highly intermittent nature, make it extraordinarily difficult to measure.  
 1387 Thus, much of our knowledge on the distribution of mixing in the ocean is inferred from  
 1388 observations of larger scales.

1389 The term “mixing” refers to the process of blending waters of different properties. The  
 1390 focus of § 4.3 is on the irreversible mixing of scalars. Diapycnal mixing or mixing across  
 1391 density surfaces is quantified using a diapycnal diffusivity, which is typically seven orders of  
 1392 magnitude smaller than the horizontal components set by along-isopycnal mesoscale stirring  
 1393 (de Lavergne et al., 2022). Mixing along isopycnals can create fine-scale gradients, e.g.,  
 1394 of temperature, which are more readily acted upon by turbulence and diapycnal mixing  
 1395 (Abernathey et al., 2022; de Lavergne et al., 2022). In addition, isopycnal mixing can lead  
 1396 to densification via cabbeling or thermobaricity, where mixing two water parcels of the same  
 1397 density results in a denser parcel due to nonlinearities in the equation of state (§2.4; Urakawa  
 1398 & Hasumi, 2012; L. N. Thomas & Shakespeare, 2015; Groeskamp et al., 2016).

1399 Direct measurements of mixing, resolving millimetre to centimetre scales, are limited  
 1400 to specialised research campaigns involving microstructure instruments (Waterman et al.,  
 1401 2013; Laurent et al., 2012; Ferris et al., 2022; Fer et al., 2016) and, for the ocean interior,  
 1402 tracer release experiments (Ledwell et al., 2011). Microstructure instruments rely on rapid-  
 1403 response velocity, temperature or salinity sensors that resolve variations with depth on the  
 1404 scale of centimetres, and provide an estimate of the dissipation of turbulent kinetic energy  $\varepsilon$   
 1405 (or tracer variance). Diapycnal diffusivity is then estimated as  $\Gamma\varepsilon/N^2$  (Osborn, 1980), where  
 1406  $\Gamma$  is generally assumed equal to 0.2 (Gregg et al., 2018) and  $N$  is the buoyancy frequency,  
 1407 defining the vertical stratification. Due to the limitations of direct observations throughout  
 1408 the Southern Ocean, finescale parameterizations of turbulent dissipation are widely used.  
 1409 Finescale methods applied to density and velocity measurements that resolve the vertical  
 1410 length scales of internal waves can infer the mixing from internal wave breaking (§ 5.3.2),  
 1411 either locally or after propagating some distance (Polzin, Naveira Garabato, Huussen, et  
 1412 al., 2014). Finescale methods have two major assumptions: 1) all the observed shear and  
 1413 strain in the ocean interior is due to internal waves, and 2) nonlinear interactions between  
 1414 the waves result in a downscale energy cascade leading to wave breaking and turbulence  
 1415 (Polzin, Naveira Garabato, Huussen, et al., 2014; Whalen et al., 2015). Fewer assumptions  
 1416 are required when both velocity and density are measured simultaneously, again limiting  
 1417 the observations to research vessels (Waterhouse et al., 2014) and autonomous instruments  
 1418 that measure both velocity and density (Meyer, Sloyan, et al., 2015; Cyriac et al., 2022).

1419 The most broadly available estimates of mixing come from the global Argo profiling float  
 1420 array (Whalen et al., 2012, 2015) that measure profiles of temperature and salinity to 2000 m.  
 1421 The absence of ocean velocity profiles in these measurements requires an assumption of the  
 1422 ratio of shear variance to strain variance, often chosen between three and seven (Kunze et al.,  
 1423 2006; Cyriac et al., 2022; Waterhouse et al., 2018). Parameterised estimates of mixing have  
 1424 been found to agree with direct measurements within a factor of two to three in the open-  
 1425 ocean thermocline (Whalen et al., 2015, 2020). This range of mixing observations provides  
 1426 some knowledge of the global-scale distribution of mixing and its seasonal variability, which  
 1427 has been shown to be closely correlated with seasonal variations in wind strength. However,  
 1428 in the Southern Ocean, apart from targeted field campaigns, there is little knowledge of  
 1429 the amplitude and variability of mixing in the surface mixed layer, below 2000 m depth,  
 1430 in boundary currents, in ice-covered regions, and at spatial scales smaller than 100 km and  
 1431 temporal scales less than a month.

1432 We organise § 4.3 by separately considering mixing within the surface boundary layer  
 1433 (§ 4.3.1), the interior (§ 4.3.2) and near the bottom (§ 4.3.3). Fig. 11 illustrates schematically  
 1434 the three layers and summarises the processes affecting mixing that will be addressed in the  
 1435 following sections.

#### 1436 4.3.1 Upper ocean mixing

1437 Air–sea exchanges in the Southern Ocean are mediated through the surface mixed  
 1438 layer and, thus, are shaped by boundary layer mixing. Surface boundary layer mixing is  
 1439 fundamental to surface ventilation and hence water mass formation (§§ 2.4.2; Fox-Kemper  
 1440 et al., 2022). The depth of the surface boundary layer is also important to the input of wind  
 1441 power that drives near-inertial oscillations and internal waves that ultimately contribute to  
 1442 deeper ocean mixing (§ 5.3). The Southern Ocean surface is characterized by strong time-  
 1443 mean and time-variable wind stress, large lateral density gradients and strong seasonally-  
 1444 varying heat and freshwater fluxes. The resulting transient near-surface mixing geography is  
 1445 shaped by a myriad of processes including surface waves (Belcher et al., 2012; Fox-Kemper  
 1446 et al., 2022), submesoscale and frontal dynamics (Du Plessis et al., 2019; Giddy et al.,  
 1447 2021; Gula et al., 2022), wind-generated near-inertial waves (Whitt et al., 2019; Whalen  
 1448 et al., 2020), which also penetrate into the interior to influence interior mixing (Alford et  
 1449 al., 2012; Cyriac et al., 2022), and sea ice interactions (Pellichero et al., 2017; Evans et  
 1450 al., 2018; S. Swart et al., 2020). Further, recent work highlights the interaction between

1451 mixing, air–sea heat fluxes and sea ice formation, leading to a two-stage transformation  
1452 of Circumpolar Deep Water, first into Winter Water and then into Antarctic Intermediate  
1453 Water (§2; [Evans et al., 2018](#)). While an understanding of these processes is developing,  
1454 observations are sparse and parameterization development has so far been based on Northern  
1455 Hemisphere data. In the Southern Ocean, the multiscale dynamics driving the mixing may  
1456 look different to other regions of the global ocean. Therefore, it is important to also test  
1457 these parameterizations with Southern Ocean data.

1458 Surface gravity waves play a vital role in both air–sea exchange and deepening of the  
1459 surface mixed layer through entrainment (Fig. 17; §5.1.1). The bubbles, spray and foam  
1460 resulting from breaking surface waves lead to a complex multiphase fluid that is a challenge  
1461 to both observe and model. This multiphase fluid is critical to both air–sea fluxes and  
1462 can also affect surface roughness and wave dynamics. Surface waves contribute to mixed  
1463 layer entrainment through the formation of deeply penetrating Langmuir turbulence and  
1464 non-breaking wave turbulence. Langmuir cells are driven by the interaction between the  
1465 wind-driven shear current and the Stokes drift current and result in pairs of parallel counter-  
1466 rotating vortices oriented in the downwind direction. [Belcher et al. \(2012\)](#) concluded surface  
1467 wave-forced Langmuir turbulence should be a major source of turbulent kinetic energy in  
1468 the Southern Ocean. Langmuir cells can contribute to entrainment even when the cells do  
1469 not reach the mixed layer base through enhancing the shear via pressure work ([Q. Li & Fox-  
1470 Kemper, 2020](#)). Non-breaking (irrotational) surface waves can enhance existing background  
1471 ocean turbulence when the orbital velocities of the irrotational waves interact with them  
1472 ([Qiao et al., 2016](#)). Observations showed that they have capacity to deepen the mixed layer  
1473 depth ([Toffoli et al., 2012](#)). Due to the extreme wave environment of the Southern Ocean,  
1474 it is likely that these processes play a key role. Simulations of the surface boundary layer at  
1475 the West Antarctic Peninsula that include parameterization of Langmuir cells demonstrate  
1476 more realistic deep mixed layers on the slope and shelf regions due to Langmuir entrainment  
1477 ([Schultz et al., 2020](#)). However, the first extensive microstructure turbulence observations  
1478 of the Southern Ocean surface boundary layer show that Langmuir circulations alone do  
1479 not explain the enhanced turbulence at the base of the mixed layer. Instead, storm forced  
1480 inertial currents provide additional shear ([Ferris et al., 2022](#)).

1481 Large inertial oscillations can be resonantly excited in the mixed layer when strong  
1482 winds turn with the inertial rotation ([Dohan & Davis, 2011](#)). These inertial oscillations can  
1483 then leave the mixed layer as propagating near-inertial waves. The inertial waves induce  
1484 shear within the base of the mixed layer in the so called “mixing transition” layer, which  
1485 results in mixing and widening of the layer ([Skylvingstad et al., 2000](#); [Forryan et al., 2015](#)).  
1486 High-resolution turbulence observations and drifter data show that the inertial oscillation-  
1487 induced turbulent dissipation rate across the layer is an order of magnitude larger than  
1488 that induced by most other mixed layer processes (with the exception of mixed layer frontal  
1489 instabilities), thereby further highlighting the importance of wind-driven inertial oscillations  
1490 for thermocline mixing ([Peng et al., 2021](#)). In a general sense, and noting that there are  
1491 large spatial variations, Southern Ocean density profiles appear to have much deeper surface  
1492 mixed-layers (hundreds of metres) than is typical in more temperate regions. However, this  
1493 layer is actually weakly but stably stratified, with the active mixing layer confined close to  
1494 the surface ([Kilbourne & Girton, 2015](#)). Therefore, a “slab model” (an analytical model  
1495 that treats the surface mixed layer as a slab to estimate the mixed layer response to wind  
1496 stress) can be applied to the actively mixing layer to estimate the near-inertial response to  
1497 wind input ([Pollard & Millard Jr, 1970](#)). Southern Ocean observations in the Indo-Pacific  
1498 sector demonstrate that near-inertial internal waves are responsible for transporting large  
1499 amounts of mean surface energy (up to 45% during one event) downward to the base of the  
1500 mixing layer where (indirect) estimates of vertical diffusivities are found to be enhanced by  
1501 up to two orders of magnitude ([Ferreira Azevedo et al., 2022](#)).

1502 The upper ocean mixing is also impacted by complex, horizontal processes emanating  
1503 from fronts, eddies and jets occurring at small spatial scales that extend down to the sub-

1504 mesoscale (tens of centimetres to tens of kilometres, and hours to days). In the Southern  
 1505 Ocean, the strong surface forcing, persistent lateral density gradients, weak vertical strat-  
 1506 ification and deep mixed layers further enhance submesoscale mixing (Gille et al., 2022).  
 1507 Submesoscale instabilities, induced by the large-scale adiabatic mesoscale stirring (§4.1),  
 1508 can lead to strong subduction of water (K. A. Adams et al., 2017) and drive intense ver-  
 1509 tical circulations (J. R. Taylor et al., 2018). Mixed layer eddies are likely to be prevalent  
 1510 in regions where the mixed layer is deep and lateral gradients are sharp. They can ar-  
 1511 rest shear-driven mixing leading to vertical entrainment and bring about spring mixed-layer  
 1512 stratification conditions earlier than with surface buoyancy forcing alone (Du Plessis et al.,  
 1513 2017). Further, the presence of submesoscale variability leads to the concentration of wind-  
 1514 driven near-inertial energy, enhancing the inertial wave shear-driven mixing below the base  
 1515 of the mixing layer (e.g., Klein et al., 2004; Meyer, Sloyan, et al., 2015; Jing et al., 2011).  
 1516 Large-scale inertial oscillations and submesoscale fronts may also induce transient modifica-  
 1517 tion of vertical stratification and thus turbulent mixing (L. N. Thomas et al., 2016). These  
 1518 observations point to the importance of the interplay of multi-scale physical processes in the  
 1519 Southern Ocean, a topic which is still largely unexplored.

1520 There is increasing evidence that some submesoscale ( $\sim 1\text{km}$ ) processes in the surface  
 1521 mixed layer break the constraint of the large-scale quasi-geostrophic dynamics (i.e., the  
 1522 dominance of planetary rotation and vertical stratification), and trigger a variety of flow  
 1523 instabilities, such as inertial instabilities (Grisouard, 2018; Peng et al., 2020), symmetric  
 1524 instabilities (D’Asaro et al., 2011; L. N. Thomas et al., 2013), and ageostrophic baroclinic  
 1525 mixed layer instabilities (Boccaletti et al., 2007; Fox-Kemper & Ferrari, 2008). Unlike other  
 1526 surface processes that draw energy from atmospheric forcing, these instabilities extract  
 1527 either potential or kinetic energy from quasi-geostrophic flow (McWilliams, 2016), inject  
 1528 it into the smaller-scales of the fastest growing modes, induce secondary Kelvin-Helmholtz  
 1529 instabilities (J. R. Taylor & Ferrari, 2009), and finally mediate energy transfer from large-  
 1530 scale circulation to smaller scales through the forward cascade of energy (J. R. Taylor &  
 1531 Thompson, 2022). Several microstructure field studies have confirmed the enhanced energy  
 1532 dissipation caused by this downscale transport of large-scale energy (D’Asaro et al., 2011;  
 1533 L. N. Thomas et al., 2016; Peng et al., 2020, 2021). Submesoscale frontal instabilities  
 1534 are especially relevant for the Southern Ocean because of the predominating atmospheric  
 1535 conditions of down-front winds and surface cooling (L. N. Thomas, 2005). However, the  
 1536 favourable atmospheric conditions for these instabilities may be easily affected by sea ice.

1537 Sea ice covers a large enough area of the Southern Ocean to have a large impact on  
 1538 air–sea interactions (§3.2.1). Fast ice provides a laterally rigid lid on the ocean that alters  
 1539 the mixing processes (Robertson et al., 1995; Stevens et al., 2009), from direct wind-forcing  
 1540 and surface wave breaking to ice-ocean frictional stresses associated with externally forced  
 1541 flows and tides (Albrecht et al., 2006). Sea ice strongly inhibits surface gravity waves and  
 1542 momentum fluxes from the wind, thereby altering upper ocean mixing (§5.1.3 Arduin et al.,  
 1543 2020). However, the extent to which surface gravity waves and the associated dynamics, such  
 1544 as Langmuir circulations, are inhibited is dependent on the extent of the ice cover. Limited  
 1545 observations of air–sea–ice fluxes exist in the Southern Ocean. Observations from an air–sea  
 1546 flux mooring at the Polar Front (Ferreira Azevedo et al., 2022) found that 45% of surface  
 1547 energy penetrated the base of the mixed layer and suggest that even in the presence of sea  
 1548 ice, strong wind events may enhance mixing. Submesoscale activity and associated mixing  
 1549 can be enhanced under sea ice and in regions close to sea ice melt due to the existence of  
 1550 strong lateral density gradients. Observations at the edge of the Antarctic sea ice cover have  
 1551 revealed submesoscale eddies generated by the fresh water being stirred by the mesoscale  
 1552 eddies (e.g., Giddy et al., 2021). Submesoscale activity has also been detected below sea ice  
 1553 by observations from seal-based sensors (Biddle & Swart, 2020). Further, Gille et al. (2022)  
 1554 speculate that lateral density gradients resulting from heterogeneity in air–sea fluxes due to  
 1555 gaps between ice floes (Fons & Kurtz, 2019) could also lead to submesoscale-driven mixing.

1556 Mixing at the face of, and underneath, ice shelves can be strongly influenced by tides  
 1557 (§ 5.2; Joughin & Padman, 2003; Padman et al., 2018). Tides generate increased turbulence  
 1558 in the layer of ocean adjacent to the ice shelf front, which modifies the temperature, salinity  
 1559 and density structure and leads to altered ocean circulation. The ice edge also induces sub-  
 1560 substantial mixing, both in the wake but also in flow acceleration, depending on tidal conditions  
 1561 (Fer et al., 2012; Stevens et al., 2014). Within the cavity, it has been suggested that the  
 1562 interaction of tides and basal ice undulations might induce relatively high-frequency vari-  
 1563 ability (Foster, 1983; Stevens et al., 2020), especially in the near-field of under-side basal  
 1564 crevasses (Lawrence et al., 2023). Under rapidly melting ice shelves, the freshwater outflow  
 1565 can generate currents that are much larger than the tidal currents. For example, the Pine  
 1566 Island Glacier has freshwater plume flow of up to  $0.5 \text{ m s}^{-1}$  (Payne et al., 2007) and tidal  
 1567 currents of only a few centimetres per second (Robertson, 2013). Where cold ocean waters  
 1568 surround the ice shelf and melt rates are low, plume flows are much weaker than tidal flows.  
 1569 In these locations, the mixing will be dominated by the tidal currents.

1570 Water mass transformation frameworks have revealed that wintertime mixing in the  
 1571 surface boundary layer of the Southern Ocean plays a key role in the diapycnal upwelling  
 1572 of Circumpolar Deep Water and the eventual formation of Antarctic Intermediate Water  
 1573 (Evans et al., 2018). Here, wintertime cooling and brine rejection during sea ice formation  
 1574 combine to weaken the stratification between the surface winter water and Circumpolar Deep  
 1575 Water below. Mixing transforms the relatively warm and salty Circumpolar Deep Water  
 1576 into colder and fresher near-surface Winter Water. Through summertime warming and sea  
 1577 ice melt, this upwelled and transformed water mass eventually forms Antarctic Intermediate  
 1578 Water, likely through nonlinear thermodynamic processes (Evans et al., 2018).

#### 1579 4.3.2 Interior diapycnal mixing

1580 Interior diapycnal mixing is wide-spread in the Southern Ocean due to the energetic  
 1581 internal wave environment (§ 5.3). The Southern Ocean has strong wind-energy input into  
 1582 near-inertial motions (Alford, 2003). Surface-generated near-inertial internal waves and  
 1583 bottom-generated internal tides and lee waves propagate into the interior, are shaped by  
 1584 interaction with other physical processes and subsequently break and generate diapycnal  
 1585 mixing. Interactions between the Southern Ocean’s energetic eddy field and internal waves  
 1586 lead to elevated diffusivity in the upper 2000 m of the ocean (Whalen et al., 2012, 2015, 2018).  
 1587 It is conceptually difficult to separate “interior” mixing from surface- and bottom-intensified  
 1588 mixing, both because of the surface/bottom boundary production of the waves that generate  
 1589 mixing and because there are many mixing hotspots associated with topography that ex-  
 1590 tends high into the water column. Nevertheless, interior mixing below 2000 m depth, where  
 1591 interior diapycnal diffusivities are generally less than  $10^{-4} \text{ m}^2 \text{ s}^{-1}$ , drives interior watermass  
 1592 transformation and thus has important modulating impacts on the overturning circulation  
 1593 (§ 2.5; Munk & Wunsch, 1998).

1594 Wave breaking is the process through which internal waves dissipate. While they prop-  
 1595 agate, internal waves exchange energy with background mesoscale flows, such as currents,  
 1596 jets, and fronts (wave–mean interactions; Grimshaw, 1984), mesoscale eddies (wave–eddy  
 1597 interactions; Kunze, 1985; Cusack et al., 2020), or other internal waves (wave–wave inter-  
 1598 actions; McComas & Bretherton, 1977) resulting in the internal gravity wave continuum. The  
 1599 net energy flux can be from internal waves to their surroundings, or from their surround-  
 1600 ings to the internal waves (§ 5.3.2). Ultimately though, when internal waves reach high  
 1601 enough wavenumbers, they steepen and break through direct shear instability or convective  
 1602 overturning, transferring their remaining energy into turbulence and diapycnal mixing (e.g.,  
 1603 Eriksen, 1978; Fringer & Street, 2003; Nikurashin & Ferrari, 2010). This internal wave  
 1604 driven mixing can happen both locally, where internal waves are generated, or remotely,  
 1605 when internal waves propagate far from their source. Such remote breaking and dissipation  
 1606 of internal waves is an important process for energy redistribution in the Southern Ocean,  
 1607 where the strong Antarctic Circumpolar Current has been documented to advect internal

1608 waves through its fronts (Meyer, Polzin, et al., 2015), jets (Waterman et al., 2021), meanders  
1609 and mesoscale eddies (Cyriac et al., 2023). Such modulation of the internal wave driven  
1610 mixing landscape by the background mesoscale flow and associated wave-mean interactions  
1611 may explain the mismatch identified in recent studies between parameterised estimates and  
1612 direct microstructure measurements of diapycnal mixing (§ 5.3; § 7; Waterman et al., 2013;  
1613 Sheen et al., 2013; Nikurashin et al., 2014; Cusack et al., 2017; Takahashi & Hibiya, 2019).

1614 Globally, of the 2TW of energy theorised to maintain the ocean stratification (Munk  
1615 & Wunsch, 1998; de Lavergne et al., 2022), about 1.2 TW of energy is provided by internal  
1616 waves generated from barotropic tides and geostrophic flows (Wunsch et al., 2004) with the  
1617 remaining energy thought to come from the work done by wind on near-inertial motions  
1618 (Alford et al., 2016). Uncertainty in these estimates is very large (§ 5.3), which leads to  
1619 poor representation of wave-driven mixing in climate models (Jochum et al., 2013). Various  
1620 estimates agree that much of the energy flux into lee waves occurs in the Southern Ocean  
1621 as expected given the uniquely deep-reaching nature of the Antarctic Circumpolar Current  
1622 and relatively weak tidal flows (§ 5.2). Lee waves apply wave drag (§ 5.1.1) to the deep flows  
1623 that generate them which are dominated by mesoscale eddies in the Southern Ocean (Yang  
1624 et al., 2018). The work done by the wave drag converts energy from the mesoscale eddy  
1625 field into smaller-scale lee waves (Yang et al., 2018), which then transfer the energy further  
1626 down to turbulence scales via direct wave breaking (e.g., Lefauve et al., 2015) or wave-wave  
1627 interactions (e.g., Polzin, 2009).

1628 Up to this point, § 4.3.2 has focused on diapycnal mixing, which is the approximate ver-  
1629 tical component of three-dimensional turbulence. Separating this mixing from the horizontal  
1630 components set by (sub-)mesoscale stirring along isopycnals is a convenient and common  
1631 approach due to the different observations and methods used to estimate diapycnal and  
1632 isopycnal diffusivities. However, it does not reflect the integrated three-dimensional nature  
1633 of oceanic thermodynamical processes. A theoretical framework based on the temperature  
1634 variance budget (Ferrari & Polzin, 2005; Naveira Garabato et al., 2016) establishes a bal-  
1635 ance between dissipation of variance by molecular mixing and the production of variance  
1636 associated with mesoscale eddy-induced isopycnal stirring and with diapycnal mixing by  
1637 small-scale turbulence acting on the large-scale mean state. The framework allows diapy-  
1638 cnal and isopycnal diffusivities to be quantified from a small number of (temperature and  
1639 velocity) microstructure measurements to provide new insight into the coupling between the  
1640 zonal flow of the Antarctic Circumpolar Current and the meridional overturning circulation  
1641 transport along sloping isopycnals. In Drake Passage (Naveira Garabato et al., 2016), the  
1642 framework reveals that isopycnal stirring is strongly suppressed in the upper 1 km of Antarc-  
1643 tic Circumpolar Current jets, consistent with earlier circumpolar work (Naveira Garabato  
1644 et al., 2011). Intensified diapycnal mixing balances the meridional overturning in this upper  
1645 1 km, the lightest layer, and also in the densest layers of the Antarctic Circumpolar Current  
1646 (Naveira Garabato et al., 2016). Both layers are near the two primary sources of internal  
1647 waves: wind-driven near-inertial oscillations and flow interactions with topography. Isopy-  
1648 cnal stirring balances the overturning in the intermediate layers and upper Circumpolar  
1649 Deep Water (Naveira Garabato et al., 2016). Application of the framework to only 10 mi-  
1650 crostructure profiles in the Brazil-Malvinas confluence (Orúe-Echevarría et al., 2021) reveals  
1651 regional variations in the roles of diapycnal and isopycnal mixing. Observational campaigns,  
1652 such as DIMES (Ledwell et al., 2011; Watson et al., 2013; Mackay et al., 2018), SOFINE  
1653 (Waterman et al., 2013; Meyer, Sloyan, et al., 2015) and DEFLECT (Cyriac et al., 2022)  
1654 emphasize the importance of interactions between mesoscale variability, circulation and mix-  
1655 ing for tracer transport (Mashayek, Ferrari, et al., 2017; Holmes et al., 2019). Greater use  
1656 of microstructure observations will help unravel the roles of mesoscale, submesoscale and  
1657 small-scale turbulent flows in governing ocean circulation and water mass structure.

### 1658 **4.3.3 Bottom-intensified diapycnal mixing**

1659 Bottom-intensified mixing shapes Antarctic Bottom Water consumption, and underpins  
 1660 a key dependence of the abyssal circulation on both topographic roughness and large-scale  
 1661 topography (de Lavergne et al., 2017; Holmes et al., 2018; Polzin & McDougall, 2022).  
 1662 Bottom-intensified mixing is primarily generated by the breaking of lee waves and internal  
 1663 tides. Lee waves are generated via interactions between mesoscale flows and rough topogra-  
 1664 phy and are particularly prominent in the Southern Ocean due to the energetic mesoscale  
 1665 activity (Garabato et al., 2004; Nikurashin & Ferrari, 2010; Sheen et al., 2013; Gille et al.,  
 1666 2022; Cyriac et al., 2022, 2023). Internal tides also play an important role in this region  
 1667 (Johnston et al., 2015; Z. Zhao et al., 2018; Waterhouse et al., 2018; Vic et al., 2019).

1668 Through nonlinear wave–wave interactions, internal waves drive a down-scale cascade  
 1669 of turbulent energy leading to mixing (Nikurashin & Legg, 2011; Polzin, Naveira Garabato,  
 1670 Huussen, et al., 2014; Whalen et al., 2020) and a bottom-intensified profile of diffusivity  
 1671 and buoyancy flux (Toole et al., 1994; Polzin et al., 1997; Waterhouse et al., 2014). Conse-  
 1672 quently, a diapycnal transport dipole is established where there is downward transport (from  
 1673 light to dense water) in a stratified “bottom mixing layer” (often referred to as the stratified  
 1674 mixing layer) above the topography, and upward transport only within a narrower “bot-  
 1675 tom boundary layer” where the turbulent buoyancy flux converges next to the topography  
 1676 (Fig. 11). The net diapycnal transport (or consumption of Antarctic Bottom Water) arises  
 1677 as a small residual of these larger up- and down-welling transformations (de Lavergne et al.,  
 1678 2016; McDougall & Ferrari, 2017; Ferrari et al., 2016; Polzin & McDougall, 2022). These  
 1679 mixing processes are shaped by mesoscale and submesoscale variability. Temporal varia-  
 1680 tions in mixing associated with mesoscale eddy kinetic energy variations link bottom water  
 1681 overturning cell variability to wind forcing (Sheen et al., 2014; Broadbridge et al., 2016).  
 1682 Recent work also highlights the important role that near-bottom submesoscale processes  
 1683 play in maintaining the stratification, and, thus, the magnitude of the diapycnal transport  
 1684 dipole, in these bottom mixing layers (Ruan et al., 2017; Wenegrat et al., 2018; Callies,  
 1685 2018; Naveira Garabato, Frajka-Williams, et al., 2019). These processes pose a particular  
 1686 challenge for Southern Ocean modelling and observations given their small spatial scales  
 1687 and variability, our limited knowledge of seafloor bathymetry at small scales and the often  
 1688 coarse vertical resolution of ocean general circulation models at the bottom boundary.

### 1689 **4.4 Closing the loops**

1690 Turbulence in the Southern Ocean involves dynamical structures on a range of scales,  
 1691 from eddies, jets and fronts (§4.1) to convection (§4.2) and down to the smallest scales of  
 1692 mixing (§4.3). The large-scale circulation is inherently linked with turbulence, for example  
 1693 the Antarctic Circumpolar Current has rich dynamics of jets and eddies, whose complicated  
 1694 interactions can act to modify the current (§2.1). The upper (§2.4) and abyssal overturning  
 1695 (§2.5) circulations are also affected by upper mixed layer and polynya convection respec-  
 1696 tively. The cryosphere connects to convection via the wintertime sea-ice formation (§3.2)  
 1697 whose subsequent brine rejection drives polynya convection. Mixing between different wa-  
 1698 ter masses can also influence key cryosphere processes involved with heat transport into ice  
 1699 shelf cavities (§3.1.2). Waves connect to eddies, jets and fronts, such as through the lens of  
 1700 mesoscale turbulence which can affect surface waves (§5.1.2). Mixing has complicated links  
 1701 with waves, for example internal waves can enhance mixing (§5.3.3) and, in turn, mixing  
 1702 can influence internal waves (§4.3). The next section will further detail the role of §5 Waves  
 1703 in the Southern Ocean.

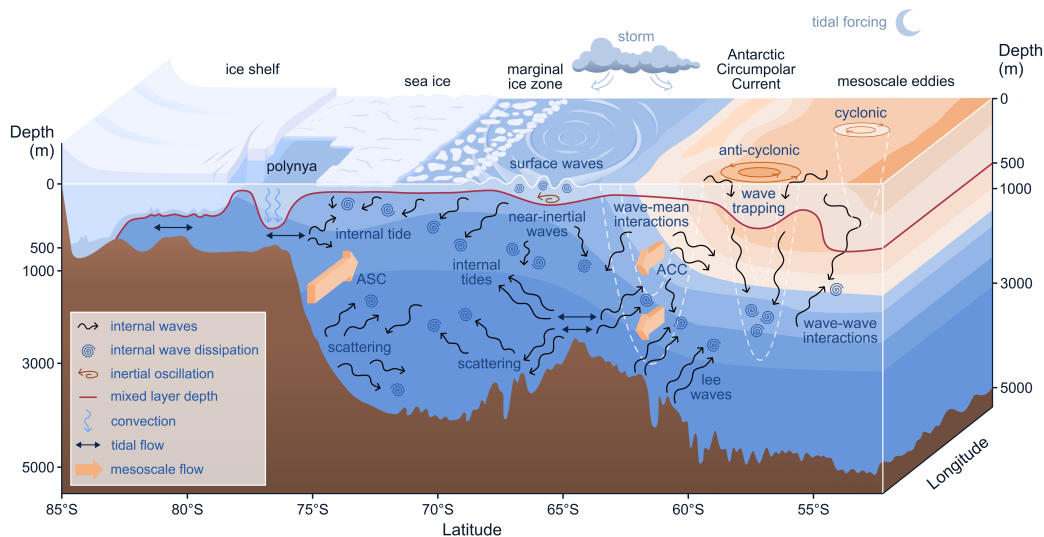


**Figure 16.** Schematic of gravity wave processes in the Southern Ocean including surface waves, internal waves and tides. At the surface, strong storm systems generate surface waves and (near-inertial) internal waves. The gravitational force of the moon and sun generate bulk motions of the water column (tides) that, in combination with other ocean flows, generate internal waves at the seafloor. The waves interact with other components of the Southern Ocean system. For example, surface waves are dissipated in the marginal ice zone, while internal waves may be trapped in eddies and currents, and/or drive diapycnal mixing in the ocean interior. Colour contours show a typical density field, ranging from lighter (dark orange) to denser (dark blue) waters.

1704

## 5 Gravity waves

1705

1706

1707

1708

1709

1710

1711

1712

1713

1714

1715

1716

1717

1718

Gravity waves in the ocean are vertical perturbations of the fluid ocean against the restoring force of gravity, including displacements of the ocean surface (surface waves; § 5.1), perturbations to the interior ocean stratification (internal waves; § 5.3), and perturbations of the entire water column (tides; § 5.2). These phenomena span from some of the smallest and fastest motions in the ocean in the case of surface waves (wavelengths of tens to hundreds of metres, periods of seconds), through intermediate length scales in the case of internal waves (horizontal wavelengths of kilometres to hundreds of kilometres), to motions that span ocean basins in the case of tides (thousands of kilometres). In all three cases, oceanic gravity waves are influenced by the Earth’s rotation — in addition to gravity — and are, therefore, more correctly termed “inertia-gravity waves”. These waves play a vital role in transporting energy and momentum throughout the ocean, thus supporting ocean mixing and circulation. Figure 16 provides a schematic overview of gravity waves in the Southern Ocean and their interactions with other components of the system. In this section, we present an overview of each class of gravity wave and its role in Southern Ocean dynamics.

1719

1720

1721

1722

1723

1724

1725

1726

1727

For further details on gravity waves, readers may wish to peruse previous reviews in addition to the content herein. While there is no previous Southern Ocean specific review of surface waves, Young et al. (2020) collates over three decades of satellite altimeter and in situ buoy observations, to conduct a statistical study of seasonal variations, including extremes and spectral analysis, and highlights some of the unique aspects of Southern Ocean waves. The fundamental governing equations of surface waves are given by, e.g., Barstow et al. (2005). Further, a series of articles (Squire et al., 1995; Squire, 2007, 2020) review the evolution in understanding of surface waves in the marginal ice zone (§ 3.2.2). For ocean tides, Pugh (2004) provides a detailed review of tidal theory and Stammer et al.

1728 (2014) reviews global tide models, with their Section 5.2 focusing on model performance in  
1729 Antarctic seas. In addition, Padman et al. (2018) describes ocean tide influences on the mass  
1730 balances of the Antarctic and Greenland Ice Sheets. For internal waves, Polzin and Lvov  
1731 (2011) provides a detailed theoretical description, a summary of the observed global ocean  
1732 internal wave field and its explanation in terms of the nonlinear wave interactions (a subject  
1733 not covered here). In addition, recent reviews have focused separately on internal waves  
1734 generated at the ocean surface (L. N. Thomas & Zhai, 2022) and the seafloor (Musgrave et  
1735 al., 2022), but with a global outlook.

## 1736 5.1 Surface waves

1737 The Southern Ocean possesses a unique surface wave climate due to the absence of  
1738 large land masses, which allows circumpolar-scale fetches (the spatial extents of the regions  
1739 over which winds blow in a coherent direction; Donelan et al., 2006) and persistently strong  
1740 westerly winds (i.e., blowing from west to east), including the notorious ‘roaring forties’,  
1741 ‘furious fifties’ and ‘screaming sixties’ (Lundy, 2010). These Southern Ocean westerlies give  
1742 rise to some of the consistently (over all seasons) largest amplitude surface waves on the  
1743 planet (Young & Donelan, 2018; Barbariol et al., 2019; Vichi et al., 2019; Young et al.,  
1744 2020; Derkani et al., 2021; Alberello et al., 2022). The wave height climate mirrors the  
1745 distribution of wind speeds, with a uniform distribution of waves across the region and the  
1746 seasons. The “significant wave height”, i.e., the average height of the highest one-third of  
1747 the waves experienced over time (Young, 1999), is in excess of 3.5 m in summer and 5 m in  
1748 winter, according to model hindcasts and satellite observations (Young et al., 2020; Schmale  
1749 et al., 2019; Derkani et al., 2021). Long term in-situ observations at several locations reveal  
1750 that extreme events, with significant wave heights greater than 10 m, occur over winter  
1751 approximately once every 80 days (Rapizo et al., 2015; Young et al., 2020).

1752 At short fetches, the wave spectrum is narrow banded (Young et al., 2020) and the wave  
1753 form is steep, facilitating occurrence of highly nonlinear dynamics (Janssen, 2003; Onorato  
1754 et al., 2009). Laboratory experiments in a circular wave flume that mimic the unlimited  
1755 fetch conditions in the Southern Ocean suggests that nonlinear dynamics have the potential  
1756 to fully develop, causing individual waves to destabilize and grow significantly taller than the  
1757 background sea state. In exceptional circumstances, this leads to so-called “rogue waves”,  
1758 which have heights greater than two times the significant wave height (Toffoli et al., 2017).  
1759 Exceptional maximum individual wave heights exceeding 19 m have been reported (Barbariol  
1760 et al., 2019), although these are not necessarily rogue waves.

1761 After long fetches, waves reach full development, becoming independent from local  
1762 winds. Further development of the wave field is associated with nonlinear interactions  
1763 (Young, 1999). As a consequence, the “wind sea” (i.e., a wave field being acted on by  
1764 winds) evolves into more regular wave fields that radiate along multiple directions from the  
1765 generation area. These so-called “swells” disperse across the Indian, Pacific, and South  
1766 Atlantic Oceans (Semedo et al., 2011).

1767 Observations around the Southern Ocean indicate that very broad directional distribu-  
1768 tions are common in the region, with energy spreading across a range up to  $\pm 80^\circ$  around  
1769 the mean wave direction (Young et al., 2020; Derkani et al., 2021). On occasions, this is the  
1770 signature of chaotic sea states, where multiple (independent) wave systems, such as wind  
1771 seas plus swells coexist (Aouf et al., 2020; Khan et al., 2021; Derkani et al., 2021; Alberello  
1772 et al., 2022). Theory, numerical simulations and experiments have demonstrated that these  
1773 multi-system seas accelerate development of nonlinear dynamics, further contributing to the  
1774 occurrence of large amplitude waves (Onorato et al., 2006; Toffoli et al., 2011).

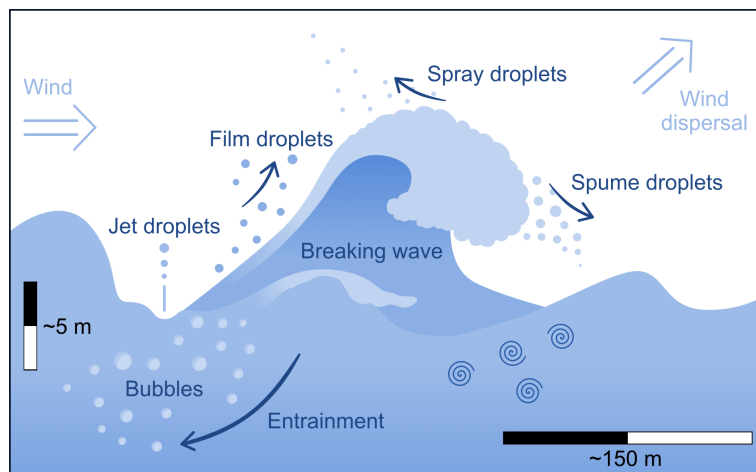


**Figure 17.** Schematic of a breaking surface gravity wave. The wave propagates in the direction of the wind and grows with time until it becomes too steep and breaks. Wave breaking induces near surface turbulence, which generates air bubbles and entrains them into the sub-surface ocean, mediating air–sea fluxes of momentum, energy, moisture and biological constituents with the ambient atmosphere. Turbulent oscillatory motion (from both breaking and non-breaking waves) drives vertical mixing (blue spirals) through the water column to a depth comparable to the wavelength, contributing to the mixed ocean surface layer.

### 1775 5.1.1 Surface wave breaking

1776 Waves grow under the forcing of wind and highly nonlinear instabilities until they  
 1777 ultimately break in the form of whitecaps (Babanin et al., 2007; Toffoli et al., 2010, 2017),  
 1778 when the ratio of wave height to wavelength is  $\approx 0.14$  (Fig. 17; Toffoli et al., 2010). Wave  
 1779 breaking and whitecapping are important surface processes that occur in all oceans when  
 1780 winds generate large amplitude waves. Thus, they are a year-round phenomenon in the  
 1781 Southern Ocean. The whitecaps can be explained as pressure pulses on the sea surface just  
 1782 downwind of the wave crest that act against wave growth (Hasselmann, 1974), dissipating  
 1783 excessive wind input and, subsequently, transferring it to the subsurface in the form of  
 1784 turbulent mixing (§4.3.1; Terray et al., 1996). However, breaking-induced turbulence decays  
 1785 rapidly in depth with distance from the surface and the contribution to ocean mixing is  
 1786 confined to a sublayer with depths comparable with the wave height (Rapp & Melville, 1990).  
 1787 Nevertheless, there is theoretical and experimental evidence that the wave oscillatory flow  
 1788 can become turbulent even in the absence of breaking (Babanin, 2006; Alberello, Onorato,  
 1789 Frascoli, & Toffoli, 2019). Hence, waves are capable of directly contributing to mixing  
 1790 throughout the water column, up to depths comparable to half of the wavelength (i.e.,  
 1791 down to about 100 m; Toffoli et al., 2012).

1792 Besides dissipation, whitecaps drive air–sea interaction processes through airborne  
 1793 droplets (Monahan et al., 1986; Landwehr et al., 2021). Generated and entrained sub-  
 1794 surface by whitecaps, bubbles rise to the surface and burst, forming film droplets or jets of  
 1795 daughter droplets (Fig. 17). If the wind shear is sufficiently intense, larger droplets known  
 1796 as “sea spray” are torn off the surface of (breaking) waves (Veron, 2015). Once ejected,  
 1797 spray drops are transported and dispersed in the marine atmospheric boundary layer, in  
 1798 which they interact and exchange momentum, heat, moisture and biological and chemical  
 1799 constituents with the ambient atmosphere (Humphries et al., 2016; Schmale et al., 2019;  
 1800 Thurnherr et al., 2020; Landwehr et al., 2021). There is evidence that marine aerosols  
 1801 generated from whitecaps are an important source of cloud condensation nuclei and cloud

1802 formation in the Southern Ocean (Schmale et al., 2019; Landwehr et al., 2021). Large sea  
 1803 spray particles do not dissolve entirely while in the atmosphere, but they return to the  
 1804 ocean with lost or gained momentum, closing the loop of air–sea interaction (Veron, 2015;  
 1805 Landwehr et al., 2021).

### 1806 *5.1.2 Influence of mesoscale turbulence in the Antarctic Circumpolar Cur-* 1807 *rent*

1808 Mesoscale ocean turbulence (approximately ten to one hundred of kilometres) can in-  
 1809 fluence the generation and propagation of surface waves. The main effect of such turbulence  
 1810 within the Antarctic Circumpolar Current (in which jet speeds may exceed  $0.75\text{ ms}^{-1}$ ;  
 1811 §§ 2.1,4.1; Derkani et al., 2021) is one of refraction, as the current flows predominantly  
 1812 in the direction of the surface waves. Therefore, the Antarctic Circumpolar Current helps  
 1813 maintain the broad directional distribution of waves observed in the region (Derkani et al.,  
 1814 2021; Young et al., 2020). As waves propagate along the current, the wave height is attenu-  
 1815 ated, although this effect is small (5–8% relative to the no-current condition; Derkani, 2021;  
 1816 Rapizo et al., 2015). More substantial interactions are reported at the upper boundary of  
 1817 the Indian Ocean sector, where large swells from Antarctica interact with the more intense  
 1818 Agulhas current, forming large amplitude waves and, often, rogue waves (White & Fornberg,  
 1819 1998).

### 1820 *5.1.3 Attenuation, dissipation and scattering by sea ice*

1821 Sea ice cover limits the distance surface waves can reach towards the Antarctic mar-  
 1822 gin, thereby suppressing the processes described in §§ 5.1.1–5.1.2. A collection of in-situ  
 1823 and remote sensing observations (originally from the Arctic but, more recently, also from  
 1824 the Southern Ocean) provide evidence that ocean wave energy decays exponentially with  
 1825 distance travelled though the marginal ice zone and that the rate of attenuation increases  
 1826 with wave frequency (Squire & Moore, 1980; Wadhams et al., 1988; Kohout et al., 2014;  
 1827 Meylan et al., 2014; Stopa et al., 2018; Montiel et al., 2018; Kohout et al., 2020; Montiel  
 1828 et al., 2022; Alberello et al., 2022). The observations suggest that the rate of exponential  
 1829 attenuation, which is known as the attenuation coefficient, has a power-law relationship  
 1830 with wave frequency (Meylan et al., 2018). Understanding how the attenuation coefficient  
 1831 emerges from the underlying dynamic processes has been the main focus of ocean waves–sea  
 1832 ice interactions research over the past half century (Squire et al., 1995; Squire, 2007, 2020;  
 1833 Golden et al., 2020).

1834 In situations where the sea ice floe have sizes comparable to the wavelengths, the floes  
 1835 scatter the waves over the directional spectrum (Fig. 6). Wave scattering is an energy-  
 1836 conserving process but an accumulation of scattering events causes waves to attenuate over  
 1837 distance (Squire, 2007, 2020). Much theoretical work has attempted to describe wave atten-  
 1838 uation due to linear wave scattering in the marginal ice zone, using phase-resolving multiple-  
 1839 scattering theory in one horizontal dimension (Kohout & Meylan, 2008; Bennetts & Squire,  
 1840 2012b) or two dimensions (Bennetts & Squire, 2009; Peter & Meylan, 2010; Bennetts et  
 1841 al., 2010; Montiel et al., 2016). There have also been theories proposed to include attenu-  
 1842 ation due to scattering in phase-averaged wave transport models, using energy sink terms  
 1843 (Dumont et al., 2011; T. D. Williams et al., 2013a, 2013b; Mosig et al., 2019), a Boltzmann-  
 1844 interaction term (Meylan et al., 1997; Meylan & Masson, 2006; Meylan & Bennetts, 2018;  
 1845 Meylan et al., 2020) or a diffusion term (X. Zhao & Shen, 2016). Wave scattering through  
 1846 random fields of ice floes results in (i) exponential attenuation at a rate that increases with  
 1847 frequency, qualitatively consistent with observations, and (ii) broadening of the directional  
 1848 spread, so that deep into the marginal ice zone the directional wave spectrum becomes  
 1849 isotropic (Wadhams et al., 1986; Meylan et al., 1997; Bennetts et al., 2010; Montiel et al.,  
 1850 2016; Squire & Montiel, 2016). Scattering models show reasonable agreement with historical  
 1851 measurements from the Arctic in the mid-frequency regime where linear scattering theory

1852 is valid (Kohout & Meylan, 2008; Bennetts et al., 2010; Bennetts & Squire, 2012a; Squire  
1853 & Montiel, 2016).

1854 Measurements of surface waves in the Antarctic marginal ice zone have been made over  
1855 the past decade, predominantly using specially designed wave buoys deployed on the surface  
1856 of ice floes (Kohout et al., 2014; Meylan et al., 2014; Kohout et al., 2020; Montiel et al.,  
1857 2022), and recently by a stereo-camera system on an icebreaker (Alberello et al., 2022).  
1858 The floe sizes during the observations were typically much smaller than wavelengths, e.g.,  
1859 pancake ice (§ 3; Alberello, Onorato, Bennetts, et al., 2019), for which dissipative processes  
1860 are likely to be the main contributors to wave attenuation. Dissipative processes can broadly  
1861 be separated into turbulent ocean processes and viscous ice processes. Turbulence through  
1862 wave–sea ice interactions occurs as a result of the differential velocity between the solid  
1863 ice boundary and the water particle orbital velocity (Voermans et al., 2019). A turbulent  
1864 boundary layer is generated at the basal surface of the sea ice cover, which can be enhanced  
1865 by the ice surface roughness (skin friction) and the presence of vertical sea ice features, e.g.,  
1866 loe edges or pressure ridges, further enhancing flow separation (form drag; Kohout et al.,  
1867 2011). Turbulence also occurs in overwash on upper surfaces of floes, resulting in wave energy  
1868 dissipation (Bennetts et al., 2015; Bennetts & Williams, 2015; Toffoli et al., 2015; Nelli et  
1869 al., 2017, 2020). Sea ice covers have been modelled as viscoelastic materials, such that they  
1870 experience viscous dissipation when strained by ocean waves (Keller, 1998; R. Wang & Shen,  
1871 2010; Mosig et al., 2015). For instance, unconsolidated grease or brash ice (§ 3) dissipates  
1872 wave energy through non-recoverable, shear stress-induced viscous deformations (Weber,  
1873 1987; G. Sutherland et al., 2019). Quantifying these dissipative processes is challenging,  
1874 as they depend on temperature, brine volume fraction and ultimately the micro-structure  
1875 of the ice cover (§ 3.2.3; Timco & Weeks, 2010). In a more heterogeneous ice cover, e.g.,  
1876 pancake ice, wave energy dissipation is more likely to be governed by eddy-generating floe–  
1877 floe collisions (Shen & Squire, 1998; Bennetts & Williams, 2015; Yiew et al., 2017; Rabault  
1878 et al., 2019; Herman et al., 2019).

## 1879 5.2 Tides

1880 Tides are a ubiquitous feature of the global ocean. Gravitational dynamics of the Earth–  
1881 Moon–Sun system, combined with the Earth’s rotation, cause oscillations of ocean height  
1882 and currents at precise periods, dominated by diurnal (daily) and semidiurnal (twice daily)  
1883 tidal constituents. Here we use the term ‘tide’ to describe the barotropic or surface tide,  
1884 as opposed to “internal tides”, i.e., tidally generated internal waves, which are described in  
1885 § 5.3. Tides provide a substantial fraction of the total kinetic energy in the Southern Ocean,  
1886 with known effects at all scales from turbulence (§ 4) to large-scale circulation (§ 2).

1887 Throughout most of the global ocean, tides exist as propagating barotropic waves.  
1888 These waves have spatial scales comparable to ocean basins and their amplitude depends on  
1889 the global distribution of continents and bathymetry. These propagating waves are relatively  
1890 straightforward to constrain in inverse models using in situ and satellite data (e.g., Egbert  
1891 & Erofeeva, 2002; Lyard et al., 2006). However, the largest tidal currents around Antarctica  
1892 are associated with diurnal-band, topographically trapped vorticity waves along the shelf  
1893 break. These waves are a specific, tidally-forced case of coastal trapped waves (§ 5.3.3).  
1894 Observations and models of diurnal topographic vorticity waves (e.g., J. H. Middleton et  
1895 al., 1987; Semper & Darelius, 2017; Skardhamar et al., 2015) show that they can have short  
1896 spatial scales, are poorly constrained by sea surface height data, are extremely sensitive to  
1897 topographic variability, stratification and mean flows, and produce strongly depth-varying  
1898 currents. Predicting these currents is a difficult modelling problem, especially at the typical  
1899 coarse grid scales of global climate models. When present, these waves have a profound effect  
1900 on cross-slope transport of ocean heat, mean flows through tidal rectification (Makinson &  
1901 Nicholls, 1999; Flexas et al., 2015), and the volume flux and hydrographic characteristics of  
1902 Dense Shelf Water and Antarctic Bottom Water outflows (e.g., Padman et al., 2009).

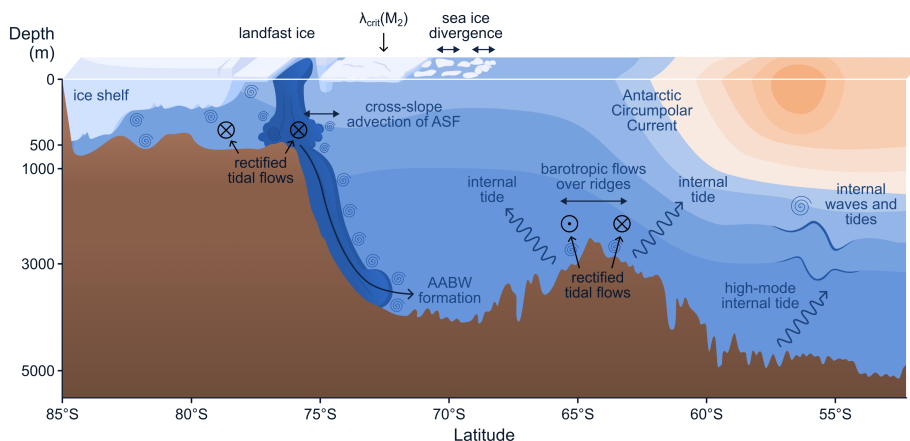


**Figure 18.** Schematic of the primary roles of tides in the Southern Ocean system. Under the ice shelf, tidal currents generate friction that modifies hydrographic properties of the water column, influencing the basal melting of the ice shelf. At the ice front and shelf break, rectified tidal currents modify water mass transport along and across these topographic barriers. Over the continental shelf and slope, tidal currents modify sea ice production and concentration. Stress at the base of landfast sea ice affects melting, and mixing controls on surface mixed layer depth. Mixing and rectification of tidal flows alters the production of Antarctic Bottom Water (AABW). Farther north, tidal flows over steep and rough topography of mid-ocean ridges generates internal (baroclinic) tides that can drive mixing in the ocean interior. Baroclinic tides may also be generated over the continental slope.

1903 The principal dynamical role of the tide is through the interactions of tidal currents  
 1904 with other components of the Southern Ocean system, including as a source of mixing (§ 4.3),  
 1905 crevasse formation and iceberg calving (§ 3.1.7), divergent stresses on sea ice (Padman &  
 1906 Kottmeier, 2000; Heil et al., 2008), and basal melting of ice shelves (Fig. 18; Richter et al.,  
 1907 2022). Tides link processes ranging from the smallest time and space scales of mixing to  
 1908 the global scales of continents, ocean basins and ice shelves that set the spatial distribution  
 1909 of tidal currents (e.g., Figs. 1b and 9b of Padman et al., 2018). The largest tidal currents  
 1910 around Antarctica are found along the shelf breaks of the Ross and Weddell seas, and under  
 1911 Ronne Ice Shelf. Along the Northwest Ross Sea shelf break, maximum spring tidal currents  
 1912 can exceed  $1 \text{ m s}^{-1}$  (Whitworth & Orsi, 2006). Tides in the Pacific sector are dominated by  
 1913 diurnal variability, while semidiurnal tides dominate elsewhere (e.g., Fig. 1c of Padman et  
 1914 al., 2018).

1915 There are relatively few in situ tide height measurements in the Southern Ocean  
 1916 (M. A. King & Padman, 2005). High quality, long-duration tidal records have histori-  
 1917 cally been limited to a few coastal tide gauges and bottom pressure recorders. However,  
 1918 recent deployments of Global Navigation Satellite System (GNSS) receivers on ice shelves  
 1919 have provided high quality tide records greater than one year long (e.g., Ray et al., 2021).  
 1920 Additional data come from satellite altimetry (reviewed in Section 2.2.2 of Padman et al.,  
 1921 2018), although this is challenging in the far Southern Ocean as the best satellites for tidal  
 1922 studies (TOPEX/Poseidon and Jason) only sample to about  $66^\circ\text{S}$  and, for these and other  
 1923 satellites with higher-latitude orbits, the presence of sea ice and ice shelves complicates the  
 1924 extraction of the tidal signal.

1925 Given the paucity of high quality data, our modern knowledge of Southern Ocean tides  
 1926 comes primarily from ocean tide models. Barotropic models solve the depth-integrated

1927 equations of motion and provide depth-averaged (‘barotropic’) currents; for example, the  
 1928 global solutions reviewed by [Stammer et al. \(2014\)](#) or regional models such as CATS2008  
 1929 ([S. L. Howard et al., 2019](#)). These models may be based entirely on dynamics (with open  
 1930 boundary conditions applied for regional models) or inverse models constrained by assimila-  
 1931 tion of ocean height data including in situ measurements and satellite altimetry. However,  
 1932 the accuracy of barotropic models in the Southern Ocean, especially in the Antarctic coastal  
 1933 seas, is typically poorer than at lower latitudes due to the reduced amount of data available  
 1934 to constrain the solutions.

### 1935 **5.2.1 Tidal rectification**

1936 Nonlinear interactions between tidal flows and a sloping seafloor (such as the continental  
 1937 shelf), in the presence of planetary rotation and spatial variations in tidal amplitude, can  
 1938 lead to the generation of a time-averaged mean flow, in a process known as ‘tidal rectification’  
 1939 ([Loder, 1980](#); [I. Robinson, 1981](#)). These time-averaged flows have speeds of approximately  
 1940 10–15% of the tidal current. Observations and models suggest that rectified tidal flows across  
 1941 the Northwest Ross Sea outer continental shelf play an important role in the Antarctic  
 1942 Bottom Water export from this region (Fig. 10 of [Padman et al., 2009](#)). [Makinson and](#)  
 1943 [Nicholls \(1999\)](#) implicated tidal rectification as playing a key role in the ventilation of the  
 1944 ocean cavity under Filchner-Ronne Ice Shelf. Numerical modelling studies ([Flexas et al.,](#)  
 1945 [2015](#)) have also shown that tidal rectification-induced volume flux convergence is essential  
 1946 to simulate a realistic Antarctic Slope Front and Current (§ 2.2).

1947 In locations where tidal currents are comparable to mean flows, they can also modify  
 1948 those mean flows through changing the time-averaged stress at the seafloor. This tidal  
 1949 rectification is distinct to that discussed above since it involves the modification of existing  
 1950 mean flows, rather than the interaction of the tide with topographic gradients to generate  
 1951 new mean flows ([Loder, 1980](#)). [Robertson et al. \(1985\)](#) postulated that strong tides around  
 1952 the perimeter of the Weddell Sea could significantly reduce the transport of the Weddell  
 1953 Gyre through tide-induced weakening of mean flows via this rectification mechanism. A  
 1954 similar response is expected in other locations where benthic tidal currents are significant,  
 1955 notably in the southern limb of the Ross Gyre.

### 1956 **5.2.2 Internal tide drag**

1957 Internal tide drag is the periodic force exerted on the surface tide when it interacts with  
 1958 seafloor topography to generate internal waves. This effect is the dominant tide–topography  
 1959 interaction in the deep, open ocean where tidal flows are weak (a few centimetres per second)  
 1960 and turbulent drag, which dominates in regions of strong tidal flow on continental shelves, is  
 1961 negligible. The key role of internal tide drag was directly identified with the advent of satel-  
 1962 lite observations and associated inverse models indicating that approximately 30% of energy  
 1963 loss from the surface tide occurred in the open ocean ([Egbert & Ray, 2000](#)), including a sig-  
 1964 nificant amount over rough topographic features in the Southern Ocean. Internal tide drag  
 1965 was subsequently implemented in forward-running tide and ocean models ([Jayne & St. Lau-](#)  
 1966 [rent, 2001](#)). It is now recognised that internal tide drag is crucial in setting the amplitude  
 1967 of the surface tide ([Buijsman et al., 2015](#); [Arbic et al., 2018](#)), and, therefore, also feeds back  
 1968 on the strength of internal tide generation ([Ansong et al., 2015](#)) (see §5.3.1). Recent work  
 1969 has shown that this internal tide drag is not purely a drag force, but also exhibits an out-  
 1970 of-phase force component, analogous to the spring in a harmonic oscillator, which can both  
 1971 damp and, in certain resonant configurations, amplify the surface tide ([Shakespeare et al.,](#)  
 1972 [2020](#)). This out-of-phase force component dominates when sub-inertial topography-trapped  
 1973 internal tides are generated (i.e., poleward of the critical latitude; § 5.3.3) and, therefore,  
 1974 may be particularly important in the Southern Ocean.

### 1975 5.3 Internal gravity waves

1976 Internal waves play a key role in transferring energy from large scale motions to small  
 1977 scale turbulence, making them a major source of interior ocean mixing. The mixing gen-  
 1978 erated by internal waves is one of the drivers of large scale ocean circulation and plays an  
 1979 important role in biological and physical interactions, including the transport of nutrients  
 1980 and larvae. Internal waves also transport momentum into the ocean from the boundaries,  
 1981 thereby directly forcing the eddying and larger-scale circulation. They are generated when  
 1982 the ocean density field is perturbed and can be identified as oscillations of these different  
 1983 layers of the stratified ocean interior. Internal waves have vertical length scales from a few  
 1984 meters to 2 km, horizontal length scales from a few meters to hundreds of kilometers, hor-  
 1985 izontal group velocities of 10–100 mm s<sup>-1</sup>, amplitudes from meters to hundreds of meters,  
 1986 and periods from several minutes to a day (Thorpe, 2007; Kantha & Clayson, 2000).

1987 Internal waves originate primarily at the ocean’s upper and lower boundaries. They are  
 1988 forced at the surface by wind stress fluctuations, and at the seabed by tides and mesoscale  
 1989 flows interacting with rough topography. Observations of near-inertial wave energy prop-  
 1990 agation from the mixed layer into the ocean interior suggest that wind-generated internal  
 1991 waves are an especially important part of the ocean mixing budget in the Southern Ocean  
 1992 (Waterman et al., 2013). The Southern Ocean has a deep-reaching mesoscale flow, some-  
 1993 times referred to as the “mean flow” or “background flow” in the internal wave literature,  
 1994 which is a mix of strong currents such as the Antarctic Circumpolar Current and associ-  
 1995 ated jets, meanders and mesoscale eddies (§§ 2.1,2.5). The interaction of this deep-reaching  
 1996 mesoscale flow with the seafloor is a major source of topographic internal waves in the  
 1997 Southern Ocean (Nikurashin & Ferrari, 2011, 2013). New maps of internal tide-induced  
 1998 sea surface height perturbations derived from repeat-orbit satellite altimetry (Zaron, 2019)  
 1999 have revealed energetic internal tides near the Kerguelen Plateau, Macquarie Ridge and  
 2000 Drake Passage, consistent with previous modelling studies (Simmons et al., 2004). Vertical  
 2001 displacement variance at 1000 m depth measured with Argo profilers, has uncovered similar  
 2002 hotspot regions, particularly in the Kerguelen Plateau and Drake Passage regions (Hennon  
 2003 et al., 2014)

#### 2004 5.3.1 Internal wave generation in the Southern Ocean

2005 The Southern Ocean storm track centred on 40°S (the roaring 40s), is associated with  
 2006 high wind work and is a key source of near inertial waves (Simmons & Alford, 2012). Wind  
 2007 blowing at the local inertial frequency band can force inertial motions through resonance in  
 2008 the ocean surface mixed layer (D’Asaro, 1985; Alford et al., 2016; L. N. Thomas & Zhai,  
 2009 2022). Those inertial motions lead to convergence and divergence at the stratified base of  
 2010 the mixed layer. This pumping generates internal waves close to the local inertial frequency  
 2011 (or Coriolis frequency) everywhere in the ocean except at the equator, which are called  
 2012 “near-inertial waves” (Fig. 19). The resonant frequency, or effective local Coriolis frequency  
 2013 at which near-inertial waves are generated is modified by the relative vorticity of the back-  
 2014 ground flow (e.g., Kunze, 1985; Schlosser, Jones, Bluteau, et al., 2019, for the Southern  
 2015 Ocean). Near-inertial waves are mostly generated from wind (other mechanisms are dis-  
 2016 cussed below), and propagate almost exclusively equatorward, since the inertial frequency  
 2017 decreases with latitude (Garrett, 2001; Chiswell, 2003; Alford & Zhao, 2007). They are  
 2018 blocked from propagating poleward, except in strongly sheared currents (Jeon et al., 2019),  
 2019 since their frequency would become sub-inertial, typically within a single wavelength. Glob-  
 2020 ally, most of the ocean’s kinetic energy (Leaman & Sanford, 1975; Garrett, 2001; Wunsch et  
 2021 al., 2004) and vertical shear (Alford et al., 2016) is in the near-inertial band, standing apart  
 2022 from the rest of the internal wave spectrum (L. N. Thomas & Zhai, 2022). Near-inertial  
 2023 waves play a crucial role in mixing the upper and deep ocean (§4.3.2; Alford et al., 2012).

2024 A number of global studies (Alford, 2003; Jiang et al., 2005; Chaigneau et al., 2008;  
 2025 Alford, 2020) have variably estimated the wind-energy input into near-inertial motions in

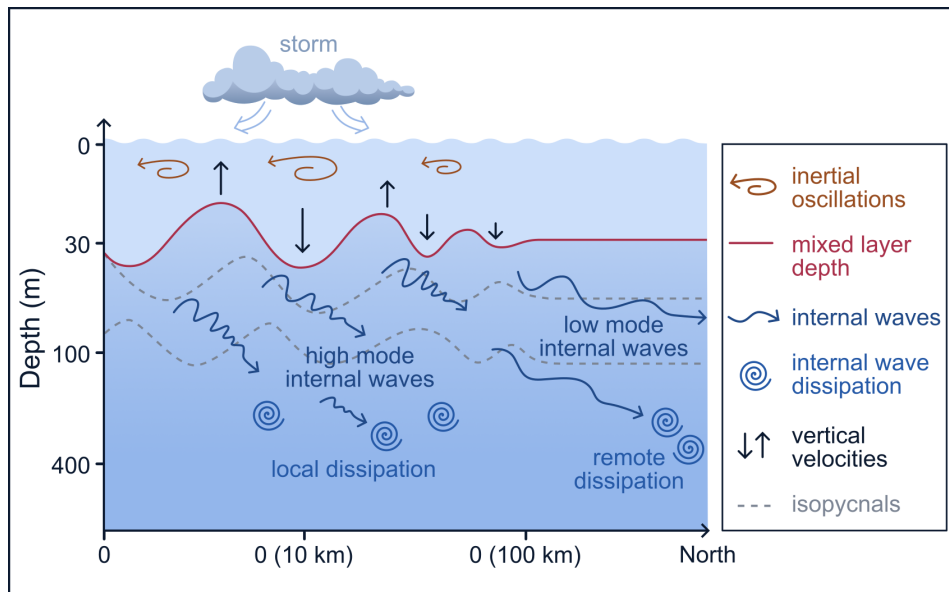


**Figure 19.** Schematic of near-inertial waves generation, propagation and dissipation. Storms generate inertial oscillations in the ocean mixed layer which drive horizontal convergences and divergences that lead to vertical velocities. These pump the base of the mixed layer generating internal waves near the local inertial frequency ( $1-1.2f$ ) that have counterclockwise polarization in the Southern Ocean. High mode near-inertial waves propagate downward and equatorward and tend to break locally due to high shear. Low mode internal waves propagate further equatorward. The interactions between near-inertial internal waves with other internal waves and with the background mesoscale flow are not represented here. Figure adapted from [Alford et al. \(2016\)](#).

2026 the mixed layer as being in the range 0.29 to 0.7 TW. This large range is partly due to  
 2027 the high sensitivity of the calculation to the wind forcing product used (Jiang et al., 2005).  
 2028 In addition, all of the above-cited studies use a slab-ocean model that does not account  
 2029 for the interaction with the background mesoscale flow, which model studies have shown  
 2030 to impact the near-inertial energy flux and decay timescale (Zhai et al., 2005; Whitt &  
 2031 Thomas, 2015). More recent studies that instead use high resolution numerical models to  
 2032 estimate wind energy input give estimates at the lower end of this range (0.23 to 0.27 TW;  
 2033 von Storch & Lüschow, 2023).

2034 The second major source of internal waves is via the interaction of ocean flows with the  
 2035 rough seafloor (Musgrave et al., 2022) and the Southern Ocean is a hotspot for a certain type  
 2036 of these topographically generated internal waves known as ‘lee waves’. When a fluid parcel  
 2037 is lifted up and over a topographic obstacle at sufficient speed, the restoring buoyancy  
 2038 force from the stratification initiates an oscillation (internal wave) which radiates energy  
 2039 away from the seafloor (Fig. 20). The ocean flow doing the lifting is a combination of  
 2040 eddies, jets and other currents (§ 4.1), which are essentially steady on the timescale of waves  
 2041 ( $< 1$  day) and the barotropic tide (§ 5.2), which varies on sub-daily timescales (frequency  
 2042  $\omega$ ). Assuming a background mesoscale flow speed of  $U$  and topographic wavenumber  $k$ ,  
 2043 generation of freely-propagating topographic internal waves can only occur in the regime  
 2044 where the intrinsic frequency is between the inertial frequency,  $f$ , and buoyancy frequency  
 2045  $N$ ; i.e.,  $|f| < |\omega + kU| < |N|$ . Therefore, barotropic tides (through frequency  $\omega$ ) and  
 2046 mesoscale flow (through speed  $U$ ) conspire in the generation of internal waves at topography  
 2047 (Bell, 1975; Shakespeare, 2020). The two end members of topographic internal waves are  
 2048 steady lee waves (when there is no tidal flow) and pure internal tides (when there is no  
 2049 quasi-steady flow). Steady lee waves are only generated at very small scale topography  
 2050 ( $f/U < |k| < N/U$ ), which for typical deep Southern Ocean conditions ( $U = 0.1\text{--}0.2\text{ m s}^{-1}$ ,  
 2051  $f = 1 \times 10^{-4}\text{ rad s}^{-1}$ ,  $N = 1 \times 10^{-3}\text{ rad s}^{-1}$ ) restricts  $2\pi/k$  to topographic scales of  
 2052 0.5–10 km. Consequently, the presence of small-scale topography critically determines the  
 2053 geographical location of lee wave generation. By contrast, pure internal tides are only  
 2054 generated where  $\omega > f$  (equatorward of  $\sim 74.5^\circ$  for semi-diurnal, and  $\sim 28^\circ$  for diurnal)  
 2055 at large scale (small  $k$ ) topography where the influence of the background mesoscale flow  
 2056 is negligible. In intermediate regimes, topographic internal waves exist as “Doppler shifted  
 2057 internal tides” (Shakespeare, 2020) but most studies have focused only on the two limiting  
 2058 cases.

2059 The energy flux into topographic internal waves is determined primarily by the strat-  
 2060 ification,  $N$ , at the ocean bottom, topographic spectrum and flow speeds:  $E \sim \rho_0 N \bar{k} U^2 h^2$   
 2061 where  $\bar{k}$  is the mean topographic wavenumber,  $h$  the root-mean-squared height of the to-  
 2062 pography, and  $U$  the appropriate tidal or quasi-steady flow speed (e.g., Garrett & Kunze,  
 2063 2007). This scaling only applies in the so-called “intermediate frequency limit”, where  
 2064  $|f| \ll |\omega + kU| \ll |N|$ . Thus, the weak stratification typical of the Southern Ocean at the  
 2065 depth of prominent bathymetric features tends to limit the production of internal waves,  
 2066 but this is somewhat counteracted by the presence of unusually rough and large amplitude  
 2067 topography, and deep-reaching, intense eddying flows. However, it is not a simple matter  
 2068 of additional lee wave generation in the Southern Ocean compensating for reduced internal  
 2069 tide generation, since the fates of these waves are likely to be very different. While lee waves  
 2070 are confined within their generating flow (e.g., jet, eddy, meander), internal tides can freely  
 2071 propagate into different flow regimes (Shakespeare, 2020). We first consider the magnitude  
 2072 of pure internal tide generation at large scales, before discussing the small-scale limit where  
 2073 both internal tides and lee waves are generated.

2074 For the dominant  $M_2$ -tidal constituent, total low-mode internal tide generation in the  
 2075 Southern Ocean has been estimated from baroclinic tide models to be 0.15 TW (compared  
 2076 with 0.87 TW globally) with almost all the energy flux occurring at three locations: Mac-  
 2077 quarie Ridge, Kerguelen Plateau, and in the vicinity of Drake Passage (Table 3 of Simmons

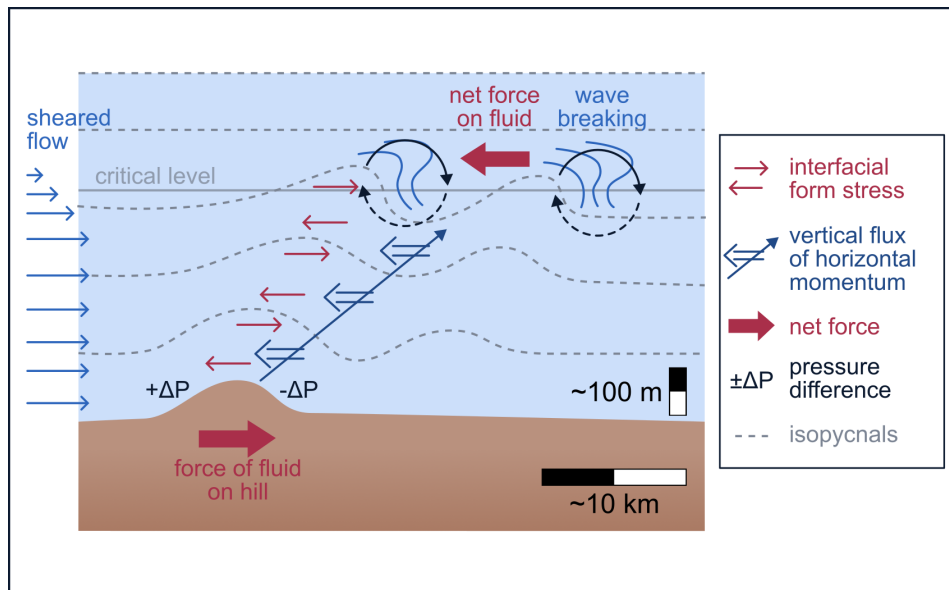


**Figure 20.** Schematic of internal lee wave generation and the associated vertical transfer of horizontal momentum flux via lee wave induced form stress across isopycnal layers. The pressure is increased on the upstream side of the hill ( $+\Delta P$ ) and decreased on the downstream side ( $-\Delta P$ ), resulting in a force from the fluid on the hill. The breaking of the wave at a critical level drives turbulent mixing and deposition of the wave momentum, resulting in a net force on the background mesoscale flow. For lee waves, this force always acts to decelerate the flow. For lee waves, critical levels only occur when the velocity reduces with height along the waves propagation path, as shown here; this usually occurs when the wave reaches the horizontal boundary of an eddy/jet, but for simplicity, the flow in this schematic is represented as horizontally uniform.

2078 *et al.*, 2004). However, other modelling (*Padman et al.*, 2006) suggests these values may be  
 2079 significantly overestimated, and that the calculation may be highly resolution dependent.

2080 At horizontal scales of  $\sim 10$  km or less, and especially in the Southern Ocean, the  
 2081 seafloor is dominated by features known as “abyssal hills” (*Goff*, 1991), which are not  
 2082 resolved in the bathymetric datasets or large scale models. However, spectral representation  
 2083 of this topography (*Goff*, 2010; *Goff & Arbic*, 2010), together with numerical model estimates  
 2084 of  $N$  and eddying flow  $U$ , may be used to estimate internal wave generation at abyssal  
 2085 hills. Globally, an additional  $M_2$  internal tide energy flux of 0.03–0.1 TW is thought to  
 2086 generated, but only perhaps 10% of this flux occurs in the Southern Ocean (*Melet et al.*,  
 2087 2013; *Shakespeare*, 2020). Many authors (*Naveira Garabato et al.*, 2013; *Scott et al.*, 2011;  
 2088 *Nikurashin & Ferrari*, 2010; *Wright et al.*, 2014; *Yang et al.*, 2018; *Shakespeare*, 2020) have  
 2089 also used linear theory (following *Bell*, 1975, but often with modifications to account for  
 2090 nonlinear effects) to calculate rates of lee wave generation globally. Predictions vary from  
 2091 0.05 to 0.85 TW, with the majority of this energy flux usually concentrated in the Southern  
 2092 Ocean. The huge range of estimated energy flux for small-scale internal tide and lee wave  
 2093 generation is due to the extreme degree of uncertainty in numerical model estimates of  
 2094 both bottom stratification and eddying flow speeds at the seafloor, as well as a paucity of  
 2095 observations to constrain the models.

2096 Other sources of internal waves in the Southern Ocean are the relative motion of sea ice  
 2097 across the upper ocean through the shape of the under-sea ice surface (*McPhee & Kantha*,  
 2098 1989), sea ice floe motions (*Waters & Bruno*, 1995), and ice tongues and ice shelf basal  
 2099 variability. Internal wave generation under sea ice is controlled by sea ice roughness, sea ice  
 2100 concentration and wind forcing (*Cole et al.*, 2018). While such sea ice generated internal  
 2101 waves have been reported in the Arctic (*Cole et al.*, 2014), there are currently few direct  
 2102 observations of internal waves under Antarctic sea ice and ice shelves, which are limited to  
 2103 internal tides (e.g., see the mooring data of *S. Howard et al.*, 2004). The magnitude of energy  
 2104 fluxes from these generation mechanisms, which are harder to observe and model, and their  
 2105 relative prevalence are unknown. Additional internal wave generation mechanisms that are  
 2106 not specific to the Southern Ocean are adjustment processes (e.g., geostrophic adjustment)  
 2107 at fronts and eddies (*Gill*, 1984; *Alford et al.*, 2013; *Nagai & Hibiya*, 2015; *Rijnsburger et*  
 2108 *al.*, 2021) and spontaneous emission via mesoscale straining (*Shakespeare*, 2019).

### 2109 **5.3.2 Influence of geostrophic turbulence on internal waves**

2110 The interaction of the strong Southern Ocean mesoscale flow with the seafloor gives  
 2111 rise to the emission of internal waves that possess a net momentum directed mostly against  
 2112 the flow (*Bell*, 1975; *Nikurashin & Ferrari*, 2011; *Naveira Garabato et al.*, 2013; *Shakespeare*  
 2113 *& Hogg*, 2019; *Shakespeare*, 2020). This momentum is transported by the waves and de-  
 2114 posited where they break and dissipate, leading to a net force on the fluid (*Eliassen*, 1961;  
 2115 *Bretherton*, 1969; *Andrews & McIntyre*, 1978). In the case of lee waves, this force is often  
 2116 termed the “lee wave drag”, which plays a significant role in Southern Ocean dynamics  
 2117 (Fig. 20; *Naveira Garabato et al.*, 2013). The wave dissipation may be triggered by vari-  
 2118 ous mechanisms including shear instabilities, wave saturation, wave–wave and wave–mean  
 2119 interactions.

2120 Wave–mean interactions encompass all mechanisms of interactions that are the result  
 2121 of wave propagation through gradients in velocity and density induced by eddies, jets or any  
 2122 other currents. For example, lee waves propagating upward and against a vertically sheared  
 2123 flow that decreases with height will lose energy to that flow, while lee waves propagating  
 2124 against a shear flow that increases with height will take energy from that flow. The former  
 2125 mechanism is an important energy sink for lee waves (*Waterman et al.*, 2014, 2021; *Kunze*  
 2126 *& Lien*, 2019). Similarly, horizontal straining of waves by the mesoscale eddy field can  
 2127 lead to significant energy exchange, and eventual wave dissipation in certain cases (*Buhler*  
 2128 *& McIntyre*, 2005). Because the Southern Ocean exhibits a vigorous and deep-reaching

2129 mesoscale eddy field, it may be a global hotspot for wave–mean interactions. However,  
 2130 numerical modelling support for this hypothesis is limited and observational evidence is  
 2131 almost non-existent for all but a few possible interaction mechanisms (Cusack et al., 2020).

2132 One key wave–mean interaction in the Southern Ocean is the phenomenon known as  
 2133 the “critical level” (or ‘inertial level’; e.g., Booker & Bretherton, 1967). A critical level  
 2134 is a height at which the internal wave phase speed equals the horizontal mean flow speed  
 2135 and will be encountered when flow-trapped (e.g., lee) waves propagate upwards through a  
 2136 mean flow that decreases in magnitude with height along the wave propagation path, which  
 2137 usually occurs when the wave reaches the horizontal boundary of an eddy or jet (Fig. 20  
 2138 shows a simplified schematic of this process), if the waves have not already dissipated via  
 2139 other means nearer the seafloor (e.g., Nikurashin et al., 2013). During the propagation  
 2140 towards critical levels, the waves’ vertical wavelength decreases while their shear increases  
 2141 until, close to the critical level, instabilities lead to dissipation of the wave and the deposition  
 2142 of the wave momentum. Critical levels have also been suggested as a mechanism for the  
 2143 observed enhancement of dissipation around the edges of mesoscale eddies in Drake Passage  
 2144 (Sheen et al., 2015), with the potential for the wave momentum associated with tidally-  
 2145 generated internal waves to “spin up” the eddies due to concomitant preferential dissipation  
 2146 of waves propagating in the direction of the mesoscale flow (Shakespeare & Hogg, 2019;  
 2147 Shakespeare, 2023). Cusack et al. (2020) found significant energy transfers from internal  
 2148 waves propagating through eddy shear at a Drake Passage mooring, suggestive of a critical  
 2149 level type mechanism.

2150 Many observational studies of wave–mean interactions in the Southern Ocean have  
 2151 been focused in regions of standing meanders downstream of major topographic obstacles  
 2152 (such as Kerguelen Plateau) that generate a vigorous eddy field (Sheen et al., 2015; Meyer,  
 2153 Polzin, et al., 2015; Waterman et al., 2021; Cyriac et al., 2023) because these are hotspots  
 2154 for key physical processes central to Southern Ocean dynamics (cf. § 4.1). Flow–topography  
 2155 interactions are elevated in these regions where the energetic jets of the Antarctic Circum-  
 2156 polar Current merge and split (Rintoul, 2018). In addition, the wind-energy input into  
 2157 near-inertial motions is high in these regions (§ 5.3). Thus, standing meanders are expected  
 2158 to be Southern Ocean mixing hotspots owing to the rich internal wave field generated from  
 2159 strong wind forcing and flow–topography interactions.

2160 The elevated shear, strain and vorticity in the background flow in meanders are impor-  
 2161 tant factors in the evolution of internal waves. A timescale characterization of the various  
 2162 processes expected to drive wave evolution suggests that the timescales associated with back-  
 2163 ground flow advection and wave-mean flow interactions dominate dissipation timescales in  
 2164 the evolution of waves (Meyer, Polzin, et al., 2015; Waterman et al., 2021; Cyriac et al.,  
 2165 2023). This timescale analysis implies that some internal waves contribute to local mixing  
 2166 by dissipating locally, while most of the waves are advected away by the mesoscale flow and  
 2167 lead to dissipation downstream of the meander, in agreement with modelling studies (e.g.,  
 2168 Zheng & Nikurashin, 2019) and theoretical descriptions (Shakespeare et al., 2021; Baker  
 2169 & Mashayek, 2021). The mixing driven by this far-field dissipation of internal waves has  
 2170 significant implications for the Southern Ocean stratification and watermass transformation  
 2171 (Meyer, Polzin, et al., 2015). Other potential mechanisms of wave–mean interactions in  
 2172 meander regions are the wave-capture (Meyer, Polzin, et al., 2015; Waterman et al., 2021)  
 2173 and near-inertial wave trapping (Meyer, Polzin, et al., 2015; Rama et al., 2022; Cyriac et al.,  
 2174 2023). Whether internal waves are located inside or outside fronts, jets and eddies controls  
 2175 which of these wave–mean interaction mechanism dominates.

### 2176 *5.3.3 High-latitude internal wave dynamics*

2177 In the Southern Ocean, the tidal frequency is everywhere less than the inertial frequency  
 2178 for the diurnal tide, and in the Ross and Weddell Seas (poleward of 74.5°S) for the most  
 2179 energetic semidiurnal tide,  $M_2$ . In these regimes, internal tides are not freely propagating,

2180 but are instead generated as waves that are trapped near the bottom topography, either  
 2181 in the open ocean (bottom trapped waves; Rhines, 1970; Falahat & Nycander, 2015), or  
 2182 along the shelf (coastal trapped waves; Huthnance, 1978; Mysak, 1980). Coastal trapped  
 2183 waves can also be initiated by wind stresses and dense water outflows that produce sub-  
 2184 inertial oscillations (J. Adams & Buchwald, 1969; Marques et al., 2014; Liao & Wang,  
 2185 2018). Unlike freely propagating waves that can travel across continental shelves and oceans,  
 2186 coastal-trapped waves must dissipate their energy near the shelf and slope and are thus a  
 2187 potential source of regionally important shelf mixing and mass transport (Musgrave et al.,  
 2188 2017). Trapped waves may also play an important role in modifying the amplitude of the  
 2189 surface tide in the Southern Ocean (§ 5.2.2). Coastal trapped waves propagate with the  
 2190 coast on their left in the Southern Hemisphere, with a form that is highly dependent on  
 2191 the characteristics of the topography and stratification (Schlosser, Jones, Musgrave, et al.,  
 2192 2019; C. W. Hughes et al., 2019).

2193 Three general categories of coastal-trapped waves have been identified as important to  
 2194 Southern Ocean dynamics. In some regions, notably the Ross and Weddell Sea shelf breaks,  
 2195 the strongest currents are associated with coastal trapped waves forced by the diurnal tide  
 2196 (§ 5.2; J. H. Middleton et al., 1987; Whitworth & Orsi, 2006; Padman et al., 2009; Semper &  
 2197 Darelius, 2017). Coastal trapped waves of subtidal frequency have also been observed along  
 2198 shelf breaks (e.g., J. H. Middleton et al., 1982). Models suggest that outflows of Dense Shelf  
 2199 Water can excite these waves along the Antarctic continental slope (Marques et al., 2014).  
 2200 A third source for coastal trapped waves is associated with the co-location of critical slope  
 2201 (slope of the topography that matches the wave ray angle, and at which the generation of  
 2202 internal waves is most efficient; e.g., Becker & Sandwell, 2008) and critical latitude for the  
 2203  $M_2$ -semidiurnal internal tidal waves along the southern Weddell Sea shelf break (Robertson,  
 2204 2001; Daae et al., 2009). Numerical modelling suggests that coastal trapped semidiurnal  
 2205 waves are generated in that region, leading to enhanced near-bed velocities at the shelf edge  
 2206 and thick bottom mixed layers ( $\sim 100$  m).

2207 Coastal trapped waves are expected to affect mixing, cross-slope exchanges, ice shelf  
 2208 cavities, melt rates and sea ice concentration. Eddy diapycnal diffusivities from both  
 2209 finescale (Daae et al., 2009) and microstructure (Fer et al., 2016) observations show ele-  
 2210 vated near bottom values at a southern Weddell Sea shelf-break location, attributed to the  
 2211 semidiurnal coastal trapped waves. Based on modelling, Marques et al. (2014) proposed  
 2212 that coastal trapped waves forced by dense-water outflows would affect benthic mixing  
 2213 and cross-slope water mass exchanges in the vicinity of sources of dense water outflows in  
 2214 the Weddell and Ross Seas. Each of these processes depends on stratification and mean  
 2215 flow along the continental slope. Therefore, we expect seasonal modulation of the coastal  
 2216 trapped waves, which has been observed for coastal trapped waves forced by the diurnal  
 2217 tides (J. H. Middleton et al., 1987; Semper & Darelius, 2017). There is substantial potential  
 2218 for feedbacks between coastal trapped waves and background stratification and mean flow  
 2219 through associated mixing (§ 4.3) and tidal rectification (§ 5.2.1).

## 2220 5.4 Closing the loops

2221 This section has described the significant influence of the three major types of gravity  
 2222 waves (surface waves, tides and internal waves) on the larger and/or slower components of  
 2223 Southern Ocean dynamics. Surface waves exert a first-order control on the air-sea fluxes  
 2224 of heat and mass in the Southern Ocean, which, in turn, drive ocean convection (§ 4.2)  
 2225 and the large-scale circulation (§ 2). Similarly, rectified tidal currents contribute to the  
 2226 Antarctic Slope Current (§ 2.2) and subpolar gyres (§ 2.3), modulating the transfer of heat  
 2227 across the Antarctic margin. Internal waves, some of which are generated by the tides, are  
 2228 responsible for significant interior diapycnal mixing (§ 4.3) and dissipating energy from the  
 2229 ocean’s mesoscale (§ 4.1) at rough Southern Ocean topography.

## 2230 6 Climate trends and future projections

2231 The Southern Ocean dynamic system is changing in response to global warming (§ 1)  
 2232 and changes in its atmospheric drivers. In recent decades, surface wind speeds have in-  
 2233 creased over the Southern Ocean (Young et al., 2011; Young & Ribal, 2019) and the maxi-  
 2234 mum in the wind speed shifted southward—these changes are often described in terms of a  
 2235 strengthening and poleward contraction of the Southern Annular Mode (the dominant mode  
 2236 of atmospheric variability over the Southern Ocean; Arblaster & Meehl, 2006; Toggweiler,  
 2237 2009; D. W. Thompson et al., 2011). Precipitation has decreased at lower latitudes and  
 2238 increased at higher latitudes (Manton et al., 2020), and evaporation has decreased over the  
 2239 Southern Ocean (Boisvert et al., 2020). This section reviews the key trends in the differ-  
 2240 ent components of the Southern Ocean dynamical system and projections for future trends  
 2241 where available. These trends in dynamical components are strongly influenced by ongoing  
 2242 changes in the thermohaline structure of the Southern Ocean. For a more detailed review  
 2243 of recent trends in the physical climate, the reader is referred to J. M. Jones et al. (2016).

### 2244 6.1 Large-scale circulation

2245 Argo and satellite observations have shown an acceleration of the zonal flow on the  
 2246 northern edge of the Antarctic Circumpolar Current (§ 2.1) (Shi et al., 2021). This trend  
 2247 is consistent with theory (Hogg, 2010) and modelling (Shi et al., 2020) which predict an  
 2248 increased “thermal wind” in response to the enhanced meridional buoyancy gradients ob-  
 2249 served in this region (Gille, 2008, 2014; Rintoul, 2018; Roemmich et al., 2015; J. M. Jones et  
 2250 al., 2016). However, uncertainty remains about whether the increased zonal flow represents  
 2251 a strengthening of the Antarctic Circumpolar Current itself or just a southward shift of the  
 2252 adjoining subtropical gyres (A. L. Stewart, 2021). Notably, the position of the Antarctic  
 2253 Circumpolar Current appears to be stable, despite shifting westerly winds (Chapman, 2017).

2254 Recent inverse models based on tracer observations suggest that the upper overturning  
 2255 circulation (§ 2.4) is currently weakening, following a period of strengthening in the 1990s  
 2256 (DeVries et al., 2017; Rintoul, 2018). These changes are opposite to the enhancement of  
 2257 the upper overturning predicted by theory and numerical models (Meredith et al., 2012;  
 2258 Morrison & Hogg, 2013) in the presence of strengthening westerly winds. One possibility is  
 2259 that the observed changes may be due to natural variability rather than atmospheric forcing  
 2260 (H. Thomas et al., 2008).

2261 While there is currently no clear trend in the abyssal branch of the overturning circu-  
 2262 lation (§ 2.5), significant changes are already being observed in the dense water formation  
 2263 processes at the Antarctic margin which feed this circulation. Enhanced heat and freshwater  
 2264 fluxes from the warming atmosphere and accelerating glacial melt (rather than significantly  
 2265 modifying the surface ocean) are being taken up by the deep ocean through modification of  
 2266 the properties of the deep waters formed in this region. A warming and freshening of the  
 2267 Antarctic Bottom Water has been observed (Purkey et al., 2019) along with an associated  
 2268 reduction in abyssal stratification (H. J. Zhang et al., 2021). It is expected that this reduced  
 2269 density of shelf waters will also lead a reduced formation rate of Antarctic Bottom Water  
 2270 (Silvano et al., 2018; Lago & England, 2019; Q. Li et al., 2023). However, changes to the  
 2271 northward volume flux of Antarctic Bottom Water (i.e., the abyssal overturning circulation)  
 2272 are presently not able to be measured with sufficient precision to detect climate trends. In  
 2273 addition, it is expected that changes in the abyssal overturning will be complicated by the  
 2274 influence of winds (A. L. Stewart et al., 2021).

2275 The impact of the increasing westerly winds on the abyssal overturning is uncertain as  
 2276 it depends on the balance of two competing influences. On the one hand, the wind-driven  
 2277 enhancement of eddies (§ 6.3) is expected to increase internal lee wave generation in the  
 2278 Southern Ocean (§ 6.4) and, thus, the deep ocean mixing and concomitant upwelling of  
 2279 Antarctic Bottom Water (D. P. Marshall & Naveira Garabato, 2008). On the other hand  
 2280 (unless fully compensated by eddies) the enhanced westerly winds and associated wind stress

2281 curl are expected to drive increased northward fluxes of upwelling mid-depth water in the  
 2282 Southern Ocean but diminishing the amount transported southward to feed Dense Shelf  
 2283 Water and Antarctic Bottom Water formation (Ito & Marshall, 2008; Nikurashin & Vallis,  
 2284 2011; Shakespeare & Hogg, 2012). The projected weakening of the polar easterly winds  
 2285 (Neme et al., 2022) will also contribute to reducing Dense Shelf Water formation, due to  
 2286 the reduced northward export of sea ice away from Antarctica and subsequent build up of  
 2287 sea ice over the dense water formation sites (Timmermann et al., 2002; McKee et al., 2011;  
 2288 Dinniman et al., 2018; Hazel & Stewart, 2020; Morrison et al., 2023). The relative influence  
 2289 of these different effects is challenging to assess even with state-of-the-art high-resolution  
 2290 global ocean models (and impossible with contemporary climate models) since they must  
 2291 be able to represent accurately Antarctic Bottom Water formation, its northward isopycnal  
 2292 volume flux, and the internal waves driving mixing on  $\sim 1$  km scales (§7; Trossman et al.,  
 2293 2016; Kiss et al., 2020; Yang et al., 2021). However, in the longer term it is expected that  
 2294 the impact of significantly increased Antarctic meltwater on the abyssal overturning (§6.3)  
 2295 will dominate over any wind-driven changes (Q. Li et al., 2023).

2296 Understanding of current and future changes in the sub-polar gyres (Q. Wang et  
 2297 al., 2013; Armitage et al., 2018; Vernet et al., 2019; Hogg & Gayen, 2020; Neme et al.,  
 2298 2021; Auger, Prandi, & Sallée, 2022) and Antarctic Slope Current (Moffat et al., 2008;  
 2299 A. F. Thompson et al., 2018; Hazel & Stewart, 2019; A. L. Stewart et al., 2019; A. F. Thomp-  
 2300 son et al., 2020; Si et al., 2021; Moorman et al., 2020; Beadling et al., 2022) is poor, due  
 2301 to the lack of observations at the Antarctic margin (especially in the winter months) and  
 2302 the complex interplay of changes in wind stress, sea ice cover, tides and freshwater input  
 2303 expected to influence the dynamics. Therefore, conclusions cannot be drawn about trends  
 2304 in these dynamical components.

## 2305 6.2 Cryosphere

2306 There are strong regional variations in ice shelf trends. The mass balance of small- to  
 2307 medium-size, warm-water cavities fringing West Antarctica and certain parts of East Antarc-  
 2308 tica, such as Getz, Totten and Pine Island, are dominated by basal mass loss (Depoorter  
 2309 et al., 2013; Rignot et al., 2013), such that they produce a substantial proportion of net  
 2310 ice-shelf basal meltwater despite only occupying a relatively small fraction of the total ice-  
 2311 shelf area (Rignot et al., 2013; Adusumilli et al., 2020). In contrast, giant, cold-cavity  
 2312 ice shelves, such as the Ross and Filchner-Ronne, are dominated by the cycle of ice-front  
 2313 advance and calving, with high basal melt rates confined to the ice fronts and grounding  
 2314 lines (Rignot et al., 2013). Overall, shelf-front processes are the strongest drivers of mass  
 2315 balance for most ice shelves (Depoorter et al., 2013; Greene et al., 2022), although thinning  
 2316 has had a greater impact on the buttressing effect (Greene et al., 2022). Based on current  
 2317 trends, certain ice shelves will lose substantial proportions of their volumes by the end of the  
 2318 twenty-first century (Paolo et al., 2015). Under high emissions pathways for future warming  
 2319 (RCP8.5), greatly enhanced ice shelf surface melt is predicted, such that several ice shelves  
 2320 will experience surface melt intensities comparable or greater than those experienced by  
 2321 Antarctic Peninsula ice shelves prior to disintegration (Trusel et al., 2015; de Conto et al.,  
 2322 2021). This may be exacerbated by loss or reduction of a sea ice barrier to the open ocean,  
 2323 which is already a trend for West Antarctic ice shelves (Reid & Massom, 2022; Teder et al.,  
 2324 2022). However, there are large uncertainties in model projections of ice shelf loss relating  
 2325 to feedbacks initiated by warming temperatures, particularly dynamic instabilities (such as  
 2326 sudden disintegration and the marine ice cliff instability), and, hence, low confidence in the  
 2327 future ice shelf trends (Fox-Kemper et al., 2021).

2328 Despite the warming atmosphere, the annual maximum Antarctic sea ice extent had  
 2329 a positive, albeit weak, trend of  $13,800 \text{ km}^2 \text{ yr}^{-1}$  from the beginning of satellite records in  
 2330 1979 until the mid 2010s (J. Liu et al., 2023). A record maximum of 20.11 million  $\text{km}^2$  was  
 2331 reached in September 2014 (NISDC, 2023). The phenomenon of increasing Antarctic winter  
 2332 sea-ice extent during an epoch of global warming is known as the “Antarctic paradox”

2333 (J. King, 2014). Dramatic Antarctic sea ice losses during both winters and summers came  
2334 shortly after the 2014 record maximum sea ice extent (Turner et al., 2022). The losses  
2335 culminated in a record low of 18.4 million km<sup>2</sup> in annual maximum sea ice extent on 31st  
2336 August 2016 (NISDC, 2023), and several consecutive records of minimum ice extent in  
2337 following years, including the lowest ever recorded Antarctic sea ice extent of 1.8 million km<sup>2</sup>  
2338 on 21st February 2023 (NISDC, 2023). These recent extremes in Antarctic sea ice match  
2339 a significant increase in variability from about 2007 onwards, with evidence they are linked  
2340 to changes in the balance of sea ice trends across different Antarctic regions (Purich &  
2341 Doddridge, 2023; Hobbs et al., 2024). A number of studies are currently underway to assess  
2342 the attribution of atmospheric versus oceanic forcing in driving the record minima (summer  
2343 2016–2017, February 2022 and February 2023; Schroeter et al., 2023; L. Zhang et al., 2022).  
2344 Due to the extreme lows in Antarctic sea ice cover in recent years, there is currently no  
2345 statistically significant net long-term trend in Antarctic sea-ice extent (Fogt et al., 2022;  
2346 J. Liu et al., 2023).

### 2347 6.3 Turbulence

2348 Since the early 1990s there has been an increase in the mesoscale turbulence field  
2349 in the Southern Ocean (Hogg et al., 2015; Martínez-Moreno et al., 2021). This has been  
2350 attributed, in part, to strengthening westerly winds (N. C. Swart et al., 2015). However, the  
2351 extent to which the mesoscale turbulence field can modulate the Southern Ocean response  
2352 to strengthening winds remains uncertain. Some studies find that the time-mean flow of the  
2353 Antarctic Circumpolar Current is at most weakly sensitive to the changes in wind stress,  
2354 with the wind instead acting to energise the mesoscale turbulence field (e.g., Munday et al.,  
2355 2013; Constantinou & Hogg, 2019). However, recent work using altimeter measurements  
2356 and a reanalysis product has found that increasing wind stress does not increase eddy  
2357 kinetic energy across the Southern Ocean (excepting one specific region near the Campbell  
2358 Plateau; Y. Zhang et al., 2021). A more regional view of the mesoscale turbulence field shows  
2359 evidence for local variability, with hotspots of increased eddy kinetic energy in regions with  
2360 topographic features (A. F. Thompson & Naveira Garabato, 2014), for example downstream  
2361 of the Kerguelen Plateau (Rosso et al., 2015). Satellite altimetry has highlighted that these  
2362 eddy hotspot regions in the Southern Ocean are strengthening in eddy kinetic energy on  
2363 the order of 5% per decade (Martínez-Moreno et al., 2021). These eddy hotspot regions are  
2364 often crucial for the uptake of heat and carbon (Langlais et al., 2017) and, hence, the trends  
2365 in these regions will influence future climate. Disentangling other processes driving trends in  
2366 eddy kinetic energy is challenging. There is a large-scale warming trend in the most strongly  
2367 eddying regions in the vicinity of the circumpolar current (§ 6.1). The local gradients in  
2368 sea surface temperature are increasing (on average), which is associated with intensifying  
2369 eddy activity. Changes in the stratification may also indirectly affect mesoscale turbulence  
2370 via other processes such as modulating internal wave drag (§ 6.4), or influencing sea ice  
2371 formation and the production of deep water masses. Cryospheric trends will also affect the  
2372 mesoscale turbulence field. For example, increasing ice shelf melt rates lead to increasing  
2373 stratification, a transient increase in sea ice area and subsurface warming (Bronse laer et al.,  
2374 2018; Haumann et al., 2020; Q. Li et al., 2023), which impacts the mesoscale turbulence.

2375 Convection is strongly influenced by buoyancy forcing trends. The deepening of the  
2376 mixed layer and strengthening of the underlying stratification may already be an indication  
2377 of enhanced convective processes. Recent studies also suggest that the mixed layer is be-  
2378 coming fresher due to global warming, driven by changes in the precipitation-evaporation  
2379 balance, accelerated melting and calving of Antarctic glaciers, and a more positive phase  
2380 of the Southern Annular Mode (J. Zhang, 2007; de Lavergne et al., 2014). Freshening of  
2381 the surface ocean around Antarctica will stabilise the water column, reducing the ability of  
2382 the mixed layer to entrain underlying water, and making coastal and open ocean convection  
2383 events less frequent (de Lavergne et al., 2014; Moorman et al., 2020). There is growing  
2384 evidence that cryospheric trends have a significant impact on both open ocean and coastal  
2385 convection. Observations show that the calving of a large iceberg reduced the rate of sea

2386 ice production in a coastal polynya by blocking the flow of sea ice (Snow et al., 2018). This  
 2387 change in surface buoyancy conditions reduced convection and Dense Shelf Water produc-  
 2388 tion, which subsequently reduced the density and volume of the local Antarctic Bottom  
 2389 Water. Another cryospheric effect is the outflow of meltwater from neighbouring ice shelves  
 2390 into coastal polynya regions. It has been observed that this can reduce nearby convection  
 2391 and the rate of Antarctic Bottom Water formation (Silvano et al., 2018). If the trend of  
 2392 ice shelves is towards more calving and melting, then we might expect less convection and  
 2393 dense water formation on the Antarctic margins (Q. Li et al., 2023). However, other forcing  
 2394 changes, such as the strengthening Southern Annular Mode, may be responsible for opening  
 2395 up other polynyas and open ocean convection regions near Maud Rise (Jena et al., 2019;  
 2396 Kurtakoti et al., 2018). Therefore, it is challenging to predict the response of convection to  
 2397 climate trends.

2398 The trends in mixing are difficult and, in many cases, near impossible to assess. Issues  
 2399 with measuring mixing (§ 4.3) impede the direct tracking of mixing trends. However, some  
 2400 work can be done with identifying trends in sources of mixing. In the upper ocean, changes  
 2401 in wind stress and surface buoyancy forcing will likely induce modifications in the mixing.  
 2402 Indeed, changes in the mixed layer depth and stratification are already being noted, which  
 2403 indicate that mixing is already adjusting in these regions. Another example is that increasing  
 2404 wind stress can produce stronger Langmuir circulation and hence more mixing in the upper  
 2405 ocean. In the interior ocean, trends in internal waves and stratification are hypothesised to  
 2406 modify the mixing rates. In the deep ocean, trends in the abyssal water mass properties  
 2407 and stratification will influence the buoyancy transport in the bottom boundary layer and  
 2408 associated mixing. It is extremely difficult to determine even the direction of these trends,  
 2409 given the various competing influences.

## 2410 6.4 Gravity waves

2411 The trend of increasing wind speeds and storminess over the Southern Ocean is influ-  
 2412 encing both the surface and internal wave climates. The enhanced winds are expected to  
 2413 lead to an increase in generation of near-inertial internal waves along storm tracks, with  
 2414 energy fluxes increasing proportional to wind stresses ( $\sim 1\%$  per decade; Cuypers et al.,  
 2415 2013; Rimac et al., 2013). However, given the paucity of internal wave observations and  
 2416 the inability of current climate models to resolve internal waves, this predicted change has  
 2417 neither been directly observed nor modelled. By contrast, satellite observations show that  
 2418 surface wave amplitudes in the Southern Ocean are growing faster than in any other region  
 2419 (Hemer, 2010; Young et al., 2011; Young & Ribal, 2019; Meucci, Young, Aarnes, & Breivik,  
 2420 2020; Timmermans et al., 2020). Over the satellite era, the Southern Ocean has regions in  
 2421 which the mean significant wave height has a positive trend of up to 10 mm per year and in  
 2422 most regions extreme waves (defined as waves with heights above the 90th percentile) are  
 2423 also increasing at up to 10 mm per year (over 1985–2018; Young & Ribal, 2019). Twentieth-  
 2424 century climate model ensembles give century-long trends (1901–2010) of 10–20 mm per  
 2425 decade in mean significant wave height (Meucci, Young, Aarnes, & Breivik, 2020; Meucci et  
 2426 al., 2023). Under the RCP8.5 high-emission scenario (Van Vuuren et al., 2011), the largest  
 2427 ensembles to date predict that by the end of the century there will be up to 15% increases in  
 2428 significant wave heights (Morim et al., 2019), 5–10% in low-frequency extreme wave events  
 2429 (1 in 100-year significant wave height return period, i.e., waves with a 1% probability of oc-  
 2430 ccurring in a given year; Meucci, Young, Hemer, et al., 2020) and 50–100% in high-frequency  
 2431 events (return periods less than one year; Morim et al., 2021). These projected changes in  
 2432 the Southern Ocean surface wave climate extremes are consistent across different datasets  
 2433 and statistical approaches (Lobeto et al., 2021; O’Grady et al., 2021).

2434 In addition to winds, changes to the ocean stratification will play a major role in mod-  
 2435 ifying the future internal wave climate. Observations broadly show increasing stratification  
 2436 in the upper Southern Ocean and reducing stratification in the abyss, although these trends  
 2437 are highly variable (Armour et al., 2016; Yamaguchi & Suga, 2019; H. J. Zhang et al.,

2438 2021). Weakened abyssal (near-bottom) stratification will tend to suppress the production  
2439 of topographically-generated internal waves (i.e., internal tides and lee waves), for which  
2440 the energy flux scales with the buoyancy frequency above the topography (Bell, 1975). In  
2441 turn, reduced internal tide generation will tend to enhance the strength of the barotropic  
2442 tide, since it dampens a key energy sink (§ 5.2.2). The stratification changes will also cause  
2443 significant variation in coastal trapped waves, which are a key component of tides along the  
2444 Antarctic continental shelf (§ 5.3.3) and are known to be highly sensitive in both structure  
2445 and amplitude to stratification (Semper & Darelius, 2017). For example, Skardhamar et  
2446 al. (2015) model large changes in the energetics of diurnal coastal trapped waves due to  
2447 seasonal changes in stratification along continental slopes (albeit in the North Atlantic).  
2448 We expect similar responses at longer time scales in the Southern Ocean, as stratification  
2449 evolves due to anthropogenic forcing.

2450 The future internal wave and tide climate in the Southern Ocean will also be modulated  
2451 by trends in the other components of the dynamical system: circulation, turbulence and  
2452 the cryosphere. For example, changes in the Antarctic Slope Current (§ 6.1) will modify  
2453 the strength and structure of coastal trapped waves (Skardhamar et al., 2015; Semper &  
2454 Darelius, 2017), while increases in bottom flow speeds due to mesoscale eddies (Martínez-  
2455 Moreno et al., 2021) and are expected to enhance internal lee wave generation. In terms  
2456 of cryospheric impacts, since ocean tides are resonant phenomena closely tied to the ocean  
2457 basin geometry, tidal elevations and currents are sensitive to changes in ice shelf thickness  
2458 and extent (Rosier et al., 2014). Changes to tides are largest near the locations where the  
2459 ice shelves change but can also exhibit non-negligible far-field effects over time (Rosier et  
2460 al., 2014; Padman et al., 2018). However, due to the resonant nature of the tides, the exact  
2461 changes are challenging to predict. Lastly, we expect decreasing sea ice cover and increasing  
2462 open water conditions to lead to increased internal wave energy, but to date all studies  
2463 of this effect have been focused in the Arctic (Cole et al., 2014, 2018; Fine & Cole, 2022;  
2464 Martini et al., 2014; Dosser & Rainville, 2016).

## 2465 7 Research priorities to close the loops on Southern Ocean dynamics

2466 Many key research questions remain regarding interactions between the different com-  
 2467 ponents of the Southern Ocean dynamic system, and how their current trends (§6) will  
 2468 affect the interactions. The knowledge gaps compromise our ability to represent the South-  
 2469 ern Ocean in global models accurately and, hence, make well informed projections of future  
 2470 climate change and sea level rise. Indeed, over half the uncertainty in projections of global  
 2471 mean sea level is due to Antarctic Ice Sheet melting (Kopp et al., 2014). Reducing this  
 2472 uncertainty requires advances on multiple fronts due to the range of processes that influ-  
 2473 ence the melt rate (Cook et al., 2023). Necessary advances include predicting trends in  
 2474 the large-scale circulation and temperature of the Southern Ocean beyond the continental  
 2475 shelf, understanding the transport mechanisms that flux heat onto the shelf and into the  
 2476 ice shelf cavities, and developing accurate parameterisations of the fine-scale convection and  
 2477 turbulence that melts the ice shelves. Similarly, a key contributor to uncertainty in global  
 2478 mean air temperatures on long timescales is the rate of heat storage in the abyssal ocean  
 2479 (Abraham et al., 2013). While most anthropogenic heat is currently stored in the upper  
 2480 ocean (Levitus et al., 2012), which overturns faster, the abyssal ocean is playing an increas-  
 2481 ing role and will be crucial to the long-timescale evolution of climate change. But it remains  
 2482 an open question whether this abyssal overturning will increase or decrease under climate  
 2483 change (§6.1). The sign and magnitude of the trend is influenced by a host of processes  
 2484 including the poorly understood dynamics of the Ross and Weddell gyres, changes in sea  
 2485 ice cover and brine rejection, the small-scale convection that leads to dense shelf water, and  
 2486 the unknown distribution and magnitude of mixing in the abyssal Southern Ocean.

2487 The overarching research priority is improving our ability to model the Southern Ocean  
 2488 system and its response to anthropogenic forcing. This requires a multi-disciplinary com-  
 2489 munity effort, involving researchers across the different components of Southern Ocean dy-  
 2490 namics, and spanning advances in theoretical understanding of individual processes, tech-  
 2491 nological developments to improve observations, novel data analysis techniques, innovative  
 2492 numerical methods, and, finally, putting these components together to develop the global  
 2493 ocean–sea-ice models that are used in climate and sea level projections. We now describe  
 2494 the specific priorities that feed into addressing the uncertainties identified above, which we  
 2495 broadly divide in process-based models (§7.1), observations (§7.2), and regional and global  
 2496 models (§7.3).

### 2497 7.1 Process-based models

2498 In recent years, process-based numerical models have proved key quantifying the role  
 2499 of lee waves in Southern Ocean abyssal mixing (e.g., Nikurashin & Ferrari, 2011, 2013), the  
 2500 dynamics of eddy hotspots and upwelling (Barthel et al., 2022), polynya convection (Sohail  
 2501 et al., 2020), abyssal upwelling along topography (Drake et al., 2022), eddy saturation  
 2502 (Constantinou, 2018; Constantinou & Hogg, 2019), Antarctic Slope Current dynamics (Ong  
 2503 et al., 2023) and more. Future priorities include investigating convection in ice shelf cavities,  
 2504 internal-wave–eddy interactions and mixing, and surface wave–sea ice interactions in the  
 2505 marginal ice zone. All of these processes currently lack a sufficiently complete theoretical  
 2506 description to permit their integration into large-scale models. Given the crucial role of these  
 2507 processes in heat and carbon uptake (mixing), sea ice formation (surface waves), ice sheet  
 2508 stability (cavity circulation), and ocean circulation (internal-wave eddy interactions), their  
 2509 parameterisation in global models is expected to have a significant impact on the resolved  
 2510 model state. In addition, while the inference of mixing made in the past from finescale  
 2511 parameterisations (§4.3) applied to observations is immensely valuable, key questions remain  
 2512 about the assumptions involved (Bluteau et al., 2013; Polzin, Naveira Garabato, Huussen,  
 2513 et al., 2014; Mashayek, Salehipour, et al., 2017; Gregg et al., 2018; Ijichi et al., 2020). These  
 2514 assumptions can be queried using idealised process-based models, and the resulting theory  
 2515 applied to improve the interpretation of extant and future observations.

Laboratory experiments have also played a major role in developing our understanding of key Southern Ocean processes, such as convection (e.g., [Vreugdenhil et al., 2017](#); [Gayen & Griffiths, 2022](#)), wave breaking and air–sea exchange (e.g., [Melville, 1996](#); [Mayer et al., 2020](#)), jet dynamics (e.g., [Von Larcher & Williams, 2014](#); [C. A. Smith et al., 2014](#)), gravity currents (e.g., [Griffiths, 1986](#)), mixing and internal waves (e.g., [Dossmann et al., 2016](#); [Tan et al., 2022](#)), and ice–ocean interactions (e.g., [Aussillous et al., 2006](#); [McCutchan & Johnson, 2022](#)). Laboratory modelling has become less common in recent years, largely due to the relative cheapness and adaptability of numerical modelling. However, laboratory experiments remain a crucial tool in understanding many (especially multi-phase) systems where the governing dynamical or thermodynamical equations and/or boundary conditions are not necessarily known (e.g., sea ice, complex glacial topologies, sediment-laden plumes, air–sea gas exchange). In particular, experiments of melting ice faces (reviewed by [McCutchan & Johnson, 2022](#)) form the basis for our current glacial melt-rate parameterisations which are used to predict future sea level, but recent comparisons ([Malyarenko et al., 2020](#); [Rosevear, Galton-Fenzi, & Stevens, 2022](#)) show that more studies are needed to examine different regimes (such as melting under the influence of tides; [Richter et al., 2022](#)). Other key next steps are the identification of thresholds between melting regimes and the development of parameterisations based on properties resolved in global models. Similarly, it is becoming vital that we better understand how the thermal and optical properties of sea ice (e.g., albedo, thermal conductivity, brine content; §3.2.3; [Perovich, 1996](#); [Light et al., 2003](#); [Pringle et al., 2007](#)) may change in the future as the climate warms, so that these effects can be included in global ocean–sea-ice models. As such, new facilities are being set up to study the thermodynamics of sea ice (e.g., [M. Thomas et al., 2021](#); [Hall et al., 2023](#)) under carefully controlled laboratory conditions. Such investigations are likely to be critical in improving the accuracy of ocean–sea ice model projections of future climate scenarios by ensuring such models are not incorrectly tuned to only describe present climate conditions.

## 7.2 Observations

Satellites provide continuous observations in time with near complete spatial coverage of the Southern Ocean surface, allowing measurement of, e.g., sea ice extent, ice sheet mass loss, surface wave fields, geostrophic eddies and currents, and ocean tides. New satellite missions now underway, e.g., Surface Water and Ocean Topography (SWOT; [Morrow et al., 2019](#)) and, Surface Wave Investigation Measurements (SWIM; [Aouf et al., 2020](#)), promise unprecedented spatial resolution. This should improve our understanding of the small eddies on the Antarctic continental shelf that are key to heat transport, and short-wave components of the surface wave field that are characteristic of the long-fetch conditions of the Southern Ocean. Such observations will be used directly in data assimilating models, and in the testing of theories and parameterisations for these small-scale processes.

In situ observations are vital for groundtruthing satellite observations and to understand processes occurring below the sea surface, which are invisible to satellites. Ship-based observations in the Southern Ocean are expensive and strongly biased towards more amenable summertime conditions, and easier to access regions ([Newman et al., 2019](#)). As such, we lack sufficient observations in many environments, such as beneath sea ice cover and in ice shelf cavities, and during rough weather conditions, which are crucial for determining ocean mixing, ice sheet melt rates and dense water formation. However, new platforms are coming online that are starting to fill some of these gaps. For example, deep Argo and other floats are now available that profile year-round and under sea ice, which should greatly expand data coverage in the far Southern Ocean ([Johnson et al., 2022](#); [van Wijk et al., 2022](#)). In addition, creative solutions such as animal-borne data acquisition are becoming more widespread ([Roquet et al., 2014](#); [Foppert et al., 2019](#)). Through-ice moorings are also providing valuable insights into hydrography, currents and turbulence (e.g., [Arzeno et al., 2014](#); [Davis & Nicholls, 2019](#); [Stevens et al., 2020](#); [Hattermann et al., 2021](#); [Herraiz-Borreguero et al., 2013](#)), and some measurements are now being obtained by autonomous underwater vehicles including submarines and gliders (e.g., [Nicholls et al.,](#)

2569 2006; Gwyther et al., 2020; Schmidt et al., 2023b). In addition, advances in surface radar  
2570 enable highly resolved (in space and time) measurements of the ice shelf base (Vaňková et  
2571 al., 2021) that are sufficiently accurate to identify tidal modulation of melt rates (Sun et al.,  
2572 2019). In terms of ocean mixing, the development of microstructure profiling Argo floats  
2573 (Roemmich et al., 2019) and gliders (Wolk et al., 2009) is a particularly enticing possibility.  
2574 Current and future trends in mixing intensity, potentially associated with trends in winds  
2575 and eddy kinetic energy (e.g. Sheen et al., 2014; Whalen et al., 2018; Martínez-Moreno et  
2576 al., 2021), remain open questions, which more observations with such platforms can help to  
2577 constrain. There remains an urgent need to prioritise longer term continuous and sustained  
2578 in situ measurements to permit the detection and analysis of long-term trends and seasonal  
2579 variability. For example, a Southern Ocean analogue of the North Atlantic RAPID array  
2580 (Cunningham et al., 2007) to monitor directly the large-scale circulation. Conceptually, the  
2581 simplest such array would be across Drake Passage to directly monitor the strength of the  
2582 Antarctic Circumpolar Current. It would arguably be more valuable to have a small number  
2583 of permanent arrays in the regions where Dense Shelf Water cascades off the continental  
2584 shelf to form Antarctic Bottom Water. Sustained direct measurements of this volume flux  
2585 (and the water mass properties) would greatly assist in our understanding of changes in the  
2586 abyssal ocean and provide early warning of future climate impacts.

2587 It is also a priority to make better use of the observations we already have, both  
2588 in terms of science (e.g., developing novel analysis methodologies) and data management.  
2589 On the science side, efforts are underway to develop novel methods of extracting Southern  
2590 Ocean bottom pressures and abyssal circulation from gravimetric satellite observations (e.g.,  
2591 GRACE; Wouters et al., 2014), an approach which has proven successful in the North  
2592 Atlantic Ocean (Landerer et al., 2015). Significant work is also being done to measure the  
2593 Southern Ocean internal tide field and associated mixing from existing satellite altimeter  
2594 data (Z. Zhao et al., 2018), including addressing the challenge of wave dephasing due to the  
2595 strong Southern Ocean eddy field using machine learning methods (H. Wang et al., 2022;  
2596 Egbert & Erofeeva, 2002).

2597 In terms of data curation, it is essential that all data generated by the Southern Ocean  
2598 community is managed in accordance with the FAIR data principle; that is, data should  
2599 be findable, accessible, interoperable and reusable (Wilkinson et al., 2016). Genuine ac-  
2600 cordance with this principle is essential for the community to gain maximum benefit from  
2601 new and existing Southern Ocean data, and ensure cost-effectiveness for funding agencies.  
2602 Community data collation efforts such as the Southern Ocean Observing System (SOOS;  
2603 Newman et al., 2019) and related projects play a key role in this effort, and should be further  
2604 expanded.

### 2605 7.3 Regional and global models

2606 Numerical ocean and climate models are our primary tool for future climate projection  
2607 and operational ocean forecasting. These models are inevitably limited by their finite spatial  
2608 resolution, with typical grid sizes of  $1^\circ$  in current generation global climate models (e.g.,  
2609 CMIP6; Roberts et al., 2020) and up to  $1/12^\circ$  in current global ocean-only models (e.g.,  
2610 Kiss et al., 2020) and ocean state estimates (e.g., Lellouche et al., 2018). Processes smaller  
2611 than the grid scale must be parameterised in such models, i.e., a mathematical model for the  
2612 process must be formulated, calibrated (e.g., with observations and process-based models)  
2613 and implemented (H. T. Hewitt et al., 2020). As outlined in this article, many of these  
2614 unresolved processes are crucial to the climate state (e.g., diapycnal mixing, deep convection,  
2615 eddies) and yet many are still not sufficiently well understood. To some extent, these  
2616 challenges are resolved by running ever-higher resolution models as computational power  
2617 increases, avoiding the need for parameterisation. For example, ocean model grids finer  
2618 than 1 km are needed to resolve eddies and their associated heat transport on the Antarctic  
2619 continental shelf (Hallberg, 2013; A. L. Stewart & Thompson, 2015) and such resolutions  
2620 are now feasible for very short global ocean simulations (Rocha et al., 2016; A. L. Stewart et

2621 al., 2018). Even if model speedups due to using graphical processing units (GPUs) render  
2622 1 km-resolution simulations close to routine (e.g., Oceananigans.jl model; [Ramadhan et al.,](#)  
2623 [2020](#)), processes such as diapycnal mixing will still not be resolved and there remains a need  
2624 to parameterise other larger-scale processes for longer duration simulations.

2625 As such, there is an urgent need for improved parameterisations of a number of key  
2626 processes in large-scale ocean and climate models, including mixing ([Melet et al., 2015](#)),  
2627 eddies ([H. T. Hewitt et al., 2020](#)), convection ([Sohail et al., 2020](#)), ice shelf melt rates  
2628 (discussed above), internal wave–eddy interactions and momentum transfer ([Shakespeare &](#)  
2629 [Hogg, 2019](#)), surface wave–sea ice interactions ([Bennetts, Bitz, et al., 2022a](#)), and surface  
2630 and bottom submesoscales ([Gula et al., 2022](#)). Of these priorities, the representation of  
2631 diapycnal mixing is recognised as particularly vital as it controls the strength and variability  
2632 of the overturning circulation realised in such models ([Melet et al., 2015](#)). While static maps  
2633 of mixing have been developed ([de Lavergne et al., 2020](#)), and parameterisations of some  
2634 specific mixing processes have been implemented in global models (e.g., lee waves; [Stanley](#)  
2635 [& Saenko, 2014](#)), development of a dynamically evolving representation of diapycnal mixing  
2636 is a key priority. In developing such parameterisations, care should be taken to account  
2637 for the unique dynamics of the Southern Ocean (e.g., high-latitude wave dynamics § 5.3.3)  
2638 that lead to different mixing properties. Due to the changing climate, it is also essential  
2639 that any parameterisation is physically based, and includes all relevant coupling with other  
2640 processes. For example, empirical parameterisations based on present-day observations may  
2641 fail in future ocean states, which will exhibit different stratification, mean currents and basin  
2642 geometry (due to ice shelf and sea level changes).

2643 It is vital that all parameterisations are “scale-aware” ([Zanna et al., 2017](#); [H. T. Hewitt](#)  
2644 [et al., 2020](#)), i.e., they adapt to the model resolution, so as to avoid both parameterising and  
2645 resolving the same process, and also to avoid the parameterisation negatively impacting the  
2646 resolved phenomena. The lack of scale-awareness is a well-known problem with the widely  
2647 used [Gent and McWilliams \(1990\)](#) mesoscale eddy parameterisation at intermediate “eddy-  
2648 permitting” resolutions ([Hallberg, 2013](#); [Jansen et al., 2019](#)). While largely abandoned at  
2649 the highest model resolutions, mesoscale eddy parameterisation remains important for lower  
2650 resolution ocean and climate models, and the [Gent and McWilliams \(1990\)](#) parameterisation  
2651 is arguably insufficient ([H. T. Hewitt et al., 2020](#)). To address such challenges, there is a  
2652 recent move towards machine learning approaches to parameterise eddies ([Bolton & Zanna,](#)  
2653 [2019](#); [Zanna & Bolton, 2020, 2021](#); [C. Zhang et al., 2023](#)) as an alternative to simple  
2654 mathematical models. The concept of these approaches is for the algorithm to learn the  
2655 governing physics of mesoscale eddies from eddy-resolving ocean models, with the resulting  
2656 formulae then applied in lower resolution ocean and climate models. Such novel methods  
2657 (although not without computational challenges; e.g., [C. Zhang et al., 2023](#)) present exciting  
2658 possibilities and may be generalisable to other physical phenomena.

2659 As noted above, the ocean state in large-scale models is highly sensitive to mixing. As  
2660 a result, elimination of unintended and spurious “numerical mixing” is of equal importance  
2661 to the accurate representation of physical mixing. Numerical mixing occurs due to the dis-  
2662 crete representation of smoothly varying tracers, such as temperature and salinity, which are  
2663 mapped onto gridpoints at each model timestep. Discrete mapping causes an unintended re-  
2664 distribution of tracer between adjoining grid cells (mixing), e.g., as the water column sloshes  
2665 up and down due to the passage of an eddy or wave ([Petersen et al., 2015](#); [A. H. Gibson et](#)  
2666 [al., 2017](#); [Megann et al., 2022](#)). Numerical mixing is difficult to quantify in complex models,  
2667 but assessments that do exist suggest it can be significant, including in the eddying regions  
2668 of the Southern Ocean ([Holmes et al., 2021](#)). This problem is important for the correct  
2669 representation of Antarctic Bottom Water and the abyssal overturning circulation in the  
2670 Southern Ocean. The amount of numerical mixing is closely tied to the vertical coordinates  
2671 used in large-scale models and significant resources at major modelling centres are being  
2672 devoted to determining an optimal vertical coordinate (e.g., [A. Gibson, 2019](#); [Klingbeil et](#)

2673 al., 2019; Griffies et al., 2020; Wise et al., 2022). It is anticipated that these efforts will lead  
2674 to increased model accuracy without the significantly increased computational expense.

2675 A further priority in large-scale modelling is the incorporation of additional missing  
2676 components of the Earth system. This includes the incorporation of ice shelf cavities and  
2677 iceberg melt into ocean models, and the coupling of ice-sheet models with their ocean-sea  
2678 ice counterparts (e.g., Favier et al., 2019; Gladstone et al., 2021; Kreuzer et al., 2021).  
2679 Both of these efforts are likely to prove crucial to the accurate projection of future melt  
2680 rates, but come with substantial computational challenges (Mathiot et al., 2017). Another  
2681 missing feature in most ocean and climate models is an explicit representation of the ocean  
2682 tides (Richter et al., 2022). Explicit inclusion of tidal currents in models, including baro-  
2683 clinic tides, would improve representation of benthic, mid-water and ice-base mixing, and  
2684 the generation of rectified flows that help ventilate cavities (Makinson & Nicholls, 1999).  
2685 However, inclusion of tides in a global model is not as simple as turning on the gravitational  
2686 forcing, since the amplitude of tides are set by a balance between the forcing and the drag  
2687 at the seafloor, some of which occurs at unresolved scales (Arbic et al., 2018). Therefore,  
2688 the inclusion of tides requires the further development and co-implementation of additional  
2689 parameterisations, supported by observations and process-based models.

2690 **8 Closing remarks**

2691 In many respects, the Southern Ocean is the final frontier of ocean science. It is a vast,  
2692 poorly observed, inhospitable and almost untouched region that has fascinated humankind  
2693 since the discovery of Antarctica in the 1820s. Scientific interest in the Southern Ocean  
2694 has grown rapidly in recent times, along with understanding of the control Southern Ocean  
2695 dynamics exert on global climate and climate change. However, progress has sometimes  
2696 been stymied by a lack of effective communication between scientists in different disci-  
2697 plines and using different methodologies. This holistic review of Southern Ocean dynamics  
2698 has sought to provide a common language and knowledge-base across the Southern Ocean  
2699 physical science community to facilitate future knowledge-sharing and collaboration. Such  
2700 collaboration is critical to address the key scientific priorities identified above that span the  
2701 disciplines of mathematics, fluid mechanics, software engineering, glaciology and oceanogra-  
2702 phy, and methodologies as diverse as laboratory experiments of individual processes through  
2703 to numerical modelling of the entire Southern Ocean system. All of these disciplines and  
2704 methodologies — and many more — have a crucial role to play in accelerating our under-  
2705 standing of Southern Ocean dynamics in the years ahead, and thereby improving our ability  
2706 to predict ocean and climate change. This outcome is critical for the global community, and  
2707 indeed forms one of the goals of the United Nations Decade of Ocean Science 2021–2030.  
2708 Facilitated by this review, we encourage the entire Southern Ocean community to come  
2709 together to support this objective.

2710 **Open Research**

2711 No new data was used in this article. All new figures appearing in this review were  
2712 made using publicly available data as cited in the relevant caption.

2713 **Acknowledgments**

2714 We thank the three anonymous referees and the handling editor for their insightful comments  
2715 on the article.

2716 We acknowledge the receipt of the Elizabeth and Frederick White Research Conference  
2717 Award from the Australian Academy of Science, which funded the initial meeting that led  
2718 to this review.

2719 The Australian Research Council supported the authors via its various grant schemes  
2720 (Grant numbers: FL150100090; DE170100184; DP190100494; DP190101173; FT180100037;  
2721 FT190100404; FT190100413; DP200102828; LP200100406; SR200100008; DE21010004; DE220101027;  
2722 DP230102994).

2723 LGB acknowledges support from the Australian Antarctic Science Program (AAS4528).  
2724 GJS acknowledges support from the Banting Postdoctoral Fellowship through funding (180031).  
2725 FM acknowledges support by the Marsden Fund (grant numbers 18-UOO-216 and 20-UOO-  
2726 173) administered by Royal Society Te Apārangi. CS, AM, and FM acknowledge the Min-  
2727 istry of Business, Innovation and Employment Antarctic Science platform (ANTA1801).

2728 Figures were produced using computational resources and data hosted by the National  
2729 Computational Infrastructure, Canberra, Australia, a facility of the Australian Common-  
2730 wealth Government.

2731 Stacey McCormack produced the schematics. Anton Steketee and Sean Chau con-  
2732 tributed to Fig. ???. Alison Kohout provided data for Fig. ??. Claire Yung provided code  
2733 used to produce Fig. 13.

2734 In keeping with the spirit of this review, we also acknowledge the many collaborative  
2735 research consortia that supported this work including the: Consortium for Ocean Sea Ice  
2736 Modelling in Australia, ARC Centre of Excellence in Climate Extremes, ARC Centre for Ex-  
2737 cellence in Antarctic Science, Australian Antarctic Partnership Program, and the Australian  
2738 Government's National Environmental Science Program Climate Systems Hub.

2739

**References**

- 2740 Abernathey, R. P., Cerovecki, I., Holland, P. R., Newsom, E., Mazloff, M., & Talley, L. D.  
2741 (2016). Water-mass transformation by sea ice in the upper branch of the Southern  
2742 Ocean overturning. *Nat. Geosci.*, *9*(8), 596–601.
- 2743 Abernathey, R. P., Gnanadesikan, A., Pradal, M.-A., & Sundermeyer, M. A. (2022). Chapter  
2744 9 – isopycnal mixing. In M. P. Meredith & A. Naveira Garabato (Eds.), *Ocean mixing*  
2745 (pp. 215–256). Elsevier. doi: [10.1016/B978-0-12-821512-8.00016-5](https://doi.org/10.1016/B978-0-12-821512-8.00016-5)
- 2746 Abernathey, R. P., Marshall, J., & Ferreira, D. (2011). The dependence of Southern Ocean  
2747 meridional overturning on wind stress. *J. Phys. Oceanogr.*, *41*(12), 2261–2278.
- 2748 Abraham, J. P., Baringer, M., Bindoff, N. L., Boyer, T., Cheng, L., Church, J. A., ...  
2749 others (2013). A review of global ocean temperature observations: Implications for  
2750 ocean heat content estimates and climate change. *Rev. Geophys.*, *51*(3), 450–483.
- 2751 Ackley, S. F., & Sullivan, C. (1994). Physical controls on the development and characteristics  
2752 of antarctic sea ice biological communities—a review and synthesis. *Deep-Sea Res. I:*  
2753 *Oceanogr. Res. Pap.*, *41*(10), 1583–1604.
- 2754 Adams, J., & Buchwald, V. (1969). The generation of continental shelf waves. *J. Fluid*  
2755 *Mech.*, *35*(4), 815–826.
- 2756 Adams, K. A., Hosegood, P., Taylor, J. R., Sallée, J.-B., Bachman, S., Torres, R., & Stamper,  
2757 M. (2017). Frontal circulation and submesoscale variability during the formation  
2758 of a Southern Ocean mesoscale eddy. *J. Phys. Oceanogr.*, *47*(7), 1737–1753.
- 2759 Adcroft, A., Anderson, W., Balaji, V., Blanton, C., Bushuk, M., Dufour, C. O., ... others  
2760 (2019). The GFDL global ocean and sea ice model OM4. 0: Model description and  
2761 simulation features. *Journal of Advances in Modeling Earth Systems*, *11*(10), 3167–  
2762 3211.
- 2763 Adusumilli, S., Fricker, H. A., Medley, B., Padman, L., & Siegfried, M. R. (2020). Interan-  
2764 nual variations in meltwater input to the Southern Ocean from antarctic ice shelves.  
2765 *Nat. Geosci.*, *13*(9), 616–620.
- 2766 Akhoudas, C. H., Sallée, J.-B., Haumann, F. A., Meredith, M. P., Naveira Garabato, A. C.,  
2767 Reverdin, G., ... others (2021). Ventilation of the abyss in the atlantic sector of the  
2768 Southern Ocean. *Sci. Rep.*, *11*(1), 1–13.
- 2769 Alberello, A., Bennetts, L. G., Heil, P., Eayrs, C., Vichi, M., MacHutchon, K., ... Toffoli,  
2770 A. (2020). Drift of pancake ice floes in the winter antarctic marginal ice zone during  
2771 polar cyclones. *J. Geophys. Res. Oceans*, *125*(3), e2019JC015418.
- 2772 Alberello, A., Bennetts, L. G., Onorato, M., Vichi, M., MacHutchon, K., Eayrs, C., ...  
2773 Toffoli, A. (2022). Three-dimensional imaging of waves and floes in the marginal ice  
2774 zone during a cyclone. *Nat. Commun.*, *13*(1), 1–11.
- 2775 Alberello, A., Onorato, M., Bennetts, L. G., Vichi, M., Eayrs, C., MacHutchon, K., &  
2776 Toffoli, A. (2019). Pancake ice floe size distribution during the winter expansion of  
2777 the Antarctic marginal ice zone. *Cryosphere*, *13*(1), 41–48.
- 2778 Alberello, A., Onorato, M., Frascoli, F., & Toffoli, A. (2019). Observation of turbulence  
2779 and intermittency in wave-induced oscillatory flows. *Wave Motion*, *84*, 81–89.
- 2780 Albrecht, N., Vennell, R., Williams, M., Stevens, C. L., Langhorne, P., Leonard, G., &  
2781 Haskell, T. (2006). Observation of sub-inertial internal tides in McMurdo Sound,  
2782 Antarctica. *Geophys. Res. Lett.*, *33*(24).
- 2783 Alford, M. H. (2003). Improved global maps and 54-year history of wind-work on ocean  
2784 inertial motions. *Geophys. Res. Lett.*, *30*(8).
- 2785 Alford, M. H. (2020). Global calculations of local and remote near-inertial-wave dissipation.  
2786 *J. Phys. Oceanogr.*, *50*(11), 3157–3164.
- 2787 Alford, M. H., Cronin, M. F., & Klymak, J. M. (2012). Annual cycle and depth penetration  
2788 of wind-generated near-inertial internal waves at ocean station papa in the northeast  
2789 pacific. *J. Phys. Oceanogr.*, *42*(6), 889–909.
- 2790 Alford, M. H., MacKinnon, J. A., Simmons, H. L., & Nash, J. D. (2016). Near-inertial  
2791 internal gravity waves in the ocean. *Ann. Rev. Mar. Sci.*, *8*, 95–123.
- 2792 Alford, M. H., Shcherbina, A. Y., & Gregg, M. C. (2013). Observations of near-inertial  
2793 internal gravity waves radiating from a frontal jet. *J. Phys. Oceanogr.*, *43*(6), 1225–

- 1239.
- 2794 Alford, M. H., & Zhao, Z. (2007). Global patterns of low-mode internal-wave propagation.  
2795 part i: Energy and energy flux. *Journal of Physical Oceanography*, *37*(7), 1829–1848.  
2796
- 2797 Aluie, H., Hecht, M., & Vallis, G. K. (2018). Mapping the energy cascade in the North  
2798 Atlantic Ocean: The coarse-graining approach. *J. Phys. Oceanogr.*, *48*(2), 225–244.
- 2799 Amblas, D., & Dowdeswell, J. (2018). Physiographic influences on dense shelf-water cas-  
2800 cading down the Antarctic continental slope. *Earth-Science Reviews*, *185*, 887–900.
- 2801 Andrews, D. G., & McIntyre, M. E. (1978). Generalized Eliassen-Palm and Charney-Drazin  
2802 theorems for waves on axisymmetric mean flows in compressible atmospheres. *J. Atmos.*  
2803 *Sci.*, *35*(2), 175–185.
- 2804 Anselin, J., Reed, B. C., Jenkins, A., & Green, J. A. M. (2023). Ice shelf basal melt  
2805 sensitivity to tide-induced mixing based on the theory of subglacial plumes. *Journal of*  
2806 *Geophysical Research: Oceans*, *128*(4). doi: <https://doi.org/10.1029/2022JC019156>
- 2807 Ansong, J. K., Arbic, B. K., Buijsman, M. C., Richman, J. G., Shriver, J. F., & Wallcraft,  
2808 A. J. (2015). Indirect evidence for substantial damping of low-mode internal tides in  
2809 the open ocean. *J. Geophys. Res. Oceans*, *120*(9), 6057–6071.
- 2810 Aoki, S., Kobayashi, R., Rintoul, S. R., Tamura, T., & Kusahara, K. (2017). Changes  
2811 in water properties and flow regime on the continental shelf off the Adélie/George V  
2812 Land coast, East Antarctica, after glacier tongue calving. *J. Geophys. Res. Oceans*,  
2813 *122*(8), 6277–6294. doi: [10.1002/2017JC012925](https://doi.org/10.1002/2017JC012925)
- 2814 Aoki, S., Takahashi, T., Yamazaki, K., Hirano, D., Ono, K., Kusahara, K., ... Williams,  
2815 G. D. (2022). Warm surface waters increase antarctic ice shelf melt and delay dense  
2816 water formation. *Communications Earth & Environment*, *3*(1), 1–8.
- 2817 Aouf, L., Hauser, D., Chapron, B., Toffoli, A., Tourrain, C., & Peureux, C. (2020). New  
2818 directional wave satellite observations: Towards improved wave forecasts and climate  
2819 description in Southern Ocean. *Geophys. Res. Lett.*, e2020GL091187.
- 2820 Arbic, B. K., Alford, M. H., Ansong, J. K., Buijsman, M. C., Ciotti, R. B., Farrar, J. T., ...  
2821 others (2018). A primer on global internal tide and internal gravity wave continuum  
2822 modeling in HYCOM and MITgcm. *New frontiers in operational oceanography*.
- 2823 Arblaster, J. M., & Meehl, G. A. (2006). Contributions of external forcings to southern  
2824 annular mode trends. *J. Climate*, *19*(12), 2896–2905.
- 2825 Ardhuin, F., Otero, M., Merrifield, S., Grouazel, A., & Terrill, E. (2020). Ice breakup  
2826 controls dissipation of wind waves across Southern Ocean sea ice. *Geophys. Res. Lett.*,  
2827 *47*(13), e2020GL087699.
- 2828 Armitage, T. W. K., Kwok, R., Thompson, A. F., & Cunningham, G. (2018). Dynamic  
2829 topography and sea level anomalies of the Southern Ocean: Variability and telecon-  
2830 nections. *J. Geophys. Res. Oceans*, *123*(1), 613–630. doi: [10.1002/2017JC013534](https://doi.org/10.1002/2017JC013534)
- 2831 Armour, K. C., Marshall, J., Scott, J. R., Donohoe, A., & Newsom, E. R. (2016). Southern  
2832 Ocean warming delayed by circumpolar upwelling and equatorward transport. *Nat.*  
2833 *Geosci.*, *9*(7), 549–554.
- 2834 Årthun, M., Holland, P. R., Nicholls, K. W., & Feltham, D. L. (2013). Eddy-driven exchange  
2835 between the open ocean and a sub-ice shelf cavity. *J. Phys. Oceanogr.*, *43*(11), 2372–  
2836 2387.
- 2837 Arthur, J. F., Stokes, C. R., Jamieson, S. S., Miles, B. W., Carr, J. R., & Leeson, A. A.  
2838 (2021). The triggers of the disaggregation of Voyeykov Ice Shelf (2007), Wilkes Land,  
2839 East Antarctica, and its subsequent evolution. *J. Glaciol.*, *67*(265), 933–951.
- 2840 Arzeno, I. B., Beardsley, R. C., Limeburner, R., Owens, B., Padman, L., Springer, S. R.,  
2841 ... Williams, M. J. (2014). Ocean variability contributing to basal melt rate near the  
2842 ice front of Ross ice shelf, Antarctica. *J. Geophys. Res. Oceans*, *119*(7), 4214–4233.
- 2843 Auger, M., Prandi, P., & Sallée, J.-B. (2022). Southern ocean sea level anomaly in the  
2844 sea ice-covered sector from multimission satellite observations. *Scientific Data*, *9*(70),  
2845 1–10. doi: [10.1038/s41597-022-01166-z](https://doi.org/10.1038/s41597-022-01166-z)
- 2846 Auger, M., Sallée, J.-B., Prandi, P., & Naveira Garabato, A. C. (2022). Subpolar Southern  
2847 Ocean seasonal variability of the geostrophic circulation from multi-mission satellite  
2848 altimetry. *J. Geophys. Res. Oceans*, e2021JC018096.

- 2849 Aussillous, P., Sederman, A. J., Gladden, L. F., Huppert, H. E., & Worster, M. G. (2006).  
 2850 Magnetic resonance imaging of structure and convection in solidifying mushy layers.  
 2851 *J. Fluid Mech.*, *552*, 99–125.
- 2852 Babanin, A. V. (2006). On a wave-induced turbulence and a wave-mixed upper ocean layer.  
 2853 *Geophys. Res. Lett.*, *33*(20).
- 2854 Babanin, A. V., Chalikov, D., Young, I. R., & Savelyev, I. (2007). Predicting the breaking  
 2855 onset of surface water waves. *Geophys. Res. Lett.*, *34*(7).
- 2856 Bai, Y., Zhao, L., Xiao, J., & Lin, S. (2022). Contraction and warming of Antarctic bottom  
 2857 water in the Amundsen Sea. *Acta Oceanologica Sinica*, *41*(4), 68–79.
- 2858 Baker, L., & Mashayek, A. (2021). Surface reflection of bottom generated oceanic lee waves.  
 2859 *J. Fluid Mech.*, *924*.
- 2860 Balwada, D., Xie, J.-H., Marino, R., & Feraco, F. (2022). Direct observational evi-  
 2861 dence of an oceanic dual kinetic energy cascade and its seasonality. *arXiv preprint*  
 2862 *arXiv:2202.08637*. doi: [10.48550/arXiv.2202.08637](https://doi.org/10.48550/arXiv.2202.08637)
- 2863 Banwell, A. F., Willis, I. C., Macdonald, G. J., Goodsell, B., Mayer, D. P., Powell, A., &  
 2864 Macayeal, D. R. (2017). Calving and rifting on the mcmurdo ice shelf, Antarctica.  
 2865 *Ann. Glaciol.*, *58*(75pt1), 78–87.
- 2866 Barbariol, F., Benetazzo, A., Bertotti, L., Cavaleri, L., Durrant, T., McComb, P., & Sclavo,  
 2867 M. (2019). Large waves and drifting buoys in the Southern Ocean. *Ocean Engineering*,  
 2868 *172*, 817–828.
- 2869 Barbat, M. M., Rackow, T., Wesche, C., Hellmer, H. H., & Mata, M. M. (2021). Automated  
 2870 iceberg tracking with a machine learning approach applied to sar imagery: A Weddell  
 2871 Sea case study. *ISPRS Journal of Photogrammetry and Remote Sensing*, *172*, 189–  
 2872 206.
- 2873 Barkan, R., Winters, K., & Llewellyn Smith, S. (2015). Energy cascades and loss of balance  
 2874 in a reentrant channel forced by wind stress and buoyancy fluxes. *J. Phys. Oceanogr.*,  
 2875 *45*(1), 272–293.
- 2876 Barstow, S. F., Bidlot, J.-R., Caires, S., Donelan, M. A., Drennan, W. M., Dupuis, H.,  
 2877 ... others (2005). *Measuring and analysing the directional spectrum of ocean waves*.  
 2878 COST office.
- 2879 Barthel, A., Hogg, A. M., Waterman, S., & Keating, S. (2022). Baroclinic control of  
 2880 Southern Ocean eddy upwelling near topography. *Geophys. Res. Lett.*, *49*(7). doi:  
 2881 [10.1029/2021GL097491](https://doi.org/10.1029/2021GL097491)
- 2882 Bassis, J. N., Fricker, H. A., Coleman, R., & Minster, J.-B. (2008). An investigation into  
 2883 the forces that drive ice-shelf rift propagation on the amery ice shelf, east Antarctica.  
 2884 *J. Glaciol.*, *54*(184), 17–27.
- 2885 Beadling, R., Krasting, J., Griffies, S., Hurlin, W., Bronselaer, B., Russell, J., ... Win-  
 2886 ton, M. (2022). Importance of the Antarctic Slope Current in the Southern Ocean  
 2887 response to ice sheet melt and wind stress change. *J. Geophys. Res. Oceans*, *127*(5),  
 2888 e2021JC017608.
- 2889 Bebieva, Y., & Speer, K. (2019). The regulation of sea ice thickness by double-diffusive  
 2890 processes in the ross gyre. *J. Geophys. Res. Oceans*, *124*(10), 7068–7081. doi:  
 2891 [10.1029/2019JC015247](https://doi.org/10.1029/2019JC015247)
- 2892 Bebieva, Y., & Speer, K. (2021). Thermohaline suppression of upper circumpolar deep  
 2893 water eddies in the ross gyre. *Geophys. Res. Lett.*, *48*(18), e2021GL094476.
- 2894 Becker, J. J., & Sandwell, D. T. (2008). Global estimates of seafloor slope from single-beam  
 2895 ship soundings. *J. Geophys. Res. Oceans*, *113*(C5). doi: [10.1029/2006JC003879](https://doi.org/10.1029/2006JC003879)
- 2896 Begeman, C. B., Tulaczyk, S. M., Marsh, O. J., Mikucki, J. A., Stanton, T. P., Hodson,  
 2897 T. O., ... King, M. A. (2018). Ocean stratification and low melt rates at the Ross  
 2898 Ice Shelf grounding zone. *J. Geophys. Res. Oceans*, *123*(10), 7438–7452.
- 2899 Belcher, S. E., Grant, A. L. M., Hanley, K. E., Fox-Kemper, B., Van Roekel, L., Sul-  
 2900 livan, P. P., ... Polton, J. A. (2012). A global perspective on Langmuir tur-  
 2901 bulence in the ocean surface boundary layer. *Geophys. Res. Lett.*, *39*(18). doi:  
 2902 [10.1029/2012GL052932](https://doi.org/10.1029/2012GL052932)

- 2903 Bell, T. (1975). Topographically generated internal waves in the open ocean. *Journal of*  
 2904 *Geophysical Research*, *80*(3), 320–327.
- 2905 Benn, D. I., Warren, C. R., & Mottram, R. H. (2007). Calving processes and the dynamics  
 2906 of calving glaciers. *Earth-Science Reviews*, *82*(3-4), 143–179.
- 2907 Bennetts, L. G., Alberello, A., Meylan, M. H., Cavaliere, C., Babanin, A. V., & Toffoli, A.  
 2908 (2015). An idealised experimental model of ocean surface wave transmission by an ice  
 2909 floe. *Ocean Model.*, *96*, 85–92.
- 2910 Bennetts, L. G., Biggs, N. R. T., & Porter, D. (2007). A multi-mode approximation to wave  
 2911 scattering by ice sheets of varying thickness. *J. Fluid Mech.*, *579*, 413–443.
- 2912 Bennetts, L. G., Bitz, C. M., Feltham, D. L., Kohout, A. L., & Meylan, M. H. (2022a).  
 2913 Marginal ice zone dynamics: future research perspectives and pathways. *Philosophical*  
 2914 *Transactions of the Royal Society A*, *380*(2235), 20210267.
- 2915 Bennetts, L. G., Bitz, C. M., Feltham, D. L., Kohout, A. L., & Meylan, M. H. (2022b).  
 2916 Theory, modelling and observations of marginal ice zone dynamics: multidisciplinary  
 2917 perspectives and outlooks. *Philos. Trans. Royal Soc. A*, *380*(2235), 20210265.
- 2918 Bennetts, L. G., Liang, J., & Pitt, J. P. A. (2022). Modelling ocean wave transfer to Ross  
 2919 Ice Shelf flexure. *Geophys. Res. Lett.*
- 2920 Bennetts, L. G., Peter, M. A., Squire, V., & Meylan, M. H. (2010). A three-dimensional  
 2921 model of wave attenuation in the marginal ice zone. *J. Geophys. Res. Oceans*,  
 2922 *115*(C12).
- 2923 Bennetts, L. G., & Squire, V. A. (2009). Wave scattering by multiple rows of circular ice  
 2924 floes. *J. Fluid Mech.*, *639*, 213–238.
- 2925 Bennetts, L. G., & Squire, V. A. (2012a). Model sensitivity analysis of scattering-induced  
 2926 attenuation of ice-coupled waves. *Ocean Model.*, *45*, 1–13.
- 2927 Bennetts, L. G., & Squire, V. A. (2012b). On the calculation of an attenuation coefficient  
 2928 for transects of ice-covered ocean. *Proc. R. Soc. A*, *468*(2137), 136–162.
- 2929 Bennetts, L. G., & Williams, T. D. (2015). Water wave transmission by an array of floating  
 2930 discs. *Proc. R. Soc. A*, *471*(2173), 20140698.
- 2931 Bhagtani, D., Hogg, A. M., Holmes, R. M., & Constantinou, N. C. (2023). Surface  
 2932 heating steers planetary-scale ocean circulation. *J. Phys. Oceanogr.*. (in review;  
 2933 arXiv:2301.11474) doi: [10.48550/arXiv.2301.11474](https://doi.org/10.48550/arXiv.2301.11474)
- 2934 Biddle, L. C., & Swart, S. (2020). The observed seasonal cycle of submesoscale processes  
 2935 in the Antarctic marginal ice zone. *J. Geophys. Res. Oceans*, *125*(6), e2019JC015587.  
 2936 doi: [10.1029/2019JC015587](https://doi.org/10.1029/2019JC015587)
- 2937 Bishop, S. P., Gent, P. R., Bryan, F. O., Thompson, A. F., Long, M. C., & Abernathey,  
 2938 R. P. (2016). Southern Ocean Overturning Compensation in an Eddy-Resolving  
 2939 Climate Simulation. *J. Phys. Oceanogr.*, *46*(5), 1575–1592.
- 2940 Bluteau, C., Jones, N., & Ivey, G. (2013). Turbulent mixing efficiency at an energetic ocean  
 2941 site. *J. Geophys. Res. Oceans*, *118*(9), 4662–4672.
- 2942 Boccaletti, G., Ferrari, R., & Fox-Kemper, B. (2007). Mixed layer instabilities and restrat-  
 2943 ification. *J. Phys. Oceanogr.*, *37*(9), 2228–2250.
- 2944 Boisvert, L., Vihma, T., & Shie, C.-L. (2020). Evaporation from the Southern Ocean  
 2945 estimated on the basis of airs satellite data. *J. Geophys. Res. Atmos.*, *125*(1),  
 2946 e2019JD030845.
- 2947 Boland, E. J. D., Thompson, A. F., Shuckburgh, E., & Haynes, P. H. (2012). The formation  
 2948 of nonzonal jets over sloped topography. *J. Phys. Oceanogr.*, *42*(10), 1635–1651.
- 2949 Bolton, T., & Zanna, L. (2019). Applications of deep learning to ocean data inference and  
 2950 subgrid parameterization. *J. Adv. Model. Earth Syst.*, *11*(1), 376–399.
- 2951 Booker, J. R., & Bretherton, F. P. (1967). The critical layer for internal gravity waves in a  
 2952 shear flow. *J. Fluid Mech.*, *27*(3), 513–539. doi: [10.1017/S0022112067000515](https://doi.org/10.1017/S0022112067000515)
- 2953 Bouhier, N., Tournadre, J., Rémy, F., & Gourves-Cousin, R. (2018). Melting and fragmen-  
 2954 tation laws from the evolution of two large Southern Ocean icebergs estimated from  
 2955 satellite data. *Cryosphere*, *12*(7), 2267–2285.
- 2956 Bowen, M. M., Fernandez, D., Forcen-Vazquez, A., Gordon, A. L., Huber, B., Castagno, P.,  
 2957 & Falco, P. (2021). The role of tides in bottom water export from the western Ross

- 2958           Sea. *Sci. Rep.*, *11*, 2246.
- 2959   Bretherton, F. P. (1969). Momentum transport by gravity waves. *Q. J. R. Meteorol. Soc.*,  
2960           *95*(404), 213–243.
- 2961   Broadbridge, M. B., Naveira Garabato, A. C., & Nurser, A. J. G. (2016). Forcing of the  
2962           overturning circulation across a circumpolar channel by internal wave breaking. *J.*  
2963           *Geophys. Res.*, *121*(8), 5436–5451. doi: [10.1002/2015JC011597](https://doi.org/10.1002/2015JC011597)
- 2964   Bromirski, P. D., Sergienko, O. V., & MacAyeal, D. R. (2010). Transoceanic infragravity  
2965           waves impacting antarctic ice shelves. *Geophys. Res. Lett.*, *37*(2).
- 2966   Bronselaeer, B., Winton, M., Griffies, S. M., Hurlin, W. J., Rodgers, K. B., Sergienko, O. V.,  
2967           ... Russell, J. L. (2018). Change in future climate due to Antarctic meltwater. *Nature*.  
2968           doi: [10.1038/s41586-018-0712-z](https://doi.org/10.1038/s41586-018-0712-z)
- 2969   Brown, E. D., & Owens, W. B. (1981). Observations of the horizontal interactions between  
2970           the internal wave field and the mesoscale flow. *J. Phys. Oceanogr.*, *11*(11), 1474–1480.
- 2971   Brown, P. J., Jullion, L., Landschützer, P., Bakker, D. C., Naveira Garabato, A. C., Meredith,  
2972           M. P., ... others (2015). Carbon dynamics of the weddell gyre, Southern Ocean.  
2973           *Global Biogeochemical Cycles*, *29*(3), 288–306.
- 2974   Brunt, K. M., Okal, E. A., & MacAYEAL, D. R. (2011). Antarctic ice-shelf calving triggered  
2975           by the honshu (japan) earthquake and tsunami, march 2011. *J. Glaciol.*, *57*(205), 785–  
2976           788.
- 2977   Bryden, H. L., & Nurser, A. J. G. (2003). Effects of strait mixing on ocean  
2978           stratification. *J. Phys. Oceanogr.*, *33*(8), 1870–1872. doi: [10.1175/1520-  
2979           0485\(2003\)033<1870:EOSMOO>2.0.CO;2](https://doi.org/10.1175/1520-0485(2003)033<1870:EOSMOO>2.0.CO;2)
- 2980   Buhler, O., & McIntyre, M. E. (2005). Wave capture and wave-vortex duality. *J. Fluid*  
2981           *Mech.*, *534*, 67–95. doi: [10.1017/S0022112005004374](https://doi.org/10.1017/S0022112005004374)
- 2982   Buijsman, M. C., Arbic, B. K., Green, J., Helber, R. W., Richman, J. G., Shriver, J. F., ...  
2983           Wallcraft, A. (2015). Optimizing internal wave drag in a forward barotropic model  
2984           with semidiurnal tides. *Ocean Model.*, *85*, 42–55.
- 2985   Buongiorno Nardelli, B., Guinehut, S., Verbrugge, N., Cotroneo, Y., Zambianchi, E., &  
2986           Iudicone, D. (2017). Southern ocean mixed-layer seasonal and interannual variations  
2987           from combined satellite and in situ data. *J. Geophys. Res. Oceans*, *122*(12), 10042–  
2988           10060. doi: [10.1002/2017JC013314](https://doi.org/10.1002/2017JC013314)
- 2989   Burgard, C., Jourdain, N. C., Reese, R., Jenkins, A., & Mathiot, P. (2022). An assessment of  
2990           basal melt parameterisations for antarctic ice shelves. *Cryosphere*, *16*(12), 4931–4975.
- 2991   Callies, J. (2018). Restratification of abyssal mixing layers by submesoscale baroclinic  
2992           eddies. *J. Phys. Oceanogr.*, *48*(9), 1995–2010. doi: [10.1175/JPO-D-18-0082.1](https://doi.org/10.1175/JPO-D-18-0082.1)
- 2993   Campbell, E. C., Wilson, E. A., Moore, G., Riser, S. C., Brayton, C. E., Mazloff, M. R.,  
2994           & Talley, L. D. (2019). Antarctic offshore polynyas linked to southern hemisphere  
2995           climate anomalies. *Nature*, *570*(7761), 319–325. doi: [10.1038/s41586-019-1294-0](https://doi.org/10.1038/s41586-019-1294-0)
- 2996   Cathles IV, L., Okal, E. A., & MacAyeal, D. R. (2009). Seismic observations of sea swell  
2997           on the floating Ross ice shelf, Antarctica. *J. Geophys. Res. Earth Surf.*, *114*(F2).
- 2998   Ceroveck, I., & Mazloff, M. R. (2016). The spatiotemporal structure of diabatic processes  
2999           governing the evolution of subantarctic mode water in the Southern Ocean. *J. Phys.*  
3000           *Oceanogr.*, *46*(2), 683–710. doi: [10.1175/JPO-D-14-0243.1](https://doi.org/10.1175/JPO-D-14-0243.1)
- 3001   Chaigneau, A., Pizarro, O., & Rojas, W. (2008). Global climatology of near-inertial current  
3002           characteristics from lagrangian observations. *Geophys. Res. Lett.*, *35*(13).
- 3003   Chapman, C. C. (2017). New perspectives on frontal variability in the Southern Ocean. *J.*  
3004           *Phys. Oceanogr.*, *47*, 1151–1168. doi: [10.1175/jpo-d-16-0222.1](https://doi.org/10.1175/jpo-d-16-0222.1)
- 3005   Chapman, C. C., Hogg, A. M., Kiss, A. E., & Rintoul, S. R. (2015). The dynamics of  
3006           Southern Ocean storm tracks. *J. Phys. Oceanogr.*, *45*(3), 884–903.
- 3007   Chapman, C. C., Lea, M.-A., Meyer, A., Sallée, J.-B., & Hindell, M. (2020). Defining  
3008           Southern Ocean fronts and their influence on biological and physical processes in a  
3009           changing climate. *Nat. Clim. Chang.*, *10*, 209–219. doi: [10.1038/s41558-020-0705-4](https://doi.org/10.1038/s41558-020-0705-4)
- 3010   Chapman, C. C., & Morrow, R. (2014). Variability of Southern Ocean jets near topography.  
3011           *J. Phys. Oceanogr.*, *44*(2), 676–693.

- 3012 Chelton, D. B., Schlax, M. G., & Samelson, R. M. (2011). Global observations of nonlinear  
3013 mesoscale eddies. *Progress in Oceanography*, *91*, 167–216.
- 3014 Chelton, D. B., Schlax, M. G., Witter, D. L., & Richman, J. G. (1990). Geosat altimeter  
3015 observations of the surface circulation of the southern ocean. *Journal of Geophysical*  
3016 *Research: Oceans*, *95*(C10), 17877–17903.
- 3017 Chen, Z., Bromirski, P., Gerstoft, P., Stephen, R., Lee, W. S., Yun, S., . . . Nyblade, A.  
3018 (2019). Ross ice shelf icequakes associated with ocean gravity wave activity. *Geophys.*  
3019 *Res. Lett.*, *46*(15), 8893–8902.
- 3020 Chen, Z., Bromirski, P. D., Gerstoft, P., Stephen, R. A., Wiens, D. A., Aster, R. C., &  
3021 Nyblade, A. A. (2018). Ocean-excited plate waves in the Ross and Pine island glacier  
3022 ice shelves. *J. Glaciol.*, *64*(247), 730–744.
- 3023 Cheon, W. G., Cho, C.-B., Gordon, A. L., Kim, Y. H., & Park, Y.-G. (2018). The role  
3024 of oscillating southern hemisphere westerly winds: Southern Ocean coastal and open-  
3025 ocean polynyas. *J. Climate*, *31*(3), 1053–1073.
- 3026 Cheon, W. G., & Gordon, A. L. (2019). Open-ocean polynyas and deep convection in the  
3027 Southern Ocean. *Sci. Rep.*, *9*(1), 1–9. doi: [10.1038/s41598-019-43466-2](https://doi.org/10.1038/s41598-019-43466-2)
- 3028 Cheon, W. G., Lee, S., Gordon, A. L., Liu, Y., Cho, C., & Park, J. J. (2015). Replicating  
3029 the 1970s&apost; Weddell Polynya using a coupled ocean-sea ice model with reanalysis  
3030 surface flux fields. *Geophys. Res. Lett.*, *42*(13), 5411–5418. doi: [10.1002/2015gl064364](https://doi.org/10.1002/2015gl064364)
- 3031 Chiswell, S. M. (2003). Deep equatorward propagation of inertial oscillations. *Geophys.*  
3032 *Res. Lett.*, *30*(10). doi: [10.1029/2003GL017057](https://doi.org/10.1029/2003GL017057)
- 3033 Chouksey, M., Eden, C., & Brüggemann, N. (2018). Internal gravity wave emission in  
3034 different dynamical regimes. *J. Phys. Oceanogr.*, *48*(8), 1709–1730. doi: [10.1175/JPO-](https://doi.org/10.1175/JPO-D-17-0158.1)  
3035 [D-17-0158.1](https://doi.org/10.1175/JPO-D-17-0158.1)
- 3036 Cimoli, L., Caulfield, C.-c. P., Johnson, H. L., Marshall, D. P., Mashayek, A., Naveira Gara-  
3037 bato, A. C., & Vic, C. (2019). Sensitivity of Deep Ocean Mixing to Local Internal  
3038 Tide Breaking and Mixing Efficiency. *Geophys. Res. Lett.*, *46*(24), 14622–14633. doi:  
3039 [10.1029/2019GL085056](https://doi.org/10.1029/2019GL085056)
- 3040 Cisewski, B., Strass, V. H., & Leach, H. (2011). Circulation and transport of water masses  
3041 in the Lazarev sea, Antarctica, during summer and winter 2006. *Deep-Sea Res. I:*  
3042 *Oceanogr. Res. Pap.*, *58*(2), 186–199.
- 3043 Clément, L., McDonagh, E., Gregory, J., Wu, Q., Marzocchi, A., Zika, J., & Nurser, A.  
3044 (2022). Mechanisms of ocean heat uptake along and across isopycnals. *J. Climate*,  
3045 1–43.
- 3046 Cole, S. T., Timmermans, M.-L., Toole, J. M., Krishfield, R. A., & Thwaites, F. T. (2014).  
3047 Ekman veering, internal waves, and turbulence observed under Arctic sea ice. *J. Phys.*  
3048 *Oceanogr.*, *44*(5), 1306–1328. doi: [10.1175/JPO-D-12-0191.1](https://doi.org/10.1175/JPO-D-12-0191.1)
- 3049 Cole, S. T., Toole, J. M., Rainville, L., & Lee, C. M. (2018). Internal waves in the Arc-  
3050 tic: Influence of ice concentration, ice roughness, and surface layer stratification. *J.*  
3051 *Geophys. Res. Oceans*, *123*(8), 5571–5586. doi: [10.1029/2018JC014096](https://doi.org/10.1029/2018JC014096)
- 3052 Comiso, J. C., & Gordon, A. L. (1987). Recurring polynyas over the Cosmonaut  
3053 Sea and the Maud Rise. *J. Geophys. Res. Oceans*, *92*(C3), 2819–2833. doi:  
3054 [10.1029/jc092ic03p02819](https://doi.org/10.1029/jc092ic03p02819)
- 3055 Constantinou, N. C. (2018). A barotropic model of eddy saturation. *J. Phys. Oceanogr.*,  
3056 *48*(2), 397–411. doi: [10.1175/JPO-D-17-0182.1](https://doi.org/10.1175/JPO-D-17-0182.1)
- 3057 Constantinou, N. C., & Hogg, A. M. (2019). Eddy saturation of the Southern Ocean: A  
3058 baroclinic versus barotropic perspective. *Geophys. Res. Lett.*, *46*(21), 12202–12212.  
3059 doi: [10.1029/2019GL084117](https://doi.org/10.1029/2019GL084117)
- 3060 Constantinou, N. C., & Young, W. R. (2017). Beta-plane turbulence above monoscale  
3061 topography. *J. Fluid Mech.*, *827*, 415–447. doi: [10.1017/jfm.2017.482](https://doi.org/10.1017/jfm.2017.482)
- 3062 Cook, S., Nicholls, K. W., Vaňková, I., Thompson, S. S., & Galton-Fenzi, B. K. (2023).  
3063 Data initiatives for ocean-driven melt of Antarctic ice shelves. *Ann. Glaciol.*, 1–6.
- 3064 Cui, W., Wang, W., Zhang, J., & Yang, J. (2019). Multicore structures and the splitting  
3065 and merging of eddies in global oceans from satellite altimeter data. *Ocean Science*,  
3066 *15*(2), 413–430.

- 3067 Cunningham, S. A., Kanzow, T., Rayner, D., Baringer, M. O., Johns, W. E., Marotzke,  
3068 J., ... others (2007). Temporal variability of the atlantic meridional overturning  
3069 circulation at 26.5 n. *Science*, *317*(5840), 935–938.
- 3070 Cusack, J. M., Brearley, J. A., Naveira Garabato, A. C., Smeed, D. A., Polzin, K. L.,  
3071 Velzeboer, N., & Shakespeare, C. J. (2020). Observed eddy–internal wave interactions  
3072 in the Southern Ocean. *J. Phys. Oceanogr.*, *50*(10), 3043–3062.
- 3073 Cusack, J. M., Garabato, A. C. N., Smeed, D. A., & Girton, J. B. (2017). Observation  
3074 of a large lee wave in the Drake Passage. *J. Phys. Oceanogr.*, *47*(4), 793–810. doi:  
3075 [10.1175/JPO-D-16-0153.1](https://doi.org/10.1175/JPO-D-16-0153.1)
- 3076 Cushman-Roisin, B., & Beckers, J.-M. (2011). Chapter 14 - Turbulence in Stratified Fluids.  
3077 In B. Cushman-Roisin & J.-M. Beckers (Eds.), *Introduction to geophysical fluid*  
3078 *dynamics* (Vol. 101, pp. 425–470). doi: [10.1016/B978-0-12-088759-0.00014-6](https://doi.org/10.1016/B978-0-12-088759-0.00014-6)
- 3079 Cuyppers, Y., Le Vaillant, X., Bouruet-Aubertot, P., Vialard, J., & McPhaden, M. J. (2013).  
3080 Tropical storm-induced near-inertial internal waves during the Cirene experiment: En-  
3081 ergy fluxes and impact on vertical mixing. *J. Geophys. Res. Oceans*, *118*(1), 358–380.  
3082 doi: [10.1029/2012JC007881](https://doi.org/10.1029/2012JC007881)
- 3083 Cyriac, A., Meyer, A., Phillips, H. E., & Bindoff, N. L. (2023). Observations of internal  
3084 wave interactions in a Southern Ocean standing meander. *J. Phys. Oceanogr.*, *53*,  
3085 1997–2011. doi: [10.1175/JPO-D-22-0157.1](https://doi.org/10.1175/JPO-D-22-0157.1)
- 3086 Cyriac, A., Phillips, H. E., Bindoff, N. L., & Polzin, K. L. (2022). Turbulent mixing vari-  
3087 ability in an energetic standing meander of the Southern Ocean. *J. Phys. Oceanogr.*,  
3088 *52*, 1593–1611. doi: [10.1175/JPO-D-21-0180.1](https://doi.org/10.1175/JPO-D-21-0180.1)
- 3089 Daae, K. L., Fer, I., & Abrahamsen, E. P. (2009). Mixing on the continental slope of the  
3090 southern Weddell Sea. *J. Geophys. Res. Oceans*, *114*(C9).
- 3091 Dai, M., Shen, H. H., Hopkins, M. A., & Ackley, S. F. (2004). Wave rafting and the  
3092 equilibrium pancake ice cover thickness. *J. Geophys. Res. Oceans*, *109*(C7).
- 3093 Darelus, E., Fer, I., & Nicholls, K. W. (2016). Observed vulnerability of filchner-ronne ice  
3094 shelf to wind-driven inflow of warm deep water. *Nat. Commun.*, *7*(1), 1–7.
- 3095 D’Asaro, E. A. (1985). The energy flux from the wind to near-inertial motions in the  
3096 surface mixed layer. *J. Phys. Oceanogr.*, *15*(8), 1043–1059. doi: [10.1175/1520-  
3097 0485\(1985\)015<1043:TEFFTW>2.0.CO;2](https://doi.org/10.1175/1520-0485(1985)015<1043:TEFFTW>2.0.CO;2)
- 3098 D’Asaro, E. A., Lee, C., Rainville, L., Harcourt, R., & Thomas, L. (2011). Enhanced  
3099 turbulence and energy dissipation at ocean fronts. *Science*, *332*(6027), 318–322.
- 3100 Davis, P. E., Jenkins, A., Nicholls, K. W., Dutrieux, P., Schröder, M., Janout, M. A., ...  
3101 McPhail, S. (2022). Observations of modified warm deep water beneath ronne ice  
3102 shelf, Antarctica, from an autonomous underwater vehicle. *J. Geophys. Res. Oceans*,  
3103 e2022JC019103.
- 3104 Davis, P. E., & Nicholls, K. W. (2019). Turbulence observations beneath larsen c ice shelf,  
3105 Antarctica. *J. Geophys. Res. Oceans*, *124*(8), 5529–5550.
- 3106 Davis, P. E., Nicholls, K. W., Holland, D. M., Schmidt, B. E., Washam, P., Riverman, K. L.,  
3107 ... others (2023). Suppressed basal melting in the eastern thwaites glacier grounding  
3108 zone. *Nature*, *614*(7948), 479–485.
- 3109 Day, N., Bennetts, L. G., O’Farrell, S. P., Alberello, A., & Montiel, F. (2023). Unsupervised  
3110 classification of the antarctic marginal ice zone. *Authorea Preprints*.
- 3111 de Lavergne, C., Groeskamp, S., Zika, J., & Johnson, H. L. (2022). Chapter 3 - the role of  
3112 mixing in the large-scale ocean circulation. In M. P. Meredith & A. C. Naveira Gara-  
3113 bato (Eds.), *Ocean mixing* (p. 35–63). Elsevier. doi: [10.1016/B978-0-12-821512-  
3114 8.00010-4](https://doi.org/10.1016/B978-0-12-821512-8.00010-4)
- 3115 de Lavergne, C., Madec, G., Le Sommer, J., Nurser, A. J. G., & Naveira Garabato, A. C.  
3116 (2016). On the Consumption of Antarctic Bottom Water in the Abyssal Ocean. *J.*  
3117 *Phys. Oceanogr.*, *46*(2), 635–661. doi: [10.1175/JPO-D-14-0201.1](https://doi.org/10.1175/JPO-D-14-0201.1)
- 3118 de Conto, R. M., Pollard, D., Alley, R. B., Velicogna, I., Gasson, E., Gomez, N., ... others  
3119 (2021). The paris climate agreement and future sea-level rise from Antarctica. *Nature*,  
3120 *593*(7857), 83–89.
- 3121 de Lavergne, C., Madec, G., Roquet, F., Holmes, R. M., & McDougall, T. J. (2017). Abyssal

- ocean overturning shaped by seafloor distribution. *Nature*, 551(7679), 181–186. doi: [10.1038/nature24472](https://doi.org/10.1038/nature24472)
- de Lavergne, C., Palter, J. B., Galbraith, E. D., Bernardello, R., & Marinov, I. (2014). Cessation of deep convection in the open Southern Ocean under anthropogenic climate change. *Nat. Clim. Change*, 4(4), 278–282.
- de Lavergne, C., Vic, C., Madec, G., Roquet, F., Waterhouse, A. F., Whalen, C. B., ... Hibiya, T. (2020). A parameterization of local and remote tidal mixing. *J. Adv. Model. Earth Syst.*, 12(5), e2020MS002065. doi: [10.1029/2020MS002065](https://doi.org/10.1029/2020MS002065)
- Depoorter, M. A., Bamber, J. L., Griggs, J. A., Lenaerts, J. T., Ligtenberg, S. R., van den Broeke, M. R., & Moholdt, G. (2013). Calving fluxes and basal melt rates of antarctic ice shelves. *Nature*, 502(7469), 89–92.
- Derkani, M. H. (2021). *Waves in the Southern Ocean and Antarctic marginal ice zone: Observations and modelling* (Unpublished doctoral dissertation). The University of Melbourne.
- Derkani, M. H., Alberello, A., Nelli, F., Bennetts, L. G., Hessner, K. G., MacHutchon, K., ... Toffoli, A. (2021). Wind, waves, and surface currents in the Southern Ocean: observations from the Antarctic circumnavigation expedition. *Earth System Science Data*, 13(3), 1189–1209. doi: [10.5194/essd-13-1189-2021](https://doi.org/10.5194/essd-13-1189-2021)
- DeVries, T., Holzer, M., & Primeau, F. (2017). Recent increase in oceanic carbon uptake driven by weaker upper-ocean overturning. *Nature*, 542(7640), 215–218.
- Dewar, W. K., & Hogg, A. M. (2010). Topographic inviscid dissipation of balanced flow. *Ocean Modelling*, 32(1-2), 1–13.
- Dinniman, M. S., Asay-Davis, X., Galton-Fenzi, B., Holland, P., Jenkins, A., & Timmermann, R. (2016). Modeling ice shelf/ocean interaction in Antarctica: A review. *Oceanography*, 29(4), 144–153. doi: [10.5670/oceanog.2016.106](https://doi.org/10.5670/oceanog.2016.106)
- Dinniman, M. S., Klinck, J. M., Hofmann, E. E., & Jr., W. O. S. (2018). Effects of projected changes in wind, atmospheric temperature, and freshwater inflow on the Ross Sea. *J. Clim.*, 31, 1619–1635. doi: [10.1175/jcli-d-17-0351.1](https://doi.org/10.1175/jcli-d-17-0351.1)
- Doble, M. J., & Wadhams, P. (2006). Dynamical contrasts between pancake and pack ice, investigated with a drifting buoy array. *J. Geophys. Res. Oceans*, 111(C11).
- Dohan, K., & Davis, R. E. (2011). Mixing in the transition layer during two storm events. *J. Phys. Oceanogr.*, 41(1), 42–66.
- Dolatshah, A., Nelli, F., Bennetts, L. G., Alberello, A., Meylan, M. H., Monty, J. P., & Toffoli, A. (2018). Hydroelastic interactions between water waves and floating freshwater ice. *Phys. Fluids*, 30(9), 091702.
- Donelan, M. A., Babanin, A. V., Young, I. R., & Banner, M. L. (2006). Wave-follower field measurements of the wind-input spectral function. Part II: Parameterization of the wind input. *J. Phys. Oceanogr.*, 36(8), 1672–1689.
- Dong, S., Gille, S. T., & Sprintall, J. (2007). An assessment of the Southern Ocean mixed layer heat budget. *J. Climate*, 20(17), 4425–4442. doi: [10.1175/JCLI4259.1](https://doi.org/10.1175/JCLI4259.1)
- Dong, S., Sprintall, J., Gille, S. T., & Talley, L. (2008). Southern ocean mixed-layer depth from argo float profiles. *J. Geophys. Res. Oceans*, 113(C6).
- Donnelly, M., Leach, H., & Strass, V. (2017). Modification of the deep salinity-maximum in the Southern Ocean by circulation in the antarctic circumpolar current and the weddell gyre. *Ocean Dynamics*, 67(7), 813–838.
- Dosser, H. V., & Rainville, L. (2016). Dynamics of the changing near-inertial internal wave field in the Arctic ocean. *J. Phys. Oceanogr.*, 46(2), 395–415. doi: [10.1175/JPO-D-15-0056.1](https://doi.org/10.1175/JPO-D-15-0056.1)
- Dossmann, Y., Bourget, B., Brouzet, C., Dauvois, T., Joubaud, S., & Odier, P. (2016). Mixing by internal waves quantified using combined piv/plif technique. *Experiments in Fluids*, 57, 1–12.
- Dotto, T. S., Naveira Garabato, A. C., Bacon, S., Tsamados, M., Holland, P. R., Hooley, J., ... Meredith, M. P. (2018). Variability of the ross gyre, Southern Ocean: Drivers and responses revealed by satellite altimetry. *Geophys. Res. Lett.*, 45(12), 6195–6204.
- Downes, S. M., Gnanadesikan, A., Griffies, S. M., & Sarmiento, J. L. (2011). Water mass

- 3177 exchange in the Southern Ocean in coupled climate models. *J. Phys. Oceanogr.*, *41*(9),  
 3178 1756-1771. doi: [10.1175/2011JPO4586.1](https://doi.org/10.1175/2011JPO4586.1)
- 3179 Drake, H. F., Ruan, X., Callies, J., Ogden, K., Thurnherr, A. M., & Ferrari, R. (2022).  
 3180 Dynamics of eddying abyssal mixing layers over sloping rough topography. *Journal of*  
 3181 *Physical Oceanography*, *52*(12), 3199–3219.
- 3182 Dumas-Lefebvre, E., & Dumont, D. (2023). Aerial observations of sea ice breakup by ship  
 3183 waves. *The Cryosphere*, *17*(2), 827–842.
- 3184 Dumont, D. (2022). Marginal ice zone dynamics: history, definitions and research perspec-  
 3185 tives. *Philos. Trans. Royal Soc. A*, *380*(2235), 20210253.
- 3186 Dumont, D., Kohout, A., & Bertino, L. (2011). A wave-based model for the marginal ice  
 3187 zone including a floe breaking parameterization. *J. Geophys. Res. Oceans*, *116*(C4).
- 3188 Du Plessis, M., Swart, S., Ansorge, I., & Mahadevan, A. (2017). Submesoscale processes  
 3189 promote seasonal restratification in the subantarctic ocean. *J. Geophys. Res. Oceans*,  
 3190 *122*(4), 2960–2975.
- 3191 Du Plessis, M., Swart, S., Ansorge, I. J., Mahadevan, A., & Thompson, A. F. (2019). South-  
 3192 ern ocean seasonal restratification delayed by submesoscale wind–front interactions.  
 3193 *J. Phys. Oceanogr.*, *49*(4), 1035–1053.
- 3194 Egbert, G. D., & Erofeeva, S. Y. (2002). Efficient inverse modeling of barotropic  
 3195 ocean tides. *J Atmos. Ocean. Technol.*, *19*(2), 183-204. doi: [10.1175/1520-  
 3196 0426\(2002\)019<0183:EIMOBO>2.0.CO;2](https://doi.org/10.1175/1520-0426(2002)019<0183:EIMOBO>2.0.CO;2)
- 3197 Egbert, G. D., & Ray, R. D. (2000). Significant dissipation of tidal energy in the deep ocean  
 3198 inferred from satellite altimeter data. *Nature*, *405*(6788), 775–778.
- 3199 Eicken, H. (2003). From the microscopic, to the macroscopic, to the regional scale: growth,  
 3200 microstructure and properties of sea ice. *Sea ice: an introduction to its physics,*  
 3201 *chemistry, biology and geology*, *22*, 81.
- 3202 Eliassen, E. P., A. (1961). On the transfer of energy in stationary mountain waves. *Geophys.*  
 3203 *Publ.*, *22*, 1-23.
- 3204 Emile-Geay, J., & Madec, G. (2009). Geothermal heating, diapycnal mixing and the abyssal  
 3205 circulation. *Ocean Science*, *5*(2), 203–217. doi: [10.5194/os-5-203-2009](https://doi.org/10.5194/os-5-203-2009)
- 3206 Eriksen, C. C. (1978). Measurements and models of fine structure, internal gravity waves,  
 3207 and wave breaking in the deep ocean. *J. Geophys. Res. Oceans*, *83*(C6), 2989-3009.  
 3208 doi: [10.1029/JC083iC06p02989](https://doi.org/10.1029/JC083iC06p02989)
- 3209 Evans, D. G., Frajka-Williams, E., Naveira Garabato, A. C., Polzin, K. L., & Forryan, A.  
 3210 (2020). Mesoscale eddy dissipation by a “zoo” of submesoscale processes at a western  
 3211 boundary. *J. Geophys. Res. Oceans*, *125*(11), e2020JC016246.
- 3212 Evans, D. G., Zika, J. D., Naveira Garabato, A. C., & Nurser, A. J. G. (2018). The cold  
 3213 transit of Southern Ocean upwelling. *Geophys. Res. Lett.*, *45*(24), 13,386-13,395. doi:  
 3214 [10.1029/2018GL079986](https://doi.org/10.1029/2018GL079986)
- 3215 Fahrbach, E., Hoppema, M., Rohardt, G., Boebel, O., Klatt, O., & Wisotzki, A. (2011).  
 3216 Warming of deep and abyssal water masses along the greenwich meridian on decadal  
 3217 time scales: The weddell gyre as a heat buffer. *Deep-Sea Res. II: Top. Stud. Oceanogr.*,  
 3218 *58*(25-26), 2509–2523.
- 3219 Fahrbach, E., Rohardt, G., & Krause, G. (1992). The Antarctic coastal current in the  
 3220 southeastern Weddell Sea. *Polar Biology*, *12*(2), 171–182. doi: [10.1007/BF00238257](https://doi.org/10.1007/BF00238257)
- 3221 Falahat, S., & Nycander, J. (2015). On the generation of bottom-trapped internal tides. *J.*  
 3222 *Phys. Oceanogr.*, *45*(2), 526–545.
- 3223 Favier, L., Jourdain, N. C., Jenkins, A., Merino, N., Durand, G., Gagliardini, O., ... Math-  
 3224 iot, P. (2019). Assessment of sub-shelf melting parameterisations using the ocean–  
 3225 ice-sheet coupled model nemo (v3. 6)–elmer/ice (v8. 3). *Geosci. Model Dev.*, *12*(6),  
 3226 2255–2283.
- 3227 Feltham, D. L. (2008). Sea ice rheology. *Annu. Rev. Fluid Mech.*, *40*, 91–112.
- 3228 Feltham, D. L., Untersteiner, N., Wettlaufer, J., & Worster, M. (2006). Sea ice is a mushy  
 3229 layer. *Geophys. Res. Lett.*, *33*(14).
- 3230 Feltham, D. L., Worster, M. G., & Wettlaufer, J. (2002). The influence of ocean flow on  
 3231 newly forming sea ice. *J. Geophys. Res. Oceans*, *107*(C2), 1–1.

- 3232 Fer, I., Darelius, E., & Daae, K. B. (2016). Observations of energetic turbulence  
3233 on the Weddell sea continental slope. *Geophys. Res. Lett.*, *43*(2), 760-766. doi:  
3234 [10.1002/2015GL067349](https://doi.org/10.1002/2015GL067349)
- 3235 Fer, I., Makinson, K., & Nicholls, K. W. (2012). Observations of thermohaline convection  
3236 adjacent to brunt ice shelf. *J. Phys. Oceanogr.*, *42*(3), 502-508.
- 3237 Ferrari, R., Mashayek, A., McDougall, T. J., Nikurashin, M., & Campin, J.-M. (2016).  
3238 Turning ocean mixing upside down. *J. Phys. Oceanogr.*, *46*(7), 2239-2261. doi:  
3239 [10.1175/JPO-D-15-0244.1](https://doi.org/10.1175/JPO-D-15-0244.1)
- 3240 Ferrari, R., & Polzin, K. L. (2005). Finescale structure of the T-S relation in the eastern  
3241 North Atlantic. *J. Phys. Oceanogr.*, *35*(8), 1437-1454.
- 3242 Ferrari, R., & Wunsch, C. (2009). Ocean circulation kinetic energy: Reservoirs,  
3243 sources, and sinks. *Annu. Rev. Fluid Mech.*, *41*(1), 253-282. doi: [10.1146/an-](https://doi.org/10.1146/annurev.fluid.40.111406.102139)  
3244 [nurev.fluid.40.111406.102139](https://doi.org/10.1146/annurev.fluid.40.111406.102139)
- 3245 Ferreira Azevedo, M., Aoki, S., & Kitade, Y. (2022). Seasonal variation and governing  
3246 dynamics of the mixed layer in the Indian sector of the Southern Ocean. *J. Geophys.*  
3247 *Res. Oceans*, *127*(4), e2021JC017838. doi: [10.1029/2021JC017838](https://doi.org/10.1029/2021JC017838)
- 3248 Ferris, L., Clayson, C. A., Gong, D., Merrifield, S., Shroyer, E. L., Smith, M., & Lau-  
3249 rent, L. S. (2022). Shear turbulence in the high-wind Southern Ocean using direct  
3250 measurements. *J. Phys. Oceanogr.* doi: [10.1175/JPO-D-21-0015.1](https://doi.org/10.1175/JPO-D-21-0015.1)
- 3251 Fine, E. C., & Cole, S. T. (2022). Decadal observations of internal wave energy, shear, and  
3252 mixing in the Western Arctic ocean. *J. Geophys. Res. Oceans*, *127*(5), e2021JC018056.  
3253 doi: [10.1029/2021JC018056](https://doi.org/10.1029/2021JC018056)
- 3254 Flexas, M. M., Schodlok, M. P., Padman, L., Menemenlis, D., & Orsi, A. H. (2015). Role of  
3255 tides on the formation of the Antarctic slope front at the Weddell-Scotia confluence.  
3256 *J. Geophys. Res. Oceans*, *120*(5), 3658-3680. doi: [10.1002/2014JC010372](https://doi.org/10.1002/2014JC010372)
- 3257 Fogt, R. L., & Marshall, G. J. (2020). The Southern Annular Mode: variability, trends,  
3258 and climate impacts across the Southern Hemisphere. *Wiley Interdiscip. Rev. Clim.*  
3259 *Change*, *11*(4), e652.
- 3260 Fogt, R. L., Sleinkofer, A. M., Raphael, M. N., & Handcock, M. S. (2022). A regime shift  
3261 in seasonal total antarctic sea ice extent in the twentieth century. *Nat. Clim. Change*,  
3262 *12*(1), 54-62.
- 3263 Fons, S. W., & Kurtz, N. T. (2019). Retrieval of snow freeboard of Antarctic sea ice using  
3264 waveform fitting of CryoSat-2 returns. *Cryosphere*, *13*(3), 861-878.
- 3265 Foppert, A. (2019). Observed storm track dynamics in Drake Passage. *J. Phys. Oceanogr.*,  
3266 *49*(3), 867-884.
- 3267 Foppert, A., Donohue, K. A., Watts, D. R., & Tracey, K. L. (2017). Eddy heat flux across the  
3268 Antarctic Circumpolar Current estimated from sea surface height standard deviation.  
3269 *J. Geophys. Res.*, *122*, 6947-6964.
- 3270 Foppert, A., Rintoul, S. R., & England, M. H. (2019). Along-slope variability of cross-  
3271 slope eddy transport in East Antarctica. *Geophys. Res. Lett.*, 8224-8233. doi:  
3272 [10.1029/2019gl082999](https://doi.org/10.1029/2019gl082999)
- 3273 Foppert, A., Rintoul, S. R., Purkey, S. G., Zilberman, N., Kobayashi, T., Sallée, J.-b., ...  
3274 Wallace, L. O. (2021). Deep Argo reveals bottom water properties and pathways in  
3275 the Australian-Antarctic Basin. *J. Geophys. Res. Oceans*, *126*(e2021JC017935). doi:  
3276 [10.1029/2021JC017935](https://doi.org/10.1029/2021JC017935)
- 3277 Forryan, A., Naveira Garabato, A. C., Polzin, K. L., & Waterman, S. N. (2015). Rapid injec-  
3278 tion of near-inertial shear into the stratified upper ocean at an Antarctic Circumpolar  
3279 Current front. *Geophys. Res. Lett.*, *42*, 3431-3441. doi: [10.1002/2015GL063494](https://doi.org/10.1002/2015GL063494)
- 3280 Foster, T. D. (1983). The temperature and salinity fine structure of the ocean under the  
3281 ross ice shelf. *J. Geophys. Res. Oceans*, *88*(C4), 2556-2564.
- 3282 Foster, T. D., & Carmack, E. C. (1976). Frontal zone mixing and Antarctic bottom wa-  
3283 ter formation in the southern Weddell Sea. In *Deep sea research and oceanographic*  
3284 *abstracts* (Vol. 23, pp. 301-317).
- 3285 Fox-Kemper, B., & Ferrari, R. (2008). Parameterization of mixed layer eddies. Part II:  
3286 Prognosis and impact. *J. Phys. Oceanogr.*, *38*(6), 1166-1179.

- 3287 Fox-Kemper, B., Hewitt, H., C. Xiao, G. A., Drijfhout, S., Edwards, T., Golledge, N., ...  
 3288 Yu, Y. (2021). Ocean, cryosphere and sea level change. In V. Masson-Delmotte et al.  
 3289 (Eds.), *Climate change 2021: The physical science basis. contribution of working group*  
 3290 *i to the sixth assessment report of the intergovernmental panel on climate change* (pp.  
 3291 1211–1362). Cambridge, UK and New York, NY, USA: Cambridge University Press.  
 3292 doi: [10.1017/9781009157896.011](https://doi.org/10.1017/9781009157896.011).
- 3293 Fox-Kemper, B., Johnson, L., & Qiao, F. (2022). Ocean near-surface layers. In *Ocean*  
 3294 *mixing* (pp. 65–94). Elsevier.
- 3295 Francis, D., Eayrs, C., Cuesta, J., & Holland, D. (2019). Polar Cyclones at the Origin of  
 3296 the Reoccurrence of the Maud Rise Polynya in Austral Winter 2017. *J. Geophys. Res.*  
 3297 *Atmos*, *124*(10), 5251–5267. doi: [10.1029/2019jd030618](https://doi.org/10.1029/2019jd030618)
- 3298 Fraser, A., Wongpan, P., Langhorne, P., Klekociuk, A., Kusahara, K., Lannuzel, D., ...  
 3299 others (2023). Antarctic landfast sea ice: A review of its physics, biogeochemistry and  
 3300 ecology. *Reviews of Geophysics*, *61*(2), e2022RG000770.
- 3301 Freeman, N. M., Lovenduski, N. S., & Gent, P. R. (2016). Temporal variability in the  
 3302 antarctic polar front (2002–2014). *J. Geophys. Res. Oceans*, *121*(10), 7263–7276.
- 3303 Fretwell, P., Pritchard, H. D., Vaughan, D. G., Bamber, J. L., Barrand, N. E., Bell, R.,  
 3304 ... others (2013). Bedmap2: improved ice bed, surface and thickness datasets for  
 3305 antarctica. *The Cryosphere*, *7*(1), 375–393.
- 3306 Fricker, H. A., Scambos, T., Bindshadler, R., & Padman, L. (2007). An active subglacial  
 3307 water system in west Antarctica mapped from space. *Science*, *315*(5815), 1544–1548.  
 3308 doi: [10.1126/science.113689](https://doi.org/10.1126/science.113689)
- 3309 Fricker, H. A., Siegfried, M. R., Carter, S. P., & Scambos, T. A. (2016). A decade of progress  
 3310 in observing and modelling Antarctic subglacial water systems. *Philos. Trans. Royal*  
 3311 *Soc. A*, *374*(2059), 20140294.
- 3312 Friedrichs, D. M., McInerney, J. B., Oldroyd, H. J., Lee, W. S., Yun, S., Yoon, S.-T., ...  
 3313 others (2022). Observations of submesoscale eddy-driven heat transport at an ice shelf  
 3314 calving front. *Communications Earth & Environment*, *3*(1), 1–9.
- 3315 Fringer, O. B., & Street, R. L. (2003). The dynamics of breaking progressive interfacial  
 3316 waves. *J. Fluid Mech.*, *494*, 319–353. doi: [10.1017/S0022112003006189](https://doi.org/10.1017/S0022112003006189)
- 3317 Frölicher, T. L., Sarmiento, J. L., Paynter, D. J., Dunne, J. P., Krasting, J. P., & Winton,  
 3318 M. (2015). Dominance of the Southern Ocean in anthropogenic carbon and heat  
 3319 uptake in CMIP5 models. *J. Clim.*, *28*, 862–886.
- 3320 Fu, L.-L., Chelton, D. B., Traon, P.-Y. L., & Morrow, R. (2010). Eddy dynamics from  
 3321 satellite altimetry. *Oceanography*, *23*(4), 14–25.
- 3322 Fukamachi, Y., Rintoul, S. R., Church, J. A., Aoki, S., Sokolov, S., Rosenberg, M. A., &  
 3323 Wakatsuchi, M. (2010). Strong export of Antarctic bottom water east of the Kerguelen  
 3324 plateau. *Nat. Geosci.*, *3*, 327–331. doi: [10.1038/ngeo842](https://doi.org/10.1038/ngeo842)
- 3325 Gallet, B., & Ferrari, R. (2020). The vortex gas scaling regime of baroclinic turbulence.  
 3326 *Proc. Natl. Acad. Sci. USA*, *117*(9), 4491–4497.
- 3327 Galton-Fenzi, B., Hunter, J., Coleman, R., Marsland, S., & Warner, R. (2012). Modeling  
 3328 the basal melting and marine ice accretion of the amery ice shelf. *J. Geophys. Res.*  
 3329 *Oceans*, *117*(C9).
- 3330 Ganachaud, A., & Wunsch, C. (2000). Improved estimates of global ocean circulation,  
 3331 heat transport and mixing from hydrographic data. *Nature*, *408*, 453–457. doi:  
 3332 [10.1038/35044048](https://doi.org/10.1038/35044048)
- 3333 Ganachaud, A., Wunsch, C., Marotzke, J., & Toole, J. (2000). Meridional overturning  
 3334 and large-scale circulation of the Indian Ocean. *J. Geophys. Res. Oceans*, *105*(C11),  
 3335 26117–26134. doi: [10.1029/2000jc900122](https://doi.org/10.1029/2000jc900122)
- 3336 Garabato, A. C. N., Polzin, K. L., King, B. A., Heywood, K. J., & Visbeck, M. (2004).  
 3337 Widespread intense turbulent mixing in the Southern Ocean. *Science*, *303*(5655),  
 3338 210–213. doi: [10.1126/science.1090929](https://doi.org/10.1126/science.1090929)
- 3339 Garrett, C. (2001). What is the “near-inertial” band and why is it different from the rest  
 3340 of the internal wave spectrum? *J. Phys. Oceanogr.*, *31*(4), 962–971.

- 3341 Garrett, C., & Kunze, E. (2007). Internal tide generation in the deep ocean. *Annu. Rev.*  
3342 *Fluid Mech.*, *39*, 57–87.
- 3343 Gayen, B., & Griffiths, R. W. (2022). Rotating horizontal convection. *Annu. Rev. Fluid*  
3344 *Mech.*, *54*, 105–132.
- 3345 Gayen, B., Griffiths, R. W., & Kerr, R. C. (2016). Simulation of convection at a ver-  
3346 tical ice face dissolving into saline water. *J. Fluid Mech.*, *798*, 284–298. doi:  
3347 [10.1017/jfm.2016.315](https://doi.org/10.1017/jfm.2016.315)
- 3348 Gent, P. R. (2016). Effects of Southern Hemisphere Wind Changes on the Meridional  
3349 Overturning Circulation in Ocean Models. *Ann. Rev. Mar. Sci.*, *8*(1), 1–16.
- 3350 Gent, P. R., & McWilliams, J. C. (1990). Isopycnal mixing in ocean circu-  
3351 lation models. *J. Phys. Oceanogr.*, *20*(1), 150–155. doi: [10.1175/1520-  
3352 0485\(1990\)020<0150:IMIOCMj2.0.CO;2](https://doi.org/10.1175/1520-0485(1990)020<0150:IMIOCMj2.0.CO;2)
- 3353 Gibson, A. (2019). *An adaptive vertical coordinate for idealised and global ocean modelling*  
3354 (Unpublished doctoral dissertation). The Australian National University (Australia).
- 3355 Gibson, A. H., Hogg, A. M., Kiss, A. E., Shakespeare, C. J., & Adcroft, A. (2017). At-  
3356 tribution of horizontal and vertical contributions to spurious mixing in an arbitrary  
3357 lagrangian–eulerian ocean model. *Ocean Model.*, *119*, 45–56.
- 3358 Giddy, I., Swart, S., du Plessis, M., Thompson, A. F., & Nicholson, S.-A. (2021). Stir-  
3359 ring of sea-ice meltwater enhances submesoscale fronts in the Southern Ocean. *J.*  
3360 *Geophys. Res. Oceans*, *126*(4), e2020JC016814. (e2020JC016814 2020JC016814) doi:  
3361 [10.1029/2020JC016814](https://doi.org/10.1029/2020JC016814)
- 3362 Gill, A. E. (1984). On the behavior of internal waves in the wakes of storms. *J. Phys.*  
3363 *Oceanogr.*, *14*(7), 1129–1151.
- 3364 Gille, S. T. (2008). Decadal-scale temperature trends in the southern hemisphere ocean. *J.*  
3365 *Climate*, *21*(18), 4749–4765.
- 3366 Gille, S. T. (2014). Meridional displacement of the Antarctic circumpolar current. *Philos.*  
3367 *Trans. Royal Soc. A*, *372*(2019), 20130273.
- 3368 Gille, S. T., & Kelly, K. A. (1996). Scales of spatial and temporal variability in the southern  
3369 ocean. *Journal of Geophysical Research: Oceans*, *101*(C4), 8759–8773.
- 3370 Gille, S. T., Sheen, K. L., Swart, S., & Thompson, A. F. (2022). Chapter 12 - mixing in the  
3371 Southern Ocean. In M. P. Meredith & A. C. Naveira Garabato (Eds.), *Ocean mixing*  
3372 (p. 301-327). Elsevier. doi: [10.1016/B978-0-12-821512-8.00019-0](https://doi.org/10.1016/B978-0-12-821512-8.00019-0)
- 3373 Gladstone, R., Galton-Fenzi, B., Gwyther, D., Zhou, Q., Hattermann, T., Zhao, C., ...  
3374 others (2021). The framework for ice sheet–ocean coupling (fisoc) v1. 1. *Geosci.*  
3375 *Model Dev.*, *14*(2), 889–905.
- 3376 Goff, J. A. (1991). A global and regional stochastic analysis of near-ridge abyssal hill  
3377 morphology. *J. Geophys. Res. Solid Earth*, *96*(B13), 21713–21737.
- 3378 Goff, J. A. (2010). Global prediction of abyssal hill root-mean-square heights from small-  
3379 scale altimetric gravity variability. *Journal of Geophysical Research: Solid Earth*,  
3380 *115*(B12).
- 3381 Goff, J. A., & Arbic, B. K. (2010). Global prediction of abyssal hill roughness statistics for  
3382 use in ocean models from digital maps of paleo-spreading rate, paleo-ridge orientation,  
3383 and sediment thickness. *Ocean Model.*, *32*(1-2), 36–43.
- 3384 Golden, K. M. (2001). Brine percolation and the transport properties of sea ice. *Ann.*  
3385 *Glaciol.*, *33*, 28–36.
- 3386 Golden, K. M. (2009). Climate change and the mathematics of transport in sea ice. *Not.*  
3387 *Am. Mat. Soc.*, *56*(5), 562–584.
- 3388 Golden, K. M., Ackley, S., & Lytle, V. (1998). The percolation phase transition in sea ice.  
3389 *Science*, *282*(5397), 2238–2241.
- 3390 Golden, K. M., Bennetts, L. G., Cherkaev, E., Eisenman, I., Feltham, D., Horvat, C., ...  
3391 Wells, A. J. (2020). Modeling sea ice. *Not. Am. Math. Soc.*, *67*(10), 1535–1555. doi:  
3392 [10.1090/noti2171](https://doi.org/10.1090/noti2171)
- 3393 Golden, K. M., Eicken, H., Heaton, A., Miner, J., Pringle, D., & Zhu, J. (2007). Thermal  
3394 evolution of permeability and microstructure in sea ice. *Geophys. Res. Lett.*, *34*(16).
- 3395 Gomez-Fell, R., Rack, W., Purdie, H., & Marsh, O. (2022). Parker ice tongue collapse,

- 3396 Antarctica, triggered by loss of stabilizing land-fast sea ice. *Geophys. Res. Lett.*, *49*(1),  
 3397 e2021GL096156.
- 3398 Gordon, A. L. (1978). Deep Antarctic Convection West of Maud Rise. *J. Phys. Oceanogr.*,  
 3399 *8*(4), 600–612. doi: [10.1175/1520-0485\(1978\)008<0600:dacwom>2.0.co;2](https://doi.org/10.1175/1520-0485(1978)008<0600:dacwom>2.0.co;2)
- 3400 Gordon, A. L. (1982). Weddell deep water variability. *J. Mar. Res.*, *40*, 199–217.
- 3401 Gordon, A. L. (1991). Two stable modes of Southern Ocean winter stratification. In P. Chu  
 3402 & J. Gascard (Eds.), *Deep convection and deep water formation in the oceans* (Vol. 57,  
 3403 p. 17-35). Elsevier. doi: [10.1016/S0422-9894\(08\)70058-8](https://doi.org/10.1016/S0422-9894(08)70058-8)
- 3404 Gordon, A. L., Orsi, A. H., Muench, R., Huber, B. A., Zambianchi, E., & Visbeck, M.  
 3405 (2009). Western ross sea continental slope gravity currents. *Deep-Sea Res. II: Top.*  
 3406 *Stud. Oceanogr.*, *56*(13-14), 796–817.
- 3407 Gordon, A. L., Visbeck, M., & Comiso, J. C. (2007). A Possible Link between the Weddell  
 3408 Polynya and the Southern Annular Mode\*. *J. Climate*, *20*(11), 2558–2571. doi:  
 3409 [10.1175/jcli4046.1](https://doi.org/10.1175/jcli4046.1)
- 3410 Graham, A. G., Wählin, A., Hogan, K. A., Nitsche, F. O., Heywood, K. J., Totten, R. L., ...  
 3411 others (2022). Rapid retreat of thwaites glacier in the pre-satellite era. *Nat. Geosci.*,  
 3412 *15*(9), 706–713.
- 3413 Greene, C. A., Gardner, A. S., Schlegel, N.-J., & Fraser, A. D. (2022). Antarctic calving  
 3414 loss rivals ice-shelf thinning. *Nature*, *609*(7929), 948–953.
- 3415 Greene, C. A., Young, D. A., Gwyther, D. E., Galton-Fenzi, B. K., & Blankenship,  
 3416 D. D. (2018). Seasonal dynamics of totten ice shelf controlled by sea ice buttressing.  
 3417 *Cryosphere*, *12*(9), 2869–2882.
- 3418 Gregg, M. C., D’Asaro, E. A., Riley, J. J., & Kunze, E. (2018). Mixing efficiency in the  
 3419 ocean. *Ann. Rev. Mar. Sci.*, *10*(1).
- 3420 Griffies, S. M., Adcroft, A., & Hallberg, R. W. (2020). A primer on the vertical lagrangian-  
 3421 remap method in ocean models based on finite volume generalized vertical coordinates.  
 3422 *J. Adv. Model. Earth Syst.*, *12*(10), e2019MS001954.
- 3423 Griffiths, R. (1986). Gravity currents in rotating systems. *Annu. Rev. Fluid Mech.*, *18*(1),  
 3424 59–89.
- 3425 Grimshaw, R. (1984). Wave action and wave-mean flow interaction, with application  
 3426 to stratified shear flows. *Annu. Rev. Fluid Mech.*, *16*(1), 11-44. doi: [10.1146/an-](https://doi.org/10.1146/annurev.fl.16.010184.000303)  
 3427 [nurev.fl.16.010184.000303](https://doi.org/10.1146/annurev.fl.16.010184.000303)
- 3428 Grisouard, N. (2018). Extraction of potential energy from geostrophic fronts by inertial-  
 3429 symmetric instabilities. *J. Phys. Oceanogr.*, *48*(5), 1033–1051.
- 3430 Groeskamp, S., Abernathy, R. P., & Klocker, A. (2016). Water mass transformation by  
 3431 cabbeling and thermobaricity. *Geophys. Res. Lett.*, *43*(20).
- 3432 Gula, J., Taylor, J., Shcherbina, A., & Mahadevan, A. (2022). Submesoscale processes and  
 3433 mixing. In *Ocean mixing* (pp. 181–214). Elsevier.
- 3434 Gülk, B., Roquet, F., Naveira Garabato, A. C., Narayanan, A., Rousset, C., & Madec,  
 3435 G. (2023). Variability and remote controls of the warm-water halo and taylor cap at  
 3436 maud rise. *Journal of Geophysical Research: Oceans*, *128*(7), e2022JC019517.
- 3437 Guo, G., Gao, L., & Shi, J. (2020). Modulation of dense shelf water salinity variability in  
 3438 the western ross sea associated with the amundsen sea low. *Environmental Research*  
 3439 *Letters*, *16*(1), 014004.
- 3440 Gupta, M., Marshall, J. C., Song, H., Campin, J.-M., & Meneghello, G. (2020). Sea-ice  
 3441 melt driven by ice-ocean stresses on the mesoscale. *J. Geophys. Res. Oceans*, *125*.  
 3442 doi: [10.1029/2020JC016404](https://doi.org/10.1029/2020JC016404)
- 3443 Gutjahr, O., Jungclaus, J. H., Brüggemann, N., Haak, H., & Marotzke, J. (2022). Air-sea  
 3444 interactions and water mass transformation during a katabatic storm in the irminger  
 3445 sea. *J. Geophys. Res. Oceans*, *127*.
- 3446 Gwyther, D. E., Galton-Fenzi, B. K., Dinniman, M. S., Roberts, J. L., & Hunter, J. R.  
 3447 (2015). The effect of basal friction on melting and freezing in ice shelf-ocean models.  
 3448 *Ocean Model.*, *95*, 38–52. doi: [10.1016/j.ocemod.2015.09.004](https://doi.org/10.1016/j.ocemod.2015.09.004)
- 3449 Gwyther, D. E., Spain, E. A., King, P., Guihen, D., Williams, G. D., Evans, E., ... Cole-  
 3450 man, R. (2020). Cold ocean cavity and weak basal melting of the sørsdal ice shelf

- 3451 revealed by surveys using autonomous platforms. *J. Geophys. Res. Oceans*, *125*(6),  
 3452 e2019JC015882.
- 3453 Hall, B., Johnson, S., Thomas, M., & Rampai, T. (2023). Review of the design considerations  
 3454 for the laboratory growth of sea ice. *Journal of Glaciology*, 1–13.
- 3455 Hallberg, R. (2013). Using a resolution function to regulate parameterizations of oceanic  
 3456 mesoscale eddy effects. *Ocean Model.*, *72*, 92–103.
- 3457 Hallberg, R., & Gnanadesikan, A. (2001). An exploration of the role of transient eddies  
 3458 in determining the transport of a zonally reentrant current. *J. Phys. Oceanogr.*, *31*,  
 3459 3312–3330. doi: [10.1175/1520-0485\(2001\)031<3312:AEOTRO>2.0.CO;2](https://doi.org/10.1175/1520-0485(2001)031<3312:AEOTRO>2.0.CO;2)
- 3460 Hallberg, R., & Gnanadesikan, A. (2006). The Role of Eddies in Determining the Structure  
 3461 and Response of the Wind-Driven Southern Hemisphere Overturning: Results from  
 3462 the Modeling Eddies in the Southern Ocean (MESO) Project. *J. Phys. Oceanogr.*,  
 3463 *36*(12), 2232–2252.
- 3464 Hanawa, K., & Talley, L. D. (2001). Mode waters. In G. S. et al. (Ed.), *Circulation and*  
 3465 *climate: A 21st century perspective* (p. 373–386). Academic Press.
- 3466 Hasselmann, K. (1974). On the spectral dissipation of ocean waves due to white capping.  
 3467 *Boundary-Layer Meteorology*, *6*(1), 107–127.
- 3468 Hattermann, T., Nicholls, K. W., Hellmer, H. H., Davis, P. E., Janout, M. A., Østerhus,  
 3469 S., ... Kanzow, T. (2021). Observed interannual changes beneath filchner-ronne ice  
 3470 shelf linked to large-scale atmospheric circulation. *Nat. Commun.*, *12*(1), 1–11.
- 3471 Haumann, A. F., Gruber, N., & Münnich, M. (2020). Sea-ice induced Southern Ocean  
 3472 subsurface warming and surface cooling in a warming climate. *AGU Advances*, *1*(2).  
 3473 doi: [10.1029/2019AV000132](https://doi.org/10.1029/2019AV000132)
- 3474 Hausmann, U., Sallée, J.-B., Jourdain, N. C., Mathiot, P., Rousset, C., Madec, G., ...  
 3475 Hattermann, T. (2020). The Role of Tides in Ocean-Ice Shelf Interactions in the  
 3476 Southwestern Weddell Sea. *J. Geophys. Res. Oceans*, *125*(6), e2019JC015847. doi:  
 3477 [10.1029/2019JC015847](https://doi.org/10.1029/2019JC015847)
- 3478 Hazel, J. E., & Stewart, A. L. (2019). Are the near-Antarctic easterly winds weakening in  
 3479 response to enhancement of the southern annular mode? *J. Climate*, *32*(6), 1895–  
 3480 1918. doi: [10.1175/JCLI-D-18-0402.1](https://doi.org/10.1175/JCLI-D-18-0402.1)
- 3481 Hazel, J. E., & Stewart, A. L. (2020). Bistability of the filchner-ronne ice shelf cav-  
 3482 ity circulation and basal melt. *Journal of Geophysical Research: Oceans*, *125*(4),  
 3483 e2019JC015848.
- 3484 Heil, P., & Allison, I. (1999). The pattern and variability of antarctic sea-ice drift in the  
 3485 indian ocean and western pacific sectors. *J. Geophys. Res. Oceans*, *104*(C7), 15789–  
 3486 15802.
- 3487 Heil, P., & Hibler, W. D. (2002). Modeling the high-frequency component of arctic sea ice  
 3488 drift and deformation. *J. Physical Oceanography*, *32*, 3039–3057.
- 3489 Heil, P., Hutchings, J. K., Worby, A. P., Johansson, M., Launiainen, J., Haas, C., & Hi-  
 3490 bler III, W. D. (2008). Tidal forcing on sea-ice drift and deformation in the western  
 3491 Weddell Sea in early austral summer, 2004. *Deep-Sea Res. II: Top. Stud. Oceanogr.*,  
 3492 *55*(8-9), 943–962.
- 3493 Hemer, M. A. (2010). Historical trends in Southern Ocean storminess: Long-term variability  
 3494 of extreme wave heights at cape sorell, tasmania. *Geophys. Res. Lett.*, *37*(18).
- 3495 Henley, S. F., Cavan, E. L., Fawcett, S. E., Kerr, R., Monteiro, T., Sherrell, R. M., ...  
 3496 others (2020). Changing biogeochemistry of the Southern Ocean and its ecosystem  
 3497 implications. *Front. Mar. Sci.*, *7*, 581.
- 3498 Hennon, T. D., Riser, S. C., & Alford, M. H. (2014). Observations of internal gravity waves  
 3499 by argo floats. *J. Phys. Oceanogr.*, *44*(9), 2370–2386.
- 3500 Herman, A., Cheng, S., & Shen, H. H. (2019). Wave energy attenuation in fields of collid-  
 3501 ing ice floes—part 1: Discrete-element modelling of dissipation due to ice–water drag.  
 3502 *Cryosphere*, *13*(11), 2887–2900.
- 3503 Herman, A., Evers, K.-U., & Reimer, N. (2018). Floe-size distributions in laboratory ice  
 3504 broken by waves. *Cryosphere*, *12*(2), 685–699.
- 3505 Herraiz-Borreguero, L., Allison, I., Craven, M., Nicholls, K. W., & Rosenberg, M. A. (2013).

- Ice shelf/ocean interactions under the amery ice shelf: Seasonal variability and its effect on marine ice formation. *J. Geophys. Res. Oceans*, 118(12), 7117–7131.
- Hewitt, H. T., Roberts, M., Mathiot, P., Biastoch, A., Blockley, E., Chassignet, E. P., ... others (2020). Resolving and parameterising the ocean mesoscale in earth system models. *Current Climate Change Reports*, 6, 137–152.
- Hewitt, I. J. (2020). Subglacial plumes. *Annu. Rev. Fluid Mech.*, 52, 145-169. doi: [10.1146/annurev-fluid-010719-060252](https://doi.org/10.1146/annurev-fluid-010719-060252)
- Heywood, K. J., Locarnini, R. A., Frew, R. D., Dennis, P. F., & King, B. A. (1998). Transport and water masses of the Antarctic Slope Front system in the eastern Weddell Sea. *Ocean, Ice and Atmosphere: Interactions at the Antarctic Continental Margin, Antarctic Research Series*, 75, 203–214.
- Heywood, K. J., Naveira Garabato, A. C., & Stevens, D. (2002). High mixing rates in the abyssal Southern Ocean. *Nature*, 45, 1011–1014. doi: [10.1038/4151011a](https://doi.org/10.1038/4151011a)
- Hobbs, W., Spence, P., Meyer, A., Schroeter, S., Fraser, A. D., Reid, P., ... others (2024). Observational evidence for a regime shift in summer antarctic sea ice. *Journal of Climate*, 35(7), 2263–2275. doi: [10.1175/JCLI-D-23-0479.1](https://doi.org/10.1175/JCLI-D-23-0479.1)
- Hofmann, M., & Morales Maqueda, M. A. (2009). Geothermal heat flux and its influence on the oceanic abyssal circulation and radiocarbon distribution. *Geophys. Res. Lett.*, 36(3), L03603. doi: [10.1029/2008GL036078](https://doi.org/10.1029/2008GL036078)
- Hogg, A. M. (2010). An Antarctic circumpolar current driven by surface buoyancy forcing. *Geophys. Res. Lett.*, 37(23).
- Hogg, A. M., & Gayen, B. (2020). Ocean gyres driven by surface buoyancy forcing. *Geophys. Res. Lett.*, 47(16), e2020GL088539.
- Hogg, A. M., Meredith, M. P., Chambers, D. P., Abrahamsen, E. P., Hughes, C. W., & Morrison, A. K. (2015). Recent trends in the Southern Ocean eddy field. *J. Geophys. Res. Oceans*, 120(1), 257–267.
- Hogg, A. M., Penduff, T., Close, S. E., Dewar, W. K., Constantinou, N. C., & Martínez-Moreno, J. (2022). Circumpolar variations in the chaotic nature of Southern Ocean eddy dynamics. *J. Geophys. Res. Oceans*, 127. doi: [10.1029/2022jc018440](https://doi.org/10.1029/2022jc018440)
- Holland, D. M. (2001). Explaining the Weddell Polynya—a Large Ocean Eddy Shed at Maud Rise. *Science*, 292(5522), 1697–1700. doi: [10.1126/science.1059322](https://doi.org/10.1126/science.1059322)
- Holland, D. M., & Jenkins, A. (1999). Modeling thermodynamic ice–ocean interactions at the base of an ice shelf. *J. Phys. Oceanogr.*, 29(8), 1787–1800.
- Holland, P. R. (2008). A model of tidally dominated ocean processes near ice shelf grounding lines. *J. Geophys. Res. Oceans*, 113(C11).
- Holmes, R. M., de Lavergne, C., & McDougall, T. J. (2018). Ridges, seamounts, troughs, and bowls: Topographic control of the dianutral circulation in the abyssal ocean. *J. Phys. Oceanogr.*, 48(4), 861-882. doi: [10.1175/JPO-D-17-0141.1](https://doi.org/10.1175/JPO-D-17-0141.1)
- Holmes, R. M., de Lavergne, C., & McDougall, T. J. (2019). Tracer transport within abyssal mixing layers. *J. Phys. Oceanogr.*, 49(10), 2669-2695. doi: [10.1175/JPO-D-19-0006.1](https://doi.org/10.1175/JPO-D-19-0006.1)
- Holmes, R. M., & McDougall, T. J. (2020). Diapycnal transport near a sloping bottom boundary. *J. Phys. Oceanogr.*, 50(11), 3253–3266. doi: [10.1175/JPO-D-20-0066.1](https://doi.org/10.1175/JPO-D-20-0066.1)
- Holmes, R. M., Zika, J. D., Griffies, S. M., Hogg, A. M., Kiss, A. E., & England, M. H. (2021). The geography of numerical mixing in a suite of global ocean models. *J. Adv. Model. Earth Syst.*, 13(7), e2020MS002333. doi: [10.1029/2020MS002333](https://doi.org/10.1029/2020MS002333)
- Holte, J. W., Talley, L. D., Chereskin, T. K., & Sloyan, B. M. (2012). The role of air-sea fluxes in subantarctic mode water formation. *J. Geophys. Res. Oceans*, 117(C3). doi: [10.1029/2011JC007798](https://doi.org/10.1029/2011JC007798)
- Hopfinger, E., & Van Heijst, G. (1993). Vortices in rotating fluids. *Annu. Rev. Fluid Mech.*, 25(1), 241–289.
- Hoppmann, M., Richter, M. E., Smith, I. J., Jendersie, S., Langhorne, P. J., Thomas, D. N., & Dieckmann, G. S. (2020). Platelet ice, the Southern Ocean’s hidden ice: a review. *Ann. Glaciol.*, 61(83), 341–368.
- Horgan, H. J., Alley, R. B., Christianson, K., Jacobel, R. W., Anandakrishnan, S., Muto, A., ... Siegfried, M. R. (2013). Estuaries beneath ice sheets. *Geology*, 41(11), 1159–1162.

- 3561 Horvat, C. (2022). Floes, the marginal ice zone and coupled wave-sea-ice feedbacks. *Philos.*  
3562 *Trans. Royal Soc. A*, *380*(2235), 20210252.
- 3563 Howard, S., Hyatt, J., & Padman, L. (2004). Mixing in the pycnocline over the western  
3564 Antarctic peninsula shelf during Southern Ocean GLOBEC. *Deep-Sea Res. II: Top.*  
3565 *Stud. Oceanogr.*, *51*(17), 1965-1979. doi: [10.1016/j.dsr2.2004.08.002](https://doi.org/10.1016/j.dsr2.2004.08.002)
- 3566 Howard, S. L., Erofeeva, S., & Padman, L. (2019). CATS2008: Circum-Antarctic  
3567 tidal simulation version 2008. *U.S. Antarctic Program (USAP) Data Center*. doi:  
3568 [10.15784/601235](https://doi.org/10.15784/601235)
- 3569 Hughes, C. W. (1997). Comments on “on the obscurantist physics of ‘form drag’ in theorizing  
3570 about the circumpolar current”. *J. Phys. Oceanogr.*, *27*(1), 209–210.
- 3571 Hughes, C. W., Fukumori, I., Griffies, S. M., Huthnance, J. M., Minobe, S., Spence, P., ...  
3572 Wise, A. (2019). Sea level and the role of coastal trapped waves in mediating the  
3573 influence of the open ocean on the coast. *Surveys in Geophysics*, *40*(6), 1467–1492.
- 3574 Hughes, T. (2002). Calving bays. *Quaternary Science Reviews*, *21*(1-3), 267–282.
- 3575 Humphries, R. S., Klekociuk, A. R., Schofield, R., Keyword, M., Ward, J., & Wilson, S. R.  
3576 (2016). Unexpectedly high ultrafine aerosol concentrations above East Antarctic sea  
3577 ice. *Atmos. Chem. Phys.*, *16*(4), 2185–2206. doi: [10.5194/acp-16-2185-2016](https://doi.org/10.5194/acp-16-2185-2016)
- 3578 Huneke, W. G. C., Morrison, A. K., & Hogg, A. M. (2022). Spatial and subannual variability  
3579 of the Antarctic Slope Current in an eddying ocean-sea ice model. *J. Phys. Oceanogr.*,  
3580 *52*(3), 347–361. doi: [10.1175/JPO-D-21-0143.1](https://doi.org/10.1175/JPO-D-21-0143.1)
- 3581 Huthnance, J. M. (1978). On coastal trapped waves: Analysis and numerical calculation  
3582 by inverse iteration. *J. Phys. Oceanogr.*, *8*(1), 74–92.
- 3583 Ijichi, T., St. Laurent, L., Polzin, K. L., & Toole, J. M. (2020). How variable is mixing  
3584 efficiency in the abyss? *Geophys. Res. Lett.*, *47*(7), e2019GL086813. doi:  
3585 [10.1029/2019GL086813](https://doi.org/10.1029/2019GL086813)
- 3586 Ito, T., & Marshall, J. (2008). Control of Lower-Limb Overturning Circulation in the South-  
3587 ern Ocean by Diapycnal Mixing and Mesoscale Eddy Transfer. *J. Phys. Oceanogr.*,  
3588 *38*(12), 2832–2845. doi: [10.1175/2008JPO3878.1](https://doi.org/10.1175/2008JPO3878.1)
- 3589 Iudicone, D., Madec, G., Blanke, B., & Speich, S. (2008). The role of Southern Ocean surface  
3590 forcings and mixing in the global conveyor. *J. Phys. Oceanogr.*, *38*(7), 1377–1400.
- 3591 Ivchenko, V. O., Tréguier, A.-M., & Best, S. (1997). A kinetic energy budget and internal  
3592 instabilities in the fine resolution antarctic model. *J. Phys. Oceanogr.*, *27*(1), 5–22.
- 3593 Jacobs, S. S. (2004). Bottom water production and its links with the thermohaline circula-  
3594 tion. *Antarctic Science*, *16*(4), 427–437.
- 3595 Jacobs, S. S., Helmer, H., Doake, C., Jenkins, A., & Frolich, R. (1992). Melting of ice  
3596 shelves and the mass balance of Antarctica. *J. Glaciol.*, *38*(130), 375–387.
- 3597 Jansen, M. F., Adcroft, A., Khani, S., & Kong, H. (2019). Toward an energetically con-  
3598 sistent, resolution aware parameterization of ocean mesoscale eddies. *J. Adv. Model.*  
3599 *Earth Syst.*, *11*(8), 2844–2860.
- 3600 Janssen, P. A. E. M. (2003). Nonlinear four-wave interactions and freak waves. *J. Phys.*  
3601 *Oceanogr.*, *33*(4), 863–884.
- 3602 Jayne, S. R., & St. Laurent, L. C. (2001). Parameterizing tidal dissipation over rough  
3603 topography. *Geophys. Res. Lett.*, *28*(5), 811–814.
- 3604 Jena, B., Ravichandran, M., & Turner, J. (2019). Recent Reoccurrence of Large Open-  
3605 Ocean Polynya on the Maud Rise Seamount. *Geophys. Res. Lett.*, *46*(8), 4320–4329.  
3606 doi: [10.1029/2018gl081482](https://doi.org/10.1029/2018gl081482)
- 3607 Jenkins, A. (1991). A one-dimensional model of ice shelf-ocean interaction. *Journal of*  
3608 *Geophysical Research: Oceans*, *96*(C11), 20671–20677.
- 3609 Jenkins, A., Nicholls, K. W., & Corr, H. F. (2010). Observation and parameterization  
3610 of ablation at the base of Ronne Ice Shelf, Antarctica. *J. Phys. Oceanogr.*, *40*(10),  
3611 2298–2312. doi: [10.1175/2010JPO4317.1](https://doi.org/10.1175/2010JPO4317.1)
- 3612 Jeon, C., Park, J.-H., Nakamura, H., Nishina, A., Zhu, X.-H., Kim, D. G., ... Hirose, N.  
3613 (2019). Poleward-propagating near-inertial waves enabled by the western boundary  
3614 current. *Sci. Rep.*, *9*(1), 9955.

- 3615 Jiang, J., Lu, Y., & Perrie, W. (2005). Estimating the energy flux from the wind to ocean  
3616 inertial motions: The sensitivity to surface wind fields. *Geophys. Res. Lett.*, *32*(15).
- 3617 Jing, Z., Wu, L., Li, L., Liu, C., Liang, X., Chen, Z., . . . Liu, Q. (2011). Turbulent diapycnal  
3618 mixing in the subtropical northwestern Pacific: Spatial-seasonal variations and role of  
3619 eddies. *J. Geophys. Res. Oceans*, *116*(C10).
- 3620 Jochum, M., Briegleb, B. P., Danabasoglu, G., Large, W. G., Norton, N. J., Jayne, S. R.,  
3621 . . . Bryan, F. O. (2013). The impact of oceanic near-inertial waves on climate. *J.*  
3622 *Climate*, *26*(9), 2833–2844.
- 3623 Johnson, G. C. (2008). Quantifying Antarctic bottom water and North Atlantic deep water  
3624 volumes. *J. Geophys. Res. Oceans*, *113*(C5). doi: [10.1029/2007JC004477](https://doi.org/10.1029/2007JC004477)
- 3625 Johnson, G. C., Hosoda, S., Jayne, S. R., Oke, P. R., Riser, S. C., Roemmich, D., . . . Xu,  
3626 J. (2022). Argo—two decades: Global oceanography, revolutionized. *Ann. Rev. Mar.*  
3627 *Sci.*, *14*, 379–403.
- 3628 Johnston, T. S., Rudnick, D. L., & Kelly, S. M. (2015). Standing internal tides in the  
3629 Tasman Sea observed by gliders. *J. Phys. Oceanogr.*, *45*(11), 2715–2737.
- 3630 Jones, H., & Marshall, J. (1997). Restratification after deep convection. *J. Phys. Oceanogr.*,  
3631 *27*(10), 2276–2287. doi: [10.1175/1520-0485\(1997\)027<2276:RADC>2.0.CO;2](https://doi.org/10.1175/1520-0485(1997)027<2276:RADC>2.0.CO;2)
- 3632 Jones, J. M., Gille, S. T., Goosse, H., Abram, N. J., Canziani, P. O., Charman, D. J., . . .  
3633 others (2016). Assessing recent trends in high-latitude southern hemisphere surface  
3634 climate. *Nature Climate Change*, *6*(10), 917–926.
- 3635 Joughin, I., Alley, R. B., & Holland, D. M. (2012). Ice-sheet response to oceanic forcing.  
3636 *science*, *338*(6111), 1172–1176.
- 3637 Joughin, I., & Padman, L. (2003). Melting and freezing beneath filchner-ronne ice shelf,  
3638 antarctica. *Geophys. Res. Lett.*, *30*(9).
- 3639 Jourdain, N. C., Asay-Davis, X., Hattermann, T., Straneo, F., Seroussi, H., Little, C. M., &  
3640 Nowicki, S. (2020). A protocol for calculating basal melt rates in the ismip6 antarctic  
3641 ice sheet projections. *Cryosphere*, *14*(9), 3111–3134.
- 3642 Jouvét, G., Weidmann, Y., Kneib, M., Detert, M., Seguinot, J., Sakakibara, D., & Sugiyama,  
3643 S. (2018). Short-lived ice speed-up and plume water flow captured by a vtol uav give  
3644 insights into subglacial hydrological system of bowdoin glacier. *Remote sensing of*  
3645 *environment*, *217*, 389–399.
- 3646 Jullien, S., Masson, S., Oerder, V., Samson, G., Colas, F., & Renault, L. (2020). Impact of  
3647 ocean-atmosphere current feedback on ocean mesoscale activity: Regional variations  
3648 and sensitivity to model resolution. *J. Climate*, *33*(7), 2585–2602. doi: [10.1175/JCLI-](https://doi.org/10.1175/JCLI-D-19-0484.1)  
3649 [D-19-0484.1](https://doi.org/10.1175/JCLI-D-19-0484.1)
- 3650 Jullien, L., Naveira Garabato, A. C., Bacon, S., Meredith, M. P., Brown, P. J., Torres-  
3651 Valdés, S., . . . others (2014). The contribution of the weddell gyre to the lower limb  
3652 of the global overturning circulation. *J. Geophys. Res. Oceans*, *119*(6), 3357–3377.
- 3653 Kacimi, S., & Kwok, R. (2020). The antarctic sea ice cover from icesat-2 and cryosat-2:  
3654 freeboard, snow depth, and ice thickness. *The Cryosphere*, *14*(12), 4453–4474.
- 3655 Kantha, L. H., & Clayson, C. A. (2000). Chapter 6 - internal waves. In *Small scale processes*  
3656 *in geophysical fluid flows* (Vol. 67, p. 615–683). Academic Press. doi: [10.1016/S0074-](https://doi.org/10.1016/S0074-6142(00)80082-0)  
3657 [6142\(00\)80082-0](https://doi.org/10.1016/S0074-6142(00)80082-0)
- 3658 Karsten, R., Jones, H., & Marshall, J. (2002). The role of eddy transfer in setting the  
3659 stratification and transport of a circumpolar current. *J. Phys. Oceanogr.*, *32*(1), 39–  
3660 54.
- 3661 Keller, J. B. (1998). Gravity waves on ice-covered water. *J. Geophys. Res. Oceans*, *103*(C4),  
3662 7663–7669.
- 3663 Kerr, R. C., & McConnochie, C. D. (2015). Dissolution of a vertical solid surface by turbulent  
3664 compositional convection. *J. Fluid Mech.*, *765*, 211–228. doi: [10.1017/jfm.2014.722](https://doi.org/10.1017/jfm.2014.722)
- 3665 Khan, S. S., Echevarria, E. R., & Hemer, M. A. (2021). Ocean swell comparisons between  
3666 Sentinel-1 and WAVEWATCH III around Australia. *J. Geophys. Res. Oceans*, *126*(2),  
3667 e2020JC016265.
- 3668 Khatiwala, S., Primeau, F., & Hall, T. (2009). Reconstruction of the history of anthro-  
3669 pogenic CO<sub>2</sub> concentrations in the ocean. *Nature*, *462*, 346–349.

- 3670 Kilbourne, B., & Girtton, J. (2015). Surface boundary layer evolution and near-inertial wind  
3671 power input. *J. Geophys. Res. Oceans*, *120*(11), 7506–7520.
- 3672 Killworth, P. D. (1983). Deep convection in the world ocean. *Rev. Geophys.*, *21*(1), 1–26.
- 3673 Kimura, S., Nicholls, K. W., & Venables, E. (2015). Estimation of ice shelf melt rate in  
3674 the presence of a thermohaline staircase. *J. Phys. Oceanogr.*, *45*(1), 133–148. doi:  
3675 [10.1175/JPO-D-14-0106.1](https://doi.org/10.1175/JPO-D-14-0106.1)
- 3676 King, J. (2014). A resolution of the antarctic paradox. *Nature*, *505*(7484), 491–492.
- 3677 King, M. A., & Padman, L. (2005). Accuracy assessment of ocean tide models around  
3678 antarctica. *Geophys. Res. Lett.*, *32*(23). doi: [10.1029/2005GL023901](https://doi.org/10.1029/2005GL023901)
- 3679 Kiss, A. E., Hogg, A. M., Hannah, N., Boeira Dias, F., Brassington, G. B., Chamberlain,  
3680 M. A., ... others (2020). ACCESS-OM2 v1.0: A global ocean–sea ice model at three  
3681 resolutions. *Geosci. Model Dev.*, *13*(2), 401–442.
- 3682 Klein, P., Lapeyre, G., & Large, W. (2004). Wind ringing of the ocean in presence of  
3683 mesoscale eddies. *Geophys. Res. Lett.*, *31*(15).
- 3684 Klingbeil, K., Burchard, H., Danilov, S., Goetz, C., & Iske, A. (2019). Reducing spurious  
3685 diapycnal mixing in ocean models. *Energy Transfers in Atmosphere and Ocean*, 245–  
3686 286.
- 3687 Klocker, A. (2018). Opening the window to the Southern Ocean: The role of jet dynamics.  
3688 *Sci. Adv.*, *4*. doi: [10.1126/sciadv.aao4719](https://doi.org/10.1126/sciadv.aao4719)
- 3689 Klocker, A., & Marshall, D. P. (2014). Advection of baroclinic eddies by depth mean flow.  
3690 *Geophys. Res. Lett.*, *41*, 3517–3521. doi: [10.1002/2014GL060001](https://doi.org/10.1002/2014GL060001)
- 3691 Klocker, A., Marshall, D. P., Keating, S. R., & Read, P. L. (2016). A regime diagram for  
3692 ocean geostrophic turbulence. *Q. J. R. Meteor. Soc.*
- 3693 Klocker, A., & McDougall, T. J. (2010). Influence of the Nonlinear Equation of State on  
3694 Global Estimates of Dianeutral Advection and Diffusion. *J. Phys. Oceanogr.*, *40*(8),  
3695 1690–1709. doi: [10.1175/2010JPO4303.1](https://doi.org/10.1175/2010JPO4303.1)
- 3696 Kohout, A. L., & Meylan, M. H. (2008). An elastic plate model for wave attenuation and  
3697 ice floe breaking in the marginal ice zone. *J. Geophys. Res. Oceans*, *113*(C9).
- 3698 Kohout, A. L., Meylan, M. H., & Plew, D. R. (2011). Wave attenuation in a marginal ice  
3699 zone due to the bottom roughness of ice floes. *Ann. Glaciol.*, *52*(57), 118–122.
- 3700 Kohout, A. L., Smith, M., Roach, L. A., Williams, G., Montiel, F., & Williams, M. J.  
3701 (2020). Observations of exponential wave attenuation in Antarctic sea ice during the  
3702 PIPERS campaign. *Ann. Glaciol.*, *61*(82), 196–209.
- 3703 Kohout, A. L., Williams, M. J. M., Dean, S. M., & Meylan, M. H. (2014). Storm-induced  
3704 sea-ice breakup and the implications for ice extent. *Nature*, *509*(7502), 604–607.
- 3705 Kopp, R. E., Horton, R. M., Little, C. M., Mitrovica, J. X., Oppenheimer, M., Rasmussen,  
3706 D., ... Tebaldi, C. (2014). Probabilistic 21st and 22nd century sea-level projections  
3707 at a global network of tide-gauge sites. *Earth's future*, *2*(8), 383–406.
- 3708 Kraitzman, N., Promislow, K., & Wetton, B. (2022). Slow migration of brine inclusions in  
3709 first-year sea ice. *SIAM Journal on Applied Mathematics*, *82*(4), 1470–1494.
- 3710 Kreuzer, M., Reese, R., Huiskamp, W. N., Petri, S., Albrecht, T., Feulner, G., & Winkel-  
3711 mann, R. (2021). Coupling framework (1.0) for the pism (1.1. 4) ice sheet model  
3712 and the mom5 (5.1. 0) ocean model via the pico ice shelf cavity model in an antarctic  
3713 domain. *Geosci. Model Dev.*, *14*(6), 3697–3714.
- 3714 Kunze, E. (1985). Near-inertial wave propagation in geostrophic shear. *J. Phys. Oceanogr.*,  
3715 *15*(5), 544–565.
- 3716 Kunze, E., Firing, E., Hummon, J. M., Chereskin, T. K., & Thurnherr, A. M. (2006).  
3717 Global abyssal mixing inferred from lowered ADCP shear and CTD strain profiles. *J.*  
3718 *Phys. Oceanogr.*, *36*(8), 1553–1576.
- 3719 Kunze, E., & Lien, R.-C. (2019). Energy sinks for lee waves in shear flow. *J. Phys. Oceanogr.*,  
3720 *49*(11), 2851–2865.
- 3721 Kurtakoti, P., Veneziani, M., Stössel, A., & Weijer, W. (2018). Preconditioning and for-  
3722 mation of Maud Rise polynyas in a high-resolution Earth system model. *J. Climate*,  
3723 *31*(23), 9659–9678. doi: [10.1175/JCLI-D-18-0392.1](https://doi.org/10.1175/JCLI-D-18-0392.1)

- 3724 Kurtakoti, P., Veneziani, M., Stössel, A., Weijer, W., & Maltrud, M. (2021). On the  
3725 Generation of Weddell Sea Polynyas in a High-Resolution Earth System Model. *J.*  
3726 *Climate*, *34*(7), 2491–2510. doi: [10.1175/jcli-d-20-0229.1](https://doi.org/10.1175/jcli-d-20-0229.1)
- 3727 Kusahara, K., & Hasumi, H. (2014). Pathways of basal meltwater from antarctic ice shelves:  
3728 A model study. *J. Geophys. Res. Oceans*, *119*(9), 5690–5704.
- 3729 Lago, V., & England, M. H. (2019). Projected slowdown of Antarctic bottom water forma-  
3730 tion in response to amplified meltwater contributions. *J. Climate*, *32*(19), 6319–6335.
- 3731 Lai, C.-Y., Kingslake, J., Wearing, M. G., Chen, P.-H. C., Gentine, P., Li, H., ... van  
3732 Wessem, J. M. (2020). Vulnerability of Antarctica’s ice shelves to meltwater-driven  
3733 fracture. *Nature*, *584*(7822), 574–578.
- 3734 Landerer, F. W., Wiese, D. N., Bentel, K., Boening, C., & Watkins, M. M. (2015). North at-  
3735 lantic meridional overturning circulation variations from grace ocean bottom pressure  
3736 anomalies. *Geophys. Res. Lett.*, *42*(19), 8114–8121.
- 3737 Landwehr, S., Volpi, M., Haumann, F. A., Robinson, C. M., Thurnherr, I., Ferracci, V.,  
3738 ... Schmale, J. (2021). Exploring the coupled ocean and atmosphere system with  
3739 a data science approach applied to observations from the Antarctic circumnavigation  
3740 expedition. *Earth Syst. Dyn.*, *12*(4), 1295–1369. doi: [10.5194/esd-12-1295-2021](https://doi.org/10.5194/esd-12-1295-2021)
- 3741 Lange, M., Ackley, S., Wadhams, P., Dieckmann, G., & Eicken, H. (1989). Development of  
3742 sea ice in the Weddell Sea. *Ann. Glaciol.*, *12*, 92–96.
- 3743 Langlais, C. E., Lenton, A., Matear, R., Monselesan, D., Legresy, B., Cougnon, E., &  
3744 Rintoul, S. (2017). Stationary rossby waves dominate subduction of anthropogenic  
3745 carbon in the Southern Ocean. *Sci. Rep.*, *7*(1), 1–10.
- 3746 Langlais, C. E., Rintoul, S. R., & Zika, J. D. (2015). Sensitivity of antarctic circumpolar  
3747 current transport and eddy activity to wind patterns in the southern ocean. *Journal*  
3748 *of Physical Oceanography*, *45*(4), 1051–1067.
- 3749 Laurent, L. S., Naveira Garabato, A. C., Ledwell, J. R., Thurnherr, A. M., Toole, J. M., &  
3750 Watson, A. J. (2012). Turbulence and diapycnal mixing in Drake Passage. *J. Phys.*  
3751 *Oceanogr.*, *42*(12), 2143–2152. doi: [10.1175/JPO-D-12-027.1](https://doi.org/10.1175/JPO-D-12-027.1)
- 3752 Lawrence, J. D., Washam, P. M., Stevens, C. L., Hulbe, C., Horgan, H. J., Dunbar, G.,  
3753 ... Schmidt, B. E. (2023). Crevasse refreezing and signatures of retreat observed at  
3754 Kamb Ice Stream grounding zone. *Nat. Geosci.*, *16*, 238–243. doi: [10.1038/s41561-023-01129-y](https://doi.org/10.1038/s41561-023-01129-y)
- 3755
- 3756 Leaman, K. D., & Sanford, T. B. (1975). Vertical energy propagation of inertial waves: A  
3757 vector spectral analysis of velocity profiles. *Journal of Geophysical Research*, *80*(15),  
3758 1975–1978.
- 3759 Ledwell, J. R., Laurent, L. C. S., Girton, J. B., & Toole, J. M. (2011). Diapycnal mixing  
3760 in the Antarctic Circumpolar Current. *J. Phys. Oceanogr.*, *41*(1), 241–246. doi:  
3761 [10.1175/2010JPO4557.1](https://doi.org/10.1175/2010JPO4557.1)
- 3762 Lefaive, A., Muller, C., & Melet, A. (2015). A three-dimensional map of tidal dissipation  
3763 over abyssal hills. *J. Geophys. Res. Oceans*, *120*(7), 4760–4777.
- 3764 Lellouche, J.-M., Le Galloudec, O., Greiner, E., Garric, G., Regnier, C., Drevillon, M., &  
3765 Le Traon, P. (2018). The copernicus marine environment monitoring service global  
3766 ocean 1/12 physical reanalysis glorys12v1: description and quality assessment. In *Egu*  
3767 *general assembly conference abstracts* (Vol. 20, p. 19806).
- 3768 Leppäranta, M. (2011). *The drift of sea ice*. Springer Science & Business Media.
- 3769 Levitus, S., Antonov, J. I., Boyer, T. P., Baranova, O. K., Garcia, H. E., Locarnini, R. A.,  
3770 ... others (2012). World ocean heat content and thermosteric sea level change (0–2000  
3771 m), 1955–2010. *Geophys. Res. Lett.*, *39*(10).
- 3772 Lewis, E., & Perkin, R. (1986). Ice pumps and their rates. *J. Geophys. Res. Oceans*,  
3773 *91*(C10), 11756–11762.
- 3774 Li, Q., England, M. H., Hogg, A. M., Rintoul, S. R., & Morrison, A. K. (2023). Abyssal  
3775 ocean overturning slowdown and warming driven by antarctic meltwater. *Nature*,  
3776 *615*(7954), 841–847.
- 3777 Li, Q., & Fox-Kemper, B. (2020). Anisotropy of Langmuir turbulence and the Langmuir-  
3778 enhanced mixed layer entrainment. *Phys. Rev. Fluids*, *5*, 013803. doi: [10.1103/Phys-](https://doi.org/10.1103/Phys-)

- 3779 [RevFluids.5.013803](#)
- 3780 Li, Q., Lee, S., & Griesel, A. (2016). Eddy fluxes and jet-scale overturning circulations in  
3781 the indo-western pacific Southern Ocean. *J. Phys. Oceanogr.*, *46*(10), 2943–2959.
- 3782 Li, Z., England, M. H., Groeskamp, S., Cerovčki, I., & Luo, Y. (2022). The origin and  
3783 fate of Antarctic intermediate water in the Southern Ocean. *J. Phys. Oceanogr.*, *52*,  
3784 2873–2890. doi: [10.1175/JPO-D-21-0221.1](#)
- 3785 Liao, F., & Wang, X. H. (2018). A study of low-frequency, wind-driven, coastal-trapped  
3786 waves along the southeast coast of australia. *J. Phys. Oceanogr.*, *48*(2), 301–316.
- 3787 Light, B., Maykut, G., & Grenfell, T. (2003). Effects of temperature on the microstructure  
3788 of first-year Arctic sea ice. *J. Geophys. Res. Oceans*, *108*(C2).
- 3789 Lipovsky, B. P. (2018). Ice shelf rift propagation and the mechanics of wave-induced fracture.  
3790 *J. Geophys. Res. Oceans*, *123*(6), 4014–4033.
- 3791 Liu, J., Zhu, Z., & Chen, D. (2023). Lowest Antarctic sea ice record broken  
3792 broken for the second year in a row. *Ocean-Land-Atmosphere Research*, *0*(ja).  
3793 doi: [10.34133/olar.0007](#)
- 3794 Liu, R., Wang, G., Chapman, C., & Chen, C. (2022). The attenuation effect of jet filament  
3795 on the eastward mesoscale eddy lifetime in the Southern Ocean. *J. Phys. Oceanogr.*,  
3796 *52*, 805–822. doi: [10.1175/JPO-D-21-0030.1](#)
- 3797 Liu, Y., Moore, J. C., Cheng, X., Gladstone, R. M., Bassis, J. N., Liu, H., ... Hui, F.  
3798 (2015). Ocean-driven thinning enhances iceberg calving and retreat of Antarctic ice  
3799 shelves. *Proc. Natl. Acad. Sci. USA*, *112*(11), 3263–3268.
- 3800 Lobeto, H., Menendez, M., & Losada, I. J. (2021). Future behavior of wind wave extremes  
3801 due to climate change. *Sci. Rep.*, *11*(1), 1–12.
- 3802 Loder, J. W. (1980). Topographic rectification of tidal currents on the sides of  
3803 Georges bank. *J. Phys. Oceanogr.*, *10*(9), 1399–1416. doi: [10.1175/1520-  
3804 0485\(1980\)010<1399:TROTCO>2.0.CO;2](#)
- 3805 Lumpkin, R., & Speer, K. (2007). Global ocean meridional overturning. *J. Phys. Oceanogr.*,  
3806 *37*(10), 2550–2562.
- 3807 Lund-Hansen, L. C., Sogaard, D. H., Sorrell, B. K., Gradinger, R., & Meiners, K. M. (2020).  
3808 *Arctic sea ice ecology*. Springer.
- 3809 Lundy, D. (2010). *Godforsaken sea: racing the world's most dangerous waters*. Vintage  
3810 Canada.
- 3811 Lyard, F., Lefevre, F., & Letellier, T. e. a. (2006). Modelling the global ocean tides: modern  
3812 insights from fes2004. *Ocean Dynamics*, *56*, 394–415.
- 3813 Lytle, V., & Ackley, S. (1996). Heat flux through sea ice in the western Weddell Sea:  
3814 convective and conductive transfer processes. *J. Geophys. Res. Oceans*, *101*(C4),  
3815 8853–8868.
- 3816 MacAyeal, D. R., Okal, E. A., Aster, R. C., Bassis, J. N., Brunt, K. M., Cathles, L. M.,  
3817 ... others (2006). Transoceanic wave propagation links iceberg calving margins of  
3818 Antarctica with storms in tropics and Northern Hemisphere. *Geophys. Res. Lett.*,  
3819 *33*(17).
- 3820 MacGilchrist, G. A., Naveira Garabato, A. C., Brown, P. J., Jullion, L., Bacon, S., Bakker,  
3821 D. C., ... Torres-Valdés, S. (2019). Reframing the carbon cycle of the subpolar  
3822 Southern Ocean. *Sci. Adv.*, *5*(8), eaav6410.
- 3823 Mack, S. L., Dinniman, M. S., Klinck, J. M., McGillicuddy Jr, D. J., & Padman, L. (2019).  
3824 Modeling ocean eddies on Antarctica's cold water continental shelves and their effects  
3825 on ice shelf basal melting. *J. Geophys. Res. Oceans*, *124*(7), 5067–5084.
- 3826 Mackay, N., Ledwell, J. R., Messias, M., Naveira Garabato, A. C., Brearley, J. A., Meijers,  
3827 A. J. S., ... Watson, A. J. (2018). Diapycnal mixing in the Southern Ocean diagnosed  
3828 using the DIMES tracer and realistic velocity fields. *J. Geophys. Res.*, *0*(0). doi:  
3829 [10.1002/2017JC013536](#)
- 3830 Magruder, L. A., Farrell, S. L., Neuenschwander, A., Duncanson, L., Csatho, B., Kacimi,  
3831 S., & Fricker, H. A. (2024). Monitoring earth's climate variables with satellite laser  
3832 altimetry. *Nature Reviews Earth & Environment*, 1–17.
- 3833 Makinson, K., Holland, P. R., Jenkins, A., Nicholls, K. W., & Holland, D. M. (2011).

- 3834 Influence of tides on melting and freezing beneath filchner-ronne ice shelf, Antarctica.  
3835 *Geophys. Res. Lett.*, *38*(6).
- 3836 Makinson, K., & Nicholls, K. W. (1999). Modeling tidal currents beneath Filchner-Ronne  
3837 ice shelf and on the adjacent continental shelf: Their effect on mixing and transport.  
3838 *J. Geophys. Res. Oceans*, *104*(C6), 13449–13465. doi: [10.1029/1999JC900008](https://doi.org/10.1029/1999JC900008)
- 3839 Malyarenko, A., Robinson, N., Williams, M., & Langhorne, P. (2019). A wedge mechanism  
3840 for summer surface water inflow into the Ross ice shelf cavity. *J. Geophys. Res. Oceans*,  
3841 *124*(2), 1196–1214.
- 3842 Malyarenko, A., Wells, A. J., Langhorne, P. J., Robinson, N. J., Williams, M. J., &  
3843 Nicholls, K. W. (2020). A synthesis of thermodynamic ablation at ice–ocean in-  
3844 terfaces from theory, observations and models. *Ocean Model.*, *154*, 101692. doi:  
3845 [10.1016/j.ocemod.2020.101692](https://doi.org/10.1016/j.ocemod.2020.101692)
- 3846 Mankoff, K. D., Jacobs, S. S., Tulaczyk, S. M., & Stammerjohn, S. E. (2012). The role  
3847 of pine island glacier ice shelf basal channels in deep-water upwelling, polynyas and  
3848 ocean circulation in pine island bay, Antarctica. *Ann. Glaciol.*, *53*(60), 123–128.
- 3849 Manton, M., Huang, Y., & Siems, S. (2020). Variations in precipitation across the Southern  
3850 Ocean. *J. Climate*, *33*(24), 10653–10670.
- 3851 Marques, G. M., Padman, L., Springer, S. R., Howard, S. L., & Özgökmen, T. M. (2014).  
3852 Topographic vorticity waves forced by Antarctic dense shelf water outflows. *Geophys.*  
3853 *Res. Lett.*, *41*(4), 1247–1254. doi: [10.1002/2013GL059153](https://doi.org/10.1002/2013GL059153)
- 3854 Marshall, D. P., Ambaum, M. H. P., Maddison, J. R., Munday, D. R., & Novak, L. (2017).  
3855 Eddy saturation and frictional control of the Antarctic Circumpolar Current. *Geophys.*  
3856 *Res. Lett.*, *44*, 286–292. doi: [10.1002/2016GL071702](https://doi.org/10.1002/2016GL071702)
- 3857 Marshall, D. P., Maddison, J. R., & Berloff, P. S. (2012). A framework for parameterizing  
3858 eddy potential vorticity fluxes. *J. Phys. Oceanogr.*, *42*(4), 539–557.
- 3859 Marshall, D. P., & Naveira Garabato, A. C. (2008). A conjecture on the role of bottom-  
3860 enhanced diapycnal mixing in the parameterization of geostrophic eddies. *J. Phys.*  
3861 *Oceanogr.*, *38*(7), 1607–1613. doi: [10.1175/2007JPO3619.1](https://doi.org/10.1175/2007JPO3619.1)
- 3862 Marshall, J., & Radko, T. (2003). Residual-mean solutions for the Antarctic Circumpolar  
3863 Current and its associated overturning circulation. *J. Phys. Oceanogr.*, *33*, 2341–2354.
- 3864 Marshall, J., & Schott, F. (1999). Open-ocean convection: Observations, theory, and models.  
3865 *Rev. Geophys.*, *37*, 1–64.
- 3866 Marshall, J., & Speer, K. (2012). Closure of the meridional overturning circulation through  
3867 Southern Ocean upwelling. *Nat. Geosci.*, *5*, 171–180.
- 3868 Martin, S., & Becker, P. (1987). High-frequency ice floe collisions in the greenland sea during  
3869 the 1984 marginal ice zone experiment. *J. Geophys. Res. Oceans*, *92*(C7), 7071–7084.
- 3870 Martin, S., & Becker, P. (1988). Ice floe collisions and their relation to ice deformation in  
3871 the bering sea during february 1983. *J. Geophys. Res. Oceans*, *93*(C2), 1303–1315.
- 3872 Martin, T., Steele, M., & Zhang, J. (2014). Seasonality and long-term trend of Arctic  
3873 Ocean surface stress in a model. *J. Geophys. Res. Oceans*, *119*, 1723–1738. doi:  
3874 [10.1002/2013JC009425](https://doi.org/10.1002/2013JC009425)
- 3875 Martínez-Moreno, J., Hogg, A. M., England, M. H., Constantinou, N. C., Kiss, A. E., &  
3876 Morrison, A. K. (2021). Global changes in oceanic mesoscale currents over the satellite  
3877 altimetry record. *Nat. Clim. Chang.*, *11*(5), 397–403. doi: [10.1038/s41558-021-01006-9](https://doi.org/10.1038/s41558-021-01006-9)
- 3878
- 3879 Martini, K. I., Simmons, H. L., Stouidt, C. A., & Hutchings, J. K. (2014). Near-inertial  
3880 internal waves and sea ice in the Beaufort Sea. *J. Phys. Oceanogr.*, *44*(8), 2212–2234.  
3881 doi: [10.1175/JPO-D-13-0160.1](https://doi.org/10.1175/JPO-D-13-0160.1)
- 3882 Martinson, D. G. (1991). Open ocean convection in the Southern Ocean. In *Elsevier*  
3883 *oceanography series* (Vol. 57, pp. 37–52). Elsevier.
- 3884 Martinson, D. G., Killworth, P. D., & Gordon, A. L. (1981). A convective model for  
3885 the Weddell polynya. *J. Phys. Oceanogr.*, *11*(4), 466–488. doi: [10.1175/1520-0485\(1981\)011<0466:acmftw>2.0.co;2](https://doi.org/10.1175/1520-0485(1981)011<0466:acmftw>2.0.co;2)
- 3886
- 3887 Mashayek, A., Ferrari, R., Merrifield, S., Ledwell, J. R., St Laurent, L., & Naveira Garabato,  
3888 A. C. (2017). Topographic enhancement of vertical turbulent mixing in the Southern

- 3889 Ocean. *Nat. Commun.*, 8(1), 14197. doi: [10.1038/ncomms14197](https://doi.org/10.1038/ncomms14197)
- 3890 Mashayek, A., Salehipour, H., Bouffard, D., Caulfield, C. P., Ferrari, R., Nikurashin,  
3891 M., ... Smyth, W. D. (2017). Efficiency of turbulent mixing in the abyssal  
3892 ocean circulation. *Geophys. Res. Lett.*, 44(12), 6296–6306. (2016GL072452) doi:  
3893 [10.1002/2016GL072452](https://doi.org/10.1002/2016GL072452)
- 3894 Masich, J., Chereskin, T. K., & Mazloff, M. R. (2015a). Topographic form stress in the  
3895 Southern Ocean State Estimate. *J. Geophys. Res. Oceans*, 120(12), 7919–7933. doi:  
3896 [10.1002/2015JC011143](https://doi.org/10.1002/2015JC011143)
- 3897 Masich, J., Chereskin, T. K., & Mazloff, M. R. (2015b). Topographic form stress in the  
3898 Southern Ocean State Estimate. *J. Geophys. Res. Oceans*, 120(12), 7919–7933.
- 3899 Massom, R. A., Drinkwater, M. R., & Haas, C. (1997). Winter snow cover on sea ice in the  
3900 Weddell sea. *J. Geophys. Res. Oceans*, 102(C1), 1101–1117.
- 3901 Massom, R. A., Eicken, H., Hass, C., Jeffries, M. O., Drinkwater, M. R., Sturm, M., ...  
3902 others (2001). Snow on antarctic sea ice. *Rev. Geophys.*, 39(3), 413–445.
- 3903 Massom, R. A., Giles, A. B., Fricker, H. A., Warner, R. C., Legrésy, B., Hyland, G., ...  
3904 Fraser, A. D. (2010). Examining the interaction between multi-year landfast sea ice  
3905 and the mertz glacier tongue, east Antarctica: Another factor in ice sheet stability?  
3906 *J. Geophys. Res. Oceans*, 115(C12).
- 3907 Massom, R. A., Giles, A. B., Warner, R. C., Fricker, H. A., Legresy, B., Hyland, G., ...  
3908 Young, N. (2015). External influences on the Mertz Glacier Tongue (East Antarctica)  
3909 in the decade leading up to its calving in 2010. *J. Geophys. Res.: Earth Surface*,  
3910 120(3), 490–506.
- 3911 Massom, R. A., Scambos, T. A., Bennetts, L. G., Reid, P., Squire, V. A., & Stammerjohn,  
3912 S. E. (2018). Antarctic ice shelf disintegration triggered by sea ice loss and ocean  
3913 swell. *Nature*, 558(7710), 383–389. doi: [10.1038/s41586-018-0212-1](https://doi.org/10.1038/s41586-018-0212-1)
- 3914 Mathiot, P., Goosse, H., Fichefet, T., Barnier, B., & Gallée, H. (2011). Modelling the  
3915 seasonal variability of the Antarctic Slope Current. *Ocean Science*, 7, 455–470. doi:  
3916 [10.5194/os-7-455-2011](https://doi.org/10.5194/os-7-455-2011)
- 3917 Mathiot, P., Jenkins, A., Harris, C., & Madec, G. (2017). Explicit representation and  
3918 parametrised impacts of under ice shelf seas in the  $z^*$  coordinate ocean model nemo  
3919 3.6. *Geosci. Model Dev.*, 10(7), 2849–2874.
- 3920 Mayer, K. J., Sauer, J. S., Dinasquet, J., & Prather, K. A. (2020). CAICE studies: In-  
3921 sights from a decade of ocean–atmosphere experiments in the laboratory. *Accounts of*  
3922 *chemical research*, 53(11), 2510–2520.
- 3923 Mazloff, M. R., Heimbach, P., & Wunsch, C. (2010). An eddy-permitting southern ocean  
3924 state estimate. *J. Phys. Oceanogr.*, 40(5), 880–899.
- 3925 McCartney, M. S. (1977). Subantarctic mode water. *Deep Sea Res.*, 24, 103–119.
- 3926 McComas, C. H., & Bretherton, F. P. (1977). Resonant interaction of oceanic internal  
3927 waves. *J. Geophys. Res.*, 82(9), 1397–1412.
- 3928 McConnochie, C. D., & Kerr, R. (2017b). Testing a common ice-ocean parameteriza-  
3929 tion with laboratory experiments. *J. Geophys. Res. Oceans*, 122(7), 5905–5915. doi:  
3930 [10.1002/2017JC012918](https://doi.org/10.1002/2017JC012918)
- 3931 McConnochie, C. D., & Kerr, R. C. (2017a). Enhanced ablation of a vertical ice  
3932 wall due to an external freshwater plume. *J. Fluid Mech.*, 810, 429–447. doi:  
3933 [10.1017/jfm.2016.761](https://doi.org/10.1017/jfm.2016.761)
- 3934 McCutchan, A. L., & Johnson, B. A. (2022). Laboratory experiments on ice melting: A  
3935 need for understanding dynamics at the ice-water interface. *Journal of Marine Science*  
3936 *and Engineering*, 10(8), 1008.
- 3937 McDougall, T. J. (1987). Thermobaricity, cabbeling, and water-mass conversion. *Journal*  
3938 *of Geophysical Research: Oceans*, 92(C5), 5448–5464.
- 3939 McDougall, T. J., & Ferrari, R. (2017). Abyssal upwelling and downwelling driven by  
3940 near-boundary mixing. *J. Phys. Oceanogr.*, 47(2), 261–283.
- 3941 McGillicuddy Jr, D. J. (2016). Mechanisms of physical-biological-biogeochemical interaction  
3942 at the oceanic mesoscale. *Ann. Rev. of Mar. Sci.*, 8, 125–159.
- 3943 McKee, D. C., Yuan, X., Gordon, A. L., Huber, B. A., & Dong, Z. (2011). Climate impact on

- interannual variability of weddell sea bottom water. *Journal of Geophysical Research: Oceans*, 116(C5).
- McPhee, M. G. (2008). *Air-ice-ocean interaction: Turbulent ocean boundary layer exchange processes*. Springer Science & Business Media.
- McPhee, M. G., & Kantha, L. H. (1989). Generation of internal waves by sea ice. *J. Geophys. Res. Oceans*, 94(C3), 3287–3302.
- McWilliams, J. C. (2016). Submesoscale currents in the ocean. *Proc. Royal Soc. Lond.*, 472(2189), 20160117.
- McWilliams, J. C. (2021). Oceanic frontogenesis. *Ann. Rev. Mar. Sci.*, 13(1), 227–253. doi: [10.1146/annurev-marine-032320-120725](https://doi.org/10.1146/annurev-marine-032320-120725)
- Megann, A., Chanut, J., & Storkey, D. (2022). Assessment of the  $z$  time-filtered arbitrary Lagrangian-Eulerian coordinate in a global eddy-permitting ocean model. *J. Adv. Model. Earth Syst.*, 14(11), e2022MS003056.
- Meier, M. (1997). The iceberg discharge process: observations and inferences drawn from the study of columbia glacier. *Byrd Polar Research Center Report No. 15*, 109–114.
- Meijer, J. J., Phillips, H. E., Bindoff, N. L., & Rintoul, A., S. R. Foppert. (2022). Dynamics of a standing meander of the subantarctic front diagnosed from satellite altimetry and along-stream anomalies of temperature and salinity. *J. Phys. Oceanogr.*, 52(6), 1073–1089.
- Melet, A., Hallberg, R., Adcroft, A., Nikurashin, M., & Legg, S. (2015). Energy flux into internal lee waves: Sensitivity to future climate changes using linear theory and a climate model. *J. Climate*, 28(6), 2365–2384. doi: [10.1175/JCLI-D-14-00432.1](https://doi.org/10.1175/JCLI-D-14-00432.1)
- Melet, A., Hallberg, R., Legg, S., & Nikurashin, M. (2014). Sensitivity of the ocean state to lee wave-driven mixing. *J. Phys. Oceanogr.*, 44(3), 900–921. doi: [10.1175/JPO-D-13-072.1](https://doi.org/10.1175/JPO-D-13-072.1)
- Melet, A., Nikurashin, M., Muller, C., Falahat, S., Nycander, J., Timko, P. G., ... Goff, J. A. (2013). Internal tide generation by abyssal hills using analytical theory. *J. Geophys. Res. Oceans*, 118(11), 6303–6318.
- Melville, W. K. (1996). The role of surface-wave breaking in air-sea interaction. *Annu. Rev. Fluid Mech.*, 28(1), 279–321.
- Meneghello, G., Marshall, J. C., Campin, J.-M., Doddridge, E. W., & Timmermans, M.-L. (2018). The ice-ocean governor: ice-ocean stress feedback limits Beaufort gyre spin-up. *Geophys. Res. Lett.*, 45, 11,293–11,299. doi: [10.1029/2018GL080171](https://doi.org/10.1029/2018GL080171)
- Meredith, M. P. (2013). Replenishing the abyss. *Nat. Geosci.*, 6(3), 166–167.
- Meredith, M. P. (2022). Carbon storage shifts around Antarctica. *Nat. Commun.*, 13(1), 1–3.
- Meredith, M. P., Gordon, A. L., Naveira Garabato, A. C., Abrahamsen, E. P., Huber, B. A., Jullion, L., & Venables, H. J. (2011). Synchronous intensification and warming of Antarctic bottom water outflow from the Weddell gyre. *Geophys. Res. Lett.*, 38(3).
- Meredith, M. P., & Hogg, A. M. (2006). Circumpolar response of Southern Ocean eddy activity to a change in the Southern Annular Mode. *Geophys. Res. Lett.*, 33, 2–5. doi: [10.1029/2006GL026499](https://doi.org/10.1029/2006GL026499)
- Meredith, M. P., Jullion, L., Brown, P. J., Naveira Garabato, A. C., & Couldrey, M. P. (2014). Dense waters of the Weddell and Scotia seas: recent changes in properties and circulation. *Philos. Trans. R. Soc. A*, 372(2019), 20130041.
- Meredith, M. P., & Naveira Garabato, A. C. (2021). *Ocean mixing: drivers, mechanisms and impacts*.
- Meredith, M. P., Naveira Garabato, A. C., Gordon, A. L., & Johnson, G. C. (2008). Evolution of the deep and bottom waters of the scotia sea, Southern Ocean, during 1995–2005. *J. Climate*, 21(13), 3327–3343.
- Meredith, M. P., Naveira Garabato, A. C., Hogg, A. M., & Farneti, R. (2012). Sensitivity of the overturning circulation in the Southern Ocean to decadal changes in wind forcing. *J. Climate*, 25(1), 99–110.
- Meucci, A., Young, I. R., Aarnes, O. J., & Breivik, Ø. (2020). Comparison of wind speed and wave height trends from twentieth-century models and satellite altimeters. *J.*

- 3999 *Climate*, 33(2), 611–624.
- 4000 Meucci, A., Young, I. R., Hemer, M., Kirezci, E., & Ranasinghe, R. (2020). Projected  
4001 21st century changes in extreme wind-wave events. *Sci. Adv.*, 6(24). doi: [10.1126/sci-adv.aaz7295](https://doi.org/10.1126/sci-adv.aaz7295)
- 4002
- 4003 Meucci, A., Young, I. R., Hemer, M., Trenham, C., & Watterson, I. G. (2023). 140 years of  
4004 global ocean wind-wave climate derived from CMIP6 ACCESS-CM2 and EC-Earth3  
4005 GCMs: Global trends, regional changes, and future projections. *J. Climate*, 36(6),  
4006 1605–1631.
- 4007 Meyer, A., Polzin, K. L., Sloyan, B. M., & Phillips, H. E. (2015). Internal waves and mixing  
4008 near the Kerguelen plateau. *J. Phys. Oceanogr.*, 46(2), 417–437. doi: [10.1175/JPO-D-15-0055.1](https://doi.org/10.1175/JPO-D-15-0055.1)
- 4009
- 4010 Meyer, A., Sloyan, B. M., Polzin, K. L., Phillips, H. E., & Bindoff, N. L. (2015). Mixing  
4011 variability in the Southern Ocean. *J. Phys. Oceanogr.*, 45(4), 966–987.
- 4012 Meylan, M. H., & Bennetts, L. G. (2018). Three-dimensional time-domain scattering of  
4013 waves in the marginal ice zone. *Philos. Trans. Royal Soc. A*, 376(2129), 20170334.
- 4014 Meylan, M. H., Bennetts, L. G., Cavaliere, C., Alberello, A., & Toffoli, A. (2015). Exper-  
4015 imental and theoretical models of wave-induced flexure of a sea ice floe. *Physics of*  
4016 *Fluids*, 27(4), 041704.
- 4017 Meylan, M. H., Bennetts, L. G., & Kohout, A. L. (2014). In situ measurements and analysis  
4018 of ocean waves in the antarctic marginal ice zone. *Geophys. Res. Lett.*, 41(14), 5046–  
4019 5051.
- 4020 Meylan, M. H., Bennetts, L. G., Mosig, J. E. M., Rogers, W., Doble, M., & Peter, M. A.  
4021 (2018). Dispersion relations, power laws, and energy loss for waves in the marginal ice  
4022 zone. *J. Geophys. Res. Oceans*, 123(5), 3322–3335.
- 4023 Meylan, M. H., & Masson, D. (2006). A linear boltzmann equation to model wave scattering  
4024 in the marginal ice zone. *Ocean Model.*, 11(3-4), 417–427.
- 4025 Meylan, M. H., Perrie, W., Toulany, B., Hu, Y., & Casey, M. P. (2020). On the three-  
4026 dimensional scattering of waves by flexible marginal ice floes. *J. Geophys. Res. Oceans*,  
4027 125(12), e2019JC015868.
- 4028 Meylan, M. H., Squire, V. A., & Fox, C. (1997). Toward realism in modeling ocean wave  
4029 behavior in marginal ice zones. *J. Geophys. Res. Oceans*, 102(C10), 22981–22991.
- 4030 Middleton, J. H., Foster, T. D., & Foldvik, A. (1982). Low-frequency currents and conti-  
4031 nental shelf waves in the southern Weddell Sea. *J. Phys. Oceanogr.*, 12(7), 618–634.
- 4032 Middleton, J. H., Foster, T. D., & Foldvik, A. (1987). Diurnal Shelf Waves in the  
4033 Southern Weddell Sea. *J. Phys. Oceanogr.*, 17(6), 784–791. doi: [10.1175/1520-0485\(1987\)017<0784:DSWITS>2.0.CO;2](https://doi.org/10.1175/1520-0485(1987)017<0784:DSWITS>2.0.CO;2)
- 4034
- 4035 Middleton, L., Davis, P. E. D., Taylor, J. R., & Nicholls, K. W. (2022). Double Diffusion  
4036 As a Driver of Turbulence in the Stratified Boundary Layer Beneath George VI Ice  
4037 Shelf. *Geophys. Res. Lett.*, 49(5), e2021GL096119. doi: [10.1029/2021GL096119](https://doi.org/10.1029/2021GL096119)
- 4038 Miles, B. W. J., Stokes, C. R., & Jamieson, S. S. R. (2018). Velocity increases at cook glacier,  
4039 east Antarctica, linked to ice shelf loss and a subglacial flood event. *Cryosphere*,  
4040 12(10), 3123–3136.
- 4041 Moffat, C., Beardsley, R. C., Owens, B., & van Lipzig, N. (2008). A first description of the  
4042 Antarctic Peninsula Coastal Current. *Deep-Sea Research Part II: Topical Studies in*  
4043 *Oceanography*, 55(3-4), 277–293. doi: [10.1016/j.dsr2.2007.10.003](https://doi.org/10.1016/j.dsr2.2007.10.003)
- 4044 Mokus, N. G. A., & Montiel, F. (2021). Wave-triggered breakup in the marginal ice  
4045 zone generates lognormal floe size distributions. *The Cryosphere Discussions*. doi:  
4046 [10.5194/tc-2021-391](https://doi.org/10.5194/tc-2021-391)
- 4047 Molemaker, M. J., McWilliams, J. C., & Yavneh, I. (2005). Baroclinic instability and loss  
4048 of balance. *J. Phys. Oceanogr.*, 35(9), 1505–1517. doi: [10.1175/JPO2770.1](https://doi.org/10.1175/JPO2770.1)
- 4049 Monahan, E. C., Spiel, D. E., & Davidson, K. L. (1986). A model of marine aerosol  
4050 generation via whitecaps and wave disruption. In E. C. Monahan & G. M. Niocaill  
4051 (Eds.), *Oceanic Whitecaps* (Vol. 2, pp. 167–174). doi: [10.1007/978-94-009-4668-2\\_16](https://doi.org/10.1007/978-94-009-4668-2_16)
- 4052 Montiel, F., Bennetts, L. G., Squire, V. A., Bonnefoy, F., & Ferrant, P. (2013). Hydroelastic  
4053 response of floating elastic discs to regular waves. part 2. modal analysis. *Journal of*

- 4054 *Fluid Mechanics*, 723, 629–652.
- 4055 Montiel, F., Bonnefoy, F., Ferrant, P., Bennetts, L. G., Squire, V. A., & Marsault, P.  
4056 (2013). Hydroelastic response of floating elastic discs to regular waves. part 1. wave  
4057 basin experiments. *Journal of Fluid Mechanics*, 723, 604–628.
- 4058 Montiel, F., Kohout, A. L., & Roach, L. A. (2022). Physical drivers of ocean wave attenu-  
4059 ation in the marginal ice zone. *J. Phys. Oceanogr.*, 52(5), 889–906.
- 4060 Montiel, F., & Mokus, N. (2022). Theoretical framework for the emergent floe size dis-  
4061 tribution: the case for log-normality. *Philos. Trans. R. Soc. A*, 380, 20210257. doi:  
4062 [10.1098/rsta.2021.0257](https://doi.org/10.1098/rsta.2021.0257)
- 4063 Montiel, F., Squire, V., & Bennetts, L. G. (2016). Attenuation and directional spreading of  
4064 ocean wave spectra in the marginal ice zone. *J. Fluid Mech.*, 790, 492–522.
- 4065 Montiel, F., Squire, V., Doble, M., Thomson, J., & Wadhams, P. (2018). Attenuation and  
4066 directional spreading of ocean waves during a storm event in the autumn beaufort sea  
4067 marginal ice zone. *J. Geophys. Res. Oceans*, 123(8), 5912–5932.
- 4068 Montiel, F., & Squire, V. A. (2017). Modelling wave-induced sea ice break-up in the marginal  
4069 ice zone. *Proc. R. Soc. A.*, 473(2206), 20170258. doi: [10.1098/rspa.2017.0258](https://doi.org/10.1098/rspa.2017.0258)
- 4070 Moorman, R., Morrison, A. K., & Hogg, A. M. (2020). Thermal responses to Antarctic ice  
4071 shelf melt in an eddy rich global ocean—sea-ice model. *J. Climate*, 33, 6599–6620.  
4072 doi: [10.1175/jcli-d-19-0846.1](https://doi.org/10.1175/jcli-d-19-0846.1)
- 4073 Morales Maqueda, M., Willmott, A., & Biggs, N. (2004). Polynya dynamics: A review of  
4074 observations and modeling. *Rev. Geophys.*, 42(1).
- 4075 Morim, J., Hemer, M., Wang, X. L., Cartwright, N., Trenham, C., Semedo, A., ... oth-  
4076 ers (2019). Robustness and uncertainties in global multivariate wind-wave climate  
4077 projections. *Nat. Clim. Change*, 9(9), 711–718.
- 4078 Morim, J., Vitousek, S., Hemer, M., Reguero, B., Erikson, L., Casas-Prat, M., ... others  
4079 (2021). Global-scale changes to extreme ocean wave events due to anthropogenic  
4080 warming. *Environmental Research Letters*, 16(7), 074056.
- 4081 Morioka, Y., & Behera, S. K. (2021). Remote and local processes controlling decadal sea  
4082 ice variability in the Weddell Sea. *J. Geophys. Res. Oceans*, 126(8), e2020JC017036.
- 4083 Morlighem, M., Rignot, E., Binder, T., Blankenship, D., Drews, R., Eagles, G., ... others  
4084 (2020). Deep glacial troughs and stabilizing ridges unveiled beneath the margins of  
4085 the Antarctic ice sheet. *Nature Geoscience*, 13(2), 132–137.
- 4086 Morrison, A. K., Frölicher, T. L., & Sarmiento, J. L. (2015). Upwelling in the Southern  
4087 Ocean. *Phys. Today*, 68, 27–32.
- 4088 Morrison, A. K., & Hogg, A. M. (2013). On the relationship between Southern Ocean  
4089 overturning and ACC Transport. *J. Phys. Oceanogr.*, 43(1), 140–148.
- 4090 Morrison, A. K., Hogg, A. M., England, M. H., & Spence, P. (2020). Warm Circumpolar  
4091 Deep Water transport toward Antarctica driven by local dense water export in canyons.  
4092 *Sci. Adv.*, 6, 1–10. doi: [10.1126/sciadv.aav2516](https://doi.org/10.1126/sciadv.aav2516)
- 4093 Morrison, A. K., Huneke, W. G., Neme, J., Spence, P., Hogg, A. M., England, M. H., &  
4094 Griffies, S. M. (2023). Sensitivity of antarctic shelf waters and abyssal overturning to  
4095 local winds. *Journal of Climate*, 1–32.
- 4096 Morrison, A. K., Waugh, D. W., Hogg, A. M., Jones, D. C., & Abernathey, R. P. (2022).  
4097 Ventilation of the Southern Ocean Pycnocline. *Ann. Rev. Mar. Sci.*, 14(1), 1–26.
- 4098 Morrow, R., Coleman, R., Church, J., & Chelton, D. (1994). Surface eddy momentum  
4099 flux and velocity variances in the Southern Ocean from geosat altimetry. *J. Phys.  
4100 Oceanogr.*, 24(10), 2050–2071.
- 4101 Morrow, R., Fu, L.-L., Ardhuin, F., Benkiran, M., Chapron, B., Cosme, E., ... others  
4102 (2019). Global observations of fine-scale ocean surface topography with the surface  
4103 water and ocean topography (swot) mission. *Front. Mar. Sci.*, 6, 232.
- 4104 Mosig, J. E. M., Montiel, F., & Squire, V. A. (2015). Comparison of viscoelastic-type  
4105 models for ocean wave attenuation in ice-covered seas. *J. Geophys. Res. Oceans*,  
4106 120(9), 6072–6090.
- 4107 Mosig, J. E. M., Montiel, F., & Squire, V. A. (2019). A transport equation for flexural-  
4108 gravity wave propagation under a sea ice cover of variable thickness. *Wave Motion*,

- 88, 153–166.
- 4109 Moun, J. N. (2021). Variations in ocean mixing from seconds to years. *Ann. Rev. Mar.*  
4110 *Sci.*, *13*(1), null. doi: [10.1146/annurev-marine-031920-122846](https://doi.org/10.1146/annurev-marine-031920-122846)
- 4111 Muchow, M., Schmitt, A. U., & Kaleschke, L. (2021). A lead-width distribution for Antarctic  
4112 sea ice: a case study for the Weddell Sea with high-resolution Sentinel-2 images.  
4113 *Cryosphere*, *15*(9), 4527–4537.
- 4114 Mueller, R. D., Hattermann, T., Howard, S. L., & Padman, L. (2018). Tidal influences on a  
4115 future evolution of the filchner–ronne ice shelf cavity in the Weddell sea, Antarctica.  
4116 *Cryosphere*, *12*(2), 453–476.
- 4117 Muench, R., Padman, L., Gordon, A., & Orsi, A. (2009). A dense water outflow from  
4118 the Ross Sea, Antarctica: Mixing and the contribution of tides. *J. Mar. Syst.*, *77*,  
4119 369–387. doi: [10.1016/j.jmarsys.2008.11.003](https://doi.org/10.1016/j.jmarsys.2008.11.003)
- 4120 Munday, D. R., Johnson, H. L., & Marshall, D. P. (2013). Eddy saturation of equilibrated  
4121 circumpolar currents. *J. Phys. Oceanogr.*, *43*(3), 507–532. doi: [10.1175/JPO-D-12-095.1](https://doi.org/10.1175/JPO-D-12-095.1)
- 4122 Munk, W. H. (1966). Abyssal recipes. In *Deep sea research and oceanographic abstracts*  
4123 (Vol. 13, pp. 707–730).
- 4124 Munk, W. H., & Palmén, E. (1951). Note on the dynamics of the antarctic circumpolar  
4125 current. *Tellus*, *3*, 53–55. doi: [10.3402/tellusa.v3i1.8609](https://doi.org/10.3402/tellusa.v3i1.8609)
- 4126 Munk, W. H., & Wunsch, C. (1998). Abyssal recipes II: energetics of tidal and wind  
4127 mixing. *Deep-Sea Res. I: Oceanogr. Res. Pap.*, *45*(12), 1977–2010. doi: [10.1016/S0967-0637\(98\)00070-3](https://doi.org/10.1016/S0967-0637(98)00070-3)
- 4128 Musgrave, R. C., MacKinnon, J. A., Pinkel, R., Waterhouse, A. F., Nash, J., & Kelly, S. M.  
4129 (2017). The influence of subinertial internal tides on near-topographic turbulence at  
4130 the Mendocino ridge: Observations and modeling. *J. Phys. Oceanogr.*, *47*(8), 2139–  
4131 2154. doi: [10.1175/JPO-D-16-0278.1](https://doi.org/10.1175/JPO-D-16-0278.1)
- 4132 Musgrave, R. C., Pollmann, F., Kelly, S., & Nikurashin, M. (2022). The lifecycle of  
4133 topographically-generated internal waves. In *Ocean mixing* (pp. 117–144). Elsevier.
- 4134 Mysak, L. A. (1980). Topographically trapped waves. *Annu. Rev. Fluid Mech.*, *12*(1),  
4135 45–76.
- 4136 Nagai, T., & Hibiya, T. (2015). Internal tides and associated vertical mixing in the Indone-  
4137 sian Archipelago. *J. Geophys. Res. Oceans*, *120*(5), 3373–3390.
- 4138 Nagai, T., Tandon, A., Kunze, E., & Mahadevan, A. (2015). Spontaneous generation of  
4139 near-inertial waves by the kuroshio front. *J. Phys. Oceanogr.*, *45*(9), 2381–2406.
- 4140 Nakayama, Y., Menemenlis, D., Zhang, H., Schodlok, M., & Rignot, E. (2018). Origin of cir-  
4141 cumpolar deep water intruding onto the amundsen and bellingshausen sea continental  
4142 shelves. *Nat. Commun.*, *9*(1), 1–9.
- 4143 Nakayama, Y., Ohshima, K. I., Matsumura, Y., Fukamachi, Y., & Hasumi, H. (2014).  
4144 A numerical investigation of formation and variability of Antarctic Bottom water off  
4145 Cape Darnley, East Antarctica. *J. Phys. Oceanogr.*, *44*, 2921–2937. doi: [10.1175/JPO-D-14-0069.1](https://doi.org/10.1175/JPO-D-14-0069.1)
- 4146 Nakayama, Y., Timmermann, R., Rodehacke, C. B., Schröder, M., & Hellmer, H. H. (2014).  
4147 Modeling the spreading of glacial meltwater from the amundsen and bellingshausen  
4148 seas. *Geophys. Res. Lett.*, *41*(22), 7942–7949.
- 4149 Narayanan, A., Gille, S. T., Mazloff, M. R., & Murali, K. (2019). Water mass characteristics  
4150 of the antarctic margins and the production and seasonality of dense shelf water. *J.*  
4151 *Geophys. Res. Oceans*, *124*(12), 9277–9294.
- 4152 Naughten, K. A., Meissner, K. J., Galton-Fenzi, B. K., England, M. H., Timmermann, R.,  
4153 & Hellmer, H. H. (2018). Future projections of Antarctic ice shelf melting based on  
4154 CMIP5 scenarios. *J. Climate*, *31*, 5243–5261. doi: [10.1175/JCLI-D-17-0854.1](https://doi.org/10.1175/JCLI-D-17-0854.1)
- 4155 Naveira Garabato, A. C., Dotto, T., Hooley, J., Bacon, S., Tsamados, M., Ridout, A.,  
4156 ... others (2019). Phased response of the subpolar Southern Ocean to changes in  
4157 circumpolar winds. *Geophys. Res. Lett.*, *46*(11), 6024–6033.
- 4158 Naveira Garabato, A. C., Ferrari, R., & Polzin, K. L. (2011). Eddy stirring in the Southern  
4159 Ocean. *J. Geophys. Res. Oceans*, *116*(C9).

- 4164 Naveira Garabato, A. C., Forryan, A., Dutrieux, P., Brannigan, L., Biddle, L. C., Heywood,  
4165 K. J., ... Kimura, S. (2017). Vigorous lateral export of the meltwater outflow from  
4166 beneath an antarctic ice shelf. *Nature*, *542*(7640), 219–222.
- 4167 Naveira Garabato, A. C., Frajka-Williams, E. E., Spingys, C. P., Legg, S., Polzin, K. L.,  
4168 Forryan, A., ... Meredith, M. P. (2019). Rapid mixing and exchange of deep-  
4169 ocean waters in an abyssal boundary current. *Proc. Roy. Soc. Lond. A*. doi:  
4170 [10.1073/pnas.1904087116](https://doi.org/10.1073/pnas.1904087116)
- 4171 Naveira Garabato, A. C., Nurser, A. G., Scott, R. B., & Goff, J. A. (2013). The impact  
4172 of small-scale topography on the dynamical balance of the ocean. *J. Phys. Oceanogr.*,  
4173 *43*(3), 647–668.
- 4174 Naveira Garabato, A. C., Polzin, K. L., Ferrari, R., Zika, J. D., & Forryan, A. (2016). A  
4175 microscale view of mixing and overturning across the Antarctic Circumpolar Current.  
4176 *J. Phys. Oceanogr.*, *46*(1), 233–254. doi: [10.1175/JPO-D-15-0025.1](https://doi.org/10.1175/JPO-D-15-0025.1)
- 4177 Nelli, F., Bennetts, L. G., Skene, D. M., Monty, J., Lee, J., Meylan, M. H., & Toffoli, A.  
4178 (2017). Reflection and transmission of regular water waves by a thin, floating plate.  
4179 *Wave Motion*, *70*, 209–221.
- 4180 Nelli, F., Bennetts, L. G., Skene, D. M., & Toffoli, A. (2020). Water wave transmission  
4181 and energy dissipation by a floating plate in the presence of overwash. *J. Fluid Mech.*,  
4182 *889*.
- 4183 Neme, J., England, M. H., & Hogg, A. M. (2021). Seasonal and interannual variability of the  
4184 weddell gyre from a high-resolution global ocean-sea ice simulation during 1958–2018.  
4185 *J. Geophys. Res. Oceans*, *126*(11), e2021JC017662.
- 4186 Neme, J., England, M. H., & Hogg, A. M. (2022). Projected changes of surface winds over  
4187 the Antarctic continental margin. *Geophys. Res. Lett.*, *49*. doi: [10.1029/2022gl098820](https://doi.org/10.1029/2022gl098820)
- 4188 Newman, L., Heil, P., Trebilco, R., Katsumata, K., Constable, A., Van Wijk, E., ... others  
4189 (2019). Delivering sustained, coordinated, and integrated observations of the Southern  
4190 Ocean for global impact. *Front. Mar. Sci.*, *6*, 433. doi: [10.3389/fmars.2019.00433](https://doi.org/10.3389/fmars.2019.00433)
- 4191 Nicholls, K., Abrahamsen, E., Buck, J., Dodd, P., Goldblatt, C., Griffiths, G., ... others  
4192 (2006). Measurements beneath an antarctic ice shelf using an autonomous underwater  
4193 vehicle. *Geophys. Res. Lett.*, *33*(8).
- 4194 Nihashi, S., & Ohshima, K. (2015). Circumpolar mapping of Antarctic coastal polynyas  
4195 and landfast sea ice: Relationship and variability. *J. Climate*, *28*, 150220142648001.  
4196 doi: [10.1175/JCLI-D-14-00369.1](https://doi.org/10.1175/JCLI-D-14-00369.1)
- 4197 Nikurashin, M., & Ferrari, R. (2010). Radiation and dissipation of internal waves gener-  
4198 ated by geostrophic motions impinging on small-scale topography: Application to the  
4199 Southern Ocean. *J. Phys. Oceanogr.*, *40*(9), 2025–2042. doi: [10.1175/2010JPO4315.1](https://doi.org/10.1175/2010JPO4315.1)
- 4200 Nikurashin, M., & Ferrari, R. (2011). Global energy conversion rate from geostrophic flows  
4201 into internal lee waves in the deep ocean. *Geophys. Res. Lett.*, *38*(8), L08610. doi:  
4202 [10.1029/2011GL046576](https://doi.org/10.1029/2011GL046576)
- 4203 Nikurashin, M., & Ferrari, R. (2013). Overturning circulation driven by breaking in-  
4204 ternal waves in the deep ocean. *Geophys. Res. Lett.*, *40*(12), 3133–3137. doi:  
4205 [10.1002/grl.50542](https://doi.org/10.1002/grl.50542)
- 4206 Nikurashin, M., Ferrari, R., Grisouard, N., & Polzin, K. (2014). The impact of finite-  
4207 amplitude bottom topography on internal wave generation in the Southern Ocean. *J.*  
4208 *Phys. Oceanogr.*, *44*(11), 2938–2950. doi: [10.1175/JPO-D-13-0201.1](https://doi.org/10.1175/JPO-D-13-0201.1)
- 4209 Nikurashin, M., & Legg, S. (2011). A mechanism for local dissipation of internal  
4210 tides generated at rough topography. *J. Phys. Oceanogr.*, *41*(2), 378–395. doi:  
4211 [10.1175/2010JPO4522.1](https://doi.org/10.1175/2010JPO4522.1)
- 4212 Nikurashin, M., & Vallis, G. (2011). A Theory of Deep Stratification and Overturning Circu-  
4213 lation in the Ocean. *J. Phys. Oceanogr.*, *41*(3), 485–502. doi: [10.1175/2010JPO4529.1](https://doi.org/10.1175/2010JPO4529.1)
- 4214 Nikurashin, M., Vallis, G. K., & Adcroft, A. (2013). Routes to energy dissipation for  
4215 geostrophic flows in the Southern Ocean. *Nat. Geosci.*, *6*(1), 48–51.
- 4216 NISDC. (2023). National snow and ice data center.
- 4217 Noble, T. L., Rohling, E. J., Aitken, A. R. A., Bostock, H. C., Chase, Z., Gomez, N., ...  
4218 Williams, T. (2020). The sensitivity of the Antarctic Ice Sheet to a changing climate:

- 4219 Past, present, and future. *Rev. Geophys.*, 58(4). doi: [10.1029/2019RG000663](https://doi.org/10.1029/2019RG000663)
- 4220 Nøst, O. A., Biuw, M., Tverberg, V., Lydersen, C., Hattermann, T., Zhou, Q., ... Ko-
- 4221 vacs, K. M. (2011). Eddy overturning of the Antarctic Slope Front controls glacial
- 4222 melting in the Eastern Weddell Sea. *J. Geophys. Res. Oceans*, 116, C11014. doi:
- 4223 [10.1029/2011JC006965](https://doi.org/10.1029/2011JC006965)
- 4224 Nycander, J., Hieronymus, M., & Roquet, F. (2015). The nonlinear equation of state of sea
- 4225 water and the global water mass distribution. *Geophys. Res. Lett.*, 42, 7714–7721.
- 4226 Oggier, M., & Eicken, H. (2022). Seasonal evolution of granular and columnar sea ice pore
- 4227 microstructure and pore network connectivity. *J. Glaciol.*, 1–16.
- 4228 O’Grady, J., Hemer, M., McInnes, K., Trenham, C., & Stephenson, A. (2021). Projected
- 4229 incremental changes to extreme wind-driven wave heights for the twenty-first century.
- 4230 *Sci. Rep.*, 11(1), 1–8.
- 4231 Ohshima, K. I., Nihashi, S., & Iwamoto, K. (2016). Global view of sea-ice production in
- 4232 polynyas and its linkage to dense/bottom water formation. *Geoscience Letters*, 3(1),
- 4233 1–14.
- 4234 Olbers, D., Borowski, D., Völker, C., & Woelff, J.-O. (2004). The dynamical balance,
- 4235 transport and circulation of the Antarctic circumpolar current. *Antarctic Science*,
- 4236 16(4), 439–470.
- 4237 Olbers, D., & Visbeck, M. (2005). A model of the zonally averaged stratification and
- 4238 overturning in the Southern Ocean. *J. Phys. Oceanogr.*, 35(7), 1190–1205.
- 4239 Ong, E. Q. Y., Doddridge, E., Constantinou, N. C., Hogg, A. M., & England, M. H. (2023).
- 4240 Episodic Antarctic shelf intrusions of circumpolar deep water via canyons.
- 4241 (in review; arXiv:2304.13225) doi: [10.48550/arXiv.2304.13225](https://doi.org/10.48550/arXiv.2304.13225)
- 4242 Onorato, M., Osborne, A. R., & Serio, M. (2006). Modulational instability in crossing sea
- 4243 states: A possible mechanism for the formation of freak waves. *Physical review letters*,
- 4244 96(1), 014503.
- 4245 Onorato, M., Waseda, T., Toffoli, A., Cavaleri, L., Gramstad, O., Janssen, P. A. E. M.,
- 4246 ... Trulsen, K. (2009). Statistical properties of directional ocean waves: the role
- 4247 of the modulational instability in the formation of extreme events. *Phys. Rev. Lett.*,
- 4248 102(114502). doi: [10.1103/PhysRevLett.102.114502](https://doi.org/10.1103/PhysRevLett.102.114502)
- 4249 Orheim, O. (1987). Evolution of under water sides of ice shelves and icebergs. *Ann. Glaciol.*,
- 4250 9, 176–182.
- 4251 Orsi, A., Johnson, G., & Bullister, J. (1999). Circulation, mixing, and production of Antarc-
- 4252 tic bottom water. *Progress in Oceanography*, 43(1), 55-109. doi: [10.1016/S0079-](https://doi.org/10.1016/S0079-6611(99)00004-X)
- 4253 [6611\(99\)00004-X](https://doi.org/10.1016/S0079-6611(99)00004-X)
- 4254 Orsi, A. H., & Wiederwohl, C. L. (2009). A recount of Ross sea waters. *Deep-Sea Res. II:*
- 4255 *Top. Stud. Oceanogr.*, 56(13-14), 778–795.
- 4256 Orúe-Echevarría, D., Pelegrí, J. L., Alonso-González, I. J., Benítez-Barrios, V. M.,
- 4257 Emelianov, M., García-Olivares, A., ... others (2021). A view of the Brazil-Malvinas
- 4258 confluence, March 2015. *Deep-Sea Res. I: Oceanogr. Res. Pap.*, 172, 103533.
- 4259 Osborn, T. (1980). Estimates of the local rate of vertical diffusion from dissipation mea-
- 4260 surements. *J. Phys. Oceanogr.*, 10(1), 83–89.
- 4261 Padman, L., Howard, S. L., & Muench, R. (2006). Internal tide generation along the
- 4262 south scotia ridge. *Deep-Sea Res. II: Top. Stud. Oceanogr.*, 53(1), 157-171. doi:
- 4263 [10.1016/j.dsr2.2005.07.011](https://doi.org/10.1016/j.dsr2.2005.07.011)
- 4264 Padman, L., Howard, S. L., Orsi, A. H., & Muench, R. D. (2009). Tides of the northwestern
- 4265 Ross Sea and their impact on dense outflows of Antarctic bottom water. *Deep-Sea*
- 4266 *Res. II: Top. Stud. Oceanogr.*, 56(13), 818-834. doi: [10.1016/j.dsr2.2008.10.026](https://doi.org/10.1016/j.dsr2.2008.10.026)
- 4267 Padman, L., & Kottmeier, C. (2000). High-frequency ice motion and divergence in the
- 4268 Weddell Sea. *J. Geophys. Res. Oceans*, 105(C2), 3379–3400.
- 4269 Padman, L., Siegfried, M. R., & Fricker, H. A. (2018). Ocean tide influences on the antarctic
- 4270 and greenland ice sheets. *Rev. Geophys.*, 56(1), 142–184.
- 4271 Paolo, F. S., Fricker, H. A., & Padman, L. (2015). Volume loss from antarctic ice shelves is
- 4272 accelerating. *Science*, 348(6232), 327–331.

- 4273 Park, H.-S., & Stewart, A. L. (2016). An analytical model for wind-driven arctic summer  
4274 sea ice drift. *The cryosphere*, *10*(1), 227–244.
- 4275 Passerotti, G., Bennetts, L. G., von Bock und Polach, R. U. F., Alberello, A., Puolakka,  
4276 O., Dolatshah, A., . . . Toffoli, A. (2022). Interactions between irregular wave fields  
4277 and sea ice: A physical model for wave attenuation and ice breakup in an ice tank. *J.*  
4278 *Phys. Oceanogr.*, *52*(7), 1431–1446.
- 4279 Pauthenet, E., Sallée, J.-B., Schmidtke, S., & Nerini, D. (2021). Seasonal variation of the  
4280 Antarctic Slope Front occurrence and position estimated from an interpolated hydro-  
4281 graphic climatology. *J. Phys. Oceanogr.*, *51*, 1539–1557. doi: [10.1175/JPO-D-20-  
4282 0186.1](https://doi.org/10.1175/JPO-D-20-0186.1)
- 4283 Payne, A. J., Holland, P. R., Shepherd, A. P., Rutt, I. C., Jenkins, A., & Joughin, I. (2007).  
4284 Numerical modeling of ocean-ice interactions under pine island bay’s ice shelf. *J.*  
4285 *Geophys. Res. Oceans*, *112*(C10).
- 4286 Pellichero, V., Sallée, J.-B., Schmidtke, S., Roquet, F., & Charrassin, J.-B. (2017). The  
4287 ocean mixed layer under Southern Ocean sea-ice: Seasonal cycle and forcing. *J.*  
4288 *Geophys. Res. Oceans*, *122*(2), 1608–1633. doi: [10.1002/2016JC011970](https://doi.org/10.1002/2016JC011970)
- 4289 Peng, J.-P., Dräger-Dietel, J., North, R. P., & Umlauf, L. (2021). Diurnal variability of  
4290 frontal dynamics, instability, and turbulence in a submesoscale upwelling filament. *J.*  
4291 *Phys. Oceanogr.*, *51*(9), 2825–2843.
- 4292 Peng, J.-P., Holtermann, P., & Umlauf, L. (2020). Frontal instability and energy dissipation  
4293 in a submesoscale upwelling filament. *J. Phys. Oceanogr.*, *50*(7), 2017–2035.
- 4294 Perovich, D. K. (1996). *The optical properties of sea ice* (Vol. 96-1). US Army, Corps of  
4295 Engineers, Cold Regions Research and Engineering Laboratory.
- 4296 Perovich, D. K., & Gow, A. J. (1996). A quantitative description of sea ice inclusions. *J.*  
4297 *Geophys. Res. Oceans*, *101*(C8), 18327–18343.
- 4298 Peter, M. A., & Meylan, M. H. (2010). Water-wave scattering by vast fields of bodies. *SIAM*  
4299 *Journal on Applied Mathematics*, *70*(5), 1567–1586.
- 4300 Petersen, M. R., Jacobsen, D. W., Ringler, T. D., Hecht, M. W., & Maltrud, M. E. (2015).  
4301 Evaluation of the arbitrary Lagrangian–Eulerian vertical coordinate method in the  
4302 MPAS-ocean model. *Ocean Model.*, *86*, 93–113.
- 4303 Phillips, H. E., & Rintoul, S. R. (2000). Eddy variability and energetics from direct cur-  
4304 rent measurements in the antarctic circumpolar current south of australia. *J. Phys.*  
4305 *Oceanogr.*, *30*(12), 3050–3076.
- 4306 Pitt, J. P., Bennetts, L. G., Meylan, M. H., Massom, R. A., & Toffoli, A. (2022). Model  
4307 predictions of wave overwash extent into the marginal ice zone. *J. Geophys. Res.*  
4308 *Oceans*, e2022JC018707.
- 4309 Pollard, R. T., & Millard Jr, R. (1970). Comparison between observed and simulated  
4310 wind-generated inertial oscillations. In *Deep sea research and oceanographic abstracts*  
4311 (Vol. 17, pp. 813–821).
- 4312 Polzin, K. L. (2008). Mesoscale eddy–internal wave coupling. Part I: Symmetry, wave  
4313 capture, and results from the mid-ocean dynamics experiment. *J. Phys. Oceanogr.*,  
4314 *38*(11), 2556–2574.
- 4315 Polzin, K. L. (2009). An abyssal recipe. *Ocean Model.*, *30*(4), 298–309.
- 4316 Polzin, K. L. (2010). Mesoscale eddy–internal wave coupling. Part II: Energetics and results  
4317 from PolyMode. *J. Phys. Oceanogr.*, *40*(4), 789–801.
- 4318 Polzin, K. L., & Lvov, Y. V. (2011). Toward regional characterizations of the oceanic  
4319 internal wavefield. *Rev. Geophys.*, *49*(4), RG4003.
- 4320 Polzin, K. L., & McDougall, T. J. (2022). Chapter 7 – Mixing at the ocean’s bottom  
4321 boundary. In M. P. Meredith & A. C. Naveira Garabato (Eds.), *Ocean mixing* (p. 145-  
4322 180). Elsevier. doi: [10.1016/B978-0-12-821512-8.00014-1](https://doi.org/10.1016/B978-0-12-821512-8.00014-1)
- 4323 Polzin, K. L., Naveira Garabato, A. C., Abrahamsen, E. P., Jullion, L., & Meredith, M. P.  
4324 (2014). Boundary mixing in Orkney passage outflow. *J. Geophys. Res. Oceans*,  
4325 *119*(12), 8627–8645. doi: [10.1002/2014JC010099](https://doi.org/10.1002/2014JC010099)
- 4326 Polzin, K. L., Naveira Garabato, A. C., Huussen, T. N., Sloyan, B. M., & Waterman, S.  
4327 (2014). Finescale parameterizations of turbulent dissipation. *J. Geophys. Res.* doi:

- 4328 [10.1002/2013JC008979](https://doi.org/10.1002/2013JC008979)
- 4329 Polzin, K. L., Toole, J. M., Ledwell, J. R., & Schmitt, R. W. (1997). Spatial variability of  
4330 turbulent mixing in the abyssal ocean. *Science*, *276*(5309), 93–96. doi: [10.1126/sci-](https://doi.org/10.1126/science.276.5309.93)  
4331 [ence.276.5309.93](https://doi.org/10.1126/science.276.5309.93)
- 4332 Pringle, D., Eicken, H., Trodahl, H., & Backstrom, L. (2007). Thermal conductivity of  
4333 landfast antarctic and arctic sea ice. *J. Geophys. Res. Oceans*, *112*(C4).
- 4334 Pugh, D. (2004). *Changing sea levels, effects of tides, weather and climate*. Cambridge  
4335 University Press.
- 4336 Purich, A., & Doddridge, E. W. (2023). Record low antarctic sea ice coverage indicates a  
4337 new sea ice state. *Communications Earth and Environment*, *4*(1), 314.
- 4338 Purkey, S. G., & Johnson, G. C. (2013). Antarctic bottom water warming and freshening:  
4339 Contributions to sea level rise, ocean freshwater budgets, and global heat gain. *J.*  
4340 *Climate*, *26*(16), 6105–6122.
- 4341 Purkey, S. G., Johnson, G. C., Talley, L. D., Sloyan, B. M., Wijffels, S. E., Smethie, W., ...  
4342 Katsumata, K. (2019). Unabated bottom water warming and freshening in the south  
4343 pacific ocean. *J. Geophys. Res. Oceans*, *124*(3), 1778–1794.
- 4344 Purkey, S. G., Smethie Jr, W. M., Gebbie, G., Gordon, A. L., Sonnerup, R. E., Warner,  
4345 M. J., & Bullister, J. L. (2018). A synoptic view of the ventilation and circulation  
4346 of Antarctic bottom water from chlorofluorocarbons and natural tracers. *Annu. Rev.*  
4347 *Mar. Sci.*, *10*, 503–527.
- 4348 Qiao, F., Yuan, Y., Deng, J., Dai, D., & Song, Z. (2016). Wave-turbulence interaction-  
4349 induced vertical mixing and its effects in ocean and climate models. *Philos. Trans.*  
4350 *Royal Soc. A*, *374*(2065), 20150201. doi: [10.1098/rsta.2015.0201](https://doi.org/10.1098/rsta.2015.0201)
- 4351 Rabault, J., Sutherland, G., Jensen, A., Christensen, K. H., & Marchenko, A. (2019).  
4352 Experiments on wave propagation in grease ice: combined wave gauges and particle  
4353 image velocimetry measurements. *J. Fluid Mech.*, *864*, 876–898.
- 4354 Radko, T. (2013). *Double diffusive convection*. Cambridge University Press.
- 4355 Rama, J., Shakespeare, C. J., & Hogg, A. M. (2022). The wavelength dependence of the  
4356 propagation of near-inertial internal waves. *J. Phys. Oceanogr.*, *52*, 2493–2514. doi:  
4357 [10.1175/JPO-D-21-0266.1](https://doi.org/10.1175/JPO-D-21-0266.1)
- 4358 Ramadhan, A., Wagner, G. L., Hill, C., Campin, J.-M., Churavy, V., Besard, T., ... Mar-  
4359 shall, J. (2020). Oceananigans.jl: Fast and friendly geophysical fluid dynamics on  
4360 GPUs. *J. Open Source Softw.*, *5*(53), 2018. doi: [10.21105/joss.02018](https://doi.org/10.21105/joss.02018)
- 4361 Rapizo, H., Babanin, A. V., Schulz, E., Hemer, M. A., & Durrant, T. H. (2015). Observation  
4362 of wind-waves from a moored buoy in the Southern Ocean. *Ocean Dynamics*, *65*(9),  
4363 1275–1288.
- 4364 Rapp, R. J., & Melville, W. K. (1990). Laboratory measurements of deep-water breaking  
4365 waves. *Philos. Trans. R. Soc. A*, *331*(1622), 735–800.
- 4366 Ray, R. D., Boy, J.-P., Arbic, B. K., Egbert, G. D., Erofeeva, S. Y., Petrov, L., & Shriver,  
4367 J. F. (2021). The problematic  $\psi_1$  ocean tide. *Geophys. J. Int.*, *227*(2), 1181–1192.  
4368 doi: [10.1093/gji/ggab263](https://doi.org/10.1093/gji/ggab263)
- 4369 Reese, R., Gudmundsson, G. H., Levermann, A., & Winkelmann, R. (2018). The far reach  
4370 of ice-shelf thinning in Antarctica. *Nat. Clim. Change*, *8*(1), 53–57.
- 4371 Reid, P., & Massom, R. (2022). Change and variability in antarctic coastal exposure,  
4372 1979–2020. *Nat. Commun.*, *13*(1), 1–11.
- 4373 Ren, L., Speer, K., & Chassignet, E. P. (2011). The mixed layer salinity budget and sea ice  
4374 in the Southern Ocean. *J. Geophys. Res. Oceans*, *116*(C8).
- 4375 Renault, L., Molemaker, M. J., McWilliams, J. C., Shchepetkin, A. F., Lemarié, F., Chelton,  
4376 D., ... Hall, A. (2016). Modulation of wind work by oceanic current interaction  
4377 with the atmosphere. *J. Phys. Oceanogr.*, *46*(6), 1685–1704. doi: [10.1175/JPO-D-15-](https://doi.org/10.1175/JPO-D-15-0232.1)  
4378 [0232.1](https://doi.org/10.1175/JPO-D-15-0232.1)
- 4379 Rhines, P. B. (1970). Edge-, bottom-, and rossby waves in a rotating stratified fluid.  
4380 *Geophys. Astrophys. Fluid Dyn.*, *1*(3-4), 273–302.
- 4381 Rhines, P. B. (1977). The dynamics of unsteady currents. *The Sea*, *6*, 189–318.

- 4382 Rhines, P. B. (1979). Geostrophic turbulence. *Annu. Rev. Fluid Mech.*, *11*(1), 401–441.  
4383 doi: [10.1146/annurev.fl.11.010179.002153](https://doi.org/10.1146/annurev.fl.11.010179.002153)
- 4384 Richter, O., Gwyther, D. E., King, M. A., & Galton-Fenzi, B. K. (2022). The impact of  
4385 tides on Antarctic ice shelf melting. *Cryosphere*, *16*(4), 1409–1429. doi: [10.5194/tc-  
4386 16-1409-2022](https://doi.org/10.5194/tc-16-1409-2022)
- 4387 Rignot, E., Jacobs, S. S., Mouginot, J., & Scheuchl, B. (2013). Ice-shelf melting around  
4388 Antarctica. *Science*, *341*(6143), 266–270.
- 4389 Rijnsburger, S., Flores, R. P., Pietrzak, J. D., Lamb, K. G., Jones, N. L., Horner-Devine,  
4390 A. R., & Souza, A. J. (2021). Observations of multiple internal wave packets  
4391 in a tidal river plume. *J. Geophys. Res. Oceans*, *126*(8), e2020JC016575. doi:  
4392 [10.1029/2020JC016575](https://doi.org/10.1029/2020JC016575)
- 4393 Rimac, A., von Storch, J.-S., Eden, C., & Haak, H. (2013). The influence of high-resolution  
4394 wind stress field on the power input to near-inertial motions in the ocean. *Geophys.  
4395 Res. Lett.*, *40*(18), 4882–4886. doi: [10.1002/grl.50929](https://doi.org/10.1002/grl.50929)
- 4396 Rintoul, S. R. (2018). The global influence of localized dynamics in the Southern Ocean.  
4397 *Nature*, *558*(7709), 209–218.
- 4398 Rintoul, S. R., & Naveira Garabato, A. C. (2013). Dynamics of the Southern Ocean  
4399 Circulation. In *International Geophysics* (Vol. 103, pp. 471–492). Elsevier. doi:  
4400 [10.1016/B978-0-12-391851-2.00018-0](https://doi.org/10.1016/B978-0-12-391851-2.00018-0)
- 4401 Roach, C. J., & Speer, K. (2019). Exchange of water between the Ross Gyre and ACC  
4402 assessed by Lagrangian particle tracking. *J. Geophys. Res. Oceans*, *124*(7), 4631–  
4403 4643.
- 4404 Roberts, M. J., Jackson, L. C., Roberts, C. D., Meccia, V., Docquier, D., Koenigk, T., ...  
4405 others (2020). Sensitivity of the Atlantic meridional overturning circulation to model  
4406 resolution in CMIP6 HighResMIP simulations and implications for future changes. *J.  
4407 Adv. Model. Earth Syst.*, *12*(8), e2019MS002014.
- 4408 Robertson, R. (2001). Internal tides and baroclinicity in the southern Weddell Sea 2. effects  
4409 of the critical latitude and stratification. *J. Geophys. Res.*
- 4410 Robertson, R. (2013). Tidally induced increases in melting of amundsen sea ice shelves. *J.  
4411 Geophys. Res. Oceans*, *118*(6), 3138–3145.
- 4412 Robertson, R., Padman, L., & Egbert, G. D. (1985). Tides in the Weddell Sea. In *Ocean,  
4413 ice, and atmosphere: Interactions at the Antarctic continental margin* (p. 341–369).  
4414 American Geophysical Union (AGU). doi: [10.1029/AR075p0341](https://doi.org/10.1029/AR075p0341)
- 4415 Robertson, R., Padman, L., & Levine, M. D. (1995). Fine structure, microstructure, and  
4416 vertical mixing processes in the upper ocean in the western Weddell sea. *J. Geophys.  
4417 Res. Oceans*, *100*(C9), 18517–18535.
- 4418 Robinson, A. R. (1983). *Eddies in marine science*. Springer-Verlag.
- 4419 Robinson, I. (1981). Tidal vorticity and residual circulation. *Deep-Sea Res. I: Oceanogr.  
4420 Res. Pap.*, *28*(3), 195–212.
- 4421 Robinson, N. J., Stevens, C. L., & McPhee, M. G. (2017). Observations of amplified  
4422 roughness from crystal accretion in the sub-ice ocean boundary layer. *Geophys. Res.  
4423 Lett.*, *44*, 1814–1822. doi: [10.1002/2016GL071491](https://doi.org/10.1002/2016GL071491)
- 4424 Rocha, C. B., Chereskin, T. K., Gille, S. T., & Menemenlis, D. (2016). Mesoscale to  
4425 submesoscale wavenumber spectra in Drake Passage. *J. Phys. Oceanogr.*, *46*(2), 601–  
4426 620.
- 4427 Roemmich, D., Alford, M. H., Claustre, H., Johnson, K., King, B., Moum, J., ... others  
4428 (2019). On the future of Argo: A global, full-depth, multi-disciplinary array. *Front.  
4429 Mar. Sci.*, *6*.
- 4430 Roemmich, D., Church, J., Gilson, J., Monselesan, D., Sutton, P., & Wijffels, S. (2015).  
4431 Unabated planetary warming and its ocean structure since 2006. *Nat. Clim. Change*,  
4432 *5*(3), 240–245.
- 4433 Roquet, F., Williams, G., Hindell, M. A., Harcourt, R., McMahon, C., Guinet, C., ...  
4434 Fedak, M. (2014). A Southern Indian Ocean database of hydrographic profiles  
4435 obtained with instrumented elephant seals. *Scientific Data*, *1*(1), 140028. doi:  
4436 [10.1038/sdata.2014.28](https://doi.org/10.1038/sdata.2014.28)

- 4437 Rosevear, M. G., Galton-Fenzi, B., & Stevens, C. L. (2022). Evaluation of basal melting  
4438 parameterisations using in situ ocean and melting observations from the Amery Ice  
4439 Shelf, East Antarctica. *Ocean Science*, *18*(4), 1109–1130. doi: [10.5194/os-18-1109-  
4440 2022](https://doi.org/10.5194/os-18-1109-2022)
- 4441 Rosevear, M. G., Gayen, B., & Galton-Fenzi, B. K. (2022). Regimes and transitions in the  
4442 basal melting of antarctic ice shelves. *J. Phys. Oceanogr.*, *52*(10), 2589–2608.
- 4443 Rosier, S. H. R., Green, J. A. M., Scourse, J. D., & Winkelmann, R. (2014). Modeling  
4444 Antarctic tides in response to ice shelf thinning and retreat. *J. Geophys. Res. Oceans*,  
4445 *119*(1), 87–97. doi: [10.1002/2013JC009240](https://doi.org/10.1002/2013JC009240)
- 4446 Rosso, I., Hogg, A. M., Kiss, A. E., & Gayen, B. (2015). Topographic influence on submeso-  
4447 scale dynamics in the Southern Ocean. *Geophys. Res. Lett.*, *42*(4), 1139–1147.
- 4448 Rottier, P. J. (1992). Floe pair interaction event rates in the marginal ice zone. *J. Geophys.*  
4449 *Res. Oceans*, *97*(C6), 9391–9400.
- 4450 Ruan, X., Thompson, A. F., Flexas, M. M., & Sprintall, J. (2017). Contribution of topo-  
4451 graphically generated submesoscale turbulence to Southern Ocean overturning. *Nature*  
4452 *Geosci.*, *10*(11), 840–845. doi: [10.1038/ngeo3053](https://doi.org/10.1038/ngeo3053)
- 4453 Ryan, S., Schröder, M., Huhn, O., & Timmermann, R. (2016). On the warm inflow at the  
4454 eastern boundary of the weddell gyre. *Deep-Sea Res. I: Oceanogr. Res. Pap.*, *107*,  
4455 70–81.
- 4456 Saenko, O. A., Gupta, A. S., & Spence, P. (2012). On Challenges in Predicting Bot-  
4457 tom Water Transport in the Southern Ocean. *J. Climate*, *25*(4), 1349–1356. doi:  
4458 [10.1175/JCLI-D-11-00040.1](https://doi.org/10.1175/JCLI-D-11-00040.1)
- 4459 Sallée, J., Speer, K., Rintoul, S. R., & Wijffels, S. (2010). Southern Ocean thermocline  
4460 ventilation. *J. Phys. Oceanogr.*, *40*, 509–529.
- 4461 Sallée, J.-B., Wienders, N., Speer, K., & Morrow, R. (2006). Formation of subantarctic  
4462 mode water in the southeastern indian ocean. *Ocean Dynamics*, *56*(5), 525–542.
- 4463 Salmon, R. (1998). *Lectures on geophysical fluid dynamics*. Oxford University Press.
- 4464 Schlosser, T. L., Jones, N. L., Bluteau, C. E., Alford, M. H., Ivey, G. N., & Lucas, A. J.  
4465 (2019). Generation and propagation of near-inertial waves in a baroclinic current on  
4466 the tasmanian shelf. *J. Phys. Oceanogr.*, *49*(10), 2653–2667. doi: [10.1175/JPO-D-18-  
4467 0208.1](https://doi.org/10.1175/JPO-D-18-0208.1)
- 4468 Schlosser, T. L., Jones, N. L., Musgrave, R. C., Bluteau, C. E., Ivey, G. N., & Lucas, A. J.  
4469 (2019). Observations of diurnal coastal-trapped waves with a thermocline-intensified  
4470 velocity field. *J. Phys. Oceanogr.*, *49*(7), 1973–1994.
- 4471 Schmale, J., Baccarini, A., Thurnherr, I., Henning, S., Efraim, A., Regayre, L., ...  
4472 others (2019). Overview of the Antarctic circumnavigation expedition: Study of  
4473 preindustrial-like aerosols and their climate effects (ACE-SPACE). *Bull. Am. Meteoro-*  
4474 *rol. Soc.*, *100*(11), 2260–2283.
- 4475 Schmidt, B. E., Washam, P., Davis, P. E., Nicholls, K. W., Holland, D. M., Lawrence, J. D.,  
4476 ... others (2023a). Heterogeneous melting near the thwaites glacier grounding line.  
4477 *Nature*, *614*(7948), 471–478.
- 4478 Schmidt, B. E., Washam, P., Davis, P. E. D., Nicholls, K. W., Holland, D. M., Lawrence,  
4479 J. D., ... Makinson, K. (2023b). Heterogeneous melting near the thwaites glacier  
4480 grounding line. *Nature*, *614*(7948), 471–478. doi: [10.1038/s41586-022-05691-0](https://doi.org/10.1038/s41586-022-05691-0)
- 4481 Schodlok, M., Menemenlis, D., & Rignot, E. (2016). Ice shelf basal melt rates around a  
4482 ntarctica from simulations and observations. *J. Geophys. Res. Oceans*, *121*(2), 1085–  
4483 1109.
- 4484 Schroeter, S., O’Kane, T. J., & Sandery, P. A. (2023). Antarctic sea ice regime shift  
4485 associated with decreasing zonal symmetry in the southern annular mode. *Cryosphere*,  
4486 *17*(2), 701–717. doi: [10.5194/tc-17-701-2023](https://doi.org/10.5194/tc-17-701-2023)
- 4487 Schultz, C., Doney, S. C., Zhang, W. G., Regan, H., Holland, P., Meredith, M. P., &  
4488 Stammerjohn, S. (2020). Modeling of the influence of sea ice cycle and Langmuir  
4489 circulation on the upper ocean mixed layer depth and freshwater distribution at the  
4490 West Antarctic peninsula. *J. Geophys. Res. Oceans*, *125*(8), e2020JC016109. doi:  
4491 [10.1029/2020JC016109](https://doi.org/10.1029/2020JC016109)

- 4492 Scott, R. B., Goff, J. A., Naveira Garabato, A. C., & Nurser, A. J. G. (2011). Global rate  
4493 and spectral characteristics of internal gravity wave generation by geostrophic flow  
4494 over topography. *J. Geophys. Res. Oceans*, *116*(C9).
- 4495 Scott, R. B., & Wang, F. (2005). Direct evidence of an oceanic inverse kinetic energy  
4496 cascade from satellite altimetry. *J. Phys. Oceanogr.*, *35*, 1650–1666.
- 4497 Scott, R. B., & Xu, Y. (2009). An update on the wind power input to the surface geostrophic  
4498 flow of the World Ocean. *Deep-Sea Res. I: Oceanogr. Res. Pap.*, *56*(3), 295–304. doi:  
4499 [10.1016/j.dsr.2008.09.010](https://doi.org/10.1016/j.dsr.2008.09.010)
- 4500 Semedo, A., Sušelj, K., Rutgersson, A., & Sterl, A. (2011). A global view on the wind sea  
4501 and swell climate and variability from era-40. *J. Climate*, *24*(5), 1461–1479.
- 4502 Semper, S., & Darelius, E. (2017). Seasonal resonance of diurnal coastal trapped waves in  
4503 the southern Weddell Sea, antarctica. *Ocean Science*, *13*(1), 77–93.
- 4504 Shadwick, E. H., Rintoul, S. R., Tilbrook, B., Williams, G. D., Young, N., Fraser, A. D.,  
4505 ... Tamura, T. (2013). Glacier tongue calving reduced dense water formation and  
4506 enhanced carbon uptake. *Geophys. Res. Lett.*, *40*(5), 904–909. doi: [10.1002/grl.50178](https://doi.org/10.1002/grl.50178)
- 4507 Shakespeare, C. J. (2019). Spontaneous generation of internal waves. *Physics Today*, *72*(6),  
4508 34. doi: [10.1063/PT.3.4225](https://doi.org/10.1063/PT.3.4225)
- 4509 Shakespeare, C. J. (2020). Interdependence of internal tide and lee wave generation at  
4510 abyssal hills: global calculations. *J. Phys. Oceanogr.*, *50*, 655–677. doi: [10.1175/JPO-D-19-0179.1](https://doi.org/10.1175/JPO-D-19-0179.1)
- 4511 Shakespeare, C. J. (2023). Eddy acceleration and decay driven by internal tides. *Journal*  
4512 *of Physical Oceanography*, *53*(12), 2787–2796.
- 4513 Shakespeare, C. J., Arbic, B. K., & McC. Hogg, A. (2020). The drag on the barotropic tide  
4514 due to the generation of baroclinic motion. *J. Phys. Oceanogr.*, *50*(12), 3467–3481.
- 4515 Shakespeare, C. J., Arbic, B. K., & McC. Hogg, A. (2021). Dissipating and reflecting  
4516 internal waves. *J. Phys. Oceanogr.*, *51*(8), 2517–2531.
- 4517 Shakespeare, C. J., & Hogg, A. M. (2012). An analytical model of the response of the  
4518 meridional overturning circulation to changes in wind and buoyancy forcing. *J. Phys.*  
4519 *Oceanogr.*, *42*(8), 1270–1287.
- 4520 Shakespeare, C. J., & Hogg, A. M. (2017). Spontaneous surface generation and interior  
4521 amplification of internal waves in a regional-scale ocean model. *J. Phys. Oceanogr.*,  
4522 *47*(4), 811–826.
- 4523 Shakespeare, C. J., & Hogg, A. M. (2019). On the momentum flux of internal tides. *J.*  
4524 *Phys. Oceanogr.*, *49*(4), 993–1013. doi: [JPO-D-18-0165.1](https://doi.org/10.1175/JPO-D-18-0165.1)
- 4525 Shaw, W. J., & Stanton, T. P. (2014). Dynamic and double-diffusive instabilities in a weak  
4526 pycnocline. Part I: Observations of heat flux and diffusivity in the vicinity of Maud  
4527 Rise, Weddell Sea. *J. Phys. Oceanogr.*, *44*(8), 1973–1991. doi: [10.1175/JPO-D-13-](https://doi.org/10.1175/JPO-D-13-042.1)  
4528 [042.1](https://doi.org/10.1175/JPO-D-13-042.1)
- 4529 Sheen, K. L., Brearley, J. A., Naveira Garabato, A. C., Smeed, D., Laurent, L. S., Meredith,  
4530 M. P., ... Waterman, S. (2015). Modification of turbulent dissipation rates by a deep  
4531 Southern Ocean eddy. *Geophys. Res. Lett.*, *42*(9), 3450–3457.
- 4532 Sheen, K. L., Brearley, J. A., Naveira Garabato, A. C., Smeed, D. A., Waterman, S., Ledwell,  
4533 J. R., ... Watson, A. J. (2013). Rates and mechanisms of turbulent dissipation and  
4534 mixing in the Southern Ocean: Results from the diapycnal and isopycnal mixing  
4535 experiment in the Southern Ocean (DIMES). *J. Geophys. Res. Oceans*, *118*(6), 2774-  
4536 2792. doi: [10.1002/jgrc.20217](https://doi.org/10.1002/jgrc.20217)
- 4537 Sheen, K. L., Naveira Garabato, A. C., Brearley, J. A., Meredith, M. P., Polzin, K. L.,  
4538 Smeed, D. A., ... Watson, A. J. (2014). Eddy-induced variability in Southern  
4539 Ocean abyssal mixing on climatic timescales. *Nature Geosci.*, *7*(8), 577–582. doi:  
4540 [10.1038/ngeo2200](https://doi.org/10.1038/ngeo2200)
- 4541 Shen, H. H., & Ackley, S. F. (1991). A one-dimensional model for wave-induced ice-floe  
4542 collisions. *Ann. Glaciol.*, *15*, 87–95.
- 4543 Shen, H. H., & Squire, V. A. (1998). Wave damping in compact pancake ice fields due  
4544 to interactions between pancakes. *Antarctic Sea Ice: Physical Processes, Interactions*  
4545 *and Variability*, *74*, 325–341.
- 4546

- 4547 Shi, J.-R., Talley, L. D., Xie, S.-P., Liu, W., & Gille, S. T. (2020). Effects of buoyancy and  
4548 wind forcing on Southern Ocean climate change. *J. Climate*, *33*(23), 10003–10020.
- 4549 Shi, J.-R., Talley, L. D., Xie, S.-P., Peng, Q., & Liu, W. (2021). Ocean warming and  
4550 accelerating Southern Ocean zonal flow. *Nat. Clim. Change*, *11*(12), 1090–1097.
- 4551 Si, Y., Stewart, A. L., & Eisenman, I. (2021). Coupled ocean/sea ice dynamics of the  
4552 Antarctic Slope Current driven by topographic eddy suppression and sea ice momen-  
4553 tum redistribution. *J. Phys. Oceanogr.*. doi: [10.1175/JPO-D-21-0142.1](https://doi.org/10.1175/JPO-D-21-0142.1)
- 4554 Siegfried, M. R., & Fricker, H. A. (2018). Thirteen years of subglacial lake activity in  
4555 Antarctica from multi-mission satellite altimetry. *Ann. Glaciol.*, *59*(76), 42–55. doi:  
4556 [10.1017/aog.2017.36](https://doi.org/10.1017/aog.2017.36)
- 4557 Siems, S. T., Huang, Y., & Manton, M. J. (2022). Southern ocean precipitation: Toward a  
4558 process-level understanding. *Wiley Interdiscip. Rev. Clim. Change*, *13*(6), e800.
- 4559 Silvano, A., Foppert, A., Rintoul, S. R., Holland, P. R., Tamura, T., Kimura, N., ...  
4560 Macdonald, A. M. (2020). Recent recovery of Antarctic Bottom Water formation in  
4561 the Ross Sea driven by climate anomalies. *Nat. Geosci.*. doi: [10.1038/s41561-020-](https://doi.org/10.1038/s41561-020-00655-3)  
4562 [00655-3](https://doi.org/10.1038/s41561-020-00655-3)
- 4563 Silvano, A., Rintoul, S. R., & Herraiz-Borreguero, L. (2016). Ocean-ice shelf interaction in  
4564 east Antarctica. *Oceanography*, *29*(4), 130–143.
- 4565 Silvano, A., Rintoul, S. R., Peña-Molino, B., Hobbs, W. R., van Wijk, E., Aoki, S., ...  
4566 Williams, G. D. (2018). Freshening by glacial meltwater enhances melting of ice  
4567 shelves and reduces formation of Antarctic bottom water. *Sci. Adv.*, *4*(4), eaap9467.
- 4568 Simmonds, I., & Budd, W. F. (1991). Sensitivity of the southern hemisphere circulation  
4569 to leads in the antarctic pack ice. *Q. J. R. Meteorol. Soc.*, *117*(501), 1003–1024. doi:  
4570 [10.1002/qj.49711750107](https://doi.org/10.1002/qj.49711750107)
- 4571 Simmons, H. L., & Alford, M. H. (2012). Simulating the long-range swell of internal waves  
4572 generated by ocean storms. *Oceanography*, *25*(2), 30–41.
- 4573 Simmons, H. L., Hallberg, R. W., & Arbic, B. K. (2004). Internal wave generation in  
4574 a global baroclinic tide model. *Deep-Sea Res. II: Top. Stud. Oceanogr.*, *51*(25–26),  
4575 3043–3068.
- 4576 Sinha, A., & Abernathy, R. P. (2016). Time scales of Southern Ocean eddy equilibration.  
4577 *J. Phys. Oceanogr.*, *46*, 2785–2805. doi: [10.1175/JPO-D-16-0041.1](https://doi.org/10.1175/JPO-D-16-0041.1)
- 4578 Skardhamar, J., Skagseth, Ø., & Albretsen, J. (2015). Diurnal tides on the barents  
4579 sea continental slope. *Deep-Sea Res. I: Oceanogr. Res. Pap.*, *97*, 40–51. doi:  
4580 [doi.org/10.1016/j.dsr.2014.11.008](https://doi.org/10.1016/j.dsr.2014.11.008)
- 4581 Skene, D. M., Bennetts, L. G., Meylan, M. H., & Toffoli, A. (2015). Modelling water wave  
4582 overwash of a thin floating plate. *J. Fluid Mech.*, *777*.
- 4583 Skyllingstad, E. D., Smyth, W., & Crawford, G. (2000). Resonant wind-driven mixing in  
4584 the ocean boundary layer. *J. Phys. Oceanogr.*, *30*(8), 1866–1890.
- 4585 Sloyan, B. M., & Rintoul, S. R. (2001). The Southern Ocean limb of the global deep  
4586 overturning circulation. *J. Phys. Oceanogr.*, *31*, 143–173.
- 4587 Smedsrud, L. H., & Jenkins, A. (2004). Frazil ice formation in an ice shelf water plume. *J.*  
4588 *Geophys. Res. Oceans*, *109*(C3). doi: [10.1029/2003JC001851](https://doi.org/10.1029/2003JC001851)
- 4589 Smith, C. A., Speer, K. G., & Griffiths, R. W. (2014). Multiple zonal jets in a differentially  
4590 heated rotating annulus. *Journal of Physical Oceanography*, *44*(9), 2273–2291.
- 4591 Smith, M., & Thomson, J. (2019). Ocean surface turbulence in newly formed marginal ice  
4592 zones. *J. Geophys. Res. Oceans*, *124*(3), 1382–1398.
- 4593 Smith, S. D., Muench, R. D., & Pease, C. H. (1990). Polynyas and leads: An overview  
4594 of physical processes and environment. *J. Geophys. Res. Oceans*, *95*(C6), 9461–9479.  
4595 doi: [10.1029/JC095iC06p09461](https://doi.org/10.1029/JC095iC06p09461)
- 4596 Snow, K., Rintoul, S., Sloyan, B., & Hogg, A. M. (2018). Change in dense shelf water and  
4597 Adélie Land bottom water precipitated by iceberg calving. *Geophys. Res. Lett.*, *45*(5),  
4598 2380–2387.
- 4599 Sohail, T., Gayen, B., & Hogg, A. M. (2020). The dynamics of mixed layer deepening during  
4600 open ocean convection. *J. Phys. Oceanogr.*, *50*(6), 1625–1641. doi: [10.1175/JPO-D-](https://doi.org/10.1175/JPO-D-19-0264.1)  
4601 [19-0264.1](https://doi.org/10.1175/JPO-D-19-0264.1)

- 4602 Solodoch, A., Stewart, A. L., Hogg, A. M., Morrison, A. K., Kiss, A. E., Thompson, A. F.,  
 4603 ... Cimoli, L. (2022). How does Antarctic bottom water cross the Southern Ocean?  
 4604 *Geophys. Res. Lett.*, *49*(7), e2021GL097211.
- 4605 Speer, K., Rintoul, S. R., & Sloyan, B. (2000). The diabatic Deacon cell. *J. Phys. Oceanogr.*,  
 4606 *30*, 3212–3222.
- 4607 Squire, V. A. (2007). Of ocean waves and sea-ice revisited. *Cold Reg. Sci. Technol.*, *49*(2),  
 4608 110–133. doi: [10.1016/j.coldregions.2007.04.007](https://doi.org/10.1016/j.coldregions.2007.04.007)
- 4609 Squire, V. A. (2011). Past, present and impendent hydroelastic challenges in the polar and  
 4610 subpolar seas. *Philos. Trans. Royal Soc. A*, *369*(1947), 2813–2831.
- 4611 Squire, V. A. (2020). Ocean wave interactions with sea ice: A reappraisal. *Annu. Rev. Fluid  
 4612 Mech.*, *52*(1), 37–60. doi: [10.1146/annurev-fluid-010719-060301](https://doi.org/10.1146/annurev-fluid-010719-060301)
- 4613 Squire, V. A., Dugan, J. P., Wadhams, P., Rottier, P. J., & Liu, A. K. (1995). Of ocean  
 4614 waves and sea ice. *Annu. Rev. Fluid Mech.*, *27*(1), 115–168.
- 4615 Squire, V. A., & Montiel, F. (2016). Evolution of directional wave spectra in the marginal ice  
 4616 zone: a new model tested with legacy data. *J. Phys. Oceanogr.*, *46*(10), 3121–3137.
- 4617 Squire, V. A., & Moore, S. C. (1980). Direct measurement of the attenuation of ocean waves  
 4618 by pack ice. *Nature*, *283*(5745), 365–368.
- 4619 Stammer, D., Ray, R. D., Andersen, O. B., Arbic, B. K., Bosch, W., Carrère, L., ... Yi, Y.  
 4620 (2014). Accuracy assessment of global barotropic ocean tide models. *Rev. Geophys.*,  
 4621 *52*(3), 243–282. doi: [10.1002/2014RG000450](https://doi.org/10.1002/2014RG000450)
- 4622 Stanley, G. J. (2013). *From winds to eddies to diapycnal mixing of the deep ocean: The  
 4623 abyssal meridional overturning circulation driven by the surface wind-stress*. (MSc  
 4624 Thesis). University of Victoria.
- 4625 Stanley, G. J., Dowling, T. E., Bradley, M. E., & Marshall, D. P. (2020). Ertel potential  
 4626 vorticity versus bernoulli potential on approximately neutral surfaces in the antarctic  
 4627 circumpolar current. *J. Phys. Oceanogr.*, *50*(9), 2621–2648. doi: [10.1175/JPO-D-19-0140.1](https://doi.org/10.1175/JPO-D-19-0140.1)
- 4628 Stanley, G. J., & Saenko, O. A. (2014). Bottom-enhanced diapycnal mixing driven by  
 4629 mesoscale Eddies: Sensitivity to wind energy supply. *J. Phys. Oceanogr.*, *44*(1), 68–  
 4630 85. doi: [10.1175/JPO-D-13-0116.1](https://doi.org/10.1175/JPO-D-13-0116.1)
- 4631 Stanton, T., Shaw, W., Truffer, M., Corr, H., Peters, L., Riverman, K., ... Anandakrishnan,  
 4632 S. (2013). Channelized ice melting in the ocean boundary layer beneath Pine Island  
 4633 Glacier, Antarctica. *Science*, *341*(6151), 1236–1239. doi: [10.1126/science.1239373](https://doi.org/10.1126/science.1239373)
- 4634 Steele, M. (1992). Sea ice melting and floe geometry in a simple ice-ocean model. *J.  
 4635 Geophys. Res. Oceans*, *97*(C11), 17729–17738.
- 4636 Steiger, N., Darelus, E., Kimura, S., Patmore, R. D., & Wåhlin, A. K. (2022). The dynamics  
 4637 of a barotropic current impinging on an ice front. *J. Phys. Oceanogr.*
- 4638 Steur, L. d., Holland, D., Muench, R., & McPhee, M. (2007). The warm-water “Halo”  
 4639 around Maud Rise: Properties, dynamics and Impact. *Deep-Sea Res. I: Oceanogr.  
 4640 Res. Pap.*, *54*(6), 871–896. doi: [10.1016/j.dsr.2007.03.009](https://doi.org/10.1016/j.dsr.2007.03.009)
- 4641 Stevens, C. L., Hulbe, C., Brewer, M., Stewart, C. L., Robinson, N., Ohneiser, C., &  
 4642 Jendersie, S. (2020). Ocean mixing and heat transport processes observed under the  
 4643 ross ice shelf control its basal melting. *Proc. Natl. Acad. Sci. USA*, *117*(29), 16799–  
 4644 16804.
- 4645 Stevens, C. L., McPhee, M., Forrest, A., Leonard, G., Stanton, T., & Haskell, T. (2014). The  
 4646 influence of an Antarctic glacier tongue on near-field ocean circulation and mixing. *J.  
 4647 Geophys. Res. Oceans*, *119*(4), 2344–2362.
- 4648 Stevens, C. L., Robinson, N. J., Williams, M. J., & Haskell, T. G. (2009). Observations of  
 4649 turbulence beneath sea ice in southern McMurdo Sound, Antarctica. *Ocean Science*,  
 4650 *5*(4), 435–445.
- 4651 Stevens, C. L., Sirguey, P., Leonard, G., & Haskell, T. (2013). The 2013 Erebus glacier  
 4652 tongue calving event. *Cryosphere*, *7*(5), 1333–1337.
- 4653 Stewart, A. L. (2021). Warming spins up the Southern Ocean. *Nat. Clim. Chang.*, *11*,  
 4654 1022–1024. doi: [10.1038/s41558-021-01227-y](https://doi.org/10.1038/s41558-021-01227-y)

- 4656 Stewart, A. L., Chi, X., Solodoch, A., & Hogg, A. M. (2021). High-frequency fluctuations  
4657 in Antarctic Bottom Water transport driven by Southern Ocean winds. *Geophys. Res.*  
4658 *Lett.*, *48*(17). doi: [10.1029/2021gl094569](https://doi.org/10.1029/2021gl094569)
- 4659 Stewart, A. L., Klocker, A., & Menemenlis, D. (2018). Circum-Antarctic shoreward heat  
4660 transport derived from an eddy-and tide-resolving simulation. *Geophys. Res. Lett.*,  
4661 *45*(2), 834–845.
- 4662 Stewart, A. L., Klocker, A., & Menemenlis, D. (2019). Acceleration and overturning of the  
4663 Antarctic slope current by winds, eddies, and tides. *J. Phys. Oceanogr.*, *49*, 2043–2074.  
4664 doi: [10.1175/JPO-D-18-0221.1](https://doi.org/10.1175/JPO-D-18-0221.1)
- 4665 Stewart, A. L., & Thompson, A. F. (2015). Eddy-mediated transport of warm Circumpolar  
4666 Deep Water across the Antarctic Shelf Break. *Geophys. Res. Lett.*, *42*(2), 432–440.  
4667 doi: [10.1002/2014GL062281](https://doi.org/10.1002/2014GL062281)
- 4668 Stewart, C. L., Christoffersen, P., W., N. K., Williams, M. J., & Dowdeswell, J. A. (2019).  
4669 Basal melting of Ross ice shelf from solar heat absorption in an ice-front polynya.  
4670 *Seismological Research Letters*, *41561*. doi: [10.1038/s41561-019-0356-0](https://doi.org/10.1038/s41561-019-0356-0)
- 4671 Stommel, H. (1957). A survey of ocean current theory. *Deep Sea Research (1953)*, *4*,  
4672 149–184. doi: [10.1016/0146-6313\(56\)90048-x](https://doi.org/10.1016/0146-6313(56)90048-x)
- 4673 Stopa, J. E., Sutherland, P., & Arduin, F. (2018). Strong and highly variable push of ocean  
4674 waves on Southern Ocean sea ice. *Proc. Natl. Acad. Sci. USA*, *115*(23), 5861–5865.
- 4675 Straub, D. N. (1993). On the transport and angular momentum balance of channel mod-  
4676 els of the Antarctic Circumpolar Current. *J. Phys. Oceanogr.*, *23*, 776–782. doi:  
4677 [10.1175/1520-0485\(1993\)023<0776:OTTAAM>2.0.CO;2](https://doi.org/10.1175/1520-0485(1993)023<0776:OTTAAM>2.0.CO;2)
- 4678 Sun, S., Hattermann, T., Pattyn, F., Nicholls, K. W., Drews, R., & Berger, S. (2019).  
4679 Topographic shelf waves control seasonal melting near Antarctic ice shelf grounding  
4680 lines. *Geophys. Res. Lett.*, *46*(16), 9824–9832. doi: [10.1029/2019GL083881](https://doi.org/10.1029/2019GL083881)
- 4681 Sutherland, G., Rabault, J., Christensen, K. H., & Jensen, A. (2019). A two layer model  
4682 for wave dissipation in sea ice. *Applied Ocean Research*, *88*, 111–118.
- 4683 Sutherland, P., & Dumont, D. (2018). Marginal ice zone thickness and extent due to wave  
4684 radiation stress. *J. Phys. Oceanogr.*, *48*(8), 1885–1901.
- 4685 Swart, N. C., Fyfe, J. C., Gillett, N., & Marshall, G. J. (2015). Comparing trends in the  
4686 southern annular mode and surface westerly jet. *J. Climate*, *28*(22), 8840–8859.
- 4687 Swart, S., du Plessis, M. D., Thompson, A. F., Biddle, L. C., Giddy, I., Linders, T., ...  
4688 Nicholson, S.-A. (2020). Submesoscale fronts in the Antarctic marginal ice zone and  
4689 their response to wind forcing. *Geophys. Res. Lett.*, *47*(6), e2019GL086649. doi:  
4690 [10.1029/2019GL086649](https://doi.org/10.1029/2019GL086649)
- 4691 Swart, S., Gille, S. T., Delille, B., Josey, S., Mazloff, M., Newman, L., ... others (2019).  
4692 Constraining Southern Ocean air-sea-ice fluxes through enhanced observations. *Front.*  
4693 *Mar. Sci.*, *6*, 421.
- 4694 Takahashi, A., & Hibiya, T. (2019). Assessment of finescale parameterizations of deep  
4695 ocean mixing in the presence of geostrophic current shear: Results of microstructure  
4696 measurements in the Antarctic circumpolar current region. *J. Geophys. Res. Oceans*,  
4697 *124*(1), 135–153. doi: [10.1029/2018JC014030](https://doi.org/10.1029/2018JC014030)
- 4698 Talley, L. D. (2008). Freshwater transport estimates and the global overturning circulation:  
4699 Shallow, deep and throughflow components. *Progress in Oceanography*, *78*(4), 257–  
4700 303.
- 4701 Talley, L. D. (2013). Closure of the global overturning circulation through the Indian,  
4702 Pacific, and Southern Oceans: schematics and transports. *Oceanography*, *26*. doi:  
4703 [10.5670/oceanog.2013.07](https://doi.org/10.5670/oceanog.2013.07)
- 4704 Talley, L. D., Reid, J. L., & Robbins, P. E. (2003). Data-based meridional overturning  
4705 streamfunctions for the global ocean. *J. Climate*, *16*(19), 3213–3226.
- 4706 Tamsitt, V., Abernathey, R. P., Mazloff, M. R., Wang, J., & Talley, L. D. (2018). Trans-  
4707 formation of deep water masses along Lagrangian upwelling pathways in the Southern  
4708 Ocean. *J. Geophys. Res. Oceans*, *123*(3), 1994–2017.
- 4709 Tamsitt, V., Drake, H. F., Morrison, A. K., Talley, L. D., Dufour, C. O., Gray, A. R., ...  
4710 Weijer, W. (2017). Spiraling pathways of global deep waters to the surface of the

- 4711 Southern Ocean. *Nat. Commun.*, 8(1), 172.
- 4712 Tamura, T., Ohshima, K. I., & Nihashi, S. (2008). Mapping of sea ice production for  
4713 antarctic coastal polynyas. *Geophys. Res. Lett.*, 35(7).
- 4714 Tamura, T., Williams, G. D., Fraser, A. D., & Ohshima, K. I. (2012). Potential regime  
4715 shift in decreased sea ice production after the Mertz Glacier calving. *Nat. Commun.*,  
4716 3, 826. doi: [10.1038/ncomms1820](https://doi.org/10.1038/ncomms1820)
- 4717 Tan, J., Chen, X., Meng, J., Liao, G., Hu, X., & Du, T. (2022). Updated parameterization of  
4718 internal tidal mixing in the deep ocean based on laboratory rotating tank experiments.  
4719 *Deep Sea Research Part II: Topical Studies in Oceanography*, 202, 105141.
- 4720 Tansley, C. E., & Marshall, D. P. (2001). On the dynamics of wind-driven circumpolar  
4721 currents. *J. Phys. Oceanogr.*, 31, 3258-3273. doi: [10.1175/1520-  
4722 0485\(2001\)031<3258:OTDOWD>2.0.CO;2](https://doi.org/10.1175/1520-0485(2001)031<3258:OTDOWD>2.0.CO;2)
- 4723 Taylor, G. I. (1923). Experiments on the motion of solid bodies in rotating fluids. *Proc.*  
4724 *Math. Phys. Eng. Sci.*, 104(725), 213–218.
- 4725 Taylor, J. R., Bachman, S., Stamper, M., Hosegood, P., Adams, K. A., Sallee, J.-B., &  
4726 Torres, R. (2018). Submesoscale Rossby waves on the Antarctic circumpolar current.  
4727 *Sci. Adv.*, 4(3), eaao2824.
- 4728 Taylor, J. R., & Ferrari, R. (2009). On the equilibration of a symmetrically unstable front  
4729 via a secondary shear instability. *J. Fluid Mech.*, 622, 103–113.
- 4730 Taylor, J. R., & Thompson, A. F. (2022). Submesoscale dynamics in the upper ocean.  
4731 *Annu. Rev. Fluid Mech.*, 55, 2023.
- 4732 Teder, N. J., Bennetts, L. G., Reid, P. A., & Massom, R. A. (2022). Sea ice-free corridors  
4733 for large swell to reach antarctic ice shelves. *Environmental Research Letters*, 17(4),  
4734 045026.
- 4735 Terray, E. A., Donelan, M. A., Agrawal, Y. C., Drennan, W. M., Kahma, K. K., Williams,  
4736 A. J., ... Kitaigorodskii, S. A. (1996). Estimates of kinetic energy dissipation under  
4737 breaking waves. *J. Phys. Oceanogr.*, 26(5), 792–807.
- 4738 Thomas, D. N. (2017). *Sea ice*. John Wiley & Sons.
- 4739 Thomas, H., Friederike Prowe, A., Lima, I. D., Doney, S. C., Wanninkhof, R., Greatbatch,  
4740 R. J., ... Corbière, A. (2008). Changes in the North Atlantic Oscillation influence  
4741 CO2 uptake in the North Atlantic over the past 2 decades. *Global Biogeochem. Cycles*,  
4742 22(4).
- 4743 Thomas, L. N. (2005). Destruction of potential vorticity by winds. *J. Phys. Oceanogr.*,  
4744 35(12), 2457–2466.
- 4745 Thomas, L. N., & Shakespeare, C. J. (2015). A new mechanism for mode water formation in-  
4746 volving cabbeling and frontogenetic strain at thermohaline fronts. *J. Phys. Oceanogr.*,  
4747 45(9), 2444–2456.
- 4748 Thomas, L. N., Taylor, J. R., D’Asaro, E. A., Lee, C. M., Klymak, J. M., & Shcherbina, A.  
4749 (2016). Symmetric instability, inertial oscillations, and turbulence at the Gulf Stream  
4750 front. *J. Phys. Oceanogr.*, 46(1), 197–217.
- 4751 Thomas, L. N., Taylor, J. R., Ferrari, R., & Joyce, T. M. (2013). Symmetric instability in  
4752 the Gulf Stream. *Deep Sea Res. Part II*, 91, 96–110.
- 4753 Thomas, L. N., & Zhai, X. (2022). The lifecycle of surface-generated near-inertial waves.  
4754 In *Ocean mixing* (pp. 95–115). Elsevier.
- 4755 Thomas, M., France, J., Crabeck, O., Hall, B., Hof, V., Notz, D., ... others (2021). The  
4756 roland von Glasow air-sea-ice chamber (RvG-ASIC): an experimental facility for study-  
4757 ing ocean–sea-ice–atmosphere interactions. *Atmospheric Measurement Techniques*,  
4758 14(3), 1833–1849.
- 4759 Thompson, A. F. (2008). The atmospheric ocean: eddies and jets in the Antarctic  
4760 Circumpolar Current. *Phil. Trans. R. Soc. A*, 366(1885), 4529-4541. doi:  
4761 [10.1098/rsta.2008.0196](https://doi.org/10.1098/rsta.2008.0196)
- 4762 Thompson, A. F. (2010). Jet formation and evolution in baroclinic turbulence with simple  
4763 topography. *J. Phys. Oceanogr.*, 40(2), 257–278.
- 4764 Thompson, A. F., & Naveira Garabato, A. C. (2014). Equilibration of the Antarctic  
4765 Circumpolar Current by standing meanders. *J. Phys. Oceanogr.*, 44(7), 1811–1828.

- 4766 Thompson, A. F., & Sallée, J.-B. (2012). Jets and topography: Jet transitions and the  
4767 impact on transport in the Antarctic Circumpolar Current. *J. Phys. Oceanogr.*, *42*(6),  
4768 956–972.
- 4769 Thompson, A. F., Speer, K. G., & Chretien, L. M. S. (2020). Genesis of the Antarctic  
4770 Slope Current in West Antarctica Supplementary Material. *Geophys. Res. Lett.*, *47*,  
4771 e2020GL087802. doi: [10.1029/2020GL087802](https://doi.org/10.1029/2020GL087802)
- 4772 Thompson, A. F., Stewart, A. L., Spence, P., & Heywood, K. J. (2018). The Antarctic  
4773 slope current in a changing climate. *Rev. Geophys.*, *56*(4), 741–770.
- 4774 Thompson, D. W., Solomon, S., Kushner, P. J., England, M. H., Grise, K. M., & Karoly,  
4775 D. J. (2011). Signatures of the antarctic ozone hole in southern hemisphere surface  
4776 climate change. *Nat. Geosci.*, *4*(11), 741–749.
- 4777 Thompson, L., Smith, M., Thomson, J., Stammerjohn, S., Ackley, S., & Loose, B. (2020).  
4778 Frazil ice growth and production during katabatic wind events in the ross sea, antarc-  
4779 tica. *The Cryosphere*, *14*(10), 3329–3347.
- 4780 Thorpe, S. A. (2007). *An introduction to ocean turbulence*. Cambridge University Press.  
4781 doi: [10.1017/CBO9780511801198](https://doi.org/10.1017/CBO9780511801198)
- 4782 Thurnherr, I., Kozachek, A., Graf, P., Weng, Y., Bolshiyarov, D., Landwehr, S., ...  
4783 Aemisegger, F. (2020). Meridional and vertical variations of the water vapour isotopic  
4784 composition in the marine boundary layer over the atlantic and Southern Ocean. *At-  
4785 mospheric Chemistry and Physics*, *20*(9), 5811–5835. doi: [10.5194/acp-20-5811-2020](https://doi.org/10.5194/acp-20-5811-2020)
- 4786 Timco, G., & Weeks, W. (2010). A review of the engineering properties of sea ice. *Cold  
4787 Reg. Sci. Technol.*, *60*(2), 107–129.
- 4788 Timmermann, R., Hellmer, H. H., & Beckmann, A. (2002). Simulations of ice-ocean dy-  
4789 namics in the Weddell Sea 2. Interannual variability 1985–1993. *J. Geophys. Res.:  
4790 Oceans*, *107*(C3), 11–1-11-9. doi: [10.1029/2000jc000742](https://doi.org/10.1029/2000jc000742)
- 4791 Timmermans, B., Gommenginger, C., Dodet, G., & Bidlot, J.-R. (2020). Global wave height  
4792 trends and variability from new multimission satellite altimeter products, reanalyses,  
4793 and wave buoys. *Geophys. Res. Lett.*, *47*(9), e2019GL086880.
- 4794 Tinto, K. J., Padman, L., Siddoway, C. S., Springer, S. R., Fricker, H., Das, I., ... others  
4795 (2019). Ross ice shelf response to climate driven by the tectonic imprint on seafloor  
4796 bathymetry. *Nat. Geosci.*, *12*(6), 441–449.
- 4797 Toffoli, A., Babanin, A., Onorato, M., & Waseda, T. (2010). Maximum steepness of oceanic  
4798 waves: Field and laboratory experiments. *Geophys. Res. Lett.*, *37*(5).
- 4799 Toffoli, A., Bennetts, L. G., Meylan, M. H., Cavaliere, C., Alberello, A., Elsnab, J., &  
4800 Monty, J. P. (2015). Sea ice floes dissipate the energy of steep ocean waves. *Geophys.  
4801 Res. Lett.*, *42*(20), 8547–8554.
- 4802 Toffoli, A., Bitner-Gregersen, E. M., Osborne, A. R., Serio, M., Monbaliu, J., & Onorato,  
4803 M. (2011). Extreme waves in random crossing seas: Laboratory experiments and  
4804 numerical simulations. *Geophys. Res. Lett.*, *38*(6).
- 4805 Toffoli, A., McConochie, J., Ghantous, M., Loffredo, L., & Babanin, A. V. (2012). The effect  
4806 of wave-induced turbulence on the ocean mixed layer during tropical cyclones: Field  
4807 observations on the Australian North-West shelf. *J. Geophys. Res.*, *117*, C00J24.
- 4808 Toffoli, A., Proment, D., Salman, H., Monbaliu, J., Frascoli, F., Dafilis, M., ... Onorato,  
4809 M. (2017). Wind generated rogue waves in an annular wave flume. *Phys. Rev. Lett.*,  
4810 *118*(14), 144503.
- 4811 Toggweiler, J. R. (2009). Shifting westerlies. *Science*, *323*(5920), 1434–1435.
- 4812 Toggweiler, J. R., & Samuels, B. (1993). Is the magnitude of the deep outflow from the  
4813 Atlantic ocean actually governed by Southern hemisphere winds? In *The global carbon  
4814 cycle* (pp. 303–331). Springer Berlin Heidelberg. doi: [10.1007/978-3-642-84608-3\\_13](https://doi.org/10.1007/978-3-642-84608-3_13)
- 4815 Toggweiler, J. R., & Samuels, B. (1995). Effect of Drake passage on the global thermohaline  
4816 circulation. *Deep-Sea Res. I: Oceanogr. Res. Pap.*, *42*(4), 477–500. doi: [10.1016/0967-  
4817 0637\(95\)00012-U](https://doi.org/10.1016/0967-0637(95)00012-U)
- 4818 Toole, J. M., Schmitt, R. W., & Polzin, K. L. (1994). Estimates of diapycnal mixing in the  
4819 abyssal ocean. *Science*, *264*(5162), 1120–1123. doi: [10.1126/science.264.5162.1120](https://doi.org/10.1126/science.264.5162.1120)

- 4820 Torres, H. S., Klein, P., Wang, J., Wineteer, A., Qiu, B., Thompson, A. F., ... Perkovic-  
4821 Martin, D. (2022). Wind work at the air-sea interface: a modeling study in anticipation  
4822 of future space missions. *Geoscientific Model Development*, *15*(21), 8041–8058. doi:  
4823 [10.5194/gmd-15-8041-2022](https://doi.org/10.5194/gmd-15-8041-2022)
- 4824 Trodahl, H., Wilkinson, S., McGuinness, M., & Haskell, T. (2001). Thermal conductivity of  
4825 sea ice; dependence on temperature and depth. *Geophys. Res. Lett.*, *28*(7), 1279–1282.
- 4826 Trossman, D. S., Arbic, B. K., Richman, J. G., Garner, S. T., Jayne, S. R., & Wallcraft,  
4827 A. J. (2016). Impact of topographic internal lee wave drag on an eddying global ocean  
4828 model. *Ocean Model.*, *97*, 109–128.
- 4829 Trusel, L. D., Frey, K. E., Das, S. B., Karnauskas, K. B., Kuipers Munneke, P., Van Meij-  
4830 gaard, E., & Van Den Broeke, M. R. (2015). Divergent trajectories of antarctic surface  
4831 melt under two twenty-first-century climate scenarios. *Nat. Geosci.*, *8*(12), 927–932.
- 4832 Tsamados, M., Feltham, D. L., Schroeder, D., Flocco, D., Farrell, S. L., Kurtz, N., ...  
4833 Bacon, S. (2014). Impact of variable atmospheric and oceanic form drag on simulations  
4834 of arctic sea ice. *J. Phys. Oceanogr.*, *44*(5), 1329–1353.
- 4835 Turner, J., Holmes, C., Caton Harrison, T., Phillips, T., Jena, B., Reeves-Francois, T., ...  
4836 Bajjish, C. (2022). Record low Antarctic sea ice cover in February 2022. *Geophys.*  
4837 *Res. Lett.*, *49*(12), e2022GL098904.
- 4838 Uchida, T., Balwada, D., Abernathey, R. P., A. McKinley, G., K. Smith, S., & Lévy, M.  
4839 (2020). Vertical eddy iron fluxes support primary production in the open Southern  
4840 Ocean. *Nat. Commun.*, *11*(1), 1125. doi: [10.1038/s41467-020-14955-0](https://doi.org/10.1038/s41467-020-14955-0)
- 4841 Urakawa, L. S., & Hasumi, H. (2012). Eddy-resolving model estimate of the cabbeling effect  
4842 on the water mass transformation in the Southern Ocean. *J. Phys. Oceanogr.*, *42*(8),  
4843 1288–1302. doi: [10.1175/JPO-D-11-0173.1](https://doi.org/10.1175/JPO-D-11-0173.1)
- 4844 van Heijst, G. (1987). On the oceanic circulation near a shelf-ice edge. In *Dynamics of the*  
4845 *west antarctic ice sheet* (pp. 37–56). Springer.
- 4846 Vaňková, I., Cook, S., Winberry, J. P., Nicholls, K. W., & Galton-Fenzi, B. K. (2021).  
4847 Deriving melt rates at a complex ice shelf base using in situ radar: Application to  
4848 Totten ice shelf. *Geophys. Res. Lett.*, *48*(7), e2021GL092692.
- 4849 Vanneste, J. (2013). Balance and spontaneous wave generation in geophysical flows. *Annu.*  
4850 *Rev. Fluid Mech.*, *45*, 147–172.
- 4851 Van Vuuren, D. P., Edmonds, J., Kainuma, M., Riahi, K., Thomson, A., Hibbard, K., ...  
4852 others (2011). The representative concentration pathways: an overview. *Climatic*  
4853 *change*, *109*(1), 5–31.
- 4854 van Wijk, E. M., Rintoul, S. R., Wallace, L. O., Ribeiro, N., & Herraiz-Borreguero, L.  
4855 (2022). Vulnerability of denman glacier to ocean heat flux revealed by profiling float  
4856 observations. *Geophysical Research Letters*, *49*(18), e2022GL100460.
- 4857 Vaughan, G. L., Bennetts, L. G., & Squire, V. A. (2009). The decay of flexural-gravity  
4858 waves in long sea ice transects. *Proc. R. Soc. A*, *465*(2109), 2785–2812.
- 4859 Vaughan, G. L., & Squire, V. (2011). Wave induced fracture probabilities for arctic sea-ice.  
4860 *Cold regions science and technology*, *67*(1-2), 31–36.
- 4861 Venables, E., Nicholls, K., Wolk, F., Makinson, K., & Anker, P. (2014). Measuring turbulent  
4862 dissipation rates beneath an Antarctic ice shelf. *Marine Technology Society Journal*,  
4863 *48*(5), 18–24. doi: [10.4031/MTSJ.48.5.8](https://doi.org/10.4031/MTSJ.48.5.8)
- 4864 Vernet, M., Geibert, W., Hoppema, M., Brown, P. J., Haas, C., Hellmer, H., ... others  
4865 (2019). The weddell gyre, Southern Ocean: present knowledge and future challenges.  
4866 *Rev. Geophys.*, *57*(3), 623–708.
- 4867 Veron, F. (2015). Ocean spray. *Annu. Rev. Fluid Mech.*, *47*, 507–538.
- 4868 Vic, C., Naveira Garabato, A. C., Green, J. A. M., Waterhouse, A. F., Zhao, Z., Melet, A.,  
4869 ... Stephenson, G. R. (2019). Deep-ocean mixing driven by small-scale internal tides.  
4870 *Nat. Commun.*, *10*(1), 2099. doi: [10.1038/s41467-019-10149-5](https://doi.org/10.1038/s41467-019-10149-5)
- 4871 Vichi, M., Eayrs, C., Alberello, A., Bekker, A., Bennetts, L. G., Holland, D. M., ... others  
4872 (2019). Effects of an explosive polar cyclone crossing the Antarctic marginal ice zone.  
4873 *Geophys. Res. Lett.*, *46*(11), 5948–5958.

- 4874 Viebahn, J., & Eden, C. (2010). Towards the impact of eddies on the response of the  
4875 Southern Ocean to climate change. *Ocean Model.*, *34*(3-4), 150–165.
- 4876 Voermans, J. J., Babanin, A., Thomson, J., Smith, M., & Shen, H. (2019). Wave attenuation  
4877 by sea ice turbulence. *Geophys. Res. Lett.*, *46*(12), 6796–6803.
- 4878 Voermans, J. J., Liu, Q., Marchenko, A., Rabault, J., Filchuk, K., Ryzhov, I., . . . Babanin,  
4879 A. V. (2021). Wave dispersion and dissipation in landfast ice: comparison of observa-  
4880 tions against models. *Cryosphere*, *15*(7), 5557–5575. doi: [10.5194/tc-15-5557-2021](https://doi.org/10.5194/tc-15-5557-2021)
- 4881 Voermans, J. J., Rabault, J., Filchuk, K., Ryzhov, I., Heil, P., Marchenko, A., . . . Babanin,  
4882 A. V. (2020). Experimental evidence for a universal threshold characterizing wave-  
4883 induced sea ice break-up. *Cryosphere*, *14*(11), 4265–4278.
- 4884 Von Larcher, T., & Williams, P. D. (2014). *Modeling atmospheric and oceanic flows: insights*  
4885 *from laboratory experiments and numerical simulations* (Vol. 205). John Wiley &  
4886 Sons.
- 4887 von Storch, J.-S., & Lüschow, V. (2023). Wind power input to ocean near-inertial waves  
4888 diagnosed from a 5-km global coupled atmosphere-ocean general circulation model.  
4889 *Journal of Geophysical Research: Oceans*, *128*(2), e2022JC019111.
- 4890 Vreugdenhil, C. A., & Gayen, B. (2021). Ocean convection. *Fluids*, *6*(10), 360.
- 4891 Vreugdenhil, C. A., Griffiths, R. W., & Gayen, B. (2017). Geostrophic and chimney regimes  
4892 in rotating horizontal convection with imposed heat flux. *J. Fluid Mech.*, *823*, 57–99.
- 4893 Vreugdenhil, C. A., & Taylor, J. R. (2019). Stratification effects in the turbulent boundary  
4894 layer beneath a melting ice shelf: insights from resolved large-eddy simulations. *J.*  
4895 *Phys. Oceanogr.*, *49*(7), 1905–1925. doi: [10.1175/JPO-D-18-0252.1](https://doi.org/10.1175/JPO-D-18-0252.1)
- 4896 Wadhams, P. (1983). A mechanism for the formation of ice edge bands. *J. Geophys. Res.*  
4897 *Oceans*, *88*(C5), 2813–2818.
- 4898 Wadhams, P. (2000). *Ice in the ocean*. CRC Press.
- 4899 Wadhams, P., Gill, A., & Linden, P. (1979). Transects by submarine of the east greenland  
4900 polar front. *Deep-Sea Res. I: Oceanogr. Res. Pap.*, *26*(12), 1311–1327.
- 4901 Wadhams, P., Squire, V. A., Ewing, J., & Pascal, R. (1986). The effect of the marginal  
4902 ice zone on the directional wave spectrum of the ocean. *J. Phys. Oceanogr.*, *16*(2),  
4903 358–376.
- 4904 Wadhams, P., Squire, V. A., Goodman, D. J., Cowan, A. M., & Moore, S. C. (1988). The  
4905 attenuation rates of ocean waves in the marginal ice zone. *J. Geophys. Res. Oceans*,  
4906 *93*(C6), 6799–6818.
- 4907 Wählin, A. K., Steiger, N., Darelius, E., Assmann, K. M., Glessmer, M. S., Ha, H. K., . . .  
4908 others (2020). Ice front blocking of ocean heat transport to an Antarctic ice shelf.  
4909 *Nature*, *578*(7796), 568–571.
- 4910 Wang, H., Grisouard, N., Salehipour, H., Nuz, A., Poon, M., & Ponte, A. L. (2022). A  
4911 deep learning approach to extract internal tides scattered by geostrophic turbulence.  
4912 *Geophys. Res. Lett.*, *49*(11), e2022GL099400.
- 4913 Wang, Q., Danilov, S., Hellmer, H., Sidorenko, D., Schröter, J., & Jung, T. (2013). Enhanced  
4914 cross-shelf exchange by tides in the western Ross Sea. *Geophys. Res. Lett.*, *40*(21),  
4915 5735–5739. doi: [10.1002/2013GL058207](https://doi.org/10.1002/2013GL058207)
- 4916 Wang, Q., Danilov, S., & Schröter, J. (2009). Bottom water formation in the southern  
4917 Weddell Sea and the influence of submarine ridges: Idealized numerical simulations.  
4918 *Ocean Model.*, *28*(1-3), 50–59. doi: [10.1016/j.ocemod.2008.08.003](https://doi.org/10.1016/j.ocemod.2008.08.003)
- 4919 Wang, R., & Shen, H. H. (2010). Gravity waves propagating into an ice-covered ocean: A  
4920 viscoelastic model. *J. Geophys. Res. Oceans*, *115*(C6).
- 4921 Wang, Z., & Meredith, M. P. (2008). Density-driven southern hemisphere subpolar gyres  
4922 in coupled climate models. *Geophys. Res. Lett.*, *35*(14).
- 4923 Ward, M. L., & Hogg, A. M. (2011). Establishment of momentum balance by form stress  
4924 in a wind-driven channel. *Ocean Model.*, *40*(2), 133–146.
- 4925 Waterhouse, A. F., Kelly, S. M., Zhao, Z., MacKinnon, J. A., Nash, J. D., Simmons, H.,  
4926 . . . Pinkel, R. (2018). Observations of the Tasman Sea internal tide beam. *J. Phys.*  
4927 *Oceanogr.*, *48*(6), 1283–1297.

- 4928 Waterhouse, A. F., MacKinnon, J. A., Nash, J. D., Alford, M. H., Kunze, E., Simmons,  
4929 H. L., ... Lee, C. M. (2014). Global patterns of diapycnal mixing from measure-  
4930 ments of the turbulent dissipation rate. *J. Phys. Oceanogr.*, *44*(7), 1854–1872. doi:  
4931 [10.1175/JPO-D-13-0104.1](https://doi.org/10.1175/JPO-D-13-0104.1)
- 4932 Waterman, S., & Hoskins, B. J. (2013). Eddy shape, orientation, propagation, and mean  
4933 flow feedback in western boundary current jets. *J. Phys. Oceanogr.*, *43*(8), 1666–1690.
- 4934 Waterman, S., & Lilly, J. M. (2015). Geometric decomposition of eddy feedbacks in  
4935 barotropic systems. *J. Phys. Oceanogr.*, *45*(4), 1009–1024.
- 4936 Waterman, S., Meyer, A., Polzin, K. L., Naveira Garabato, A. C., & Sheen, K. L. (2021).  
4937 Antarctic circumpolar current impacts on internal wave life cycles. *Geophys. Res.*  
4938 *Let.*, *48*(8), e2020GL089471. doi: [10.1029/2020GL089471](https://doi.org/10.1029/2020GL089471)
- 4939 Waterman, S., Naveira Garabato, A. C., & Polzin, K. L. (2013). Internal waves and  
4940 turbulence in the Antarctic Circumpolar Current. *J. Phys. Oceanogr.*, *43*(2), 259–  
4941 282. doi: [10.1175/JPO-D-11-0194.1](https://doi.org/10.1175/JPO-D-11-0194.1)
- 4942 Waterman, S., Polzin, K. L., Naveira Garabato, A. C., Sheen, K. L., & Forryan, A. (2014).  
4943 Suppression of internal wave breaking in the Antarctic circumpolar current near to-  
4944 pography. *J. Phys. Oceanogr.*, *44*(5), 1466–1492.
- 4945 Waters, J. K., & Bruno, M. S. (1995). Internal wave generation by ice floes moving in  
4946 stratified water: Results from a laboratory study. *J. Geophys. Res. Oceans*, *100*(C7),  
4947 13635–13639. doi: [10.1029/95JC01220](https://doi.org/10.1029/95JC01220)
- 4948 Watson, A. J., Ledwell, J. R., Messias, M.-J., King, B. A., Mackay, N., Meredith, M. P., ...  
4949 Naveira Garabato, A. C. (2013). Rapid cross-density ocean mixing at mid-depths in  
4950 the Drake Passage measured by tracer release. *Nature*, *501*, 408–411. doi: [10.1038/na-  
4951 ture12432](https://doi.org/10.1038/nature12432)
- 4952 Watts, D. R., Tracey, K. L., Donohue, K. A., & Chereskin, T. K. (2016). Estimates of  
4953 eddy heat flux crossing the Antarctic Circumpolar Current from observations in Drake  
4954 Passage. *J. Phys. Oceanogr.*, *46*(7), 2103–2122. doi: [10.1175/JPO-D-16-0029.1](https://doi.org/10.1175/JPO-D-16-0029.1)
- 4955 Webb, D. J. (1993). A simple model of the effect of the Kerguelen Plateau on the strength of  
4956 the Antarctic Circumpolar Current. *Geophys. Astrophys. Fluid Dyn.*, *70*(1-4), 57–84.
- 4957 Weber, J. E. (1987). Wave attenuation and wave drift in the marginal ice zone. *J. Phys.*  
4958 *Oceanogr.*, *17*(12), 2351–2361.
- 4959 Weeks, W. (2010). *On sea ice*. University of Alaska Press.
- 4960 Wei, W., Blankenship, D. D., Greenbaum, J. S., Gourmelen, N., Dow, C. F., Richter, T. G.,  
4961 ... others (2020). Getz ice shelf melt enhanced by freshwater discharge from beneath  
4962 the West Antarctic ice sheet. *Cryosphere*, *14*(4), 1399–1408.
- 4963 Wei, Z., Zhang, Z., Wang, X., Chen, Y., & Zhou, M. (2022). The thermodynamic and  
4964 dynamic control of the sensible heat polynya in the western Cosmonaut Sea. *Deep-Sea*  
4965 *Res. II: Top. Stud. Oceanogr.*, *195*, 105000. doi: [10.1016/j.dsr2.2021.105000](https://doi.org/10.1016/j.dsr2.2021.105000)
- 4966 Weissenberger, J., Dieckmann, G., Gradinger, R., & Spindler, M. (1992). Sea ice: a cast  
4967 technique to examine and analyze brine pockets and channel structure. *Limnology and*  
4968 *Oceanography*, *37*(1), 179–183.
- 4969 Wells, A., Wettlaufer, J., & Orszag, S. (2011). Brine fluxes from growing sea ice. *Geophys.*  
4970 *Res. Let.*, *38*(4).
- 4971 Wells, A. J., Hitchen, J. R., & Parkinson, J. R. (2019). Mushy-layer growth and convection,  
4972 with application to sea ice. *Philos. Trans. Royal Soc. A*, *377*(2146), 20180165.
- 4973 Wenegrat, J. O., Callies, J., & Thomas, L. N. (2018). Submesoscale baroclinic instability  
4974 in the bottom boundary layer. *J. Phys. Oceanogr.*, *48*, 2571–2592. doi: [10.1175/JPO-D-  
4975 17-0264.1](https://doi.org/10.1175/JPO-D-17-0264.1)
- 4976 Wenegrat, J. O., & Thomas, L. N. (2020). Centrifugal and symmetric instability during  
4977 Ekman adjustment of the bottom boundary layer. *J. Phys. Oceanogr.*, *50*(6), 1793–  
4978 1812. doi: [10.1175/JPO-D-20-0027.1](https://doi.org/10.1175/JPO-D-20-0027.1)
- 4979 Whalen, C. B., de Lavergne, C., Naveira Garabato, A. C., Klymak, J. M., MacKinnon,  
4980 J. A., & Sheen, K. L. (2020). Internal wave-driven mixing: Governing processes and  
4981 consequences for climate. *Nat. Rev. Earth Environ.*, *1*, 606–621. doi: [10.1038/s43017-  
4982 020-0097-z](https://doi.org/10.1038/s43017-020-0097-z)

- 4983 Whalen, C. B., MacKinnon, J. A., & Talley, L. D. (2018). Large-scale impacts of the  
4984 mesoscale environment on mixing from wind-driven internal waves. *Nat. Geosci.*,  
4985 *11*(11), 842–847. doi: [10.1038/s41561-018-0213-6](https://doi.org/10.1038/s41561-018-0213-6)
- 4986 Whalen, C. B., MacKinnon, J. A., Talley, L. D., & Waterhouse, A. F. (2015). Estimating  
4987 the Mean Diapycnal Mixing Using a Finescale Strain Parameterization. *J. Phys.*  
4988 *Oceanogr.*, *45*(4), 1174–1188. doi: [10.1175/JPO-D-14-0167.1](https://doi.org/10.1175/JPO-D-14-0167.1)
- 4989 Whalen, C. B., Talley, L. D., & MacKinnon, J. A. (2012). Spatial and temporal variability  
4990 of global ocean mixing inferred from argo profiles. *Geophys. Res. Lett.*, *39*(18).
- 4991 White, B. S., & Fornberg, B. (1998). On the chance of freak waves at sea. *J. Fluid Mech.*,  
4992 *355*, 113–138.
- 4993 Whitt, D. B., Nicholson, S. A., & Carranza, M. M. (2019). Global impacts of subseasonal  
4994 (<60 day) wind variability on ocean surface stress, buoyancy flux, and mixed layer  
4995 depth. *J. Geophys. Res. Oceans*, *124*(12), 8798–8831. doi: [10.1029/2019JC015166](https://doi.org/10.1029/2019JC015166)
- 4996 Whitt, D. B., & Thomas, L. N. (2015). Resonant generation and energetics of wind-forced  
4997 near-inertial motions in a geostrophic flow. *J. Phys. Oceanogr.*, *45*(1), 181–208.
- 4998 Whitworth, T., & Orsi, A. H. (2006). Antarctic bottom water production and export by  
4999 tides in the Ross Sea. *Geophys. Res. Lett.*, *33*(12). doi: [10.1029/2006GL026357](https://doi.org/10.1029/2006GL026357)
- 5000 Wilkinson, M. D., Dumontier, M., Aalbersberg, I. J., Appleton, G., Axton, M., Baak, A.,  
5001 ... others (2016). The fair guiding principles for scientific data management and  
5002 stewardship. *Scientific data*, *3*(1), 1–9.
- 5003 Williams, R. G., Wilson, C., & Hughes, C. W. (2007). Ocean and atmosphere storm tracks:  
5004 The role of eddy vorticity forcing. *J. Phys. Oceanogr.*, *37*(9), 2267–2289.
- 5005 Williams, T. D., Bennetts, L. G., Squire, V. A., Dumont, D., & Bertino, L. (2013a). Wave–  
5006 ice interactions in the marginal ice zone. part 1: Theoretical foundations. *Ocean*  
5007 *Model.*, *71*, 81–91.
- 5008 Williams, T. D., Bennetts, L. G., Squire, V. A., Dumont, D., & Bertino, L. (2013b).  
5009 Wave–ice interactions in the marginal ice zone. part 2: Numerical implementation  
5010 and sensitivity studies along 1d transects of the ocean surface. *Ocean Model.*, *71*,  
5011 92–101.
- 5012 Williams, T. D., Rampal, P., & Bouillon, S. (2017). Wave–ice interactions in the nextsim  
5013 sea-ice model. *Cryosphere*, *11*(5), 2117–2135.
- 5014 Wilson, E. A., Riser, S. C., Campbell, E. C., & Wong, A. P. (2019). Winter upper-ocean  
5015 stability and ice–ocean feedbacks in the sea ice–covered Southern Ocean. *J. Phys.*  
5016 *Oceanogr.*, *49*(4), 1099–1117. doi: [10.1175/JPO-D-18-0184.1](https://doi.org/10.1175/JPO-D-18-0184.1)
- 5017 Wilson, E. A., Thompson, A. F., Stewart, A. L., & Sun, S. (2022). Bathymetric control  
5018 of subpolar gyres and the overturning circulation in the Southern Ocean. *J. Phys.*  
5019 *Oceanogr.*, *52*(2), 205–223.
- 5020 Wise, A., Harle, J., Bruciaferri, D., O’Dea, E., & Polton, J. (2022). The effect of vertical  
5021 coordinates on the accuracy of a shelf sea model. *Ocean Modelling*, *170*, 101935.
- 5022 Wolfe, C. L., & Cessi, P. (2015). Multiple regimes and low-frequency variability in the  
5023 quasi-adiabatic overturning circulation. *Journal of Physical Oceanography*, *45*(6),  
5024 1690–1708.
- 5025 Wolk, F., Lueck, R., & Laurent, L. S. (2009). Turbulence measurements from a glider. In  
5026 *Oceans* (pp. 1–6).
- 5027 Wong, A. P. S. (2005). Subantarctic Mode Water and Antarctic Intermediate Water in  
5028 the south Indian Ocean based on profiling float data 2000–2004. *J. Mar. Res.*, *63*,  
5029 789–812.
- 5030 Worster, M. G., Batchelor, G., & Moffatt, H. (2000). Solidification of fluids. *Perspectives*  
5031 *in Fluid Dynamics*, *742*, 393–446.
- 5032 Worster, M. G., & Jones, D. W. R. (2015). Sea-ice thermodynamics and brine drainage.  
5033 *Phil. Trans. R. Soc. A*, *373*(2045), 20140166.
- 5034 Wouters, B., Bonin, J. A., Chambers, D. P., Riva, R. E., Sasgen, I., & Wahr, J. (2014).  
5035 Grace, time-varying gravity, earth system dynamics and climate change. *Reports on*  
5036 *Progress in Physics*, *77*(11), 116801.

- 5037 Wright, C. J., Scott, R. B., Ailliot, P., & Furnival, D. (2014). Lee wave generation rates in  
5038 the deep ocean. *Geophys. Res. Lett.*, *41*(7), 2434–2440.
- 5039 Wright, C. J., Scott, R. B., Furnival, D., Ailliot, P., & Vermet, F. (2013). Global observations  
5040 of ocean-bottom subinertial current dissipation. *J. Phys. Oceanogr.*, *43*(2), 402–417.  
5041 doi: [10.1175/JPO-D-12-082.1](https://doi.org/10.1175/JPO-D-12-082.1)
- 5042 Wunsch, C. (1998). The work done by the wind on the oceanic general  
5043 circulation. *J. Phys. Oceanogr.*, *28*(11), 2332–2340. doi: [10.1175/1520-  
5044 0485\(1998\)028<2332:TWDBTW>2.0.CO;2](https://doi.org/10.1175/1520-0485(1998)028<2332:TWDBTW>2.0.CO;2)
- 5045 Wunsch, C., Ferrari, R., et al. (2004). Vertical mixing, energy, and the general circulation  
5046 of the oceans. *Annu. Rev. Fluid Mech.*, *36*(1), 281–314.
- 5047 Yamaguchi, R., & Suga, T. (2019). Trend and variability in global upper-ocean strat-  
5048 ification since the 1960s. *J. Geophys. Res. Oceans*, *124*(12), 8933–8948. doi:  
5049 [10.1029/2019JC015439](https://doi.org/10.1029/2019JC015439)
- 5050 Yang, L., Nikurashin, M., Hogg, A. M., & Sloyan, B. M. (2018). Energy loss from transient  
5051 eddies due to lee wave generation in the Southern Ocean. *J. Phys. Oceanogr.*, *48*(12),  
5052 2867–2885.
- 5053 Yang, L., Nikurashin, M., McC. Hogg, A., & Sloyan, B. M. (2021). The impact of lee waves  
5054 on the Southern Ocean circulation. *J. Phys. Oceanogr.*, *51*(9), 2933–2950.
- 5055 Yiew, L. J., G, Meylan, M., Thomas, G. A., & French, B. J. (2017). Wave-induced collisions  
5056 of thin floating disks. *Phys. Fluids*, *29*(12), 127102.
- 5057 Yoon, S.-T., Lee, W. S., Nam, S., Lee, C.-K., Yun, S., Heywood, K. J., ... others (2022).  
5058 Ice front retreat reconfigures meltwater-driven gyres modulating ocean heat delivery  
5059 to an Antarctic ice shelf. *Nat. Commun.*, *13*(1), 1–8.
- 5060 Young, I. R. (1999). *Wind generated ocean waves*. Elsevier.
- 5061 Young, I. R., & Donelan, M. A. (2018). On the determination of global ocean wind and wave  
5062 climate from satellite observations. *Remote Sensing of Environment*, *215*, 228–241.
- 5063 Young, I. R., Fontaine, E., Liu, Q., & Babanin, A. V. (2020). The wave climate of the  
5064 Southern Ocean. *J. Phys. Oceanogr.*, *50*(5), 1417–1433. doi: [10.1175/JPO-D-20-  
5065 0031.1](https://doi.org/10.1175/JPO-D-20-0031.1)
- 5066 Young, I. R., & Ribal, A. (2019). Multiplatform evaluation of global trends in wind speed  
5067 and wave height. *Science*, *364*(6440), 548–552. doi: [10.1126/science.aav9527](https://doi.org/10.1126/science.aav9527)
- 5068 Young, I. R., Zieger, S., & Babanin, A. V. (2011). Global trends in wind speed and wave  
5069 height. *Science*, *332*(6028), 451–455.
- 5070 Youngs, M. K., Thompson, A. F., Lazar, A., & Richards, K. J. (2017). ACC meanders,  
5071 energy transfer, and mixed barotropic–baroclinic instability. *J. Phys. Oceanogr.*, *47*,  
5072 1291–1305. doi: [10.1175/JPO-D-16-0160.1](https://doi.org/10.1175/JPO-D-16-0160.1)
- 5073 Yung, C. K., Morrison, A. K., & Hogg, A. M. (2022). Topographic hotspots of Southern  
5074 Ocean eddy upwelling. *Front. Mar. Sci.*, *9*, 855785. doi: [10.3389/fmars.2022.855785](https://doi.org/10.3389/fmars.2022.855785)
- 5075 Zanna, L., & Bolton, T. (2020). Data-driven equation discovery of ocean mesoscale closures.  
5076 *Geophys. Res. Lett.*, *47*(17), e2020GL088376.
- 5077 Zanna, L., & Bolton, T. (2021). Deep learning of unresolved turbulent ocean processes in  
5078 climate models. *Deep Learning for the Earth Sciences: A Comprehensive Approach to  
5079 Remote Sensing, Climate Science, and Geosciences*, 298–306.
- 5080 Zanna, L., Khatiwala, S., Gregory, J. M., Ison, J., & Heimbach, P. (2019). Global recon-  
5081 struction of historical ocean heat storage and transport. *Proc. Natl. Acad. Sci. USA*,  
5082 *116*, 1126–1131.
- 5083 Zanna, L., Mana, P. P., Anstey, J., David, T., & Bolton, T. (2017). Scale-aware deterministic  
5084 and stochastic parametrizations of eddy-mean flow interaction. *Ocean Modelling*, *111*,  
5085 66–80.
- 5086 Zaron, E. D. (2019). Baroclinic tidal sea level from exact-repeat mission altimetry. *J. Phys.  
5087 Oceanogr.*, *49*(1), 193–210.
- 5088 Zhai, X., Greatbatch, R. J., & Zhao, J. (2005). Enhanced vertical propagation of storm-  
5089 induced near-inertial energy in an eddying ocean channel model. *Geophys. Res. Lett.*,  
5090 *32*(18).

- 5091 Zhai, X., Johnson, H. L., & Marshall, D. P. (2010). Significant sink of ocean-eddy energy  
5092 near western boundaries. *Nat. Geosci.*, *3*(9), 608–612.
- 5093 Zhai, X., Johnson, H. L., Marshall, D. P., & Wunsch, C. (2012). On the wind power  
5094 input to the ocean general circulation. *J. Phys. Oceanogr.*, *42*(8), 1357–1365. doi:  
5095 [10.1175/JPO-D-12-09.1](https://doi.org/10.1175/JPO-D-12-09.1)
- 5096 Zhang, C., Perezhugin, P., Gultekin, C., Adcroft, A., Fernandez-Granda, C., & Zanna, L.  
5097 (2023). Implementation and evaluation of a machine learned mesoscale eddy parame-  
5098 terization into a numerical ocean circulation model. *arXiv preprint arXiv:2303.00962*.
- 5099 Zhang, H. J., Whalen, C. B., Kumar, N., & Purkey, S. G. (2021). Decreased stratification in  
5100 the abyssal southwest pacific basin and implications for the energy budget. *Geophys.*  
5101 *Res. Lett.*, *48*(19), e2021GL094322.
- 5102 Zhang, J. (2007). Increasing Antarctic sea ice under warming atmospheric and oceanic  
5103 conditions. *J. Climate*, *20*(11), 2515–2529. doi: [10.1175/JCLI4136.1](https://doi.org/10.1175/JCLI4136.1)
- 5104 Zhang, L., Delworth, T., Yang, X., & et al. (2022). The relative role of the subsurface  
5105 Southern Ocean in driving negative Antarctic sea ice extent anomalies in 2016–2021.  
5106 *Communications Earth & Environment*, *3*, 302. doi: [10.1038/s43247-022-00624-1](https://doi.org/10.1038/s43247-022-00624-1)
- 5107 Zhang, Y., Chambers, D., & Liang, X. (2021). Regional trends in southern ocean eddy  
5108 kinetic energy. *Journal of Geophysical Research: Oceans*, *126*(6), e2020JC016973.
- 5109 Zhao, X., & Shen, H. (2016). A diffusion approximation for ocean wave scatterings by  
5110 randomly distributed ice floes. *Ocean Model.*, *107*, 21–27.
- 5111 Zhao, Z., Alford, M. H., Simmons, H. L., Brazhnikov, D., & Pinkel, R. (2018). Satellite  
5112 investigation of the M2 internal tide in the Tasman Sea. *J. Phys. Oceanogr.*, *48*(3),  
5113 687–703.
- 5114 Zheng, K., & Nikurashin, M. (2019). Downstream propagation and remote dissipation of  
5115 internal waves in the Southern Ocean. *J. Phys. Oceanogr.*, *49*(7), 1873–1887.
- 5116 Zhou, L., Heuzé, C., & Mohrmann, M. (2022). Early winter triggering of the maud rise  
5117 polynya. *Geophys. Res. Lett.*, *49*(2), e2021GL096246.
- 5118 Zhou, L., Heuzé, C., & Mohrmann, M. (2023). Sea ice production in the 2016 and 2017 maud  
5119 rise polynyas. *Journal of Geophysical Research: Oceans*, *128*(2), e2022JC019148.